Development Strategies of Cocatalysts for Photocatalytic Conversion of Carbon Dioxide by Using Water as an Electron Donor

Xuanwen Xu

2022

Preface

Because of the growing energy and climate crises, green and sustainable energy technologies are urgently required. Although energy-generation strategies such as wind, nuclear, and hydropower have been developed in recent years, they have not completely resolved these crises. Further, some of these technologies pose risks to the environment. In contrast, the use of solar energy is environmentally friendly and sustainable, and the photocatalytic conversion of CO_2 using H_2O as an electron donor, which is a type of complete artificial photosynthesis, is considered a particularly promising technology. Many types of photocatalysts have been developed for the photocatalytic conversion of CO_2 in the presence of H_2O, for example, $NaTaO_3$, Ga_2O_3, and $SrTiO_3$. However, the current photocatalysts show very low selectivities, and, thus, appropriate cocatalysts are required.

In this thesis, the development of effective cocatalysts for the photocatalytic conversion of CO_2 using H_2O as the electron donor is discussed. In particular, the effect of cocatalysts on the CO evolution selectivity and activity over Ta- and Ga-based photocatalysts is reported.

The thesis is divided into three parts consisting of seven chapters. In the first part, the in situ addition of chromate ions as cocatalysts for enhancing CO evolution and suppressing H_2 production is discussed. The critical factors affecting the catalytic performance were systematically studied by characterization and photocatalytic experiments. In the second part, Zn-based non-metal compounds, such as $Zn(OH)_2$, and amorphous $ZnGa_2O_4$ and $ZnSiO_3$ as cocatalysts over a series of Ta- and Ga-based photocatalysts, including $ZnTa_2O_6$ and $ZnGa_2O_4$, are discussed. In addition, the use of $Cd(OH)_2$ as a cocatalyst is also discussed. The Cd^{2+} ions were found to suppress the O_2 reduction reaction on the CO evolution active sites. In the third part, the effects of the size and morphology of Ag nanoparticles loaded on $NaTaO_3$ on the performance of this photocatalyst for the photocatalytic conversion of CO_2 using H_2O as the electron donor

was investigated. It was found that larger polycrystalline Ag nanoparticles favored the production of CO. In addition, high selectivity toward CO evolution was achieved over the Ag-loaded β-Ga_2O_3 by using the optimal modification method for the Ag nanoparticles. Intriguingly, the high selectivity toward CO evolution over Ag-loaded β-Ga_2O_3 originates from the selective poisoning of the O_2 reduction reaction on the active sites for the formation of H_2.

The work described in this thesis was carried out in the group of Prof. Tsunehiro Tanaka and Prof. Kentaro Teramura at the Department of Molecular Engineering, Graduate School of Engineering, Kyoto University, Japan, from 2019 to 2022. I would like to thank Prof. Tsunehiro Tanaka and Prof. Kentaro Teramura for their supervision. During the doctoral course, they provided financial, technical, methodological, and conceptual support and guidance for my research. Without these, it would have been impossible to complete this thesis. In addition, I would like to thank Prof. Saburo Hosokawa and Dr. Hiroyuki Asakura for their helpful discussions, comments, and guidance.

I would also like to acknowledge Dr. Kazuki Tamai, Dr. Rui Pang, Dr. Kikkawa Soichi, and Dr. Shuying Wang for their help during my research. Further, I thank Mr. Hiroyuki Tanaka, Mr. Masashige Morishita, Ms. Yoko Yoshitake, and Ms. Mami Nishio for helping me during my time in Japan and study at Kyoto University. Finally, I add further thanks to Mr. Masaatsu Ishida, Ms. Sumika Yoshizawa, Mr. Shotaro Kidera, Mr. Yuto Nakatani, Ms. Sayaka Soma, Mr. Hiroki Matsuo, and Mr. Sotaro Honda.

Finally, I thank the China Scholarship Council and my family for supporting me during my time living and studying in Japan.

Xuanwen Xu

June 2022 in Kyoto University

Contents

General Introduction

1. Background

1.1. Energy and Environmental Challenges

Since the first industrial revolution, huge amounts of carbon dioxide (CO_2) have been emitted to the atmosphere as a result of the consumption of fossil fuels [1,2], and this has caused problems such as global warming [3,4] and rising sea levels [5]. Although various energy-generation technologies based on nuclear fuel [6], hydropower [7], and wind power [8] have been developed to reduce our dependence on fossil fuels, global warming has continued to increase. Further, some of these technologies, such as nuclear and wind power, have been proven to be harmful to the environment and ecology [9,10]. Therefore, of the non-fossil-fuel-based energy sources, solar energy [11] is the best choice for achieving green and sustainable power. Silicon [12] is currently the most widely used material in industrial solar-based electricity generation, but its manufacture by the Siemen's process is energy-intensive [13]. As a result, in recent years, interest in photocatalysis for the storage and conversion of solar energy has increased, for example, the photocatalytic conversion of biomass [14] and CO_2 [15] to value-added compounds, the development of photoelectrochemical cells [16], and overall water splitting for hydrogen generation [17].

1.2. Principles of Photocatalysis

As shown in Scheme 1(a), on light irradiation, the electrons in a typical semiconductor photocatalyst are excited from the valence band (VB) to the conduction band (CB) across the band gap. The photogenerated electrons and holes can be consumed by two pathways: (1) recombination or (2) reaction with acceptors and donors. The reduction and oxidation potentials of the photogenerated electrons and holes depend significantly on the characteristics of the CB and VB of each photocatalyst. To enable the use of solar energy in the visible region of the spectrum ($\lambda > 420$ nm) [18], Z-scheme photocatalysts are promising. Similar to natural photosynthesis, these systems comprise two photosystems (PS), PS I and PS II, and an electron mediator that enables charge-

carrier transport between the two PS, as shown in Scheme 1(b). For the transfer of electrons and holes between PS I and PS II, redox pairs such as Fe^{2+}/Fe^{3+} [19] and IO_3^-/I^- [20] are often used. For example, Domen et al. [21] developed all-solid-state Z-scheme RuO_x/$BiVO_4$:Mo/Au/La and Rh:$SrTiO_3$/Ru catalysts using Au as the electron and hole mediator for overall water splitting, achieving an efficiency of 1%.

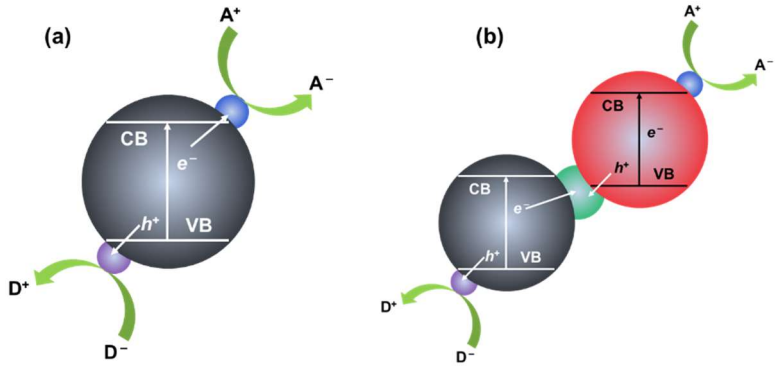

Scheme 1. Schematic of (a) a single photocatalyst and (b) Z-scheme photocatalyst showing PS I and PS II connected by the electron mediator. Here, CB and VB are the conduction and valence bands, respectively, e^- and h^+ are electrons and holes, respectively, and A and D electron acceptor and donor species, respectively.

1.3. Progress in Photocatalyst Development

The first photocatalyst was reported by Fujishima and Honda [22] in 1972. They found that the electrochemical activity of a TiO_2 electrode was enhanced by photoirradiation. Since then, many types of semiconductor photocatalysts have been developed. Photocatalysts can be classified using various criteria, for example, their water solubility or insolubility, such as in the case of supramolecular [23] and metal oxide [24] photocatalysts; structure, for example, organic [25], inorganic [26], or metal complex [27]; visible-light activity ($\lambda > 420$ nm); and band gap size. Photocatalysts with narrow band gaps, such as metal sulfides (e.g., $CuGaS_2$) [28], metal nitrides (e.g., Ta_3N_5) [29], and metal oxides (e.g., $BiVO_4$) [30] can be used for photocatalysis in the visible-light region. However, these materials cannot be used for the photocatalytic conversion of CO_2 because of their insufficient

reduction potentials. In comparison, photocatalysts with wide bandgaps, such as Ti-based (TiO_2 [31]), Ta-based ($NaTaO_3$ [32] and Ta_2O_5 [33]), and Ga-based (Ga_2O_3 [34] and $ZnGa_2O_4$ [35]) catalysts, show excellent performance for the evolution of O_2 from H_2O and H_2 and CO from protons and CO_2.

1.4. Role of Cocatalysts

Photocatalyst performance is significantly affected by (1) the rate of recombination of photogenerated electrons and holes and (2) the active sites for the evolution of H_2, O_2, and CO. By modifying a photocatalyst with an appropriate cocatalyst, high photocatalytic activity and product selectivity can be achieved. A typical strategy for suppressing the recombination of electrons and holes is to use charge-carrier trap species. For this purpose, Pt [36], Pd [37], Rh [38], and NiO [39] are excellent candidate cocatalysts. In addition, MnO_x [40], CoPi [41], CoOOH [42], and RuO_x [21] have been shown to have good performance as cocatalysts for the O_2 evolution reaction as a result of their good charge-carrier separation ability. The design of the active sites for the reduction of CO_2 is also important, and several strategies to enhance the photocatalytic conversion of CO_2 have been reported, including modification with halogens [43] and cyano groups [44], the addition of surface defects [45,46], and the introduction of frustrated Lewis pairs [47] and surface basicity [48] onto the photocatalyst surface.

2. Photocatalytic CO_2 Conversion

2.1. Electron Sources

Currently, highly active photocatalyst systems for the conversion of CO_2 use sacrificial reagents, such as triethanolamine (TEOA) [49], Na_2SO_3 [50], I^- [51], and S^{2-} [52]. Using these sacrificial reagents, the photocatalytic conversion of CO_2 over visible-light-active photocatalysts, such as metal-based polycarbazoles [53], g-C_3N_4 [54], and carbon nanoparticles [55], has been reported. However, the use of sacrificial reagents is unsuitable for industrial production because of the wastage and expense. In contrast, the use of H_2O as an electron donor would be perfect. Unfortunately, few photocatalysts for the photocatalytic conversion of CO_2 using H_2O as the electron donor have been reported. In

most cases, only photocatalysts having wide band gaps, such as Ga_2O_3 [56], $SrNb_2O_6$ [57], and $NaTaO_3$ [32], have been reported to achieve the photocatalytic conversion of CO_2 using H_2O as the electron donor.

2.2. Criteria for the Successful Photocatalytic Conversion of CO_2 using H_2O as the Electron Donor

Two criteria are crucial for the photocatalytic conversion of CO_2 using H_2O as the electron donor. One is the balance between the electrons provided by H_2O (O_2 evolution) and those consumed by CO_2 and protons (CH_xO_y and H_2 evolution), as shown in Equation (1). The other is the selectivity of the products derived from the photoreduction of CO_2 by the H_2 produced from water splitting, as shown in Equation (2).

$$e^-/h^+ = (2R_{HCOOH} + 2R_{CO} + 4R_{HCHO} + 6R_{CH_3OH} + 8R_{CH_4} + 2R_{H_2})/4R_{O_2} \quad (1)$$

$$\text{Selectivity} = (2R_{HCOOH} + 2R_{CO} + 4R_{HCHO} + 6R_{CH_3OH} + 8R_{CH_4})/(2R_{HCOOH} + 2R_{CO} + 4R_{HCHO} + 6R_{CH_3OH} + 8R_{CH_4} + 2R_{H_2}) \times 100\% \quad (2)$$

Here, R represents the rate of formation of each product formed by the photocatalytic conversion of CO_2 using H_2O as the electron donor.

However, achieving a higher selectivity toward carbon products, such as CO, CH_3OH, and CH_4, is difficult because water splitting is a strongly competitive reaction. As listed in Table 1 [58], the reduction potential of protons in water is much lower than those of HCOOH, CO, and HCHO; thus, the evolution of H_2 in the photocatalytic conversion of CO_2 using H_2O as the electron donor dominates the consumption of the photogenerated electrons. Although the required potentials for the formation of CH_3OH and CH_4 are lower than that of H_2, these reactions require a high concentration of protons, which will inevitably suppress the dissolution of CO_2. Further, the photocatalytic conversion of CO_2 is difficult because of its low solubility, as shown by the importance of using $NaHCO_3$ as an additive, which enhances the dissolution of CO_2 in the reactions[32,57].

Table 1. Potentials (*E*) vs. the normal hydrogen electrode (NHE) at pH 7.0 required to produce HCOOH, CO, HCHO, CH_3OH, CH_4, and H_2.

Reaction	E (V vs. NHE) at pH 7.0	Equation
$CO_2 + 2H^+ + 2e^- \rightarrow HCOOH$	-0.665	(1)
$CO_2 + 2H^+ + 2e^- \rightarrow CO + H_2O$	-0.521	(2)
$CO_2 + 4H^+ + 4e^- \rightarrow HCHO + H_2O$	-0.485	(3)
$CO_2 + 6H^+ + 6e^- \rightarrow CH_3OH + H_2O$	-0.399	(4)
$CO_2 + 8H^+ + 8e^- \rightarrow CH_4 + H_2O$	-0.246	(5)
$2H^+ + 2e^- \rightarrow H_2$	-0.414	(6)

2.3. Progress in the Highly Selective Photocatalytic Conversion of CO_2 Using H_2O as the Electron Donor

Although many materials, such as metal–organic frameworks (MOF) [59], covalent organic frameworks (COF) [60], metal carbides [61], and metal complexes [62], have been reported to be selective for the evolution of CO in the photocatalytic conversion of CO_2, few are capable of using H_2O as the electron donor, and few such catalysts have been reported to date. Of the reported examples, Ag-loaded $BaLa_4Ti_4O_{15}$, which was reported by Kudo et al. [63], was the first material that produced CO (61.4%) in excess of H_2 with stoichiometric amounts of O_2 evolved simultaneously. Recently, higher CO selectivity and photocatalytic activity was achieved by using Sr-doped $NaTaO_3$ with Ag nanoparticles as the cocatalyst. Recently, Yoshida et al. reported Ag-loaded $M_2Ti_6O_{13}$ (M: Na [64] and K [65]) and $CaTiO_3$ [66] for the photocatalytic conversion of CO_2 using H_2O as the electron donor. However, these photocatalysts all require Ag nanoparticle cocatalysts for the generation of carbon products, thus revealing the crucial role of cocatalysts in the photocatalytic conversion of CO_2 in the presence of H_2O.

3. Cocatalysts Matter: Highly Selective Photocatalytic Conversion of CO_2 Using H_2O as the Electron Donor

3.1 Metal Cocatalysts

3.1.1 Comparison of Pt, Pd, Au, Cu, Zn, and Ag

Although metals such as Pt [67], Pd [68], Au [69–71], Cu [72], and Zn [73] exhibit excellent performance in the electrochemical reduction of CO_2, they have rarely been reported as cocatalysts for the photocatalytic conversion of CO_2 in aqueous solution. Crucially, the H_2 formation rates over these cocatalysts far exceed those of CO. Iguchi et al. recently compared a series of metal cocatalysts for the photocatalytic conversion of CO_2 using H_2O as the electron donor, including Pt, Pd, Au, Cu, and Ag [37], with $ZnTa_2O_6$, which was synthesized through a solid-state reaction method. The results indicated that trace amounts of CO were produced with Pt, Pd, Au, and Cu as cocatalysts, and only Ag nanoparticles yielded significant CO selectivity (43.4%). This was also confirmed by Pang et al. [36], who found that a Ag nanoparticle cocatalyst covered with a $Cr(OH)_3$ shell on Ga_2O_3 produced CO at a rate of 480.3 μmol h^{-1}. In contrast, when using Au, Pd, or Pt cocatalysts with a $Cr(OH)_3$ shell, the CO formation rates were less than 0.5 μmol h^{-1}.

3.1.2 Ag Nanoparticles

Thus, to date, only Ag nanoparticles have been shown to exhibit high selectivity and activity for the photocatalytic conversion of CO_2 in aqueous solution, as shown by reports of their use with metal oxide photocatalysts based on Nb, Ti, Ta, and Ga. For example, Pang et al. [57] reported Ag-modified $SrNb_2O_6$, which yielded CO at a rate of 51.2 μmol h^{-1} and had a CO selectivity of approximately 98.0%. In addition to Ag-loaded $BLa_4Ti_4O_{15}$, $La_2Ti_2O_7$ modified with Ag nanoparticles yielded a higher CO formation rate than that of H_2 in pure water, as reported by Wang et al. [74]. Moreover, Zhu et al. reported Ag-loaded $Na_2Ti_6O_{13}$ [64], which yielded a CO selectivity of 90.0%, and the selectivity exceeded 95.0% when the Ag nanoparticles were loaded on $K_2Ti_6O_{13}$ [65] and $CaTiO_3$ [66].

Ag nanoparticles loaded on $NaTaO_3$ doped with alkaline earth elements, including Ca, Sr, and Ba, have also been shown to enhance the photocatalytic production of CO,

yielding a CO formation rate of 176 μmol h^{-1} and selectivities of greater than 90% [32]. Similarly, Iguchi et al. [37] reported a Ag-loaded $ZnTa_2O_6$ photocatalyst having a CO selectivity of 43.4%. Wang et al. [75] also found that Ag nanoparticles on Zn-modified $ZnTa_2O_6$ resulted in excellent photocatalytic performance. Crucially, the H_2 evolution activity was effectively suppressed. For other Ta-based photocatalysts such as Sr-doped Ta_2O_5 [33] and $A_2BTa_5O_{15}$ (A = Sr or Ba and B = K or Na) [76–79], modification with Ag nanoparticles was also found to result in enhanced CO production with high selectivity.

In contrast, the CO selectivities of Ag nanoparticles loaded on pristine Ga_2O_3 [34,80–83] have generally been reported to be lower than 50.0%, although higher activities can obtained compared with Ta-, Nb-, and Ti-based photocatalysts. Interestingly, a $ZnGa_2O_4$ [35] photocatalyst showed an excellent CO formation rate (155.0 μmol h^{-1}) and CO selectivity (95%) when modified with a Ag nanoparticle cocatalyst.

3.2. Factors Influencing the Performance of Ag Nanoparticles as Cocatalysts

3.2.1 Additives

$NaHCO_3$ plays an important role in photocatalysis using Ag nanoparticle cocatalysts for the conversion of CO_2 to CO using H_2O as the electron donor. For example, Kudo et al. [32] compared the performance of Ag-loaded Sr-doped $NaTaO_3$ for the production of CO with and without $NaHCO_3$: 176.0 μmol h^{-1} CO was produced in the presence of $NaHCO_3$, whereas no CO was evolved without $NaHCO_3$. Pang et al. [84] systematically investigated the role of $NaHCO_3$ over Ag-loaded $SrNb_2O_6$ by comparing the performance of this catalyst system in the presence of various additives, including Na_2CO_3, NH_4HCO_3, Na_2CO_3, NaOH, Na_2HPO_4/NaH_2PO_4, and Na_2CO_3/CO_2. It was concluded that the dissociation of HCO_3^- to CO_2, which was then captured by the Ag nanoparticles, was the critical step resulting in the high CO evolution activity.

3.2.2 Photocatalyst Surface Properties

The performance of Ag nanoparticles as cocatalysts is significantly affected by the photocatalyst surface properties. For example, the CO selectivity of Ta_2O_5 with a Ag nanoparticle cocatalyst was promoted from 18.0% to 68.0% on doping with 0.5 mol%

SrO [33]. The positive influence of Sr on the photocatalytic performance was confirmed by in situ Fourier transform infrared (FT-IR) spectroscopy measurements of Ag-loaded $Sr_{1.6}K_{0.37}Na_{1.43}Ta_5O_{15}$ [76] during the photocatalytic conversion of CO_2 using H_2O as the electron donor. The characteristic bands located at 1210, 1565, and 2146 cm^{-1} indicated that the active Sr sites favored the monodentate adsorption of bicarbonate species, which were subsequently transformed to bidentate carbonates and CO. In addition, doping with alkali metals to yield Ca- Ga_2O_3 [85], Zn-$ZnTa_2O_6$ [75], and Zn-Ga_2O_3 [86] photocatalysts has been shown to improve the performance of Ag nanoparticles for this photocatalytic reaction.

Tatsumi et al. [34] investigated the performance and CO selectivity of a photocatalytic system involving Ag nanoparticles on rare-earth-element-doped Ga_2O_3. Pr and Ce promoted the CO selectivity significantly, whereas Y, La, Nd, Sm, Gd, Dy, Ho, Er, Yb, and Eu yielded limited selectivity enhancement. In particular, for a Ag-nanoparticle-modified $K_2BTa_5O_{15}$ photocatalyst[87] (B = La, Ce, Pr, Nd, Sm, Eu, Gd, Tb, Dy, Ho, Y, Er, Tm, Yb, Lu, and Sc), it was found that La, Nd, Sm, Gd, Dy, Ho, Y, and Er had a positive effect on the CO selectivity. The similar effects of these elements on the Ag nanoparticles confirmed that the photocatalytic conversion of CO_2 using H_2O was influenced by the surface properties of the photocatalysts.

In some cases, the use of Ag nanoparticles does not result in the sufficient separation of the photogenerated electrons and holes; for example, pristine $SrTiO_3$ (cubic shape) [88] shows almost no activity for the photocatalytic production of CO from CO_2 using H_2O as the electron donor. However, electrons were successfully trapped by Ag nanoparticles on Al-doped $SrTiO_3$, resulting in a significant enhancement in CO production. This is because Al doping induces an anisotropic morphology in $SrTiO_3$, resulting in the electrons and holes being directed to the (100) and (110) facets, respectively.

3.2.3 Sizes and Location of Ag Nanoparticles

The properties and locations of the Ag nanoparticles are affected by the loading method. Wang et al. [35] compared the effects of several methods, including

photodeposition, chemical reduction, and impregnation, on the loading of Ag nanoparticles on a $ZnGa_2O_4$ photocatalyst. As a result, the photodeposition method was found to yield the largest Ag nanoparticles (larger than 200 nm), whereas the formed particles were only 20–30 nm when produced by the impregnation method. Wang et al. also found that the chemical reduction method could deposit Ag nanoparticles randomly on Al-doped $SrTiO_3$, whereas the photodeposition method selectively loaded Ag onto the (100) faces [89]. In some cases, the locations of the Ag nanoparticles can change during reaction. For example, Ag nanoparticles randomly deposited on Al-doped $SrTiO_3$ [89] and rod-like $SrNb_2O_6$ [57] by chemical reduction can move to specific facets on photoirradiation.

3.2.4 Ag Nanoparticle Morphologies

Hori et al. [90] compared the performance of single-crystalline Ag(111), Ag(100), and Ag(110) electrodes for the electrochemical reduction of CO_2. The results showed that the (110) facet exhibited the highest partial current density for CO evolution. Ishida et al. attempted the electrochemical reduction of CO_2 over an O_3-treated Ag electrode [91] to investigate the effects of the facets. The results clearly indicated that larger amounts of the (111) facet would give a higher partial current density and faradaic efficiency for CO evolution. Lee et al. [92] found that better performance in the electrochemical reduction of CO_2 could be achieved if the Ag electrodes had a coral-like nanostructure. In addition, Li [93] and Wang et al. [94] reported that porosity has a positive influence on the performance of Ag electrodes. Unfortunately, the influence of the morphology of Ag nanoparticles on the photocatalytic conversion of CO_2 using H_2O has not been reported in detail to date.

3.3. Dual Cocatalysts Based on Ag nanoparticles

Ag-based dual-cocatalyst nanoparticles have been shown to affect the photocatalytic conversion of CO_2 using H_2O as the electron donor significantly. Pang et al. developed a strategy [81] in which a $Cr(OH)_3$ shell was formed on Ag nanoparticles loaded on Ga_2O_3, and this resulted in a significant improvement in CO evolution, from 140.0 to 480.0 μmol h^{-1}. In addition, their studies indicated that the rate of CO formation is dependent on the thickness of the $Cr(OH)_3$ shell [36]. Wang et al. developed Ag-Co dual cocatalysts [42]

using a chemical reduction method, and these species separately interacted with the (100) and (110) facets of Al-doped $SrTiO_3$. Using X-ray absorption near edge structure (XANES) spectroscopy, the Co species was determined to be CoOOH, which is well known to have good O_2 evolution performance. The CO evolution activity and selectivity over Al-doped $SrTiO_3$ modified with the Ag-Co dual cocatalyst were approximately 52.7 $\mu mol\ h^{-1}$ and 99.8%, respectively, approximately 11.2-times as high as that over Ag nanoparticles alone. Recently, a series of Ag-M (M = Fe, Co, Ni, and Pt) dual cocatalysts was used to modify Al-doped $SrTiO_3$ [95], and it was found that the Ag-Fe dual cocatalyst clearly enhanced CO evolution. XANES characterization of the Fe K-edge showed that the Fe species derived from the photodeposition method was present as FeOOH. However, the Ag-Ni and Ag-Pt dual cocatalysts promoted the evolution of H_2 rather than CO. Moreover, Zhu et al. [96] also found that a Ag-Mn dual cocatalyst loaded on $K_2Ti_6O_{13}$ was more active for the production of CO from CO_2 than the Ag nanoparticles alone. It was found that the Ag and Mn species were selectively photodeposited on the stems and ends, respectively, of the rod-like $K_2Ti_6O_{13}$ [97].

4. Nonmetal Cocatalysts

So far, only Ag nanoparticle cocatalysts have been shown to have broad applicability in the photocatalytic conversion of CO_2 using H_2O as the electron donor, and the contributions of nonmetal cocatalysts to the selective evolution of CO from this reaction have rarely been reported. Iguchi et al. found that Ni-Al layered double hydroxide (LDH) [98] photocatalysts showed selectivity for CO_2 conversion rather than H_2 evolution in aqueous NaCl. By tuning the atomic ratio of Ni to Al, the selectivity for CO and CH_4 evolution were increased from 57.0% to 100.0%, although chloride ions were necessary as sacrificial reagents. Therefore, LDH compounds are promising cocatalysts for the selective photocatalytic conversion of CO_2 using H_2O as the electron donor. Recently, fluorinated Mg-Al and Ni-Al LDH photocatalysts have also been investigated [99], and these showed higher CO formation rates than the nonfluorinated photocatalysts. A wider series of M_1-M_2 LDH photocatalysts [100] including Co-M_2, Ni-M_2, Cu-M_2, and Zn-M_2 (M_2

= V, Cr, Mn, and Fe) for the photocatalytic conversion of CO_2 in 0.1 M aqueous NaCl solution were next studied, and it was found that the Co-M_2, Ni-V, Cu-Mn, and Zn-V LDH photocatalysts have excellent selectivity for CO and CH_4 (> 90%). The advantageous performance of LDH compounds was also observed when using Ag-loaded Ga_2O_3. Crucially, the modification of Ag-loaded Ga_2O_3 with Mg-Al LDH drastically improved the CO formation rate [80].

According to Takemoto et al. [101], $ZnGa_2O_4$ prepared using a typical solid-state reaction has a Zn-rich surface. Interestingly, Wang et al. found that bare $ZnGa_2O_4$ fabricated using a solid-state reaction method was capable of producing considerable amounts of CO (75.0 μmol h^{-1}) [35]. This observation implies that the Zn species favored the evolution of CO during the photocatalytic conversion of CO_2 in the presence of H_2O. This speculation was then confirmed by Wang et al. on a Zn-modified $ZnTa_2O_6$ photocatalyst [75], for which a CO selectivity of approximately 76.0% was achieved.

5. Outline of this Thesis

This thesis is divided into three parts consisting of seven chapters that focus on the investigation of effective cocatalysts for the photocatalytic conversion of CO_2 using H_2O as the electron donor.

Chapter 1 describes the influence of the in situ addition of Na_2CrO_4 on the photocatalytic conversion of CO_2 in the presence of H_2O over a $ZnTa_2O_6$ photocatalyst fabricated by a solid-state reaction. The in situ addition of chromates suppressed and enhanced the evolution of H_2 and CO, respectively. Consequently, the selectivity toward CO was promoted.

Chapter 2 introduces the effect of the in situ addition of chromate ions on H_2 evolution during the photocatalytic conversion of CO_2 in the presence of H_2O. Based on a series of comparison experiments, it was determined that the in situ addition of chromate ions suppressed the evolution of H_2 when the photocatalyst surfaces were highly protonated. In contrast, the in situ addition of chromate ions was found to enhance H_2 evolution when the concentration of H^+ was low near the photocatalyst surface.

Chapter 3 describes the use of zinc hydroxide as an abundant and universal cocatalyst for the selective photocatalytic conversion of CO_2 in the presence of H_2O. In this chapter, $Zn(OH)_2$ was used to modify a series of photocatalysts, including $ZnTa_2O_6$, $NaTaO_3$, Ga_2O_3, Ta_2O_5, $ZnGa_2O_4$, and $SrTa_2O_6$. As a result of the modification, the CO formation rates over these photocatalysts significantly increased. It was found that the dissolved Zn^{2+} ions in the reaction solution and the alkaline surface properties of the photocatalysts were critical in achieving the excellent photocatalytic activity of $Zn(OH)_2$.

Chapter 4 explores a series of Zn-based cocatalysts, including $ZnGa_2O_4$ and $ZnSiO_3$, that are effective in improving the production of CO via the photocatalytic conversion of CO_2 using H_2O as the electron donor. The Zn-based cocatalysts showed broad applicability for CO production over Ta- and Ga-based photocatalysts, whereas they had almost no influence on Nb- and Ti-based photocatalysts. However, it was found that the performance of the Zn-based cocatalysts for the photocatalytic conversion of CO_2 was affected by the counter anion in the cocatalyst (i.e., $Zn(NO_3)_2$, $ZnAl_2O_4$, and $Zn(OH)_2$).

Chapter 5 discusses $Cd(OH)_2$ as an effective cocatalyst for the selective photocatalytic conversion of CO_2 using H_2O as an electron donor. The modification of $ZnTa_2O_6$ with $Cd(OH)_2$ significantly suppressed and improved the evolution of H_2 and CO, respectively. The $Cd(OH)_2$ cocatalyst can be used with a wide range of photocatalysts, such as $ZnGa_2O_4$ and $NaTaO_3$. Using $ZnGa_2O_4$ as an example, the photocatalytic mechanism of $Cd(OH)_2$ was studied, and it was concluded the Cd^{2+} selectively protected the active sites for CO evolution from poisoning by O_2 reduction reactions.

Chapter 6 describes the strategies for tuning and optimizing the photocatalytic conversion of CO_2 using H_2O as the electron donor over photocatalysts comprising Ag nanoparticles loaded on $NaTaO_3$ by photodeposition. In particular, the Ag nanoparticle size was tuned effectively by controlling the photodeposition time from 0.5 to 12 h. It was found that the use of larger Ag nanoparticles enhanced the CO selectivity. Further, Ag-loaded $NaTaO_3$ showed poor stability, even though the loading of Ag nanoparticles was optimized. This unexpected result arises from the morphological change to the Ag

nanoparticles from polycrystalline to single-crystalline. However, by modifying the Ag nanoparticles with chromium, stable CO selectivity with respect to time was achieved.

Chapter 7 presents studies on the performance of Ag-loaded β-Ga_2O_3 for the photocatalytic conversion of CO_2 using H_2O as the electron donor. By using the appropriate loading method for the Ag nanoparticles, the CO selectivity over Ag-loaded β-Ga_2O_3 increased above 80%. The loading of Ag nanoparticles required to achieve high CO selectivities was much lower for the chemical reduction method (2 wt%) than that of the photodeposition method (8 wt%). By optimizing the amount of photocatalyst used in the reaction, the origin of the high selectivity for CO evolution of the Ag-loaded β-Ga_2O_3 was found to be the selective poisoning of the active sites for H_2 production by O_2 reduction reactions. As a result, the formation rate of CO far exceeded that of H_2 when larger amounts of Ag-loaded β-Ga_2O_3 were used.

References

1. P. Friedlingstein, R. A. Houghton, G. Marland, J. Hackler, T. A. Boden, T. J. Conway, J. G. Candadell, M. R. Raupach, P Ciais and C. L. Quere. Nature Geosicience 2010, 3, 811-812.
2. G. Marland, R. M. Rotty and N. L. Treat. Tellus 1985, 37B, 243-258.
3. T. L. Frölicher, M. Winton and J. L. Sarmiento. Nature Climate Change 2014, 4, 40-44.
4. J. Rogelj, A. Popp, K. V. Calvin, G. Luderer, J. Emmerling, D. Gernaat, S. Fujimori, J. Strefler, T. Hasegawa, G. Marangoni, V. Krey, E. Kriegler, K. Riahi, D. P. V. Vuuren, J. Doelman, L. Drouet, J. Edmonds, O. Fricko, M. Harmsen, P. Havlik, F. Humpenoder, E. Stehfest and M. Tavoni. Nature Climate Change 2018, 8, 325-332.
5. C. M. Domingues, J. A. Church, N. J. White, P. J. Gleckler, S. E. Wijffels, P. M. Barker and J. R. Dunn. Nature 2008, 453, 1090-1093.
6. L. W. Davis. J. Econ. Perspect. 2012, 26, 49–66.
7. E. F. Moran, M. C. Lopez, N. Moore, N. Müller and D. W. Hyndman. PNAS 2018, 115, 11891–11898.
8. P. Gipe. Wind Engineering 2004, 28, 629–632.
9. S. A. Calero. J. Polit. Ecol. 2017, 24, 992–1012.
10. B. A. Thayer. Security Studies 1994, 3, 428-493.
11. B. D. Adams and W. W. Adams III. Nature 2000, 403, 371-373.
12. T. M. Bruton. Sol. Energy Mater. Sol. Cells 2002, 72, 3–10.
13. R. Fu, T. L. James and M. IEEE J. Photovoltaics 2015, **5**, 515–524.
14. L. I. Granone, F. Sieland, N. Zheng, R. Dillert and D. W. Bahnemann. Green Chem. 2018, 20, 1169-1192.
15. W. Tu, Y. Zhou and Z. Zou. Adv. Mater. 2014, 26, 4607–4626.
16. T. Hisatomi, J. Kubota and K. Domen. Chem. Soc. Rev 2014, 43, 7520-7535.
17. Q. Wang and K. Domen. Chem. Rev. 2020, 120, 919–985.

18. D. M. Gates. Science 1966, 151, 523–529.
19. Y. Bai, K. Nakagawa, A. J. Cowan, C. M. Aitchison, Y. Yamaguchi, M. A. Zwijnenburg, A. Kudo, R. S. Sprick and A. I. Cooper. J. Mater. Chem. A 2020, 8, 16283-16290.
20. R. Abe, T. Takata, H. Sugihara and K. Domen. Chem. Commun. 2005, 3829-3831.
21. Q. Wang, T. Hisatomi, Q. Jia, H. Tokudome, M. Zhong, C. Wang, Z. Pan, T. Takata, M. Nakabayashi, N. Shibata, Y. Li, I. D. Sharp, A. Kudo, T. Yamada and K. Domen. Nature Materials 2016, 15, 611-615.
22. A. Fujishima and K. Honda. Nature 1972, 238, 37–38.
23. Y. Tamaki and O. Ishitani. ACS Catal. 2017, 7, 3394-3409.
24. S. Gautam, H. Agrawal, M. Thakur, A. Akbari, H. Sharda, R. Kaur and M. Amini. J. Environ. Chem. Eng. 2020, 8, 103726.
25. Y. Z. Chen, W. H. Li, L. Li and L. N. Wang. Rare Met. 2018, 37, 1-12.
26. J. Xing, W. Q. Fang, H. J. Zhao and H. G. Yang. Chem. An Asian J. 2012, 7, 642–657.
27. Q. Wang, Q. Gao, A. M. Al-Enizi, A. Nafady and S. Ma. Inorg. Chem. Front. 2020, 7, 300–339.
28. T. Kato, Y. Hakari, S. Ikeda, Q. Jia, A. Iwase and A. Kudo. J. Phys. Chem. Lett. 2015, 6, 1042-1047.
29. Y. Li, T. Takata, D. Cha, K. Takanabe, T. Minegishi, J. Kubota and K. Domen. Adv. Mater. 2013, 25, 125–131.
30. Y. Kuang, Q. Jia, H. Nishiyama, T. Yamada, A. Kudo and K. Domen. Adv. Energy Mater. 2016, 6, 1501645.
31. W. N. Wang, W. J. An, B. Ramalingam, S. Mukherjee, D. M. Niedzwiedzki, S. Gangopadhyay and P. Biswas. J. Am. Chem. Soc 2012, 134, 11276–11281.
32. H. Nakanishi, K. Iizuka, T. Takayama, A. Iwase and A. Kudo. ChemSusChem 2017, 10, 112–118.
33. K. Teramura, H. Tatsumi, Z. Wang, S. Hosokawa and T. Tanaka. Bull. Chem. Soc.

Jpn. 2015, 88, 431–437.

34. H.Tatsumi, K. Teramura, Z. Huang, Z. Wang, H. Asakura, S. Hosokawa and T. Tanaka. Langmuir, 2017, 33, 13929-13935.
35. Z. Wang, K. Teramura, S. Hosokawa and T. Tanaka.J. Mater. Chem. A 2015, 3, 11313-11319.
36. R.Pang, K. Teramura, H. Asakura, S. Hosokawa and T. Tanaka. ACS Sustainable Chem. Eng. 2019, 7, 2083-2090.
37. S. Iguchi, K. Teramura, S. Hosokawa and T. Tanaka. Catal. Sci. Technol. 2014, 6, 4978.
38. T. Takata, J. Jiang, Y. Sakata, M. Nakabayashi, N. Shibata, V. Nandal, K. Seki, T. Hisatomi and K. Domen. Nature 2020, 581, 411-414.
39. H. Kato, K. Asakura and A. Kudo. J. Am. Chem. Soc. 2003, 125, 3082-3089.
40. K. Maeda, A. Xiong, T. Yoshinaga, T. Ikeda, N. Sakamoto, T. Hisatomi, M. Takashima, D. Lu, M. Kanehara, T. Setoyama, T. Teranishi and K. Domen. Angew. Chemie 2010, 122, 4190–4193.
41. D. Wang, R. Li, J. Zhu, J. Shi, J. Han, X. Zong and C. Li. J. Phys. Chem. C 2012, 116, 5082-5089.
42. S. Wang, K. Teramura, T. Hisatomi, K. Domen, H. Asakura, S. Hosokawa and T. Tanaka. Chem. Sci. 2021, 12, 4940-4948.
43. J. Sheng, Y. He, J. Li, C. Yuan, H. Huang, S. Wang, Y. Sun, Z. Wang and F. Dong. ACS Nano 2020, 14, 13103–13114.
44. F. Li, X. Yue, H. Zhou, J. Fan and Q. Xiang. Chinese J. Catal. 2021, 42, 1608–1616.
45. X. Shi, X. Dong, Y. He, P. Yan and F. Dong. Sci. Bull. doi:10.1016/J.SCIB.2022.01.013.
46. H. Zhao, F. Pan and Y. Li. J. Mater. 2017, 3, 17–32.
47. J. Sheng, Y. He, M. Huang, C. Yuan, S. Wang and F. Dong. ACS Catal. 2022, 12, 2915-2926.

48. L. Jin, E. Shaaban, S. Bamonte, D. Cintron, S. Shuster, L. Zhang, G. Li and J. He. ACS Appl. Mater. Interfaces 2021, 13, 38603.
49. M. Abdellah, A. M. EI-Zohry, L. J. Antila, C. D. Windle, E. Reisner and L. Hammarsrom. J. Am. Chem. Soc. 2017, 139, 1226-1232.
50. A. D. Handoko and J. Tang. Int. J. Hydrogen Energy 2013, 38, 13017–13022.
51. L. Zhang, D. Zhu, G. M. Nathanson and R. J. Hamers. Angew. Chemie 2014, 126, 9904–9908.
52. M. Kanemoto, T. Shiragami, C. Pac and S.Yanagida. J. Phys. Chem. 1992, 96, 3521-3526.
53. H. P. Liang, A. Acharjya, D. A. Anito, S. Vogl, T. X. Wang, A. Thomas and B. Han. ACS Catal. 2019, 9, 3959-3968.
54. Y. N. Gong, B. Shao, J. Mei, W. Yang, D. Chang and T. Lu. Nano Research 2022, 15, 551-556.
55. L. Cao, S. Sahu, P. Anilkumar, C. E. Bunker, J. Xu, K. A. S. Fernando, P. Wang, E. A. Guliant, K. N. Tackett and Y. Sun. J. Am. Chem. Soc 2011, 133, 4754-4757.
56. R. Pang, K. Teramura, H. Asakura, S. Hosokawa and T. Tanaka. (2019) J. Phys. Chem. C 2019, 123, 2894-2899.
57. R. Pang, K. Teramura, H. Asakura, S. Hosokawa and T. Tanaka. Appl. Catal. B Environ. 2017, 218, 770–778.
58. J. L. White, M. F. Baruch, J. E. Pander, Y. Hu, I. C. Formeyer, J. E. Park, T. Zhang, K. Liao, J. Gu, Y. Yan, T. W. Shaw, E. Abelev and A. Bocarsly. Chem. Rev. 2015, 115, 12888-12935.
59. B. Han, X. Qu, Z. Deng, Y. Song, C. Tian, H. Deng, Y. Xu and Z. Lin. Angew. Chemie. Int. Ed. 2018, 57, 16811–16815.
60. W. Zhong, R. Sa, L. Li, Y. He, L. Li, J. Bi, Z. Zhuang, Y. Yu and Z. Zou. J. Am. Chem. Soc 2019, 141, 7615–7621.
61. Y. L. Men, Y. You, Y. Pan, H. Gao, Y. Xia, D. Cheng, J. Song, D. Cui, N. Wu, Y. Li, S. Xin and B. Goodenough. J. Am. Chem. Soc. 2018, 140, 13071-13077.

62. M. F. Kuehnel, K. L. Orchard, K. E. Dalle and E. Reisner. J. Am. Chem. Soc 139, 7217−7223.
63. K. Iizuka, T. Wato, Y. Miseki, K. Saito and A. Kudo. J. Am. Chem. Soc. 2011, 133, 20863–20868.
64. X. Zhu, A. Anzai, A. Yamamoto and H. Yoshida. Appl. Catal. B Environ. 2019, 243, 47–56.
65. X. Zhu, A. Yamamoto and H. Yoshida. Dalton Trans. 2021, 50, 7976.
66. A. Anzai, N. Fukuo, A. Yamamoto and H. Yoshida. Catal. Commun. 2017, 100, 134–138.
67. T. Zhan, A. Kumar, M. Sevilla, A. Sridhar and X. Zeng. J. Phys. Chem. C 2020, 124, 26094-26105.
68. Q. He, J. H. Lee, D. Liu, Y. Liu, Z. Lin, Z. Xie, S. Hwang, S. Kattel, L. Song, J. G. Chen. Adv. Funct. Mater. 2020, 30, 2000407.
69. X. Feng, K. Jiang, S. Fan and M. W. Kanan. J. Am. Chem. Soc 2015, 137, 4606-4609.
70. R. G. Mariano, K. McKelvey, H. S. White and M. W. Kanan. Science 2017, 358, 1187–1192.
71. K. S. Kim, W. J. Kim, H. K. Lim, E. K. Lee and H. Kim.ACS Catal. 2016, 6, 4443-4448.
72. Z. Chen, T. Wang, B. Liu, D. Cheng, C. Hu, G. Zhang, W. Zhu, H. Wang, Z. Zhao and J. Gong. J. Am. Chem. Soc. 2020, 142, 6878-6883.
73. J. Rosen, G. S. Hutchings, Q. Liu, R. V. Forest, A. Moore and F. Jiao. ACS Catal. 2015, 5, 4586-4591.
74. Z. Wang, K. Teramura, S. Hosokawa and T. Tanaka. Appl. Catal. B Environ. 2015, 163, 241–247.
75. S. Wang, K. Teramura, H. Asakura, S. Hosokawa and T. Tanaka. J. Phys. Chem. C 2021, 125, 1304–1312.
76. S. Yoshizawa, Z. Huang, K. Teramura, H. Asakura, S. Hosokawa and T.

Tanaka.ACS Appl. Mater. Interface 2019, 11, 37875-37884.

77. Z. Huang, S. Yoshizawa, K. Teramura, H. Asakura, S. Hosokawa and T. Tanaka. ACS Sustain. Chem. Eng. 2018, 6, 8247–8255.

78. Z. Huang, S. Yoshizawa, K. Teramura, H. Asakura, S. Hosokawa and T. Tanaka. ACS Omega 2017, 2, 8187-8197.

79. Z. Huang, K. Teramura, S. Hosokawa and T. Tanaka. Appl. Catal. B Environ. 2016, 199, 272–281.

80. S. Iguchi, Y. Hasegawa, K. Teramura, S. Kidera, S. Kikkawa, S. Hosokawa, H. Asakura and T. Tanaka. Sustainable Energy Fuel 2017, **1**, 1633–1848.

81. R. Pang, K. Teramura, H. Asakura, S. Hosokawa and T. Tanaka. Chem. Commun. 2018, 54, 1053-1056.

82. Z. Huang, K. Teramura, H. Asakura, S. Hosokawa and T. Tanaka. J. Mater. Chem. A 2017, 5, 19351-19357.

83. Y. Kawaguchi, M. Akatsuka, M. Yamamoto, K. Yoshioka, A. Ozawa, Y. Kato and T. Yoshida. J. Photochem. Photobiol. A Chem. 2018, 358, 459–464.

84. R. Pang, K. Teramura, H. Asakura, S. Hosokawa and T. Tanaka. ACS Appl. Energy Mater 2019, 2, 5397-5405.

85. R. Pang, K. Teramura, M. Morishita, H. Asakura, S. Hosokawa and T. Tanaka. doi.org/10.1038/s42004-020-00381-2.

86. K. Teramura, Z. Wang, S. Hosokawa, Y. Sakata and T. Tanaka. Chem. A Eur. J. 2014, 20, 9906–9909.

87. Z. Huang, K. Teramura, H. Asakura, S. Hosokawa and T. Tanaka. Catal. Today 2018, 300, 173–182.

88. S. Wang, K. Teramura, T. Hisatomi, K. Domen, H. Asakura, S. Hosokawa and T. Tanaka. ACS Appl. Energy Mater 2020, 1468–1475.

89. S. Wang, K. Teramura, T. Hisatomi, K. Domen, H. Asakura, S. Hosokawa and T. Tanaka. ChemistrySelect 2020, 5, 8779–8786.

90. N. Hoshi, M. Kato and Y. Hori. J. Electroanal. Chem. 1997, 440, 283–286.

91. M. Ishida, S. Kikkawa, K. Hori, K. Teramura, H. Asakura, S. Hosokawa and T. Tanaka.ACS Appl. Energy Mater. 2020, 3, 6552-6560.
92. W. H. Lee, Y. J. Ko, Y. Choi, S. Y. Lee, C. H. Choi, Y. J. Hwang, B. K. Min, P. Strasser and H. S. Oh. Nano Energy 2020, 76, 105030.
93. S. Li, X. Dong, W. Chen, Y. Song, G. Li, W. Wei and Y. Sun. Catalysts 2022, 12, 453.
94. H. Wang, Z. Han, L. Zhang, C. Cui, X. Zhu, X. Liu, J. Han and Q. Ge. J. CO_2 Util. 2016, 15, 41–49 (2016).
95. S. Wang, K. Teramura, T. Hisatomi, K. Domen, H. Asakura, S. Hosokawa and T. Tanaka. ACS Sustainable Chem. Eng. 2021, 9, 9327-9335.
96. X. Zhu, A. Yamamoto, S. Imai, A. Tanaka, H. Kominami and H. Yoshida. Chem. Commun. 2019, 55, 13514–13517.
97. X. Zhu, A. Yamamoto, S. Imai, A. Tanaka, H. Kominami and H. Yoshida. Appl. Catal. B Environ. 2020, 274, 119085.
98. S. Iguchi, K. Teramura, S. Hosokawa and T. Tanaka. Catal. Today 2015, 251, 140–144.
99. S. Iguchi, K. Teramura, S. Hosokawa and T. Tanaka. Appl. Catal. A Gen. 2016, 521, 160–167.
100. S. Iguchi, Y. Hasegawa, K. Teramura, S. Hosokawa and T. Tanaka. J. CO_2 Util. 2016, 15, 6–14.
101. M. Takemoto, Y. Tokudome, S. Kikkawa, K. Teramura, T. Tanaka, K. Okada, H. Murata, A. Nakahira and M. Takahashi. RSC Adv. 2020, 10, 8066-8073.

Part I

The influence of in situ added chromate ions on the photocatalytic conversion of CO_2 using H_2O as an electron donor

Chapter 1

Shift of active sites via in-situ photodeposition of chromate achieving highly selective photocatalytic conversion of CO_2 by H_2O over $ZnTa_2O_6$

Abstract

In-situ photodeposition of trace amounts of chromates was found effective in achieving high selectivity toward CO evolution over $ZnTa_2O_6$ for the photocatalytic conversion of CO_2 by H_2O. Photodeposited $Cr(OH)_3$ produced CO at 6.3 μmol h^{-1} with a selectivity of 80%, while bare $ZnTa_2O_6$ shows a predominant activity in H_2 production (22.0 μmol h^{-1} H_2 vs. 1.2 μmol h^{-1} CO) with 0.1 g photocatalyst. $ZnTa_2O_6$, synthesized via a solid-state reaction method, contained two types of surfaces with stoichiometric and Zn-excessive Zn:Ta ratios, respectively. The stoichiometric surfaces were responsible for overall water splitting. By in-situ photodeposition of trace chromates during the reaction, the active sites of the synthesized $ZnTa_2O_6$ shifted from the stoichiometric to the Zn-excessive surfaces and $Cr(OH)_3$-modified Zn-excessive surfaces were found to evolve CO as the main product.

1. Introduction

Humankind has been relying heavily on fossil fuels such as coal, petroleum, and natural gas since the first industrial revolution. With the development of our society, however, people have faced increasingly more challenges in the sustainability of energy sources [1] as well as environmental problems such as global warming. [2,3] In recent years, technologies based on solar energy utilization, such as photocatalytic H_2O splitting, [4] photovoltaic cells, [5] conversion of biomass [6] and CO_2 [7] have attracted considerable attention due to their sustainable and environment-friendly features. Among these technologies, the photocatalytic conversion of CO_2 using H_2O as an electron donor is particularly promising because it not only achieves recycling of energy but also produces useful intermediate chemical species such as CO, CHOOH, HCHO, CH_3OH and CH_4. This process requires at least two critical factors indicating a successful photocatalytic conversion of CO_2: one is the selectivity toward CO_2-derived chemicals (Equation (1)); the other is a balance between electrons and holes (e^-/h^+) generated by charge transfer (Equation (2)). [8]

$$\text{Selectivity} = (2R_{HCOOH} + 2R_{CO} + 4R_{HCHO} + 6R_{CH_3OH} + 8R_{CH_4})/(2R_{HCOOH} + 2R_{CO} + 4R_{HCHO} + 6R_{CH_3OH} + 8R_{CH_4} + 2R_{H_2}) \times 100\% \quad (1)$$

$$e^-/h^+ = (2R_{HCOOH} + 2R_{CO} + 4R_{HCHO} + 6R_{CH_3OH} + 8R_{CH_4} + 2R_{H_2}) / 4R_{O_2} \quad (2)$$

R_x in the equations represents the rate of formation of product x. The above expressions can be simplified as:

$$\text{Selectivity} = 2R_{CO} /(2R_{CO} + 2R_{H_2}) \times 100\% \quad (3)$$

$$e^-/h^+ = (2R_{CO} + 2R_{H_2}) / 4R_{O_2} \quad (4)$$

when only CO and H_2 are produced with O_2 during the photocatalytic conversion of CO_2 by H_2O.

However, H_2O splitting always occurs as a competitive reaction against the photoreduction of CO_2 [8] because the redox potential (vs. SHE) of the proton (−0.41 V) is

more positive than that of CO (−0.52 V). To the best knowledges of the author, Ag-loaded $BaLa_4Ti_4O_{15}$ reported by Kudo et al. [9] was the first photocatalyst showing selective formation of CO with a stoichiometric amount of O_2 from H_2O. Other compounds found effective in the photocatalytic conversion of CO_2 using H_2O as the electron donor were alkaline earth metal-doped $NaTaO_3$ [10] and Ta_2O_5, [11] Ga_2O_3, [12] $ZnGa_2O_4$, [13] $CaMO_3$ (M: Ti [14] or Zr [15]), $SrNb_2O_6$, [16] $Sr_2KTa_5O_{15}$, [17] Al-doped $SrTiO_3$, [18] and $La_2Ti_2O_7$; [19] however, it was necessary to modify them with metallic Ag nanoparticles as a cocatalyst. To improve selectivity in CO_2 conversion, Iguchi et al. previously investigated various cocatalysts including Pt, Cu, Au, Ag, [20,21] Pd, [20] and Ni, [21] and found that only Ag could increase the selectivity toward CO evolution.

On the other hand, Ag was reported as an ineffective cocatalyst in several instances, for example in 3 wt% Ag/Ta_2O_5 (18% CO selectivity), [11] 1 wt% Ag/Ga_2O_3 (30%), [13] 3 wt% $Ag/SrZrO_3$ (10%), [15] and 3 wt% $Ag/ZnTa_2O_6$ (50%). [21] In sum, researchers still have insufficient information on possible methods to achieve a highly selective photocatalytic conversion of CO_2. In particular, it is difficult to map a comprehensive mechanism for the specific reduction of CO_2 rather than H_2O in an aqueous solution. Therefore, here the author proposes a new strategy circumventing the limitations of Ag as a cocatalyst to improve the selectivity toward the reduction products of CO_2 such as CO. Because the reduction of CO_2 competes with that of protons, the author has hypothesized that the active site for H_2 production should be covered. This can be achieved using oxometallate ions such as chromate (CrO_4^{2-}), permanganate (MnO_4^-), and vanadate (VO_4^{3-}), which possess a more positive redox potential than the proton and are reduced to MO_xH_y (M: Cr, Mn or V) on the surfaces of photocatalysts under photoirradiation. Notably, these hydroxide species are generally water-insoluble. According to newly developed method, the in-situ photodeposition of oxometallate ions can suppress H_2 evolution significantly and simultaneously promote the selectivity toward CO evolution.

2. Experimental Section

2.1. Preparation of $ZnTa_2O_6$

$ZnTa_2O_6$ used in this work was synthesized by a typical solid-state reaction (SSR) method, in which stoichiometric amounts of ZnO (99.0%, Wako, Japan) and Ta_2O_5 (99.9%, High Purity Chemicals, Japan) were impregnated with 5 mL pure water and ground in an aluminum mortar for 1 h. The wet mixtures were dried at 383 K for 1 h and then transferred to an aluminum crucible for 50 h of calcination at 1273 K under air atmosphere. The obtained sample was named ZTO_50A (where "A" stands for "air atmosphere"). For comparison, a series of samples including ZTO_12A, ZTO_12N (where "N" stands for "nitrogen atmosphere"), and ZTO_12A/(0.95) were synthesized by controlling the atmosphere composition, calcination time, and ZnO/Ta_2O_5 ratio. Specifically, ZTO_12A was obtained in the same conditions as ZTO_50A except the calcination time, which was reduced to 12 h. ZTO_12N and ZTO_12A/(0.95) were prepared in nitrogen atmosphere instead of air, and with 5 mol% less ZnO in the starting reagents, respectively.

2.2. Reaction procedure

The photocatalytic conversion of CO_2 using H_2O as an electron donor was carried out at approximately 298 to 303 K and ambient pressure in an inner irradiation reactor with a quartz jacket connected to cooling water. The light source was a 400 W high-pressure mercury lamp (Sen Lights Corp.). ZTO_50A (0.1 g) was added to 1.0 L aqueous solution containing $NaHCO_3$ (99.5%, Wako, Japan). If necessary, various cocatalyst precursors, including $Na_2CrO_4 \cdot 4H_2O$ (99.0%), K_2CrO_4 (99.0%), $Na_2Cr_2O_7 \cdot 2H_2O$ (99.0%), $Cr(NO_3)_3 \cdot 9H_2O$ (99.9%), $CrCl_3 \cdot 6H_2O$ (99.5%), $Na_2MoO_4 \cdot 2H_2O$ (99.0%), Na_3VO_4 (90.0%), and $KMnO_4$ (99.3%) were added into the suspension before photoirradiation. All these reagents were purchased from Wako Corporation. The concentrations of $NaHCO_3$ and cocatalyst precursors varied depending on the specific experiments. Air was purged from the system using CO_2 (5 N) gas at a flow rate of 60 mL min^{-1} before photoirradiation. Then, the CO_2 flow rate was shifted to 30 mL min^{-1} during reactions. Gaseous products (e.g., H_2, O_2, and CO) were detected by two GC-8A gas chromatographs (Shimadzu Corp.) equipped, respectively, with a thermal conductivity

detector (carrier gas: Ar) and a methanizer-connected flame ionization detector (carrier gas: N_2).

2.3. Characterization of photocatalysts

The morphology of the synthesized ZTO_50A was examined using field emission scanning electron microscopy (FE-SEM, SU-8220, Hitachi High-Technologies) at an accelerating voltage of 3.0 kV and emission current of 10 μA. An energy dispersive X-ray spectroscopy (EDS) unit was employed to determine the atomic ratio of Zn, Ta, and Cr elements at different positions on the surface of ZTO_50A. The accelerating voltage for this measurement was set at 15.0 kV. X-ray diffraction (XRD) patterns of the photocatalyst were obtained with a Rigaku Ultima IV powder diffractometer using a Cu Kα radiation generated in the working conditions of 40 kV and 40 mA. UV-vis diffuse reflectance spectroscopy (UV-vis DRS) was performed on a JASCO V-670 spectrometer to confirm the absorption properties of the photocatalysts. The chemical states of various elements were characterized by means of X-ray photoelectron spectroscopy (XPS) on an ESCA 3400 instrument (Shimadzu Corp.); the applied voltage and emission current in the experiments were set at 10 kV and 20 mA, respectively. The amount of Cr species photodeposited on ZTO_50A after the reaction was determined via X-ray fluorescence spectroscopy (XRF, EDX-8000, Shimadzu Corp.) under ambient pressure at room temperature.

3. Results and Discussion

3.1. Composition and formation mechanism of ZTO_50A

The UV-vis DRS of synthesized ZTO_50A revealed an absorption edge of $ZnTa_2O_6$ located at approximately 280 nm as shown in Figure 1a, corresponding to a band gap of 4.4 eV in agreement with the previous report. [21] Figure 1b shows the experimental XRD pattern of ZTO_50A compared with that present in the ICSD database (# 36289). The characteristic peaks of the $ZnTa_2O_6$ phase are clearly observed from the pattern, which indicates $ZnTa_2O_6$ was successfully synthesized. In addition, impurity component was found at approximately 26.6°, 34.7°, 38.0°, and 52.5°. For the identification of the

impurity, the author compared the diffraction peaks of the impurity with XRD patterns of TaO_2 (ICSD # 60627), $TaO_{1.7}$ (ICSD # 60148), and $TaO_{1.6}$ (ICSD # 20499) (Figure 2). It is found that XRD pattern of the impurity are fairly consistent with TaO_2, but slightly shifted to lower 2 theta values. A similar shift was observed in $TaO_{1.6}$ in relation to $TaO_{1.7}$. Thus, the impurity contained in the ZTO_50A sample was identified as $TaO_{2-\delta}$. This phenomenon was probably caused by the poor mobilities of Zn and Ta ions during SSR. The presence of $TaO_{2-\delta}$ indicated that some unconverted ZnO remained in ZTO_50A because stoichiometric amounts of ZnO and Ta_2O_5 were used in the starting reagents. As displayed in Figure 1c, the peaks derived from the $TaO_{2-\delta}$ phase in ZTO_12A showed relatively stronger intensities compared with those observed in ZTO_50A. This suggests that $TaO_{2-\delta}$ was likely a transition compound which was slowly converted into $ZnTa_2O_6$ during calcination. On the other hand, a considerably higher content of $TaO_{2-\delta}$ was noticed in sample ZTO_12N, indicating that a lack of oxygen suppressed the formation of $ZnTa_2O_6$. In addition, the XRD pattern of sample ZTO_12A/(0.95) revealed that a high content of $TaO_{2-\delta}$ phase formed when using 5 mol% deficient ZnO in the starting materials. Based on the set of experiments, the formation mechanism of $ZnTa_2O_6$ in the SSR method can be illustrated according to Equations (5) to (7):

$$ZnO + Ta_2O_5 \rightarrow ZnTa_2O_6 \quad (5)$$

$$2Ta_2O_5 \rightarrow 4TaO_{2-\delta} + (1+2\delta)\,O_2 \quad (6)$$

$$2ZnO + 4TaO_{2-\delta} + (1+2\delta)O_2 \rightarrow 2ZnTa_2O_6 \quad (7)$$

The three reactions above probably took place simultaneously during calcination. Ta_2O_5 possibly underwent direct conversion into $ZnTa_2O_6$ by reacting with ZnO (Equation (5)), while it concurrently decomposed into $TaO_{2-\delta}$, which was also converted into $ZnTa_2O_6$ by further reacting with ZnO and O_2 (Equations (6) and (7)). It should be noted that the decomposition of Ta_2O_5 into $TaO_{2-\delta}$ was only observed when a mixed powder of ZnO and Ta_2O_5 was calcined. According to XRD analysis, $TaO_{2-\delta}$ did not form if the author calcined Ta_2O_5 alone.

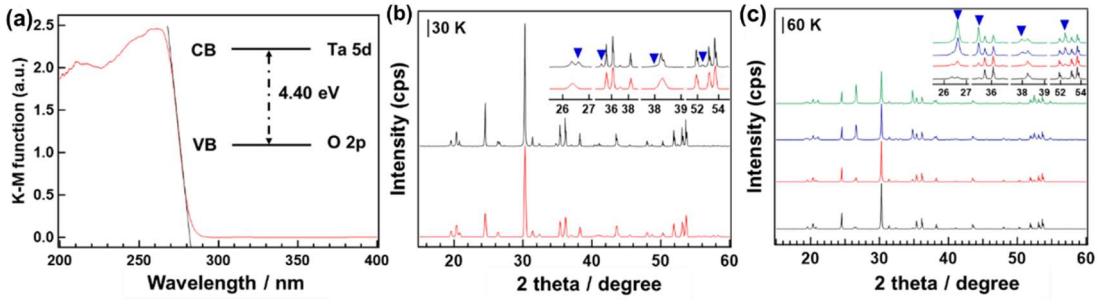

Figure 1. Characterization of $ZnTa_2O_6$ fabricated at 1273 K. (a) UV/vis diffuse reflectance spectra of ZTO_50A; (b) XRD patterns of ZTO_50A (black line) and reference pattern of ZTO (ICSD # 36289, red line); (c) XRD patterns of ZTO_50A (black line), ZTO_12A (red line), ZTO_12N (blue line), and ZTO_12A/(0.95) (green line). The insets in (b) and (c) are enlarged views of the peaks belonging to $TaO_{2-\delta}$ (blue triangles).

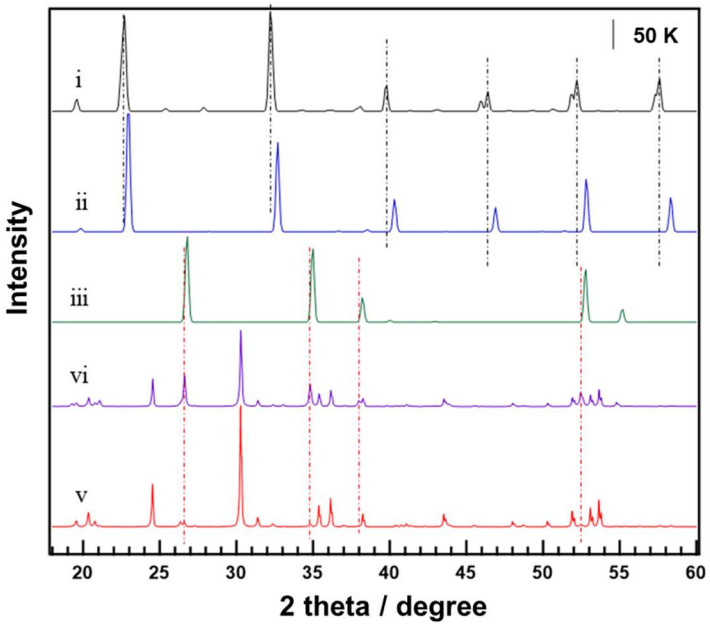

Figure 2. XRD patterns of (i) $TaO_{1.6}$ (ICSD #20499), (ii) $TaO_{1.7}$ (ICSD #60148), (iii) TaO_2 (ICSD #60627), (iv) ZTO_12N, (v) ZTO_50A.

3.2. Locations of $TaO_{2-\delta}$ and ZnO

No diffraction peaks attributable to unconverted ZnO were observed in the XRD pattern, suggesting the existence of ZnO in an amorphous or solid solution state. The unconverted ZnO did not form particles, as evidenced by the FE-SEM image of sample

ZTO_50A in Figure 3(a). Such a morphology indicates that ZnO was probably dissolved in the solid sample. Moreover, EDS mapping showed that the dispersion of unconverted ZnO on the surface was not the same in each site. Site A was characterized by a stoichiometric Zn:Ta ratio of approximately 1:2 (Figure 3(b)), while site B exhibited a Zn excess with a ratio of 1:1.55 (Figure 3(c)). Such inhomogeneity between sites could be caused by a poor mobility of Zn atoms in the calcination process, and this yielded the two types of surfaces observed in sample ZTO_50A. The binding energy of Ta $4f_{7/2}$ was 26.0 eV (Figure 4a), indicative of the Ta^{5+} state. [22] There were no peaks in $TaO_{2-\delta}$ corresponding to Ta^{4+}, which is reported in the literature as being 1.3–1.6 eV lower than Ta^{5+}. [23–25] The XPS profiles of Ta 4f in ZTO_50A (Figure 4a) and ZTO_12N (Figure 4b) could be deconvolved, even though several peaks assigned to $TaO_{2-\delta}$ were observed in the XRD patterns; the peak fitting parameters are provided in the Table 1. This implies that $TaO_{2-\delta}$ existed mainly in the bulk rather than on the surface of ZTO_50A, as depicted in Scheme 1.

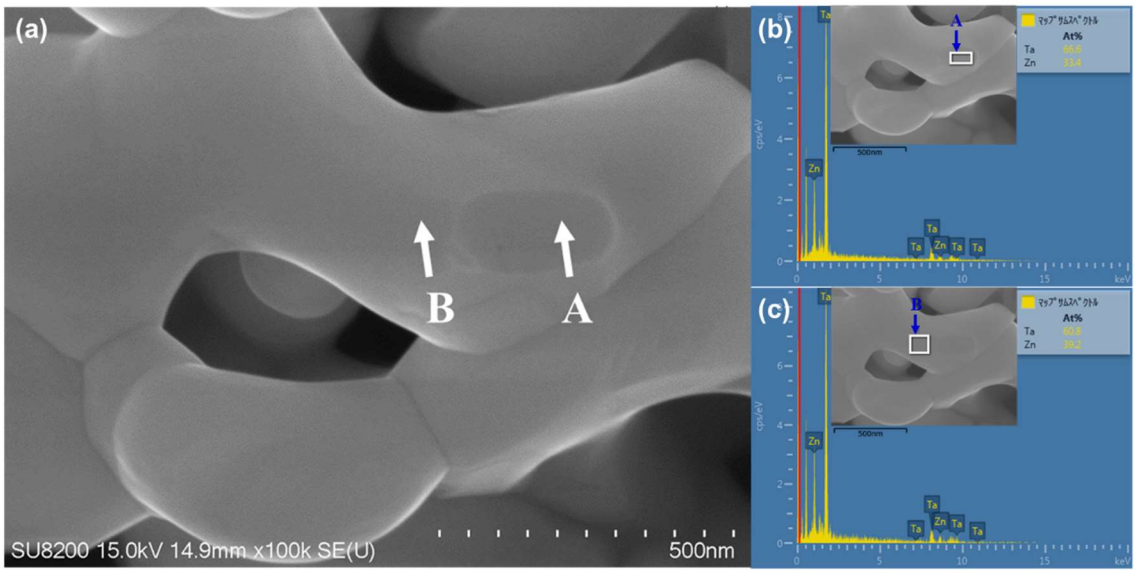

Figure 3. (a) FE-SEM image of ZTO_50A including sites A and B. EDS mapping on ZTO_50A (b) site A with atomic ratios of Ta and Zn 66.6% and 33.4% respectively, and (c) site B with atomic ratios of Ta and Zn 60.8% and 39.2%, respectively.

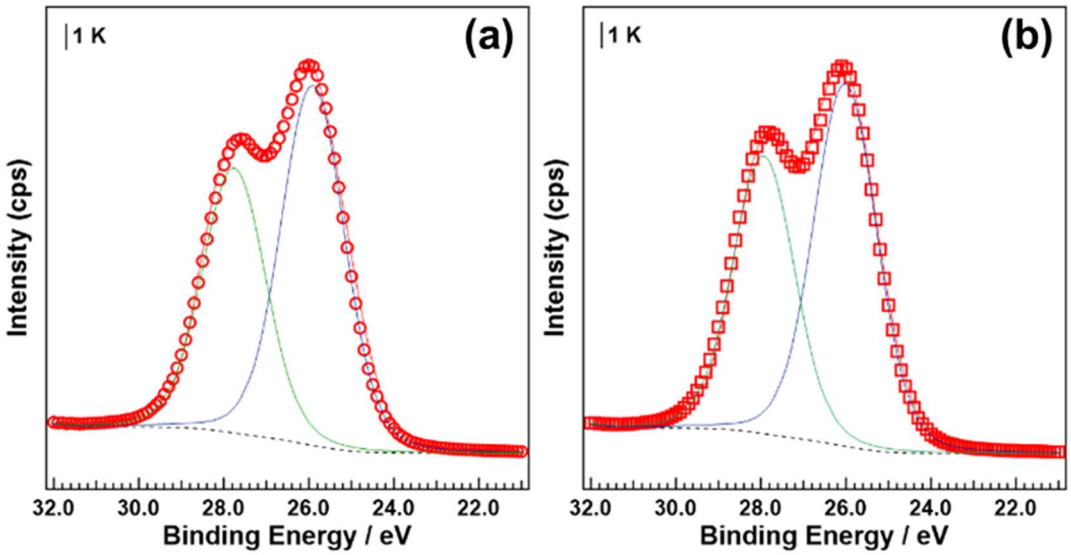

Figure 4. XPS (resolution: 0.1 eV) characterization of (a) Ta 4f in ZTO_50A, and (b) Ta 4f in ZTO_12N.

Table 1. Parameters for fitting peaks of Ta 4f in synthesized ZTO samples in CasaXPS software. Resolution: 0.1 eV.

	ZTO [a]		ZTO [b]	
	Ta 4f			
	5/2	7/2	5/2	7/2
Area ratio	0.74	1	0.75	1
FWHM / eV	1.75	1.75	1.75	1.75
Binding energy / eV	27.76	25.91	27.94	26.02

[a] ZTO_50A, [b] ZTO_12N.

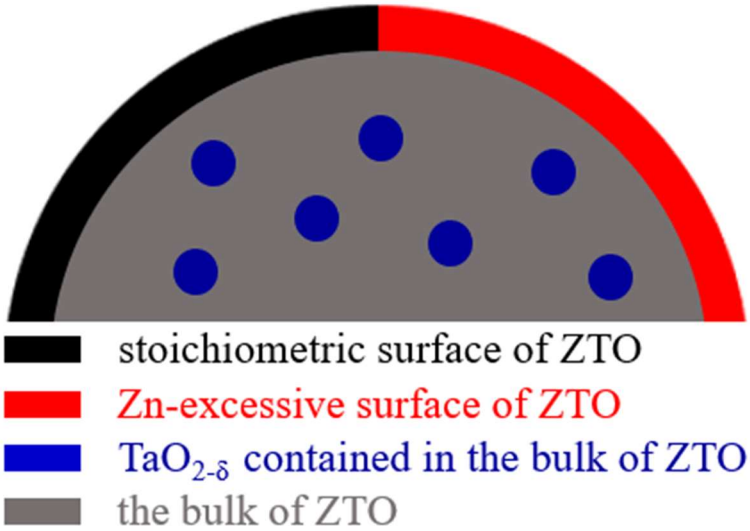

Scheme 1. Compositions of synthesized ZTO_50A including surfaces with stoichiometric ratio of zinc to tantalum (black) and excessive zinc (red), respectively, and $TaO_{2-\delta}$ (blue) in the bulk (grey) of ZTO_50A.

3.3. In-situ photodeposition of Na_2CrO_4

The author attempted to add several oxometallates, such as $KMnO_4$, Na_3VO_4, Na_2MoO_4, and Na_2CrO_4, for the photocatalytic conversion of CO_2 by H_2O over ZTO_50A. These oxometallates would then be reduced on the surface (in-situ photodeposition). Table 2 shows the formation rates of H_2, O_2, and CO in the presence of the oxometallates. The author found that all the species derived from these precursors suppressed H_2 evolution significantly, except for Na_2MoO_4 which is known to succeed in photocatalytic water splitting. [26,27] In particular, only Cr species derived from Na_2CrO_4 promoted a distinct evolution of CO in the photocatalytic conversion of CO_2 by H_2O. Table 3 displayed the dispersions of in-situ photodeposited Cr species on two types of surfaces at various amounts of Na_2CrO_4. Photodeposited Cr species were only found on the stoichiometric-type surfaces on ZTO_50A when the added Na_2CrO_4 was less than 2.5 μmol, according to the EDS mapping results. The priority in photodeposition of Na_2CrO_4 was probably caused by the local circumstance near the stoichiometric surfaces. Zinc oxide has a reported point of zero charge at pH 9.2, [28] suggesting that the Zn-excessive

surfaces were probably more positively charged [29] than the stoichiometric ones in the reaction conditions (pH 6.87). In this case, the local pH near the latter should be correspondingly lower than in the former, as depicted in Scheme 2(a), so that the stoichiometric surfaces should be much more competitive in the reduction of protons and chromates, with both reactions being favored by the high concentration of protons. The chromate ions surrounding the Zn-excessive surfaces had a low probability of being reduced as their diffusion rate toward the stoichiometric surfaces was much faster than that of reduction.

Table 2. formation rates of H_2, O_2 and CO over ZTO_50A with in-situ photodeposition of various oxometallates in the reaction. Photoirradiation time: 1.5 h, photocatalyst: 0.1 g, reaction solution: 1 L of 0.1 M $NaHCO_3$ aqueous solution, flow rate of CO_2: 30 mL min^{-1}, light source: 400 W high-pressure Hg lamp.

Additive	Formation rates of gases / μmol h^{-1}		
	H_2	O_2	CO
none	22	10.7	1.2
Na_2CrO_4	1.9	4.4	6.3
$KMnO_4$	4.7	3.1	1.8
Na_3VO_4	2.9	1.5	0.34
Na_2MoO_4	283	133	0.2

Table 3. Atomic ratios of photodeposited Cr species with different amounts of added Na_2CrO_4 after reaction at Zn-excessive and stoichiometric sites on the surface of ZTO_50A. Photoirradiation time: 1.5 h; photocatalyst: 0.1 g; reaction solution: 1 L of a 0.1 M $NaHCO_3$ aqueous solution; CO_2 flow rate: 30 mL min^{-1}; light source: 400 W high-pressure Hg lamp. ("n.d." stands for "not detected", average on 10 counts for each kind of site).

Na_2CrO_4 (μmol)	Positions			
	Zn-excessive sites		Stoichiometric sites	
	Ta:Zn	Cr ratio At%	Ta:Zn	Cr ratio At%
1.0	1.73	n.d.	1.97	0.22
2.5	1.70	n.d.	1.97	0.90
3.5	1.70	0.16	1.97	1.60
4.0	1.75	0.35	2.01	2.07
5.0	1.71	0.66	2.05	2.81

The author was interested in the mechanism leading to the photodeposition of Na_2CrO_4 on Zn-excessive surfaces when its amount was higher than 3.5 μmol. XPS analysis of ZTO_50A after reaction in the Na_2CrO_4-containing solution revealed a binding energy peak at 576.5 eV attributable to Cr^{3+} (Figure 5(a)), while UV-vis DRS showed that the absorption spectrum of the photodeposited Cr species presented the same peaks as $Cr(OH)_3$ (Figure 5(b)). This demonstrated that the in-situ photodeposited Cr species could exist in the form of $Cr(OH)_3$, in agreement with the results obtained by Francoise et al. [30] at the same pH as in reactions of the author. On the other hand, $Cr(OH)_3$ exhibited a similar Zeta potential (+30 mV) [31] to ZnO (+35 mV) [29] according to Medina's experiments at pH ≈ 7. The concentration of hydroxide ions in the local solution near the stoichiometric surfaces would inevitably increase upon deposition of positively charged

$Cr(OH)_3$, as shown in Scheme 2(b). Consequently, the local pH near these surfaces gradually approached that near the Zn-excessive ones, and the two types of surfaces became equally competitive in the reduction of CrO_4^{2-}. In this case, CrO_4^{2-} could be reduced at the Zn-excessive surfaces as well.

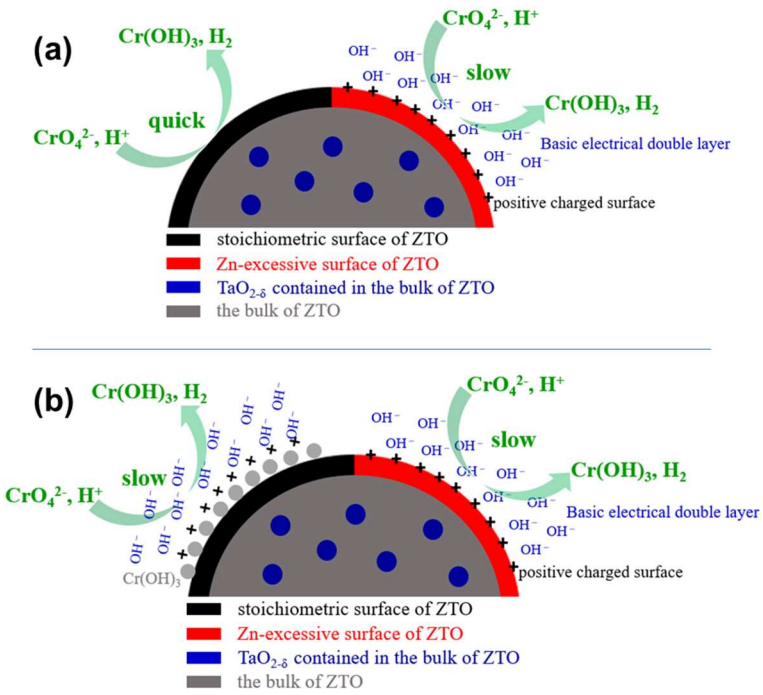

Scheme 2. (a) Proposed mechanisms on differences between stoichiometric and Zn-excessive surfaces of ZTO_50A in photoreduction activities of chromate ions and protons. (b) Changes of photoreduction activities for chromate ions and protons on stoichiometric surface of ZTO after in-situ modification with $Cr(OH)_3$.

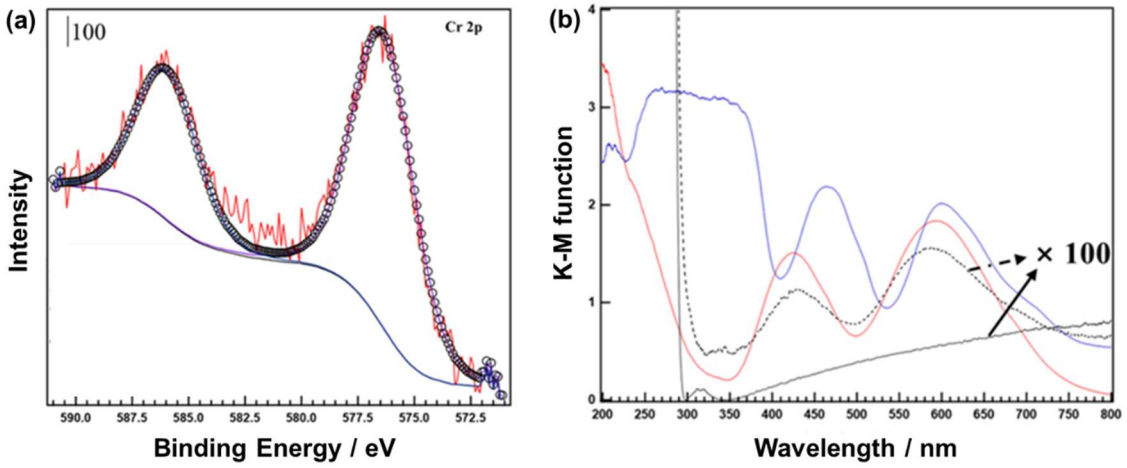

Figure 5. Characterizations on photodeposited chromium species on the surface of ZTO_50A. (a) XPS measurement of Cr 2p on ZTO after photoreduction of CO_2 by H_2O with addition of 5 μmol Na_2CrO_4 in the reaction, (b) UV/vis diffuse reflectance spectra of bare ZTO_50A (black), $Cr(OH)_3$ (red), Cr_2O_3 (blue) and ZTO_50A after reaction in 5 μmol Na_2CrO_4 contained solution (black dash line). Photoirradiation time: 1.5 h, photocatalyst: 0.1 g, reaction solution: 1 L of 0.1 M $NaHCO_3$ aqueous solution, flow rate of CO_2: 30 mL min^{-1}, light source: 400 W high-pressure Hg lamp.

3.4. Performance in photocatalytic conversion of CO_2 by H_2O

Figure 6 shows the dependence of the formation rates of gaseous products on the amount of Na_2CrO_4 corresponding to Table 3. The formation rate of H_2 over bare ZTO_50A reached 22.0 μmol h^{-1}, whereas only 1.2 μmol h^{-1} of CO was produced. The e^-/h^+ balance calculated from Equation (4) was close to 1.0, indicating that the electrons consumed for CO_2 reduction were supplied by H_2O rather than other sacrificial reagents such as carbon impurities on the photocatalyst. H_2 evolution over ZTO_50A was significantly suppressed (22.0 vs. 12.8 μmol h^{-1}) by adding just 1.0 μmol Na_2CrO_4 to the reaction solution. By increasing the amount of added Na_2CrO_4 to 10 μmol, the formation rate of H_2 decreased to 1.3 μmol h^{-1}, whereas that of CO was distinctly promoted from 1.2 to 6.0 μmol h^{-1}. Remarkably, the in-situ photodeposition of Na_2CrO_4 only suppressed H_2 evolution without increasing CO evolution if its amount was lower than 2.5 μmol, even though Cr species were successfully photodeposited on the catalyst surface, as

determined by XPS (Figure 7). After the loading amount reached 3.5 μmol, the formation rate of CO was clearly enhanced and showed no variations for Na_2CrO_4 amounts higher than 5 μmol. Through a comprehensive comparison of the trends presented in Figure 6 and Table 3, the author can conclude that H_2 was produced mainly on the stoichiometric surfaces of bare ZTO_50A, and the active sites for the photocatalytic conversion of CO_2 by H_2O were shifted from the stoichiometric to Zn-excessive surfaces during the in-situ photodeposition of Na_2CrO_4.

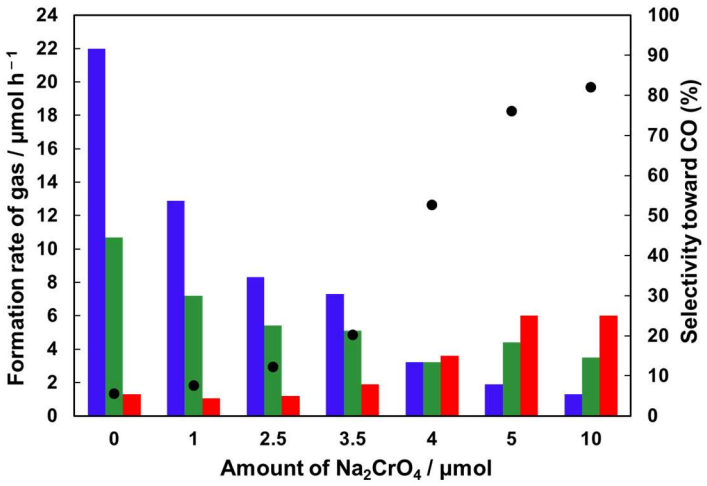

Figure 6. Formation rates of H_2 (blue), O_2 (green), and CO (red), and selectivity (black dots) toward CO evolution over ZTO_50A with different amounts of Na_2CrO_4 in the reaction. Photoirradiation time: 1.5 h; photocatalyst: 0.1 g; reaction solution: 1 L of a 0.1 M $NaHCO_3$ aqueous solution; CO_2 flow rate: 30 mL min^{-1}; light source: 400 W high-pressure Hg lamp.

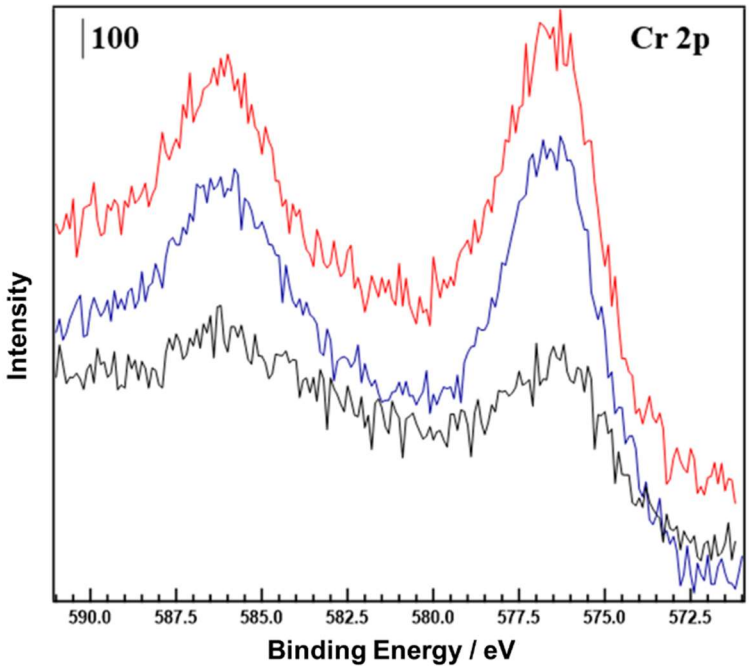

Figure 7. XPS characterizations of Cr 2p on photodeposited chromium species on the surface of ZTO_50A after photoreduction of CO_2 by H_2O with in-situ addition of 1 μmol (black), 2.5 μmol (blue) and 5 μmol (red) Na_2CrO_4 for the reaction, respectively. Photoirradiation time: 1.5 h, photocatalyst: 0.1 g, reaction solution: 1 L of 0.1 M $NaHCO_3$ aqueous solution, flow rate of CO_2: 30 mL min^{-1}, light source: 400 W high-pressure Hg lamp.

3.5. Effect of UV/O_3 treatment

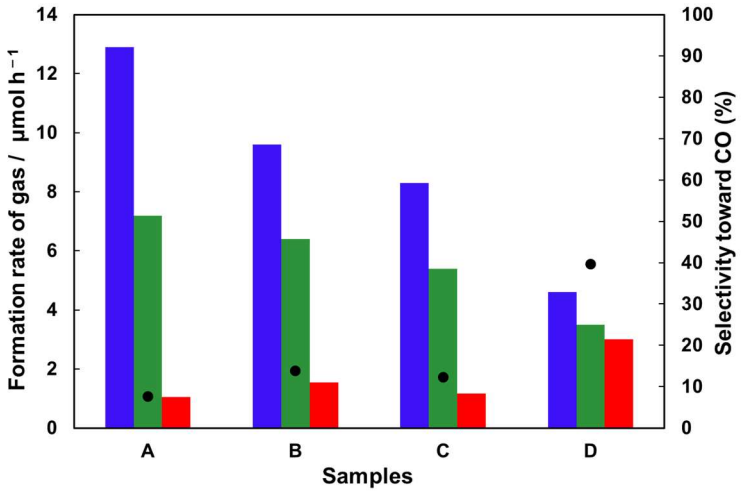

Figure 8. Formation rates of H_2 (blue), O_2 (green), and CO (red), and selectivity (black dots) toward CO evolution. Samples A and C: ZTO_50A with addition of 1 and 2.5 μmol Na_2CrO_4, respectively; samples B and D: ZTO_50A treated by UV/O_3 for 24 h with addition of 1 and 2.5 μmol Na_2CrO_4, respectively. Photoirradiation time: 1.5 h; photocatalyst: 0.1 g; reaction solution: 1 L of a 0.1 M $NaHCO_3$ aqueous solution; CO_2 flow rate: 30 mL min^{-1}; light source: 400 W high-pressure Hg lamp.

On the other hand, the fact that the stoichiometric surfaces did not selectively produce CO like the Zn-excessive ones after the in-situ photodeposition of Na_2CrO_4 remained unexplained. One possibility was that some unconverted ZnO on the Zn-excessive surfaces could enhance the adsorption and activation of CO_2 from the solution owing to its basicity. Such a speculation would be in agreement with the previous work, in which the author found that Sr oxide modifications on Ta_2O_5 [11] and Zn doping on Ga_2O_3 [32] clearly enhanced the photoreduction of CO_2 by H_2O. However, unconverted ZnO on the Zn-excessive surfaces seemed not to be the only reason for its capability of CO_2 photoreduction by H_2O. The author performed a UV/O_3 annealing treatment on the synthesized ZTO_50A and then carried out CO_2 photoreduction on the treated samples at the same conditions as done previously. Interestingly, the author found that the formation rate of CO over O_3-treated ZTO_50A was promoted by the addition of 1 μmol Na_2CrO_4, as shown in Figure 8. Such a promotion effect was more visible when 2.5 μmol Na_2CrO_4 was used, with a CO formation rate almost 3 times higher than that over untreated ZTO_50A. At the same time, EDS mapping still revealed the presence of photodeposited Cr species only on the stoichiometric surfaces of the O_3-treated sample (Table 4). Evidently, the stoichiometric surfaces could also promote the evolution of CO after O_3 treatment. The UV/O_3 annealing treatment was reported as a successful method to remove oxygen defects in Ta_2O_5 by Shinriki et al. [33] This suggested that lattice oxygen on the surface of ZTO_50A was also necessary for CO evolution. Stoichiometric surfaces modified with $Cr(OH)_3$ did not exhibit CO evolution probably because they were rich in

oxygen defects. Surface oxygen in metal oxides has been considered to favor the chemical adsorption and activation of CO_2, [17,34–36] in which one pair of electrons, acting as Lewis base, would be donated to positive carbon atoms to form a transition state. On the other hand, $Cr(OH)_3$ is a known amphoteric compound and it can act as Lewis acid in catalysis. The importance of surface oxygen and its synergetic effect with modified $Cr(OH)_3$ implied that Lewis pairs, [37–40] which have been widely demonstrated to be excellent active sites for CO_2 transformation, were probably responsible for the promotion of CO_2 photoreduction over ZTO_50A. It is interesting to discuss the difference in oxygen defects between the stoichiometric and Zn-excessive surfaces. As presented in Equations (5) to (7), a $TaO_{2-\delta}$ phase formed during ZTO_50A synthesis: this impurity, consisting of low-valent Ta, would inevitably introduce oxygen vacancies into the structure. [41,42] On the other hand, these oxygen vacancies would be removed gradually by further reaction with ZnO in calcination. It was conceivable that oxygen vacancies could be removed more completely by a sufficient amount of surrounding ZnO, such as in Zn-excessive surfaces. In contrast, an insufficient content of ZnO would leave residual oxygen vacancies, such as in stoichiometric areas.

Table 4. Atomic ratio of photodeposited chromium species after reaction at Zn-excessive and stoichiometric sites, respectively, on the surface of ZTO_50A treated by UV/O_3 for 24 h. Photoirradiation time: 1.5 h, photocatalyst: 0.1 g, reaction solution: 1 L of 0.1 M $NaHCO_3$ aqueous solution, flow rate of CO_2: 30 mL min^{-1}, light source: 400 W high-pressure Hg lamp. ("n.d." stands for "not detected", average on 10 counts for each kind of site).

Na_2CrO_4 (μmol)	Positions			
	Zn-excessive sites		Stoichiometric sites	
	Ta:Zn	Cr ratio At%	Ta:Zn	Cr ratio At%
2.5	1.69	n.d.	1.96	1.07

3.6. The importance of pH and Cr precursors

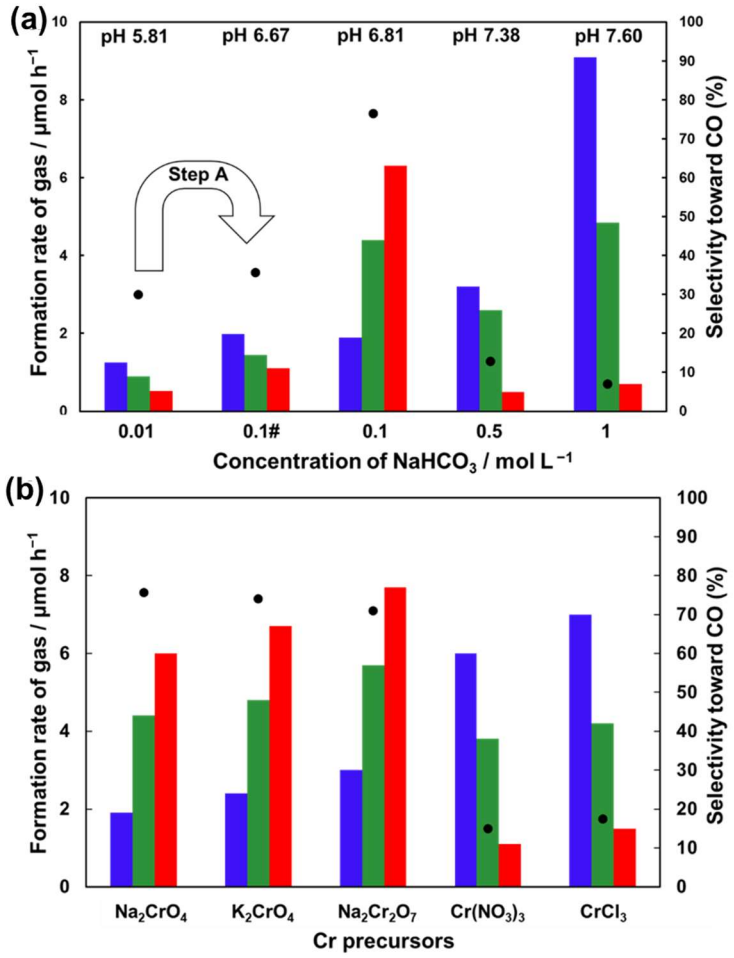

Figure 9. Formation rates of H_2 (blue), O_2 (green), and CO (red), and selectivity (black dots) toward CO evolution over ZTO_50A with (a) addition of 5 μmol Na_2CrO_4 in the reaction mixture at different pH tuned by various concentration of $NaHCO_3$ additives, and (b) addition of 5 μmol of various Cr precursors at 0.1 M $NaHCO_3$. Photocatalyst: 0.1 g; CO_2 flow rate: 30 mL min^{-1}; volume of the reaction solution: 1 L; light source: 400 W high-pressure Hg lamp. (Step A in panel a: addition of 0.09 mol $NaHCO_3$ to the reaction suspension containing 0.01 mol $NaHCO_3$ for further reaction in 0.1# M $NaHCO_3$ aqueous solution.)

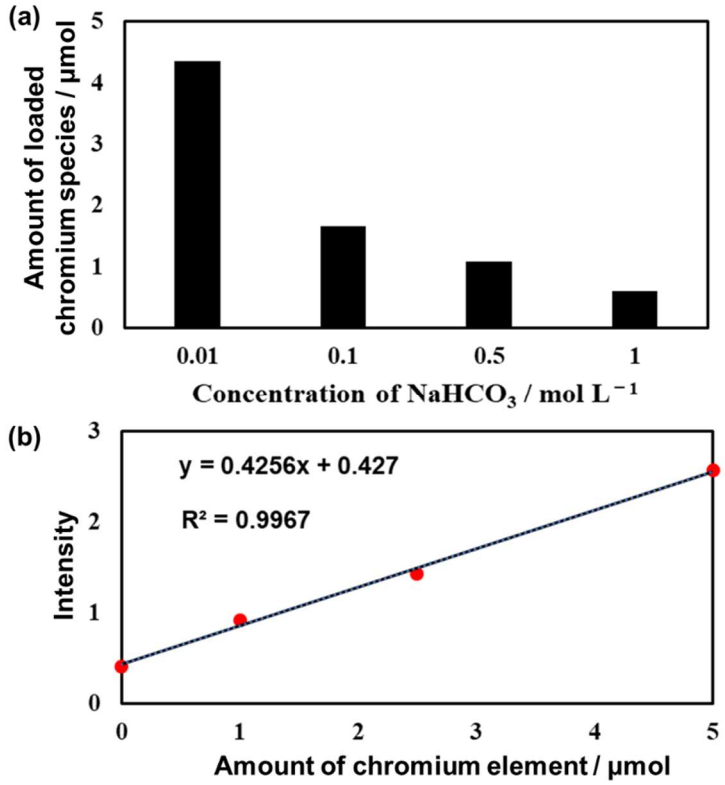

Figure 10. (a) amount of loaded chromium species on ZTO_50A after in-situ photodeposition of 5 μmol Na_2CrO_4 at various concentration of $NaHCO_3$, photoirradiation time: 1.5 h, photocatalyst: 0.1 g, flow rate of CO_2: 30 mL min^{-1}, volume of the reaction solution: 1 L, light source: 400 W high-pressure Hg lamp; (b) Calibration on amount of chromium elements for XRF characterization on EDX-8000.

The reduction of added chromates was largely subjected to the pH value in the reaction solution. [43] Therefore, the author predicted that the pH value would also affect the formation rates of H_2 and CO in the reactions. The different concentrations of $NaHCO_3$ in aqueous solutions (0.01 to 1 M) were used to tune the pH for the photocatalytic conversion of CO_2 by H_2O, as shown in Figure 9(a). The pH values of the solutions increased from 6.81 to 7.60 while increasing the concentration of $NaHCO_3$ from 0.1 to 1.0 M. Following such a change, H_2 evolution was promoted to approximately 9.3 from 2.5 μmol h^{-1}, while the formation rate of CO decreased to 0.7 from 6.0 μmol h^{-1}.

This behavior can be explained by a suppression of the photodeposition of Cr species following the increase in pH. According to the XRF measurements shown in Figure 10, the loaded amount of Cr species decreased from 1.7 to 0.6 μmol with increasing pH. However, the formation rate of CO was abnormally low in 0.01 M $NaHCO_3$ aqueous solution (pH 5.81) even though the amount of modified Cr species reached 4.3 μmol. Increasing the concentration of $NaHCO_3$ to 0.1 M (column 0.1#) by adding 0.09 mol of $NaHCO_3$ did not affect the CO formation rate, indicating that the factor of additive concentration was not the cause of such a low activity. EDS mapping revealed that Cr species were mainly photodeposited on the stoichiometric surfaces, which showed no activity in producing CO at a concentration of 0.01 M $NaHCO_3$ as shown in Table 5. This implied that the location of photodeposited Cr species did not only depend on the amount of added Na_2CrO_4 but also on pH. Moreover, the Cr precursors used in this work were also a decisive factor for the suppression of H_2 and promotion of CO. As presented in Figure 9b, the selectivity toward CO evolution depended on the types of chromate and dichromate salts. Employing Cr(VI) precursors is paramount to obtaining a high selectivity toward CO evolution, whereas Cr(III) precursors had only limited influence on H_2 suppression. $Cr(OH)_3$ was expected to deposit randomly on the surfaces of ZTO_50A upon hydrolysis of Cr(III) precursors based on its K_{sp} (7×10^{-31}) at pH 6.8. This difference highlighted the importance of directional photodeposition of Cr species at reductive sites.

Table 5. Atomic ratio of photodeposited chromium element on stoichiometric and Zn-excessive surfaces of ZTO_50A, respectively, after photoreduction of CO_2 by H_2O in 0.01 M $NaHCO_3$ aqueous solution. Photoirradiation time: 1.5 h, photocatalyst: 0.1 g, volume of reaction solution: 1 L, flow rate of CO_2: 30 mL min^{-1}, light source: 400 W high-pressure Hg lamp. ("n.d." stands for "not detected", average on 10 counts for each kind of site).

	Stoichiometric site		Zn-excessive site	
	Ta:Zn	Ratio of Cr (At%)	Ta:Zn	Ratio of Cr (At%)
ZTO	2.07	4.36	1.68	0.06

Based on above the discussion, the author proposes the following steps (Scheme 3) outlining the mechanism of selective photoreduction of CO_2 by H_2O on $Cr(OH)_3$-loaded ZTO_50A: i) $Cr(OH)_3$ was first formed on the surfaces with stoichiometric Zn:Ta ratio because of the lower local pH, and even though H_2 evolution was prohibited, CO evolution was not enhanced in this stage due to the presence of oxygen defects on these surfaces; ii) $Cr(OH)_3$ started to be deposited on the surfaces containing an excessive amount of ZnO because the two types of surfaces were equally competitive in the photoreduction of chromate ions when the stoichiometric ones were covered by $Cr(OH)_3$, and CO evolution was promoted on $Cr(OH)_3$-modified Zn-excessive surfaces.

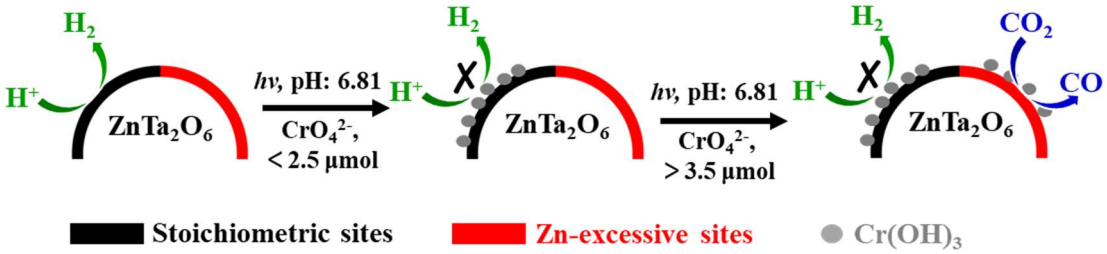

Scheme 3. Mechanism of highly selective CO_2 photoreduction by H_2O toward CO evolution over 0.1 g ZTO_50A achieved by in-situ photodeposition of Na_2CrO_4 in the reaction mixture.

4. Conclusion

The author successfully improved the formation rate of CO and selectivity toward CO evolution for the photocatalytic conversion of CO_2 by H_2O as an electron donor by developing a new strategy that does not make use of the widely employed Ag cocatalyst. Trace amounts of chromates were photodeposited in-situ on $ZnTa_2O_6$ fabricated via an SSR method during the reaction. As a result, the selectivity toward CO evolution was

achieved at 80% and the formation rate of CO (6.0 μmol h^{-1}; 0.1 g) was maintained well in comparison with the previous data (obtained from 0.5 g of 3 wt% Ag-loaded $ZnTa_2O_6$ which yielded 20.0 μmol h^{-1} of CO with a selectivity of approximately 50%). [21] The $ZnTa_2O_6$ photocatalysts fabricated in this study contained two types of active surfaces with stoichiometric and Zn-excessive Zn:Ta ratios, respectively. The active sites of the synthesized $ZnTa_2O_6$ shifted from stoichiometric to Zn-excessive surfaces during the in-situ photodeposition of chromates.

References

1. J. Goldemberg, World energy assessment: energy and the challenge of sustainability. (UN. 2001).
2. J. Hansen, R. Ruedy, M. Sato and K. Lo. Rev. Geophys. 2010, 48, 1–29.
3. J. Hansen, L. Nazarenko, R. Ruedy, M. Sato, J. Wills, A. D. Genio, D. Koch, A. Lacis, K. Lo, S. Menon, T. Novakov, J. Perlwitz, G. Russell, G. A. Schmidt and N. Tausnev. Science 2005, 308, 1431–1436.
4. Y. Zhao, C. Ding, J. Zhu, W. Qin, X. Tao, F. Fan, R. Li and C. Li. Angew. Chemie. Int. Ed. 2020, 132, 9740–9745.
5. A. Kojima, K. Teshima, Y. Shirai, and T. Miyasaka. J. Am. Chem. Soc. 2009, 131, 6050–6051.
6. H. Kasap, D. S. Achilleos, A. J. Am. Chem. Soc. 2018, 140, 11604–11607.
7. K. Sayama and H. Arakawa. J. Phys. Chem. 1993, 97, 531–533.
8. K. Teramura and T. Tanaka. Phys. Chem. Chem. Phys. 2018, 20, 8423–8431.
9. K. Iizuka, T. Wato, Y. Miseki, K. Saito and A. Kudo. J. Am. Chem. Soc. 2011, 133, 20863–20868.
10. H. Nakanishi, K. Iizuka, T. Takayama, A. Iwase and A. Kudo. ChemSusChem 2017, 10, 112–118.
11. K. Teramura, H. Tatsumi, Z. Wang, S. Hosokawa and T. Tanaka. Bulletin of the Chemical Society of Japan 2015, 88 431–437.
12. T. Yoshida, N. Yamamoto, T. Mizutani, M. Yamamoto, S. Ogawa, S. Yagi, H. Nameki and H. Yoshida. Catal. Today 2018, 303, 320–326.
13. Z. Wang, K. Teramura, Z. Huang, S. Hosokawa, Y. Sakata and T. Tanaka. Catal. Sci. Technol. 2016, 6, 1025–1032.
14. A. Anzai, N. Fukuo, A. Yamamoto and H. Yoshida. Catal. Commun. 2017, 100, 134–138.
15. T. Ishii, A. Anzai, A. Yamamoto and H. Yoshida. Appl. Catal. B Environ. 2020, 277, 119192.

16. R. Pang, K. Teramura, H. Asakura, S. Hosokawa and T. Tanaka. Appl. Catal. B Environ. 2017, 218, 770–778.
17. S. Yoshizawa, Z. Huang, K. Teramura, H. Asakura, S. Hosokawa and T. Tanaka. ACS Appl. Mater. Interfaces 2019, 11, 37875-37884.
18. S. Wang, K. Teramura, T. Hisatomi, K. Domen, H. Asakura, S. Hosokawa and T. Tanaka. ACS Appl. Energy Mater. 2020, 3, 1468–1475.
19. Z. Wang, K. Teramura, S. Hosokawa and T. Tanaka. Appl. Catal. B Environ. 2015, 163, 241–247.
20. R. Pang, K. Teramura, H. Asakura, S. Hosokawa and T. Tanaka. ACS Sustain. Chem. Eng. 2019, 7, 2083–2090.
21. S. Iguchi, K. Teramura, S. Hosokawa and T. Tanaka. Catal. Sci. Technol. 2016, 6, 4978–4985.
22. N. Wu, P. Bai, T. Yang, H. Li, J. Zhang, Z. Chai and X. Wang. Photochem. Photobiol. Sci 2020, 19, 1042.
23. Y. Li, S. Sanna, K. Norrman, D. V. Christensen, C. S. Pedersen, J. M. G. Lastra, M. L. Traulsen, V. Esposito and N. Pryds. Appl. Surf. Sci. 2019, 470, 1071–1074.
24. R. Simpson, R. G. White, J. F. Watts and M. A. Baker. Appl. Surf. Sci. 2017, 405, 79–87.
25. C. S. Pedersen, J. H. Chang, Y. Li, N. Pryds and J. M. G. Lastra. APL Mater. 2020, 8, 071108.
26. Q. Wang, T. Hisatomi, Q. Jia, H. Tokudome, M. Zhong, C. Wang, Z. Pan, T. Takata, M. Nakabayashi, N. Shibata, Y. Li, I. D. Sharp, A. Kudo, T. Yamada and K. Domen. Nat. Mater. 2016, 15, 611–615.
27. H. Zhang, P. Zhang, M. Qiu, J. Dong, Y. Zhang and X. W. Lou. Adv. Mater. 2019, 31, 1804883, 1–7.
28. X. Zhai, Z. Chen, S. Zhao, H. Wang and L. Yang. J. Environ. Sci. 2010, 22, 1527–1533.
29. R. Marsalek. Apcbee Procedia 2014, 9, 13–17.

30. F. C. Richard and A. C. M. Bourg. Water Res. 1991, 25, 807–816.
31. B. Y. Medina, M. L. Torem and L. M. S. De Mesquita. Miner. Eng. 2005, 18, 225–231.
32. K. Teramura, Z. Wang, S. Hosokawa, Y. Sakata and T. Tanaka. Chem. A Eur. J. 2014, 20, 9906–9909.
33. H. Shinriki and M. Nakata. IEEE Trans. Electron Devices 1991, 38, 455–462.
34. D. Gao, Y. Zhang, Z. Zhou, F. Cai, X. Zhao, W. Huang, Y. Li, J. Zhu, P. Liu, F. Yang, G. Wang and X. Bao. J. Am. Chem. Soc. 2017, 139, 5652–5655.
35. M. Yamamoto, T. Yoshida, N. Yamamoto, H. Yoshida and S. Yagi. Surf. Sci. Nanotechnol. 2014, 12, 299–303.
36. H. Tsuneoka, K. Teramura, T. Shishido and T. Tanaka. J. Phys. Chem. C 2010, 114, 8892–8898.
37. G. Ménard and D. W. Stephan. Angew. Chemie. Int. Ed. 2011, 123, 8546–8549.
38. J. Jia, C. Qian, Y. Dong, Y. Li, H. Wang, M. Ghoussoub, K.T. Butler, A. Walsh and G. A. Ozin. Chem. Soc. Rev. 2017, 46, 4631–4644.
39. K. K. Ghuman, L. B. Hoch, P. Szymanski, J. Y. Y. Loh, N. P. Kherani, M. A. ElSayed, G. A. Ozin and C. V. Singh. J. Am. Chem. Soc. 2016, 138, 1206–1214.
40. S. Zhang, Z. Xia, Y. Zou, F. Cao, Y. Liu, Y. Ma and Y. Qu. J. Am. Chem. Soc. 2019, 141, 11353–11357.
41. J. Wang, S. Su, B. Liu, M. Cao and C. Hu. Chem. Commun. 2013, 49, 7830–7832.
42. C. Tealdi, M. S. Islam, L. Malavasi and G. Flor. J. Solid State Chem. 2004, 177, 4359–4367.
43. B. Xie, C. Shan, Z. Xu, Xu. Li, X. Zhang, J. Chen, B. Pan. Chem. Eng. J. 2017, 308, 791–797.

Chapter 2

Effect of the in situ addition of chromate ions on H_2 evolution during the photocatalytic conversion of CO_2 using H_2O as the electron donor

Abstract

Chromium-based cocatalysts influence H_2 evolution during the overall water splitting reaction in the photocatalytic conversion of CO_2 in the presence of H_2O as an electron donor. To clarify the mechanism by which chromium species promote or suppress H_2 evolution, the reaction was carried out in the presence of α- and β-Ga_2O_3, $NaTaO_3$, $ZnTa_2O_6$, and $SrTa_2O_6$ photocatalysts with the in situ addition of chromate ions. The author found that chromate ions suppress H_2 evolution during the photocatalytic conversion of CO_2 by H_2O when the surface of the photocatalyst is highly protonated.

1. Introduction

Sunlight is a sustainable energy source [1], making it an attractive replacement for fossil fuels in the battle against global warming [2]. In particular, the direct utilization of solar energy is advantageous compared to the use of nuclear [3] and wind [4] energy because of its low environmental impact. Therefore, the development of technologies for the conversion of solar energy, such as photovoltaic cells [5], water (H_2O) splitting [6], biomass production [7], and the photocatalytic conversion of carbon dioxide (CO_2) [8–10], have drawn significant interest. In particular, the photocatalytic conversion of CO_2 in the presence of H_2O reduces the concentration of CO_2, a powerful greenhouse gas, in the atmosphere and converts it to a valuable energy source or chemical feedstock via artificial photosynthesis. Equations (1) and (2) show that the photocatalytic conversion of CO_2 in the presence of H_2O must satisfy two criteria: a balance of consumed holes and electrons and high selectivity toward CO_2 derived productions rather than H_2 from H_2O splitting.

$$e^-/h^+ = (2R_{HCOOH} + 2R_{CO} + 4R_{HCHO} + 6R_{CH_3OH} + 8R_{CH_4} + 2R_{H_2})/4R_{O_2} \quad (1)$$

$$\text{Selectivity} = (2R_{HCOOH} + 2R_{CO} + 4R_{HCHO} + 6R_{CH_3OH} + 8R_{CH_4})/(2R_{HCOOH} + 2R_{CO} + 4R_{HCHO} + 6R_{CH_3OH} + 8R_{CH_4} + 2R_{H_2}) \times 100\% \quad (2)$$

In these equations, R represents the rate of formation of each product formed by the photocatalytic conversion of CO_2 in the presence of H_2O. Thus, the evolution of H_2 should be suppressed as much as possible. Ag has been widely reported as an effective cocatalyst for enhancing the CO evolution while suppressing H_2 evolution over Sr-doped $NaTaO_3$ [11], $CaTiO_3$ [12], Al-doped $SrTiO_3$ [13], Ga_2O_3 [14], $ZnGa_2O_4$ [13], and $SrNb_2O_6$ [16]. However, Ag nanoparticles do not always function as effective cocatalysts for the photocatalytic conversion of CO_2 using H_2O. In many cases, the evolution of H_2 is dominant, even in the presence of CO_2. Recently, Pang et al. found that the use of Ag/Cr core–shell cocatalysts to modify the surface of commercial Ga_2O_3 can decrease the H_2 production activity, even though Pt/Cr, Au/Cr, and Pd/Cr core–shell cocatalysts significantly promote the evolution of H_2 [17]. This phenomenon indicates that the effect of chromium species on

the evolution of H_2 (suppression or promotion) depends on the specific photocatalysts and cocatalysts. However, the critical conditions under which chromium species suppress or enhance the evolution of H_2 derived from overall water splitting, even in the presence of CO_2, are not clear.

Importantly, the evolution of H_2 during the photocatalytic conversion of CO_2 in the presence of H_2O must be controlled to obtain high selectivity toward CO evolution. However, it is necessary to clarify how chromium species promote or suppress the evolution of H_2. In previous work, the author found that the in situ addition of chromate ions suppressed the rate of formation of H_2 almost completely during the photocatalytic conversion of CO_2 using H_2O as the electron donor over $ZnTa_2O_6$ synthesized through a solid-state reaction [18]. As a result, the selectivity for CO evolution increased significantly. Unfortunately, the chromate ions added to the reaction solution did not always suppress the evolution of H_2 during the photocatalytic conversion of CO_2 by H_2O over a few photocatalysts, such as commercial Ga_2O_3. These findings indicate that control over the surface properties of photocatalysts is important when using chromate ions as H_2 evolution inhibitors. Therefore, in this study, the author investigated the relationship between chromate ions and the surface properties of photocatalysts to obtain high selectivity toward CO evolution for the photocatalytic conversion of CO_2 using H_2O.

2. Experimental section

2.1. Photocatalyst preparation

All reagents used for the synthesis of the main photocatalysts are listed in Table 1. Except for the commercial photocatalysts, the main photocatalysts used in this study were fabricated by solid-state reaction (SSR) or flux methods. Details of each photocatalyst are listed in Table 2.

Table 1. Reagents used in this work.

Reagent	Company	Purity
Na_2CrO_4•$4H_2O$	Wako	99.0%
ZnO	Wako	99.0%
Ta_2O_5	High purity chemicals	99.9%
$SrCO_3$	Wako	99.99%
H_3BO_3	Wako	99.5%
$NaHCO_3$	Wako	99.5-100.3%
Commercial Ga_2O_3	High purity chemicals	99.99%
$Al(NO_3)_3$•$9H_2O$	Wako	97.0%
NaOH	Wako	97.0%
$Ga(NO_3)_3$•xH_2O	High purity chemicals	99.999%
Na_2CO_3	Wako	99.8%

Table 2: Synthesis of the main photocatalysts used in this work.

Photocatalyst	Precursors	Pre-treatment	Conditions	Post-treatment	Ref.
$ZnTa_2O_6$ (SSR)	ZnO + Ta_2O_5	Physical mixture	1273 K, 12 h		
$ZnTa_2O_6$ (flux)	1.1 ZnO + Ta_2O_5 + 0.2 H_3BO_3	Physical mixture	1373 K, 2 h	Wash in water, 353 K, 2 h	
$SrTa_2O_6$ (SSR)	$SrCO_3$ + Ta_2O_5	Physical mixture	1423 K, 24 h		
$SrTa_2O_6$ (flux)	1.1 $SrCO_3$ + Ta_2O_5 + 0.2 H_3BO_3	Physical mixture	1423 K, 5 h	Wash in water, 353 K, 2 h	
Ga_2O_3	Commercial				
Ta_2O_5	Commercial				
$NaTaO_3$	Na_2CO_3 + Ta_2O_5	Physical mixture	1423 K, 20 h		
GaOOH	$NaGaO_2$ + HCl		353 K, 2 h		
α − Ga_2O_3	GaOOH		723 K, 3 h		
β − Ga_2O_3	Commercial Ga_2O_3		1423 K, 24 h		

2.2. Photocatalyst characterization

The structures of the main photocatalysts synthesized in this work were determined by X-ray diffraction (XRD) measurements using a Rigaku Ultima IV powder diffractometer with Cu-K_α radiation generated at a voltage of 40 kV and a current of 40

mA. The step size for characterizations was set as 0.02°.

2.3. Photocatalytic experiments

The photocatalytic conversion of CO_2 by H_2O over the photocatalysts was conducted in an inner irradiation reactor equipped with a quartz jacket connected to a cooling system. The reaction temperature was controlled from 298 to 303 K. The light source was a 400-W high-pressure mercury lamp (Sen Lights Corp.). For reaction, the photocatalyst was added to the reactor, and 60 mL min^{-1} CO_2 (5N) was added to purge residual air from the system. Subsequently, the flow rate of CO_2 was shifted to 30 mL min^{-1} during photoirradiation. The products (H_2, O_2, and CO) were detected by a thermal conductivity detector (TCD) or flame ionization detector (FID) in a GC-8A gas chromatograph (Shimadzu).

3. Results and Discussion

3.1. Photocatalysts fabricated via SSR

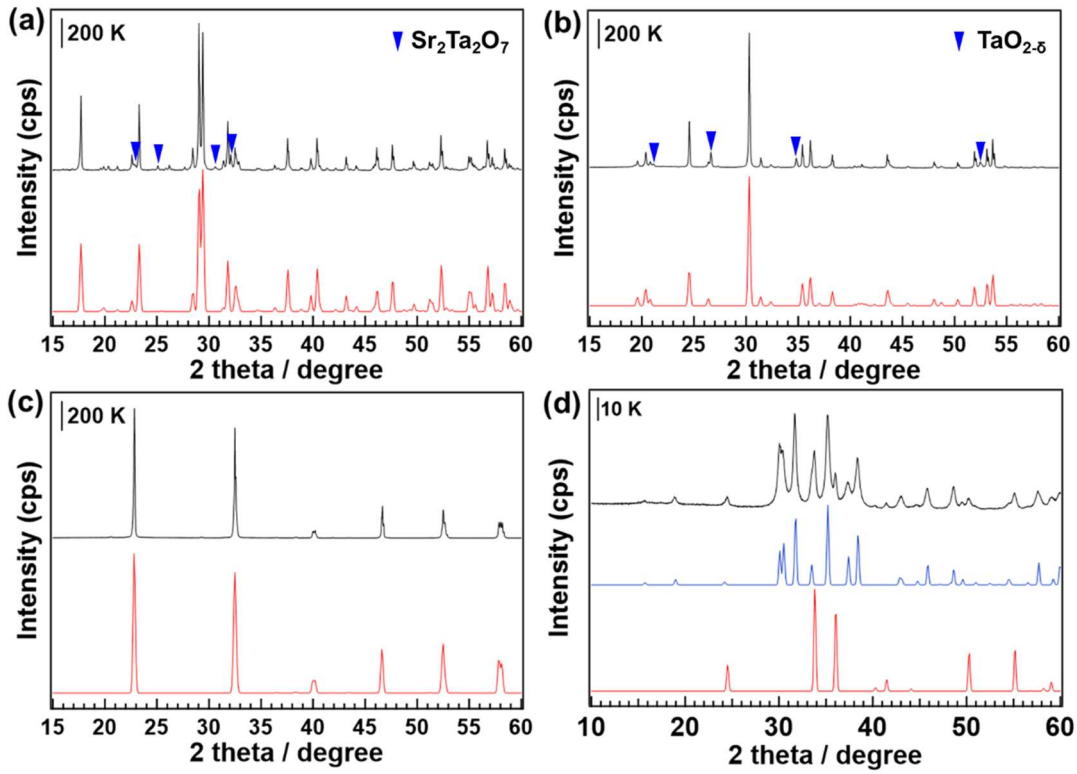

Figure 1. X-ray diffraction patterns (black and red lines are the patterns of the sample and

ICSD card, respectively) of fabricated (a) $SrTa_2O_6$, (b) $ZnTa_2O_6$, (c) $NaTaO_3$, and (d) commercial Ga_2O_3. For (d), ICSD patterns of α-Ga_2O_3 (red) and β -Ga_2O_3 (blue) are shown.

Figure 1 shows the XRD patterns of the target photocatalysts used in this study. Trace amounts of $TaO_{2-\delta}$ and $Sr_2Ta_2O_7$ impurities were observed in the patterns of the $ZnTa_2O_6$ and $Sr_2Ta_2O_6$ samples (Figures 1(a) and 1(b), respectively). The presence of $TaO_{2-\delta}$ implies that the ZnO used in the precursor was not completely converted to $ZnTa_2O_6$ during SSR. However, peaks corresponding to unconverted ZnO were not observed in the XRD pattern of $ZnTa_2O_6$ synthesized by SSR. This indicates that the remaining ZnO probably exists in the form of a solid solution with $ZnTa_2O_6$. Because ZnO possesses a positive zeta potential [19] at neutral pH, it should be protonated during the photocatalytic conversion of CO_2 in the presence of H_2O (pH 6.8). Because the molar ratio of Sr to Ta in the precursor for the synthesis of $SrTa_2O_6$ was 1:2, the formation of $Sr_2Ta_2O_7$ in the obtained $SrTa_2O_6$ suggests that the mobility of the Sr species was poor during calcination. This would inevitably result in the SrO species not being completely converted into $SrTa_2O_6$, similar to the unconverted ZnO in $ZnTa_2O_6$. Therefore, the $SrTa_2O_6$ synthesized by the SSR method would also possess a positive zeta potential during the reaction because SrO species bind protons strongly [20]. In contrast, a pure phase of $NaTaO_3$ was successfully obtained, as shown in Figure 1(c), because the Na_2CO_3 precursor acted as the flux reagent owing to its low melting point. By comparing the relative intensities of the (100) and (110) peaks at 22.8 °and 32.5°, respectively, the space group of the synthesized $NaTaO_3$ was determined to be *Pbnm* which indicated that the unit cell of $NaTaO_3$ was in the orthorhombic symmetry. Figure 1(d) clearly reveals that commercial Ga_2O_3 contains both α and β phases, possibly because of the moderate calcination temperature used for synthesis. In particular, it has been reported that the use of low calcination temperatures results in the formation of α-Ga_2O_3, which can be easily converted into the β phase if the calcination temperature is increased [21].

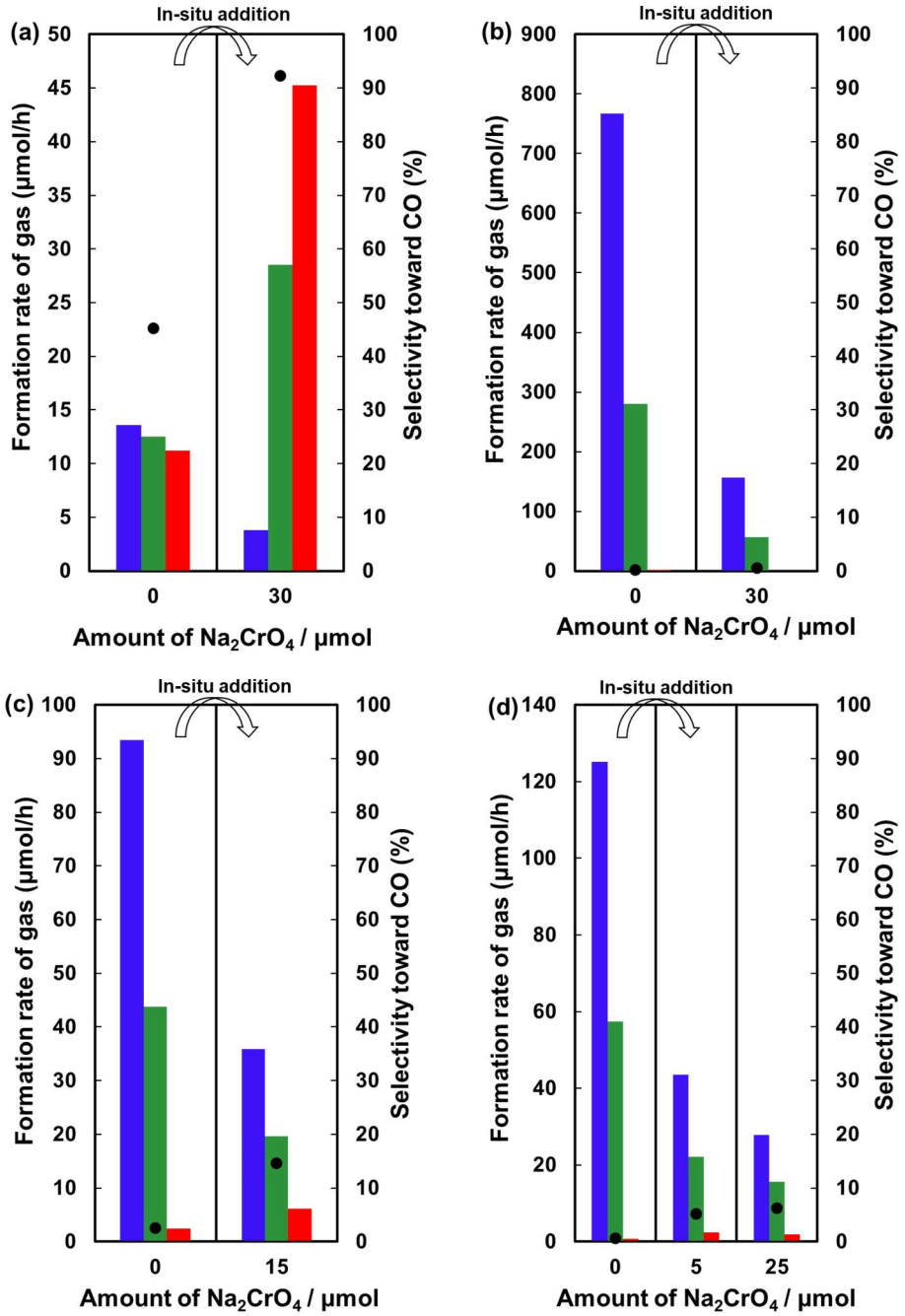

Figure 2. H_2 (blue), O_2 (green), and CO (red) formation rates and CO evolution selectivity (black dots) for the photocatalytic conversion of CO_2 in H_2O with and without Na_2CrO_4 in the reaction solution over (a) $ZnTa_2O_6$, (b) $SrTa_2O_6$, (c) $NaTaO_3$, and (d) commercial Ga_2O_3 catalysts. Photoirradiation time: 0.5 h per unit Na_2CrO_4; amount of main photocatalyst: 0.5 g; reaction solution: 1.0 L of 0.1 M aqueous $NaHCO_3$; CO_2 flow rate: 30 mL min^{-1}; light source: 400-W high-pressure Hg lamp. Na_2CrO_4 was added in situ

without treatment into the reaction solution containing the photocatalysts.

Figure 2 shows the rates of H_2, O_2, and CO formation and the CO evolution selectivity for the photocatalytic conversion of CO_2 in the presence of H_2O over the photocatalysts with and without Na_2CrO_4 in the reaction solution. The H_2 production activity of $ZnTa_2O_6$ was 13.6 μmol h^{-1}, whereas this was reduced to 3.8 μmol h^{-1} after the addition of 30 μmol Na_2CrO_4, as shown in Figure 2(a). Correspondingly, the selectivity for CO evolution increased from 45.2% to 92.3%. As shown in Figure 2(b), H_2 evolution was suppressed over $SrTa_2O_6$ (from 768 to 157 μmol h^{-1}) after the addition of Na_2CrO_4. However, the CO evolution selectivity did not increase significantly because the activity was too low. Similarly, the rate of H_2 formation visibly decreased owing to the presence of Na_2CrO_4 in the case of $NaTaO_3$ (93.4 to 35.8 μmol h^{-1}), as shown in Figure 2(c), and commercial Ga_2O_3 (125–27.8 μmol h^{-1}) in Figure 2(d). The suppression effect of the rate of H_2 formation could be observed every addition of chromate ion as shown in Figure 3, although the rate of H_2 formation was gradually increased.

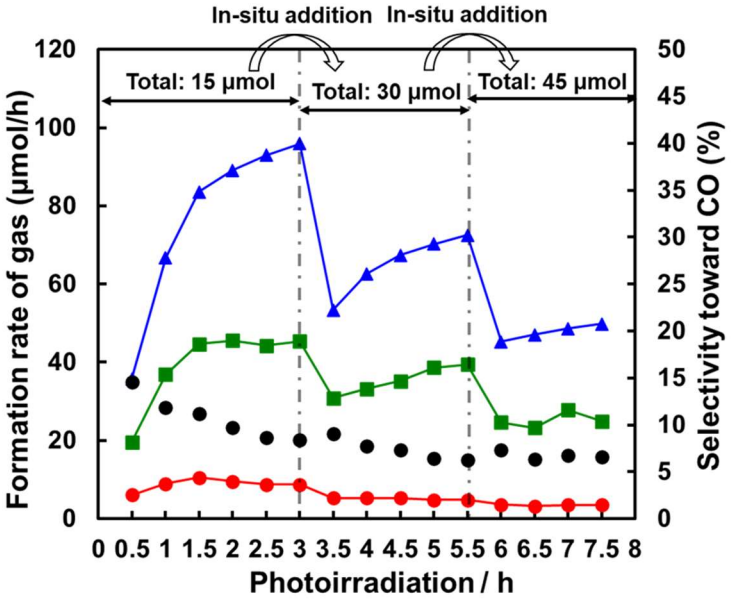

Figure 3. H_2 (blue), O_2 (green), and CO (red) formation rates and CO evolution selectivity (black dots) for the photocatalytic conversion of CO_2 in the presence of H_2O with 15 to 45 μmol Na_2CrO_4 in the reaction solution over bare $NaTaO_3$. Photocatalyst: 0.5 g; reaction

solution: 1.0 L of 0.1 M aqueous $NaHCO_3$; CO_2 flow rate: 30 mL min^{-1}; light source: 400-W high-pressure Hg lamp.

3.2. Photocatalyst fabrication

As described in Section 3.1, the addition of chromate ions to the reaction solution suppresses the evolution of H_2 over various photocatalysts. To clarify the critical factors affecting H_2 evolution, the author attempted to synthesize $ZnTa_2O_6$ and $SrTa_2O_6$ samples using an H_3BO_3 flux to change the surface properties of the photocatalysts. Figure 4 shows the XRD patterns of $ZnTa_2O_6$ and $SrTa_2O_6$ synthesized by the SSR and flux methods. $ZnTa_2O_6$ fabricated by the flux method did not contain $TaO_{2-\delta}$ impurities, unlike those synthesized by SSR. A pure $SrTa_2O_6$ phase was also obtained by the H_3BO_3 flux method, as shown in Figure 4(b). Thus, the author succeeded in fabricating pure phases of $ZnTa_2O_6$ and $SrTa_2O_6$ using the flux method.

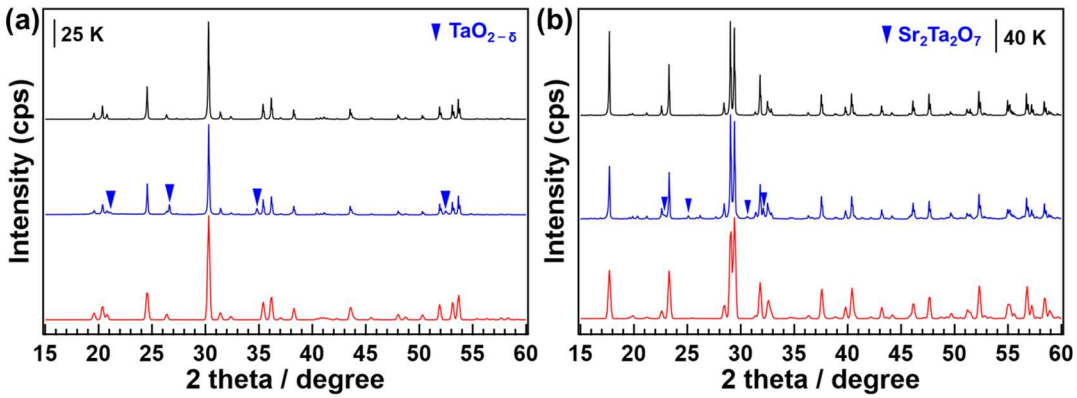

Figure 4. XRD patterns of (a) $ZnTa_2O_6$ and (b) $SrTa_2O_6$ synthesized by SSR (blue), the flux method (black), and the reference pattern from the ICSD database (red), respectively. The peaks corresponding to impurities are marked by arrows.

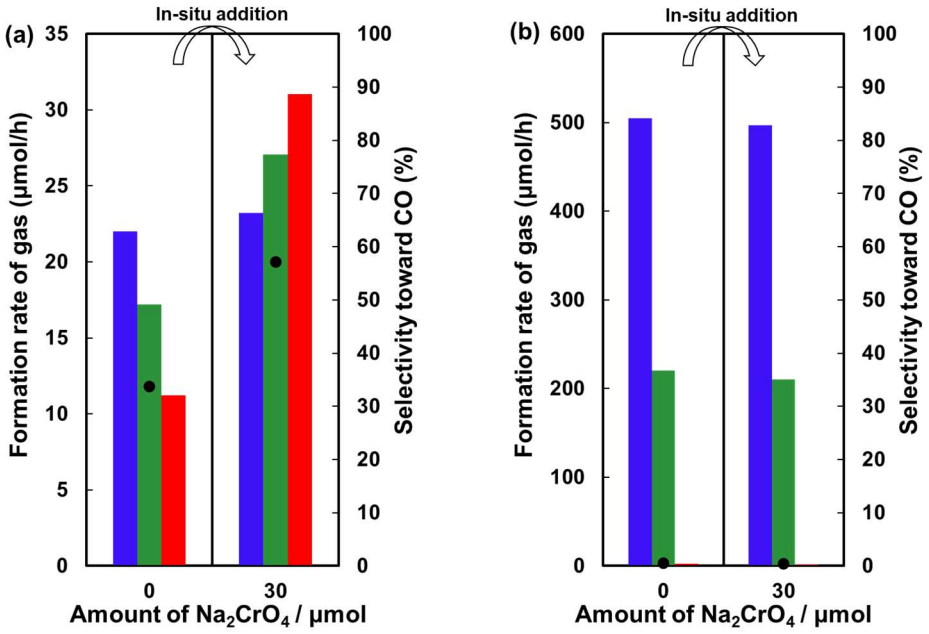

Figure 5. H_2 (blue), O_2 (green), and CO (red) formation rates and CO evolution selectivity (black dots) for the photocatalytic conversion of CO_2 by H_2O with and without Na_2CrO_4 in the reaction solution over (a) $ZnTa_2O_6$ and (b) $SrTa_2O_6$ synthesized via the H_3BO_3 flux method. Photoirradiation time: 0.5 h; main photocatalyst: 0.5 g; reaction solution: 1.0 L of 0.1 M aqueous $NaHCO_3$; CO_2 flow rate: 30 mL min^{-1}; light source: 400-W high-pressure Hg lamp. Na_2CrO_4 was added in situ without treatment into the reaction solution containing the photocatalysts.

Figure 5 shows the rates of H_2, O_2, and CO formation and CO evolution selectivity for the photocatalytic conversion of CO_2 in the presence of H_2O with and without Na_2CrO_4 in the reaction solution. The chromate ions added to the reaction solution promoted the evolution of CO from 11.2 to 31.0 μmol h^{-1} during the photocatalytic reaction, but the evolution of H_2 was not suppressed (22.0 vs. 23.2 μmol h^{-1}) over $ZnTa_2O_6$ from the flux method Figure 5(a). A similar phenomenon was observed for $SrTa_2O_6$ fabricated using the flux method, as shown in Figure 5(b): the H_2 formation rate was 505.1 μmol h^{-1} before the addition of chromate ions, and there was almost no change after the addition of 30 μmol of chromate ions (497 μmol h^{-1}). Compared to the samples

synthesized by SSR, there were no impurities (unconverted ZnO and SrO) that would have positive zeta potentials during the surface reactions of the $ZnTa_2O_6$ and $SrTa_2O_6$ samples fabricated by the flux method. This resulted in a low degree of protonation on the surface of the photocatalyst. Possibly, trace amounts of boron species from the H_3BO_3 flux reagent remain on the surfaces of the photocatalysts fabricated by the flux method, even though the samples were washed with hot water after calcination, and these species suppressed the protonation of the surfaces during reaction because of the strong bonds to surface OH^- groups.

3.3. Amount of photocatalyst

Based on the discussion in Section 3.2, the author speculates that the degree of surface protonation is key to suppressing the evolution of H_2, and this is likely dependent on the amount of photocatalyst. Further, the rate of H_2 formation is affected by the addition of chromate ions during the photocatalytic conversion of CO_2 in the presence of H_2O.

Indeed, as shown in Figure 6(a) for the commercial Ga_2O_3 catalyst, the rate of H_2 formation during the photocatalytic conversion of CO_2 in the presence of H_2O is dependent on the amount of photocatalyst. Specifically, 0.1 g of commercial Ga_2O_3 produced H_2 at a rate of 281.0 μmol h^{-1}, but, unexpectedly, the rate decreased when a larger amount of catalyst was used: 0.5 and 1.5 g of commercial Ga_2O_3 produced only H_2 at 125 and 96.7 μmol h^{-1}, respectively. This finding indicates that the backward reaction from H_2 and O_2 to H_2O is favored in the presence of a large amount of this catalyst. In particular, the oxidation of H_2 produces large numbers of protons on the surface; thus, the degree of protonation on the surface is expected to increase when a large amount of commercial Ga_2O_3 is used. Surprisingly, the rate of H_2 formation was improved from 281 to 552 μmol h^{-1} on adding chromate ions when relatively low amounts of photocatalyst (0.1 g) were used, as shown in Figure 6(b) Compared to the data in Figures 2(d), those in Figure 6(b) show that the addition of chromate ions had the reverse effect when a large amount of photocatalyst was used (0.5 g in Figure 2(d)).

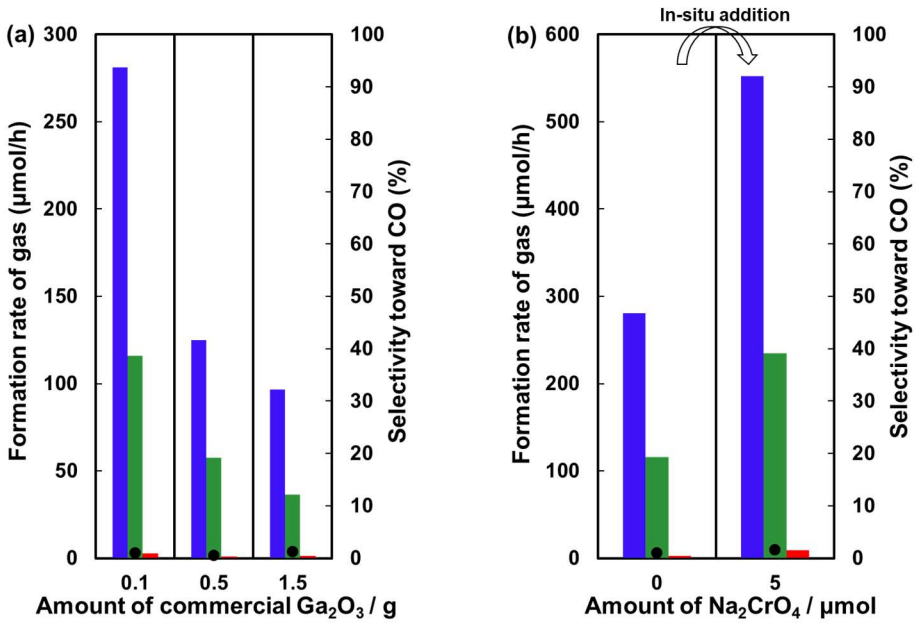

Figure 6. H_2 (blue), O_2 (green), and CO (red) formation rates and CO evolution selectivity (black dots) for the photocatalytic conversion of CO_2 in the presence of H_2O in the reaction solution over (a) commercial Ga_2O_3 without Na_2CrO_4 and (b) 0.1 g commercial Ga_2O_3 with and without Na_2CrO_4. Photoirradiation time: 0.5 h per unit Ga_2O_3 and Na_2CrO_4; reaction solution: 1.0 L of 0.1 M aqueous $NaHCO_3$; CO_2 flow rate: 30 mL min^{-1}; light source: 400-W high-pressure Hg lamp. Na_2CrO_4 was added in situ without treatment into the reaction solution containing the photocatalysts.

3.4. Type of photocatalyst

The discussion in Sections 3.1 to 3.3 suggest that the in situ addition of chromate ions to the reaction solution suppresses the evolution of H_2 during the photocatalytic conversion of CO_2 in the presence of H_2O when the surfaces of the photocatalysts are highly protonated. To confirm this conclusion, the author synthesized α-and β-Ga_2O_3 via SSR because Ga_2O_3 has highly positive [22] (α-phase, H^+ adsorbed) and negative [23] (β-phase, OH^- adsorbed) zeta potentials at neutral pH. Figure 7 shows the XRD patterns of the α- and β-Ga_2O_3 catalysts fabricated in this study. After synthesizing pure α- and β-Ga_2O_3, the photocatalytic conversion of CO_2 in the presence of H_2O was performed, as shown in

Figure 8. Clearly, the addition of chromate ions to the reaction solution suppressed H_2 evolution over α-Ga_2O_3: H_2 formation decreased from 320 to 178 μmol h^{-1}. Interestingly, in the case of β-Ga_2O_3, the author observed the opposite trend. and the H_2 formation rate visibly increased from 263 to 671 μmol h^{-1} after the addition of chromate ions to the reaction solution. The comparable results over α-and β-Ga_2O_3 which have relatively high and low degrees of protonation, respectively, are consistent with the results presented in Sections 3.1 to 3.3.

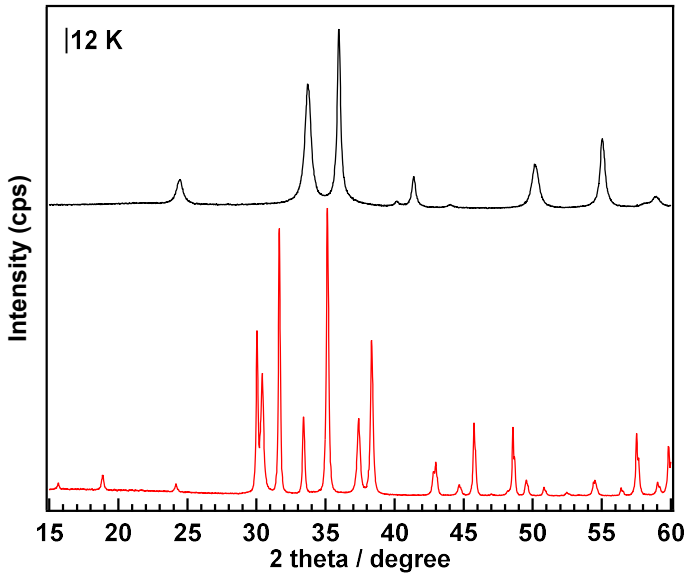

Figure 7. XRD patterns of (a) α- (black) and (b) β-Ga_2O_3 (red) fabricated by SSR.

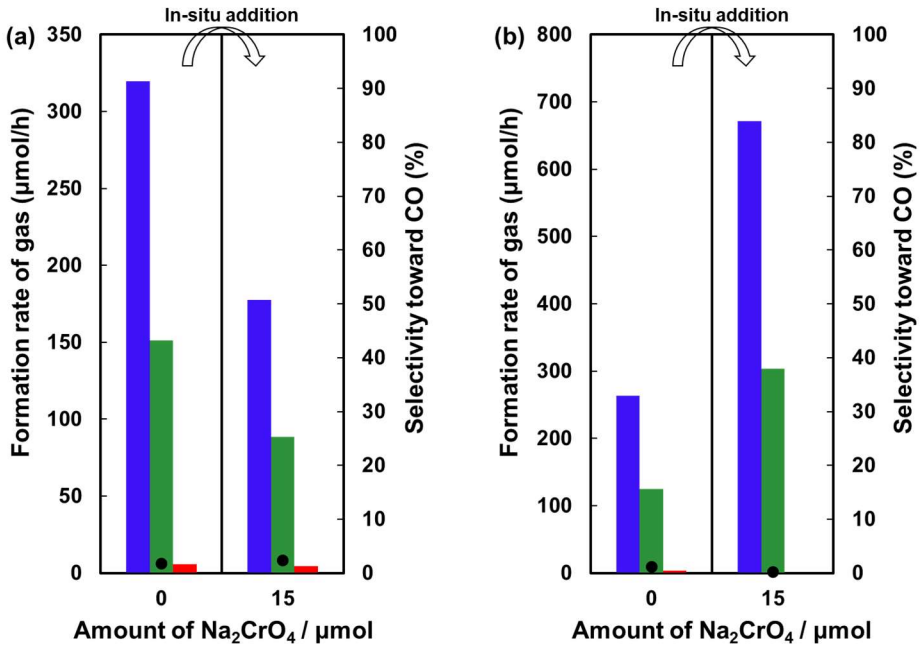

Figure 8. H_2 (blue), O_2 (green), and CO (red) formation rates and CO evolution selectivity (black dots) for the photocatalytic conversion of CO_2 in the presence of H_2O with and without Na_2CrO_4 in the reaction solution over (a) α- and (b) β-Ga_2O_3. Photoirradiation time: 0.5 h; amount of photocatalyst: 0.5 g; reaction solution: 1.0 L of aqueous 0.1 M $NaHCO_3$; CO_2 flow rate: 30 mL min^{-1}; light source: 400-W high-pressure Hg lamp. Na_2CrO_4 was added in situ without treatment into the reaction solution containing the photocatalysts.

3.5. Photocatalyst surface modification

To reduce the degree of protonation on the photocatalyst surface, the author modified the photocatalysts with $Al(OH)_3$ and $Ga(OH)_3$ to scavenge adsorbed protons. The author attempted to modify $SrTa_2O_6$, $NaTaO_3$, and $ZnTa_2O_6$ synthesized via SSR using 10 mol% $Al(OH)_3$ and 10 mol% $Ga(OH)_3$. Figure 9 shows the rates of H_2, O_2, and CO formation and the CO evolution selectivity during the photocatalytic conversion of CO_2 in the presence of H_2O with and without Na_2CrO_4 in the reaction solution over $Al(OH)_3/SrTa_2O_6$, $Ga(OH)_3/ZnTa_2O_6$, and $Ga(OH)_3/NaTaO_3$. As shown in Figures 2(b) and 9(a), the H_2 formation rate over $SrTa_2O_6$ prepared by SSR increased significantly from 768 to

1680 μmol h^{-1} after modification with $Al(OH)_3$ and from 1680 to 2670 μmol h^{-1} after the in situ addition of Na_2CrO_4. The $Ga(OH)_3$-modified $ZnTa_2O_6$ fabricated by the SSR method resulted in a high rate of H_2 formation (195 μmol h^{-1}) after the in situ addition of chromate ions into the reaction solution, as shown in Figure 9(b). Similarly, the H_2 formation rate over $Ga(OH)_3$-modified $NaTaO_3$ fabricated by SSR was promoted from 12.0 to 71.3 μmol h^{-1} after the in situ addition of chromate ions into the reaction solution in Figure 9(c). The rate of H_2 formation was increased to approximately 900 μmol h^{-1} and then became stable (Figure 10).

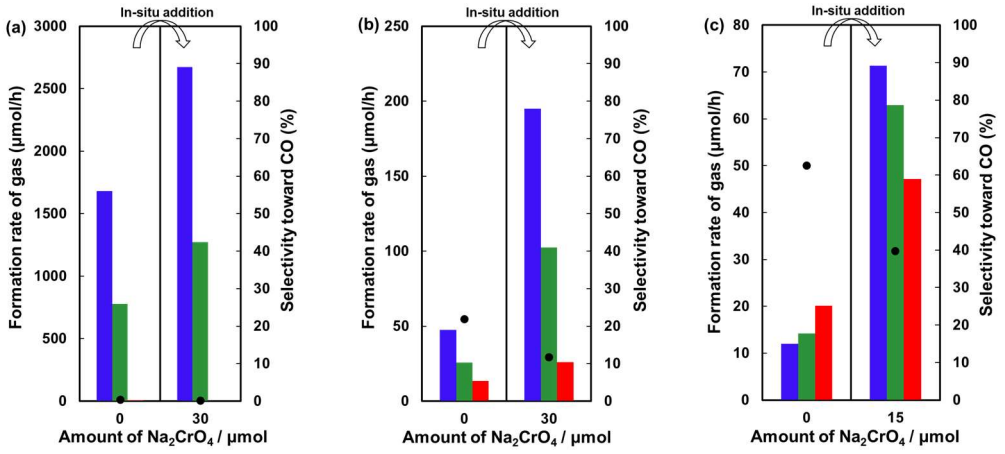

Figure 9. H_2 (blue), O_2 (green), and CO (red) formation rates and CO evolution selectivity (black dots) for the photocatalytic conversion of CO_2 in the presence of H_2O with and without Na_2CrO_4 in the reaction solution over (a) 10 mol% $Al(OH)_3$- modified $SrTa_2O_6$, (b) 10 mol% $Ga(OH)_3$- modified $ZnTa_2O_6$, and (c) 10 mol% $Ga(OH)_3$- modified $NaTaO_3$ (all prepared by SSR). Photoirradiation time: 0.5 h per unit Na_2CrO_4; main photocatalyst: 0.5 g; reaction solution: 1.0 L of 0.1 M aqueous $NaHCO_3$; CO_2 flow rate: 30 mL min^{-1}; light source: 400-W high-pressure Hg lamp. Na_2CrO_4 was added in situ without treatment into the reaction solution containing the photocatalysts.

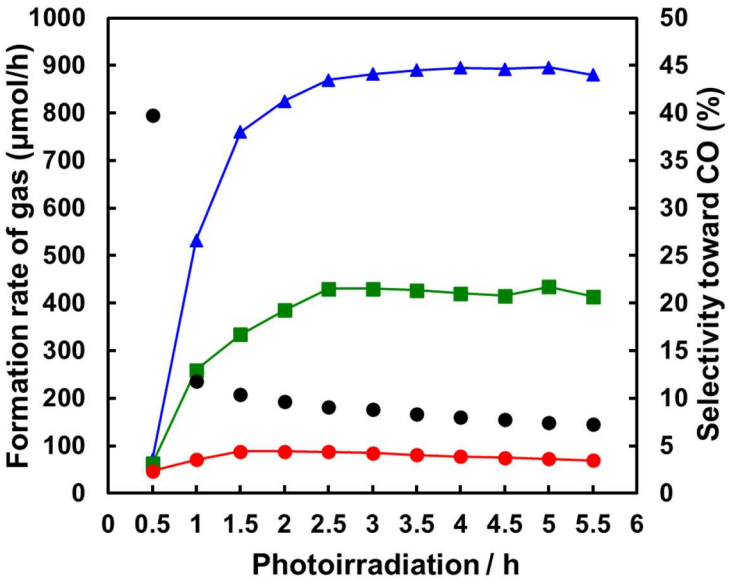

Figure 10. H_2 (blue), O_2 (green), and CO (red) formation rates and CO evolution selectivity (black dots) for the photocatalytic conversion of CO_2 in the presence of H_2O with 15 μmol Na_2CrO_4 in the reaction solution over 10 mol% $Ga(OH)_3$-decorated $NaTaO_3$. Photocatalyst: 0.5 g; reaction solution: 1.0 L of 0.1 M aqueous $NaHCO_3$; CO_2 flow rate: 30 mL min^{-1}; light source: 400-W high-pressure Hg lamp.

3.6. Proposed mechanism

Based on a comparison of the results obtained with $NaTaO_3$ and $Ga(OH)_3$-modified $NaTaO_3$, the author investigated the mechanisms by which the addition of chromate ions to the reaction solution has positive and negative influences on H_2 evolution during the photocatalytic conversion of CO_2 in the presence of H_2O. First, the author obtained Cr 2p X-ray photoelectron spectra of $NaTaO_3$ and $Ga(OH)_3$-modified $NaTaO_3$ after the addition of chromate ions (Figure 11). Peaks assigned to Cr $2p_{3/2}$ and Cr $2p_{1/2}$ (calibrated to the C 1s at 284.6 eV) were observed at 576.5 and 586.5 eV, indicating that Cr^{3+} species were mainly formed on the surfaces of both $NaTaO_3$ and $Ga(OH)_3$-modified $NaTaO_3$ after the reaction with added chromate ions.

Figure 12 shows the UV-vis diffuse reflectance (DR) spectra of $NaTaO_3$ and $Ga(OH)_3$-modified $NaTaO_3$ after the photocatalytic conversion of CO_2 in the presence of

H_2O and chromate ions. The peaks attributed to $Cr(OH)_3$ were observed at 415 and 595 nm for the $Ga(OH)_3$-modified $NaTaO_3$ after the reaction in the presence of chromate, indicating that $Cr(OH)_3$ had been deposited on the surface. In addition, peaks at 375 nm were observed in the spectra of both samples after the reactions with added chromate ions. By comparison with UV-vis DR spectrum of $NaTaO_3$ impregnated with Na_2CrO_4, the peaks were assigned to chromate ions adsorbed on the surface of the samples during reaction.

To confirm the importance of the chromate ions adsorbed on the surfaces and dissolved in the reaction solution, the author carried out recycling tests over the $NaTaO_3$ and $Ga(OH)_3$-modified $NaTaO_3$. Figure 13 shows the rates of formation of H_2, O_2, and CO, as well as the CO evolution selectivity, for the photocatalytic conversion of CO_2 in the presence of H_2O with and without Na_2CrO_4 in the reaction solution. The rate of H_2 formation over $NaTaO_3$ was significantly suppressed by the in situ addition of 15 μmol Na_2CrO_4 (from cycles 1 to 2, 96.1, to 27.6 μmol h^{-1}, respectively). Between cycles, the chromate dissolved in the solution, which was not reduced to Cr^{3+}, was removed from the reaction solution by filtration. Interestingly, the H_2 formation rate improved markedly (from cycles 2 to 3, 27.6 to 58.4 μmol h^{-1}, respectively) after filtration. Compared to cycle 1, the H_2 formation rate in cycle 3 was still suppressed. This was probably caused by the residual trace amount of chromate ions adsorbed on the surface of $NaTaO_3$. Undoubtedly, the chromate ions dissolved in the solution and adsorbed on the surfaces are in adsorption equilibrium. However, between cycles, the chromate ions dissolved in the solution were removed by filtration, whereas the chromate ions adsorbed on the surfaces remained and, thus, contributed to the reaction in cycle 3. Then, some of the adsorbed chromate ions became dissolved in the solution during cycle 3 as adsorption equilibrium was maintained, resulting in only trace amounts of chromate being adsorbed on the surface of $NaTaO_3$. Interestingly, the author found that the H_2 formation rate decreased on the addition of a small amount of chromate, as shown in Figure 13(b). The chromate ions dissolved in solution also had the same influence on $Ga(OH)_3$-modified $NaTaO_3$ as on bare $NaTaO_3$.

As shown in Figure 13(c), the H_2 and CO formation rates decreased to 49.5 and 17.1 μmol h^{-1}, respectively, after the removal of chromate ions by filtration.

Based on the above discussion, the author proposes the following mechanism by which the in situ addition of chromate ions to the reaction solution influences the evolution of H_2 during the photocatalytic conversion of CO_2 in the presence of H_2O (see Scheme 1). In this mechanism, three reactions including (1) the oxidation of H_2O to O_2, (2) the backward reduction of the produced O_2 into H_2O, and (3) the reduction of H^+ to H_2 proceed simultaneously, whereas the photocatalytic reduction of CO_2 by H_2O proceeds separately. After the in situ addition of chromate ions to the reaction solution, it was expected that the chromate ions which were adsorbed on the surface of bare $NaTaO_3$ acted as recombination centers for the photogenerated electrons and holes (Scheme 1(a)), resulting in the suppression of overall photocatalytic activity. Subsequently, the amount of chromate adsorbed on the surface is decreased by filtration, and the H_2 formation rate recovers. In the case of $Ga(OH)_3$-modified $NaTaO_3$, the chromate ions adsorbed on the surface were reserved as shells of $Cr(OH)_3$ (Scheme 1(b)), which is a well-known chromate conversion coating (CCC) [24–26] used as a corrosion inhibitor for various metals. This corrosion inhibitor suppresses the backward reduction of the produced O_2 to H_2O; therefore, a greater number of electrons generated by charge transfer can move to the surface for the reduction of H^+ and CO_2. However, filtration to remove the chromate ions from the solution damages the corrosion inhibiting film, and the rates of formation of H_2 and CO decrease again.

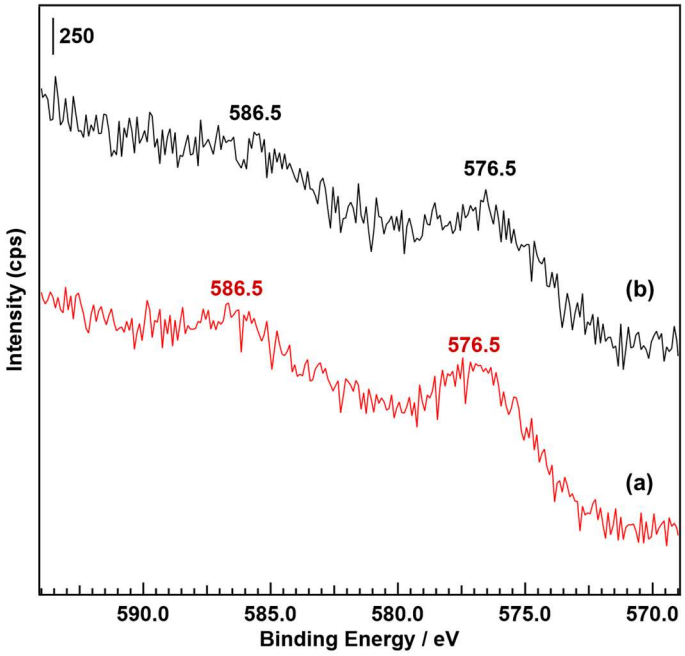

Figure 11. X-ray photoelectron Cr 2p spectra of (a) $NaTaO_3$ (red) and (b) $Ga(OH)_3$-modified $NaTaO_3$ (black) after the photocatalytic conversion of CO_2 in the presence of H_2O with the in situ addition of chromate ions.

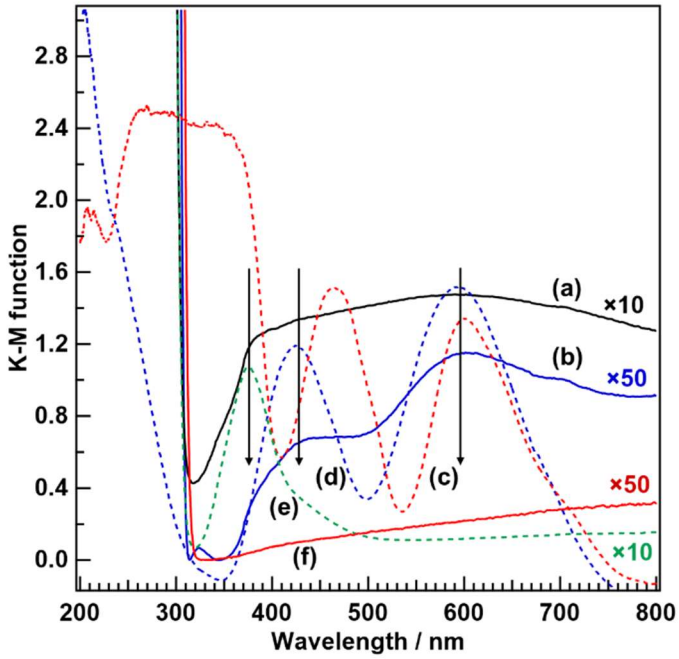

Figure 12. UV-vis diffuse reflectance spectra of (a) $NaTaO_3$ (black solid) and (b)

$Ga(OH)_3$-modified $NaTaO_3$ (blue solid) after the photocatalytic conversion of CO_2 in the presence of H_2O with the in situ addition of chromate ions and (c) commercial Cr_2O_3 (red dashed line), (d) synthesized $Cr(OH)_3$ (blue dashed line), (e) $NaTaO_3$ (green dashed line) impregnated with Na_2CrO_4, and (f) bare $NaTaO_3$ (red solid line).

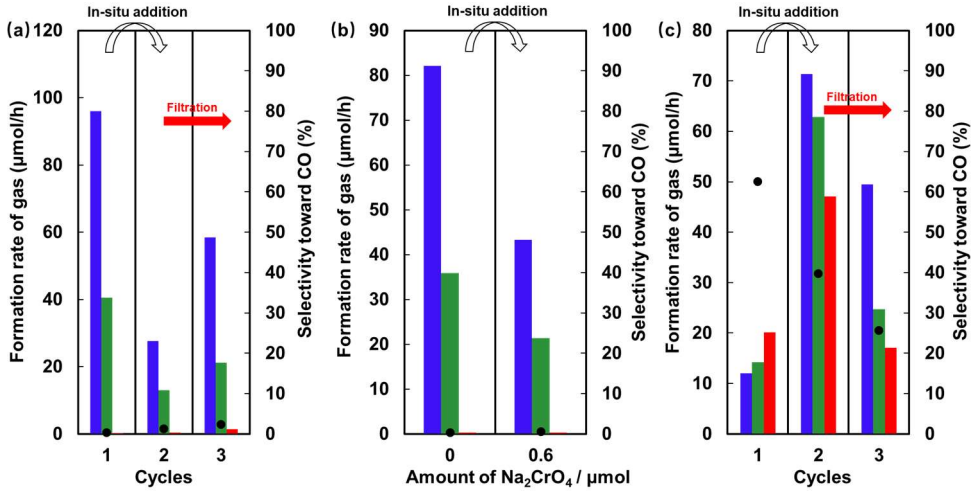

Figure 13. H_2 (blue), O_2 (green), and CO (red) formation rates and CO evolution selectivity (black dots) for the photocatalytic conversion of CO_2 in the presence of H_2O with and without Na_2CrO_4 in the reaction solution. (a) Recycling tests over $NaTaO_3$ and (b) $NaTaO_3$ with the in situ addition of trace amounts of chromate. (c) Recycling tests over 10 mol% $Ga(OH)_3$-decorated $NaTaO_3$ fabricated by SSR. Photoirradiation time: 0.5 h; main photocatalyst: 0.5 g; reaction solution: 1.0 L of 0.1 M aqueous $NaHCO_3$; CO_2 flow rate: 30 mL min^{-1}; light source: 400-W high-pressure Hg lamp. Na_2CrO_4 was added in situ without treatment to the reaction solution containing the photocatalysts. Cycle 1: the photocatalysts were used for the photocatalytic conversion of CO_2 in the presence of H_2O without the addition of chromate. Cycle 2: in situ addition of 15 μmol. Cycle 3: reactions after the removal of dissolved chromate by filtration.

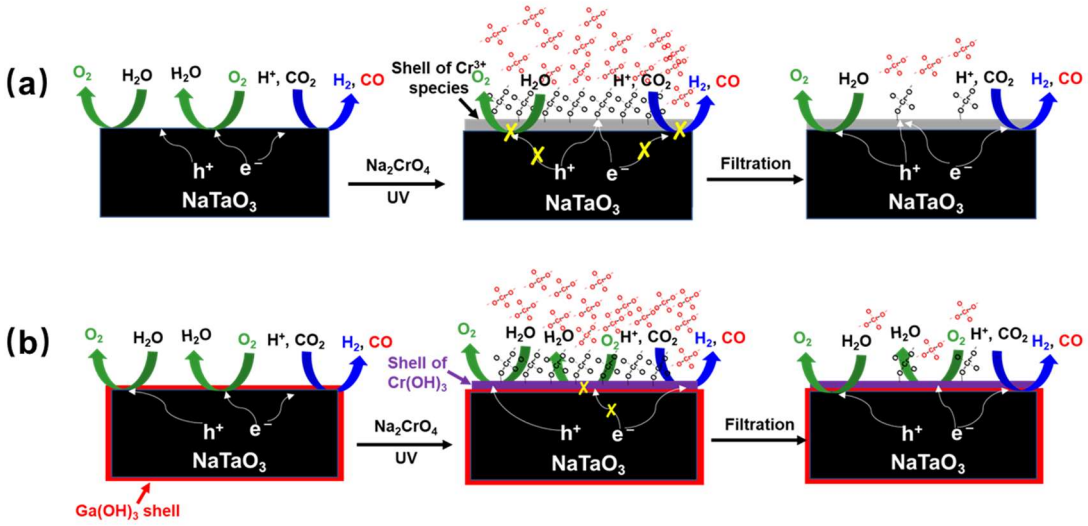

Scheme 1. Proposed reaction mechanism showing the influence of in situ added chromate on (a) $NaTaO_3$ and (b) $Ga(OH)_3$-modified $NaTaO_3$ during the photocatalytic conversion of CO_2 in the presence of H_2O.

4. Conclusion

The author investigated the effect of the in situ addition of chromate ions on the evolution of H_2 during the photocatalytic conversion of CO_2 in the presence of H_2O over $NaTaO_3$, Ga_2O_3, $ZnTa_2O_6$, and $SrTa_2O_6$ photocatalysts synthesized by different fabrication and modification methods. The results showed that the in situ addition of chromate ions suppressed the evolution of H_2 when the photocatalyst surfaces were highly protonated. In particular, the highly protonated surfaces failed to form $Cr(OH)_3$ when chromate ions were added during the photocatalytic reaction, and the chromate ions adsorbed on the surface of the photocatalysts acted as recombination centers for photogenerated electrons and holes. In contrast, the in situ addition of chromate ions was found to enhance the evolution of H_2 during reactions when the concentration of H^+ was low near the photocatalyst surface, and, under these conditions, hydroxides were generated on the surface. Subsequently, $Cr(OH)_3$ was formed, and the chromate-adsorbed $Cr(OH)_3$ shell on the surface acted as a corrosion inhibitor, suppressing the backward

reduction of the produced O_2 into H_2O.

References

1. D. M. Gates, Science 1966, 151, 523-529.
2. A. Raval and V. Ramanathan, Nature 1989, 342, 758-761.
3. B. A. Thayer, Security Studies 2008, 3, 428-493.
4. S. A. Calero, Journal of Political Ecology 2017, 992-1012.
5. A. K. Jena, A. Kulkarni, T. Miyasaka, Chemical Reviews 2019, 119, 3036-3103.
6. Q. Wang, K. Domen , Chemical Reviews 2020, 120, 919-985.
7. L. I. Granone, F. Sieland, N. Zheng, R. Dillert, D. W. Bahnemann, Green Chemistry 2018, 20, 1169-1192.
8. Y. Chai, Y. Chen, J. Shen, M. Ni, B. Wang, D. Li, Z. Zhang and X. Wang. ACS Catal. 2021, 11, 11029–11039.
9. Y. Wang, Z. Zhang, L. Zhang, Z. Luo, J. Shen, H. Lin, J. Long, J. C. S. Wu, X. Fu, X. Wang and C. Li. J. Am. Chem. Soc. 2018, 140, 14595–14598.
10. Y. Wang, X. Shang, J. Shen, Z. Zhang, D. Wang, J. Lin, J. C. S. Wu, X. Fu, X. Wang and C. Li. Nat. Commun. 2020, 11, 1–11.
11. H. Nakanishi, K. Iizuka, T. Takayama, A. Iwase, A. Kudo, ChemSusChem. 2017, 10, 112-118.
12. A. Anzai, N. Fukuo, A. Yamamoto, H. Yoshida, Catalysis Communications 2017, 100, 134-138.
13. S. Y. Wang, K. Teramura, T. Hisatomi, K. Domen, H. Asakura, S. Hosokawa and T. Tanaka, ACS Appl. Energy Mater. 2020, 3, 1468–1475.
14. M. Yamamoto, T. Yoshida, N. Yamamoto, H. Yoshida, S. Yagi. e-Journal of Surface Science and Nanotechnology 2014, 12, 299-303.
15. Z. Wang, K. Teramura, S. Hosokawa, T. Tanaka. Journal of Materials Chemistry A 2015, 3, 11313-11319.
16. Pang, R., Teramura, K., Asakura, H., Hosokawa, S. & Tanaka, T. Appl. Catal. B Environ. **218**, 770–778 (2017).
17. R. Pang, K. Teramura, H. Asakura, S. Hosokawa, T. Tanaka, Applied Catalysis B:

Environmental 2017, 218, 770-778.

18. X. X. Xu, K. Teramura, H. Asakura, S. Hosokawa, T. Tanaka, Applied Catalysis B: Environmental. 2021, 298, 120508.
19. J. Zhai, X. Tao, Y. Pu, X. F. Zeng, J. F. Chen, Applied Surface Science. 2010, 257, 393-397.
20. D. Boyd, M. R. Towler, S. Watts, R. G. Hill, A. W. Wren, O. M. Clarkin, Journal of Materials Science: Materials in Medicine 2007, 19, 953-957.
21. X. Wang, Q. Xu, M. Li, Angewandte Chemie. 2012, 124, 13266-13269.
22. J. N. Díaz de León, Appl. Catal. B Environ. 2016, 181, 524–533.
23. S. Mandal, K. Arts, H. C. M. Knoops, J. A. Cuenca, G. M. Klemencic and O. A. Williams, Carbon 2021,. 181, 79–86.
24. A. I. Onuchukwu and J. A. Lori, Corrosion Science 1984, 24, 833-841.
25. L. Xia and R. McCreery, J. Electrochem. Soc.1998, 145, 3083.
26. L. Xia, G. Frankel and R. McCreery et al., J. Electrochem. Soc.2000, 147, 2556.

Part II

Developments of non-metal cocatalysts for the photocatalytic conversion of CO_2 using H_2O as an electron donor

Chapter 3

Development of zinc hydroxide as an abundant and universal cocatalyst for the selective photocatalytic conversion of CO_2 by H_2O

Abstract

New energy and material sources that replace fossil fuels are important to address growing energy and environmental concerns. In this regard, the catalytic conversion of CO_2 using solar energy is especial advantageous from sustainability, safety, and environmental perspectives. To that end, the author shows that $Zn(OH)_2$ functions as a good cocatalyst for the photocatalytic conversion of CO_2 using H_2O as the electron donor, despite only metal nanoparticles, such as sliver, previously shown to enhance activity. Carbon monoxide (CO) was selectively generated over a $ZnTa_2O_6$ photocatalyst prepared by the solid-state reaction method (i.e., $ZnTa_2O_6$(S)) modified with $Zn(OH)_2$ as a cocatalyst. The rate of formation of H_2, which is secondarily generated from H_2O, was suppressed (from 32.8 to 5.8 μmol h^{-1}), while the formation of CO was dramatically promoted (from 18.4 to 81.4 μmol h^{-1}) by the incorporation of the cocatalyst. Zn ions dissolved in solution and an alkaline electrical double layer are believed to be important for the formation of $Zn(OH)_2$ on the surface of $ZnTa_2O_6$(S). $Zn(OH)_2$ showed good cocatalyst universality, with CO selectively generated on various typical photocatalysts, including $NaTaO_3$, Ta_2O_5, and Ga_2O_3.

1. Introduction

For many years much research effort has been directed toward finding new energy sources to replace fossil fuels that have dominated human life, including solar[1], nuclear[2], wind,[3] and hydro[4] energy, among others, a result of growing energy[5] and environmental concerns[6,7]. Among these strategies, the conversion of solar energy is especial advantageous because it integrates sustainability and safety while not harming ecology. Silicon is now the most widely used material for the industrialization of solar-driven electricity[8], despite its manufacture by the Siemens process[9] being very expensive. In recent years, chemists have been interested in developing new pathways for the conversion of solar energy, including the production of hydrogen from water (H_2O)[10], the conversion of biomass[11], carbon fuels from carbon dioxide (CO_2),[12] and perovskite photovoltaic cells[13], among others. The photocatalytic conversion of CO_2 into useful chemicals, including carbon monoxide (CO), formic acid (HCOOH), methanol (CH_3OH), and methane (CH_4) over a semiconductor photocatalyst with H_2O as the electron donor is attractive because the products formed are useful in many fields, including organic synthesis and energy supply. On the other hand, the selective evolution of certain products, especially CO, which is a critical intermediate reagent, is quite important during the photocatalytic conversion of CO_2 using H_2O as the electron donor, as subsequent separation processes for the various evolved chemicals need to be avoided as far as possible from an economic perspective. Despite many kinds of material, including metal–organic frameworks (MOFs)[14], covalent organic frameworks (COFs)[15], metal carbides,[16] and metal complexes[17] reported to selectively evolve CO during CO_2 photoreduction, these materials have very complicated structures and are difficult to synthesize, and few of them are able to function with H_2O as the electron donor.

Water splitting to evolve H_2 always strongly competes with the reduction of CO_2 to CO during the photocatalytic conversion of CO_2 by H_2O because the redox potential of the former (−0.41 V vs. SHE) is more positive than that of the latter (−0.52 V vs. SHE);

hence, only limited types of photocatalyst show high selectivity, as calculated by **equation (1)** for this reaction. In addition, the balance between the photogenerated electrons consumed by protons and CO_2, and the holes extracted from H_2O (e^-/h^+), as given by **equation (2)**, is also a critical indicator of success for the photoreduction of CO_2 by H_2O.

$$\text{Selectivity} = (2R_{HCOOH} + 2R_{CO} + 4R_{HCHO} + 6R_{CH_3OH} + 8R_{CH_4})/(2R_{HCOOH} + 2R_{CO} + 4R_{HCHO} + 6R_{CH_3OH} + 8R_{CH_4} + 2R_{H_2}) \times 100\% \quad (1)$$

$$e^-/h^+ = (2R_{HCOOH} + 2R_{CO} + 4R_{HCHO} + 6R_{CH_3OH} + 8R_{CH_4} + 2R_{H_2})/4R_{O_2} \quad (2)$$

In equations 1 and 2, R represents the formation rate of each product formed by the photocatalytic conversion of CO_2 by H_2O. Unfortunately, researchers have achieved very little progress in this field if the works are confined to above mentioned two factors.

To the best knowledges of the author, silver-cocatalyst-modified $BaLa_4Ti_4O_{15}$, which was reported by Kudo et al.[18], was the first photocatalyst to show high selectivity for the evolution of CO and HCOOH during the photoreduction of CO_2 by H_2O, with an e^-/h^+ balance close to one observed. Deeper investigations led to a variety of materials, including tantalum-based $NaTaO_3$[19], Ta_2O,[20] and $Sr_2KTa_5O_{15}$[21], titanium-based $CaTiO_3$[22], $La_2Ti_2O_7$,[23] and $SrTiO_3$[24], gallium-based Ga_2O_3[25,26], and $ZnGa_2O_4$[27] and $SrNb_2O_6$[28] found to effectively extract electrons from H_2O for the photocatalytic conversion of CO_2 into CO. However, these photocatalyst materials showed excellent CO-evolution activities only when used together with Ag as the cocatalyst. The specificness of Ag as the cocatalyst for the selective photocatalytic conversion of CO_2 by H_2O was further demonstrated in previous work, in which various cocatalysts, including Au, Cu, Pd, Pt, Ni, and Ag, were compared over $ZnTa_2O_6$[29], with only Ag shown to improve CO evolution.

It would seem that no cocatalyst capable of outperforming Ag for the selective photocatalytic conversion of CO_2 by H_2O, from the perspectives of simplicity, economy, and universality, has been discovered to date. Single cocatalyst examples appear not to

provide sufficient fundamental clues for researchers to enable clear insight into the necessary conditions under which CO_2 is effectively photocatalytically converted by H_2O to be gained. Although Ag has been demonstrated to be an excellent material for both the photocatalytic and electrocatalytic[30–32] conversion of CO_2, the critical factors responsible for the reduction of CO_2 remain largely unknown. Therefore, investigations leading to the development of excellent cocatalysts for the selective photoreduction of CO_2 by H_2O are somewhat overdue.

Zn-based cocatalysts and electrodes are significantly superior to Ag from an economical perspective. Although Zn oxide and Zn electrodes with specific morphologies have already been demonstrated to effectively hydrogenate[33,34] and electrocatalytic convert[35–37] CO_2 into CH_3OH and CO respectively, Zn-based cocatalysts have not been shown to selectively photocatalytically convert CO_2 by H_2O. On the other hand, based to previous investigations, Zn species are known to have a certain attractive but unclear influence on CO-evolution activity during the photocatalytic conversion of CO_2 by H_2O. Bare Ga_2O_3 produced CO a rate of just 5.4 μmol h^{-1} (0.5 g)[38], while Zn-modified Ga_2O_3 promoted CO formation by a factor of almost three (20 μmol h^{-1}, 0.5 g)[39]. Moreover, doping $ZnTa_2O_6$ with Zn species was also observed to enhance activity (9 vs. 19 μmol h^{-1})[40], and nearly 80 μmol h^{-1} of CO was formed over $ZnGa_2O_4$[27] without any cocatalyst during the photocatalytic conversion of CO_2 by H_2O. These results reveal that Zn species are potentially promising cocatalysts for CO evolution during the photocatalytic conversion of CO_2 by H_2O.

Herein, the author shows that $Zn(OH)_2$ exhibits a significant ability to photocatalytically convert CO_2 into CO by H_2O on various photocatalysts, including $ZnTa_2O_6$, $NaTaO_3$, and Ga_2O_3, among others. Compared to the Ag cocatalyst, high CO-formation rates were obtained over the $Zn(OH)_2$ cocatalyst; in particular, selectivity toward CO evolution over $Zn(OH)_2$-decorated $ZnTa_2O_6$ fabricated by solid-state reaction exceeded 90%. To the best knowledges, the author reports for the first time that $Zn(OH)_2$ functions as an effective and universal cocatalyst for the photocatalytic conversion of CO_2

by H_2O.

2. Experimental section

2.1. Preparing $ZnTa_2O_6$

A typical solid state reaction (SSR) with stoichiometric amounts of commercial Ta_2O_5 (99.9%, High Purity Chemicals, Japan) and ZnO (99.0%, Wako, Japan), as precursors, was used to synthesize $ZnTa_2O_6$. In detail, the two reagents were ground together in an aluminum mortar for 30 min, transferred to 200 mL of pure water, and sonicated for 50 min. The suspension was further mixed by stirring at room temperature for 50 min, after which the solid was collected by vacuum filtration. The wet powder was dried at 383 K for 1 h and then reground in 5 mL of pure water for 30 min. The wet mixture was collected and dried at 383 K, followed by calcination at 1273 K for 12 h. This sample is referred to as "$ZnTa_2O_6$(S)".

For comparison, $ZnTa_2O_6$ was also prepared using the ZnB_2O_4 flux method (referred to as "$ZnTa_2O_6$(F)"). In detail, ZnO, H_3BO_3 (99.5%, Wako, Japan), and Ta_2O_5 in a 1.005:0.01:1 molar ratio was mixed and ground well in an aluminum mortar; the transformation is represented by **equation (3)**. The mixture was calcined at 1273 K for 1 h, and then at 1373 K for 2 h. The powder had condensed into a hard bulk solid during calcination. The solid was smashed into small particles by grinding in the mortar, and then washed with water at 358 K for 2 h to remove the ZnB_2O_4 flux species.

$1.005\ ZnO + Ta_2O_5 + 0.01\ H_3BO_3 \rightarrow ZnTa_2O_6 + 0.005\ ZnB_2O_4$ (flux) $+ 0.015\ H_2O$ (3)

2.2. Preparing $Zn(OH)_2$-modified $ZnTa_2O_6$(S)

The fabricated $ZnTa_2O_6$(S) sample was used directly without any pre-treatment. $ZnTa_2O_6$(S) (0.5 g) was suspended, with stirring, in 200 mL of pure water containing a specific amount of $Zn(NO_3)_2$•$6H_2O$ (99.9%, Wako, Japan). A stoichiometric amount of NaOH (97.0%, Wako, Japan) relative to $Zn(NO_3)_2$•$6H_2O$) was gradually dropped (by pump) as an aqueous solution (200 mL) to the suspension to precipitate $Zn(OH)_2$. A series

of $Zn(OH)_2$ modified $ZnTa_2O_6$(S) samples was fabricated by tuning the amount of $Zn(NO_3)_2$•$9H_2O$ (0–20 mol%) added to the $ZnTa_2O_6$(S) suspension.

2.3. Photocatalytic conversion of CO_2 by H_2O

The suspension containing the $Zn(OH)_2$-modified $ZnTa_2O_6$(S) was collected by vacuum filtration and then used to directly photocatalytically convert CO_2 by H_2O. Note that exposure of the photocatalyst to air for prolonged times should be avoided because $Zn(OH)_2$ can decompose by dehydration. CO_2 was photocatalytically converted by H_2O in an inner irradiation reactor with a quartz jacket as the lamp holder. The jacket was connected to cooling water to ensure a room-temperature reaction. A 400-W high-pressure mercury lamp was used to supply the UV light. A 0.5-g sample of the photocatalyst was added to 1.0 L of 0.1 M aqueous $NaHCO_3$ (99.5%, Wako, Japan) solution, after which CO_2 was flowed into the system at 60 mL min^{-1} to remove residual air. The CO_2 flow-rate was lowered to 30 mL min^{-1} during the reaction. H_2 and O_2 were determined by gas chromatography (GC-8A, Shimadzu Corp., Japan) using a 5A molecular sieve column and a thermal conductivity detector (TCD) (carrier gas: Ar). In addition, CO (as the main product) was analyzed using the abovementioned gas chromatograph equipped with a methanizer, a ShinCarbon ST column, and a flame ionization detector (FID) (carrier gas: N_2).

2.4. Characterization

The structures of $ZnTa_2O_6$(S) and (F) were determined by X-ray diffractometry (XRD) on a Rigaku Ultima IV powder diffractometer using Cu Kα radiation. The applied voltage and current were set to 40 kV and 40 mA, respectively. Sample morphologies and compositions were examined by field-emission scanning electron microscopy (SEM, SU-8220, Hitachi High-Technologies, Japan) augmented by energy dispersive X-ray spectroscopy (EDS). Accelerator voltages of 3.0 and 15.0 kV were used for SEM and EDS, respectively. The chemical states of $ZnTa_2O_6$ were determined by X-ray photoelectron spectroscopy (XPS) (ESCA 3400, Shimadzu Corp., Japan), with an applied

voltage and emission current of 10 kV and 20 mA, respectively. Concentrations of Zn ions in reaction solutions were determined by inductively coupled plasma optical emission spectrometry (ICP-OES, iCAP7400, Thermo Fisher Scientific, Inc., USA).

3. Results and Discussions

The XRD patterns of $ZnTa_2O_6$ samples synthesized by the SSR and flux methods are displayed in Figure 1. Compared to the reference pattern from the ICSD database, the $ZnTa_2O_6$(F) sample exhibits a very pure $ZnTa_2O_6$ phase, while four impurity peaks at 2θ values of 26.6°, 34.7°, 38° and 52.5°, which correspond to the $TaO_{2-\delta}$ phase, were observed in the pattern of $ZnTa_2O_6$(S).

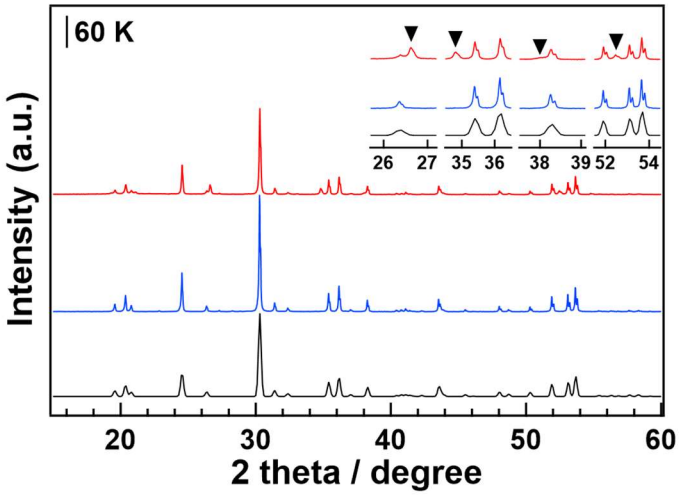

Figure 1. XRD patterns of $ZnTa_2O_6$(S) (red), $ZnTa_2O_6$(F) (blue), and the $ZnTa_2O_6$ reference (black, ICSD No. 36289). Impurity peaks are indicated by black arrows.

Ta 4f XPS spectra of $ZnTa_2O_6$(S) and $ZnTa_2O_6$(F) are presented in Figure 2. In addition to peaks for Ta^{5+} species at 26.0 and 27.9 eV, small peaks corresponding to Ta^{4+} were observed at energies 1.3 eV lower [41–43] than those of Ta^{5+} in the deconvoluted spectra of both samples. Lower-valence tantalum species, relative to Ta^{4+}, were not detected during characterization. Comparing the peak-areas of the Ta^{4+} and Ta^{5+} species reveals that $ZnTa_2O_6$(S) contains 6.3% Ta^{4+} on its surface, while a Ta^{4+} content of 12.7% was determined for the $ZnTa_2O_6$(F) surface. The Ta^{4+} content on the $ZnTa_2O_6$(S) surface

should be much higher than that of $ZnTa_2O_6$(F) if the Ta^{4+} species originate from the $TaO_{2-\delta}$ impurity, which mainly consists of Ta^{4+} because $ZnTa_2O_6$(F) does not contain this impurity. A lower Ta^{4+} content on the $ZnTa_2O_6$(S) surface implies that the $TaO_{2-\delta}$ impurity exists in the bulk of the $ZnTa_2O_6$(S) sample, rather than on its surfaces. Actually, the author suspects that the Ta^{4+} contents on the surfaces of the synthesized samples are probably related to calcination time. $ZnTa_2O_6$(F) contains much more Ta^{4+} on its surface than $ZnTa_2O_6$(S) because it was calcined for a much shorter time than the latter (3 h vs. 12 h) during fabrication. This hypothesis was confirmed by examining the SSR-synthesized $ZnTa_2O_6$ sample calcined at 1273 K for 50 h in air; no peaks corresponding to Ta^{4+} were observed in the deconvoluted pattern of the sample synthesized under these conditions (Figure 3(a)), despite the $TaO_{2-\delta}$ impurity still observed by XRD (Figure 3(b)).

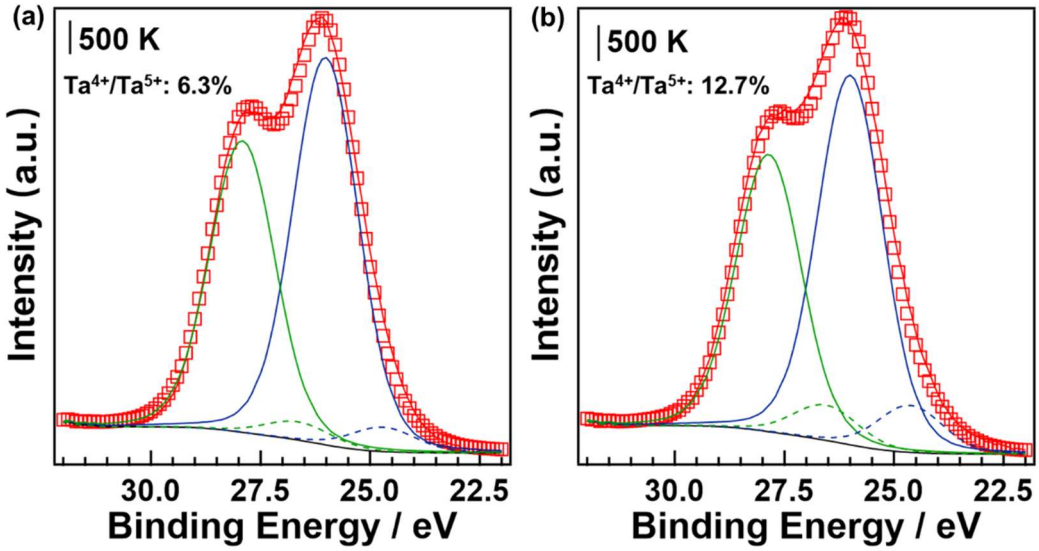

Figure 2. Ta 4f X-ray photoelectron spectra of as-synthesized (a) $ZnTa_2O_6$(S) and (b) $ZnTa_2O_6$(F). Deconvoluted spectra: Ta^{4+} (dotted trace) and Ta^{5+} (solid trace). Resolution: 0.1 eV.

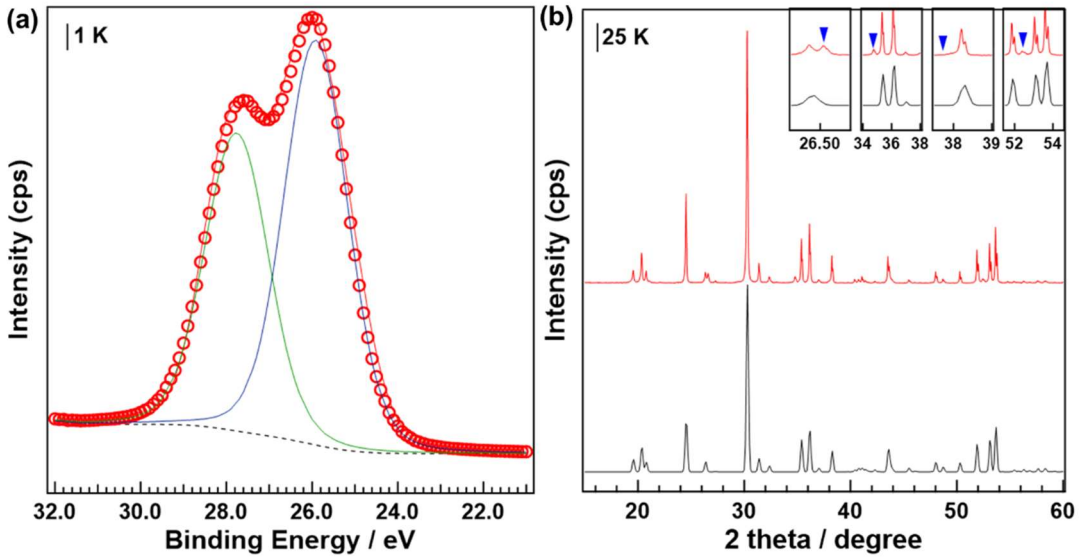

Figure 3. (a) XPS characterization on Ta 4f and (b) XRD pattern of $ZnTa_2O_6$ fabricated by solid state reaction method at 1273 K for 50 h under air atmosphere; synthesized $ZnTa_2O_6$ (red), reference $ZnTa_2O_6$ (black).

Figure 4(a) shows a SEM image and corresponding EDS mapping data for $ZnTa_2O_6$(S). The Ta/Zn atomic ratio in the selected area on the $ZnTa_2O_6$(S) surface was found to be only about 1.62, which is far lower than the theoretical value for $ZnTa_2O_6$ (Ta/Zn = 2.00). The average Ta/Zn atomic ratio in the $ZnTa_2O_6$(S) sample was determined by examining ten randomly selected positions, which resulted in a ratio of about 1.63 (Figure 4(b)). This value indicates that residual ZnO mainly exists on the $ZnTa_2O_6$(S) surface.

As discussed above (Figure 1), no peaks assignable to ZnO were observed in the XRD pattern of the $ZnTa_2O_6$(S) sample, which means that residual ZnO probably exists in an amorphous state or is dissolved in the $ZnTa_2O_6$ phase as a solid solution. Based on this discussion, the author concludes that the $ZnTa_2O_6$(S) sample is most likely composed of a $TaO_{2-\delta}$-rich $ZnTa_2O_6$ core and a ZnO-rich $ZnTa_2O_6$ shell. On the other hand, a Ta/Zn atomic ratio of 2.00 was found for the $ZnTa_2O_6$(F) sample (Figure 4(b)), which corresponds exactly to the theoretical value. In summary, the surface of the SSR-

fabricated $ZnTa_2O_6$(S) sample is rich in unconverted ZnO, while the $ZnTa_2O_6$(F) sample prepared by the flux method has no unconverted ZnO on its surface.

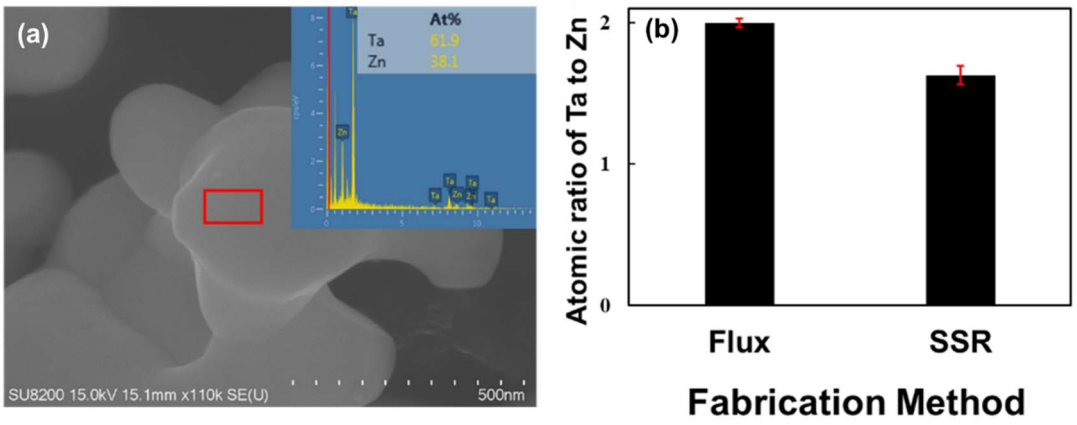

Figure 4. (a) SEM image of $ZnTa_2O_6$(S) with EDS mapping data (inset) acquired in the selected area (red rectangle). (b) Average elemental Ta/Zn atomic ratios for $ZnTa_2O_6$(F) and $ZnTa_2O_6$(S) (ten sample points for each sample).

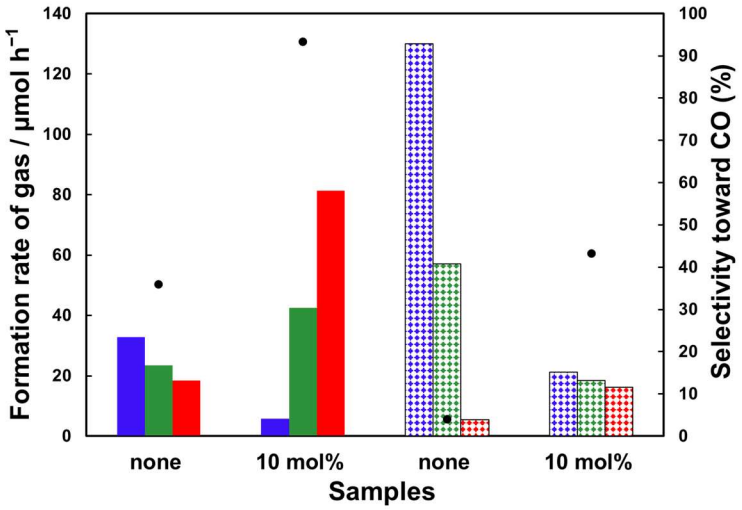

Figure 5. Rates of formation of H_2 (blue), O_2 (green), and CO (red), and selectivities (black dots) toward CO evolution over $ZnTa_2O_6$(S) (solid bars) and $ZnTa_2O_6$(F) (dotted bars) during the photoreduction of CO_2 by H_2O with and without 10 mol% $Zn(OH)_2$ as the cocatalyst. Photocatalyst: 0.5 g, reaction solution: 0.1 M aqueous $NaHCO_3$ (1 L), CO_2 flow rate: 30 mL min^{-1}, light source: 400-W high-pressure Hg lamp.

Figure 5 compares the performance of $ZnTa_2O_6$(S) and $ZnTa_2O_6$(F) with and without modification by 10 mol% $Zn(OH)_2$ for the photoreduction of CO_2 by H_2O. Bare $ZnTa_2O_6$(F) was found to show much higher activity for H_2 evolution (129.9 μmol h^{-1}) than bare $ZnTa_2O_6$(S) (32.8 μmol h^{-1}), while the CO-formation rate (5.4 μmol h^{-1}) over $ZnTa_2O_6$(F) was notably lower than over $ZnTa_2O_6$(S) (18.4 μmol h^{-1}). It should be noted that boron species were completely absent, as confirmed by XPS (Figure 6); therefore, the differences in the performance of $ZnTa_2O_6$(S) and $ZnTa_2O_6$(F) are not due to residual flux compound.

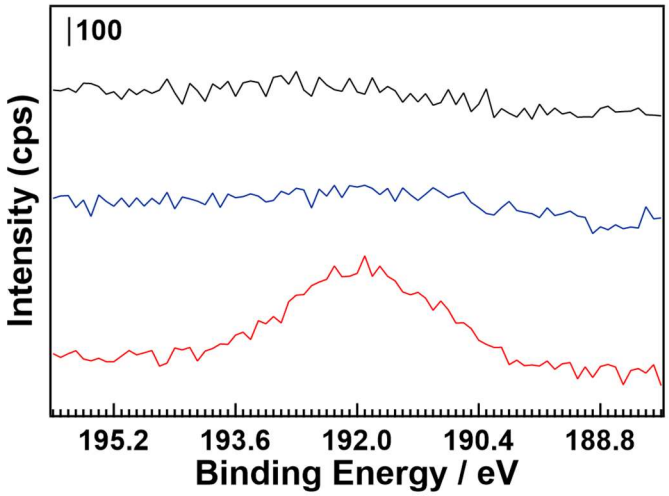

Figure 6. XPS characterizations of boron species on $ZnTa_2O_6$ synthesized by solid state reaction method (black), hot water washed $ZnTa_2O_6$(F) (blue) and unwashed (red) $ZnTa_2O_6$(F) synthesized by flux method.

ZnO has been reported to have a zeta potential of about +35 mV [44] at pH ~7, which means that the $ZnTa_2O_6$(S) surface is probably positively charged by protons due to the presence of unconverted ZnO. The electrical double layer at the interface between $ZnTa_2O_6$(S) and the bulk solution is inevitably dominated by anions, such as OH^- or CO_3^{2-}, among others, to balance the positive charges on the $ZnTa_2O_6$(S) surface. However, the $ZnTa_2O_6$(F) sample does not contain unconverted ZnO on its surface (Figure 4(b)); therefore, compared to $ZnTa_2O_6$(S), $ZnTa_2O_6$(F) is expected to have a relatively acidic

electrical double layer. On the other hand, $ZnTa_2O_6$(F) contains significantly more surface Ta^{4+} species than $ZnTa_2O_6$(S). Incorporating Ta^{4+} into the structure of $ZnTa_2O_6$ inevitably creates oxygen vacancies on its surface that generally act as Lewis acids. These Lewis acidic sites bond to more OH^- in solution, which leads to a negatively charged surface that attracts more protons from the solution surrounding the $ZnTa_2O_6$(F) surface and further decreases the pH of the electrical double layer. An acidic electrical double layer is believed to provide more protons for the production of H_2 and suppress the adsorption of CO_2. Moreover, $Zn(OH)_2$ should be sensitive to the pH of the electrical double layer. An alkaline electrical double layer is expected to benefit the formation and stabilization of $Zn(OH)_2$ on the $ZnTa_2O_6$(S) surface, while an acidic electrical double layer suppresses the precipitation of $Zn(OH)_2$ on the $ZnTa_2O_6$(F) surface. The differences between these two kinds of surface led to significantly different sample performance for the photocatalytic conversion of CO_2 by H_2O, both of which were modified by 10 mol% $Zn(OH)_2$, as seen in Figure 5. $ZnTa_2O_6$(S) modified with 10 mol% $Zn(OH)_2$ produced CO at a rate of 81.4 μmol h^{-1} and a selectivity of 93.3%, while $ZnTa_2O_6$(F) modified with the same amount of $Zn(OH)_2$ only showed limited suppression of H_2 (21.3 μmol h^{-1}) and promotion of CO (16.2 μmol h^{-1}) compared to $ZnTa_2O_6$(S).

In addition to the alkaline electrical double layer that forms $Zn(OH)_2$ on the $ZnTa_2O_6$(S) surface due to its ZnO richness, the author expected that the concentration of dissolved Zn ions in the reaction solution would be another critical factor that determines the performance of $Zn(OH)_2$-modified $ZnTa_2O_6$(S) due to the equilibrium established between the Zn ions in solution (liquid phase) and the precipitated $Zn(OH)_2$ on the surface of the $ZnTa_2O_6$ (solid phase). To confirm the importance of dissolved Zn ions, the author recycle-tested the $ZnTa_2O_6$(S) sample modified with 10 mol% $Zn(OH)_2$ for the photocatalytic conversion of CO_2 by H_2O. Figure 7 shows the formation rates of H_2, O_2, and CO during each testing cycle.

According to ICP-OES, 34.4 mM of Zn ions leached into solution when photoirradiated during the first reaction cycle. Note that bare $ZnTa_2O_6$(S) was very stable

during this reaction, and no Zn species were detected in solution by ICP-OES. Therefore, the Zn ions in solution appear to originate from the loaded $Zn(OH)_2$ rather than the Zn species in $ZnTa_2O_6$(S), such as unconverted surface ZnO. Correspondingly, CO evolved with a considerable level of selectivity (93.3%) and activity (81.4 μmol h^{-1}) with this concentration of Zn ions dissolved in solution. The photocatalyst used during the first reaction cycle was collected by vacuum filtration to remove dissolved Zn ions, after which it was directly used in a second reaction without any pre-treatment under the same conditions. Interestingly, no Zn ions were detected by ICP-OES in solution after the second reaction cycle. As expected, the CO-formation rate was dramatically lower and the production of H_2 dominated; as a result, the selectivity toward CO evolution was very low. This observation clearly shows that the dissolved Zn ions play very important roles in solution during the photoreduction of CO_2 by H_2O. To confirm the importance of the dissolved Zn species, the author added $Zn(OH)_2$ (64.6 mM) directly into the solution during a third reaction cycle. Surprisingly, almost the same formation rates of products and selectivity toward CO evolution were obtained in the first reaction cycle. It should be noted that the Zn ions dissolved in solution are excluded as active species for the photocatalytic conversion of CO_2 by H_2O, as confirmed by comparing the performance of $ZnTa_2O_6$(S) and $ZnTa_2O_6$(F) (Figure 5). Despite introducing the same amounts of $Zn(OH)_2$ (10 mol%) into the reactions involving both samples, $ZnTa_2O_6$(F) was much less active and showed lower CO-evolution selectivity.

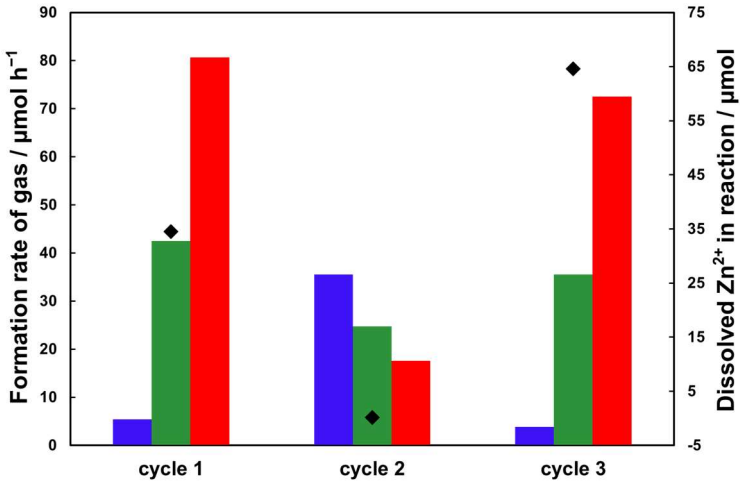

Figure 7. Rates of formation of H_2 (blue), O_2 (green), and CO (red) during recycle testing over 10 mol% $Zn(OH)_2/ZnTa_2O_6$(S) for the photocatalytic conversion of CO_2 by H_2O and the concentrations of Zn ions (black rhomboids) dissolved in solution. Photocatalyst: 0.5 g, reaction solution: 0.1 M aqueous $NaHCO_3$ (1 L), CO_2 flow rate: 30 mL min^{-1}, light source: 400-W high-pressure Hg lamp.

Figure 8 shows relationships between the $Zn(OH)_2$ cocatalyst loading and the H_2-, O_2-, and CO-formation rates and selectivity toward CO evolution during the photocatalytic conversion of CO_2 by H_2O. Increasing the $Zn(OH)_2$ loading from 10 to 20 mol% did not have any obvious influence on the activity and selectivity for CO evolution. However, the selectivity toward CO evolution was clearly lower when the $Zn(OH)_2$ loading was reduced to 5 mol%, with evolution rates of 22.5 and 58.5 μmol h^{-1} for H_2 and CO observed, respectively. These $ZnTa_2O_6$(S)-modification dependences confirm that $Zn(OH)_2$ is the active cocatalyst because lower amounts of $Zn(OH)_2$ led to fewer $Zn(OH)_2$ species on the $ZnTa_2O_6$(S) surface due to the dissolution equilibrium. Note that the e^-/h^+ balances during these reactions are close to 1.0, and the used photocatalysts were white before and after their respective reactions, indicating that Zn^{2+} is not reduced into Zn^0 and, consequently, Zn^0 species are not active cocatalysts.

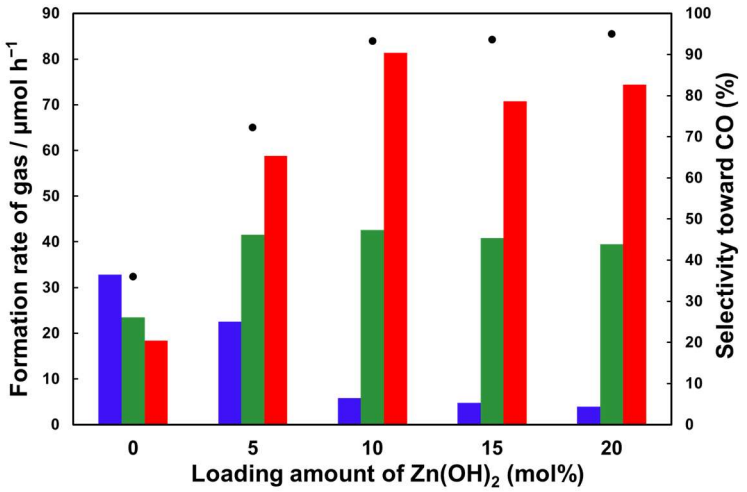

Figure 8. Relationships between $Zn(OH)_2$ loading on $ZnTa_2O_6$(S) and the formation rates for H_2 (blue), O_2 (green), and CO (red), and selectivities toward CO evolution (black dots)

during the photocatalytic conversion of CO_2 by H_2O. Photocatalyst: 0.5 g, reaction solution: 0.1 M aqueous $NaHCO_3$ (1 L), CO_2 flow rate: 30 mL min^{-1}, light source: 400-W high-pressure Hg lamp.

ZnO is probably formed through the decomposition of $Zn(OH)_2$ during these reactions. In addition, $ZnCO_3$ can also theoretically exist in this reaction system. To exclude the possibilities that these species act as active cocatalysts, the author carried out half reactions for the photocatalytic conversion of CO_2 over them using NaI as the electron donor. Table 1 shows that $Zn(OH)_2$ exhibits a selectivity for CO evolution of about 90.3%, which is close to that of the $Zn(OH)_2$-modified $ZnTa_2O_6$(S) sample, while $ZnCO_3$ and commercial ZnO only provided values of 24.3% and 6.9% respectively. Therefore, it is reasonable to conclude that the $Zn(OH)_2$ precipitated on the $ZnTa_2O_6$(S) surface is the cocatalyst.

Table 1. CO_2 photoreduction on commercial ZnO, and synthesized $Zn(OH)_2$ and $ZnCO_3$, using NaI as the electron donor.

Entry	Photocatalyst	Formation rates (μmol h^{-1})		CO Selectivity (%)
		H_2	CO	
1	ZnO [a]	10.6	0.8	6.9
2	$Zn(OH)_2$ [b]	0.6	5.2	90.3
3	$ZnCO_3$ [b]	11.6	3.7	24.3

Photocatalyst amounts: (a) 0.5 g and (b): 2 g. Reaction solution: 0.1 M aqueous $NaHCO_3$ (1 L), CO_2 flow rate: 30 mL min^{-1}, light source: 400-W high-pressure Hg lamp, NaI: 500 μmol.

Based on above discussion, the author proposes a mechanism for how $Zn(OH)_2$ enhances the formation of CO during the photoreduction of CO_2 by H_2O (Scheme 1). The

low pH results in the dissolution of the added $Zn(OH)_2$ in solution during the reaction; however, the unconverted ZnO on the particle surfaces promotes the formation of an alkaline electrical double layer that surrounds each $ZnTa_2O_6$(S) particle, providing an environment for the precipitation of $Zn(OH)_2$. The photogenerated electrons move to the formed $Zn(OH)_2$ dots and are consumed by CO_2 during the reaction. It was very difficult to observe the formation of $Zn(OH)_2$ on the photocatalyst surface because $ZnTa_2O_6$(S) itself contains many Zn species, resulting in a situation in which the $Zn(OH)_2$ on the $ZnTa_2O_6$(S) surface was unable to be discriminated by typical strategies, such as XPS, EDS, and X-ray absorption fine structure analysis.

Instead of using the synthesized $ZnTa_2O_6$(S) containing unconverted ZnO on its surface, in this work, the author also investigated the formation of $Zn(OH)_2$ on the surface of commercial Ga_2O_3 (99.99%, High Purity Chemicals, Japan), which has a similar zeta potential to ZnO (+34.8[45] vs. +35 mV[44], respectively). In detail, 0.5 g of Ga_2O_3 was added to 1 L of a 0.1 M aqueous $NaHCO_3$ solution saturated by a flow of CO_2, after which 266.7 μmol of $Zn(OH)_2$ (10 mol% relative to Ga_2O_3) was added to the suspension with stirring at room temperature for 1 h. The $Zn(OH)_2$-modified Ga_2O_3 was collected by vacuum filtration.

XPS data are displayed in Figure 9(a), which clearly shows peaks corresponding to Zn^{2+} on Ga_2O_3, indicating that $Zn(OH)_2$ was also able to form on the $ZnTa_2O_6$(S) surface. Moreover, to reveal the importance of the alkaline electrical double layer surrounding $ZnTa_2O_6$(S) during the formation of the $Zn(OH)_2$ cocatalyst on its surface, the author competitively formed $Zn(OH)_2$ on the surfaces of commercial Ga_2O_3 and SiO_2 (Wako, Japan; zeta potential: −35 mV[46]), which has an acidic electrical double layer. In this experiment, 0.5 g Ga_2O_3 and 0.5 g SiO_2 were suspended in a solution containing 266.7 μmol of $Zn(OH)_2$ under the same conditions used in the previous impregnation experiment. The collected mixture was observed by SEM-EDS after drying at room temperature. The EDS maps shown in Figure 9(b) reveal that most of the elemental Zn is present on the surfaces of the Ga_2O_3 particles rather than the SiO_2 particles.

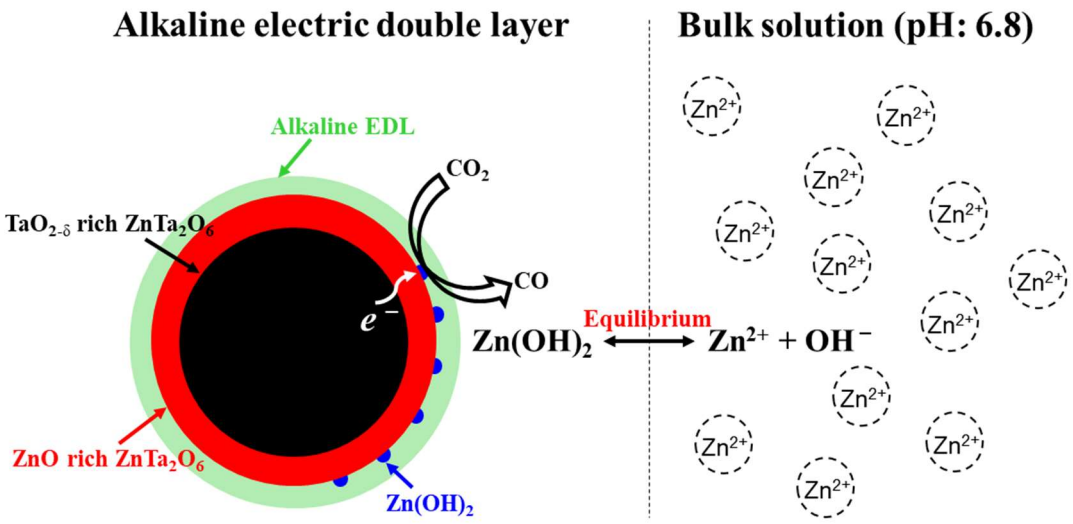

Scheme 1. Proposed mechanism for how $Zn(OH)_2$ acts to promote high activity and selectivity toward CO evolution during the photoreduction of CO_2 by H_2O.

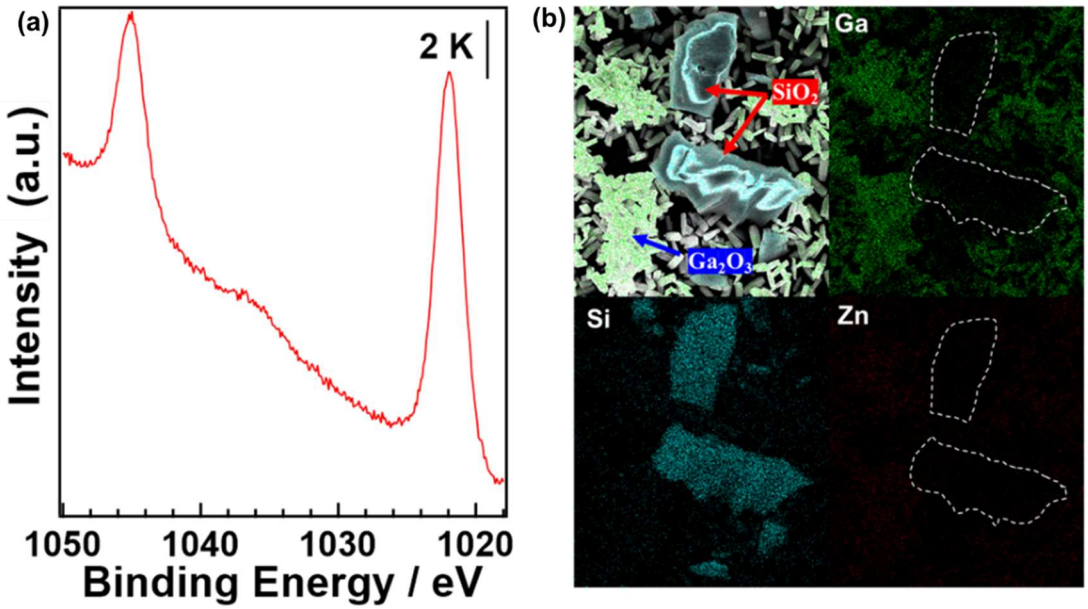

Figure 9. (a) Zn 2p XPS spectrum of the surface formed on commercial Ga_2O_3. (b) SEM image and EDS maps of Zn on the surfaces of commercial Ga_2O_3 and SiO_2 during the competitive precipitation of $Zn(OH)_2$.

Table 2. The synthesis conditions of photocatalysts

Entry	Photocatalyst	Precursor	Pre-treatment	Condition	Post-treatment	Remarks
1	$NaTaO_3$	Na_2CO_3 + Ta_2O_5	Physical grounding	1423 K, 20 h	Washed in H_2O, 353 K	
2	$MgTa_2O_6$	$Mg(NO_3)_2$ + 2.0 NaOH + Ta_2O_5	Impregnation	1423 K, 24 h	Washed in H_2O, 353 K	
3	$SrTa_2O_6$	$SrCO_3$ + Ta_2O_5	Physical grounding	1423 K, 48 h	Washed in H_2O, 353 K	
4	$Sr_{0.2}Na_{0.8}TaO_3$	$SrCO_3$ + Ta_2O_5	Physical grounding	1273 K, 2 h	Washed in H_2O, 353 K	15 g NaCl flux
5	$ZnGa_2O_4$	ZnO + Ga_2O_3	Physical grounding	1273 K, 12 h		
6	Ta_2O_5					Commercial
7	Ga_2O_3					Commercial

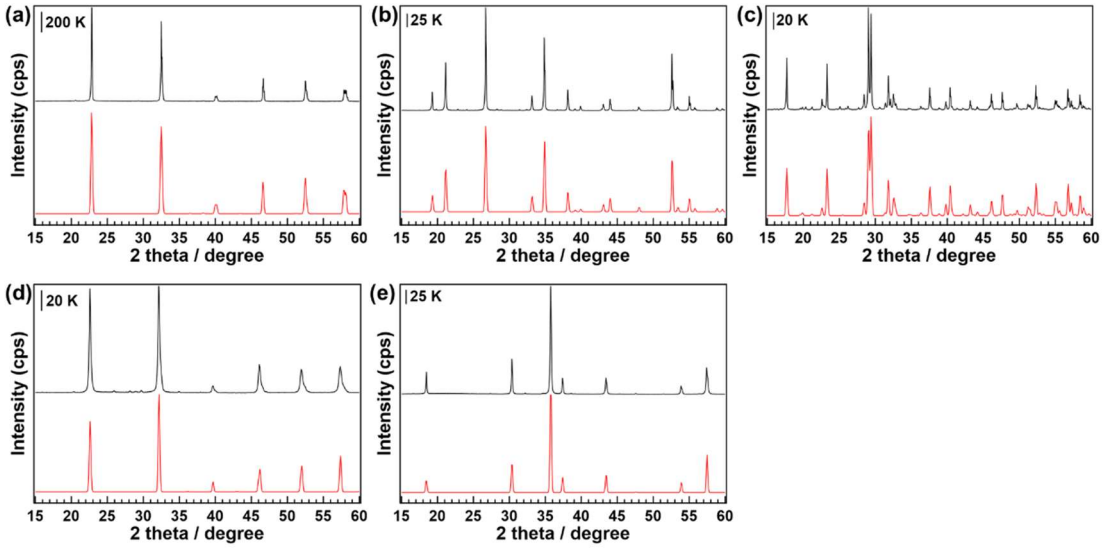

Figure 10. XRD patterns of synthesized (a) $NaTaO_3$, (b) $MgTa_2O_6$, (c) $SrTa_2O_6$, (d) $Sr_{0.2}Na_{0.8}TaO_3$ and (e) $ZnGa_2O_4$. Black: patterns of synthesized samples; Red: references from ICSD database.

To confirm the universality of $Zn(OH)_2$, the $Zn(OH)_2$ cocatalyst was introduced onto various photocatalysts, including $NaTaO_3$, $MgTa_2O_6$, $SrTa_2O_6$, $Sr_{0.2}Na_{0.8}TaO_3$, Ta_2O_5, $ZnGa_2O_4$, and Ga_2O_3. Detailed methods for the synthesis of these materials are provided in the Table 2. The structures of synthesized photocatalysts are presented in Figure 10. Table 3 lists the formation rates of products, selectivities toward CO evolution, and $\boldsymbol{e^-/h^+}$ balances for the photocatalytic conversion of CO_2 by H_2O over various photocatalysts with and without $Zn(OH)_2$ as the cocatalyst. Selectivities toward CO evolution were found to be significantly promoted by the introduction of $Zn(OH)_2$ over all photocatalysts

in this study. With the exception of Ga_2O_3, H_2-formation rates were lower, while CO-formation rates were dramatically higher in all cases. Promotion in H_2 evolution over $Zn(OH)_2$ modified Ga_2O_3 is probably caused by that backward reaction sites for H_2 and O_2 on Ga_2O_3 were covered by $Zn(OH)_2$ rather than $Zn(OH)_2$ acting as the active sites for H_2 evolution. From Table 4, it was found that 0.1 g Ga_2O_3 was able to produce H_2 by about 281.0 μmol h^{-1} in 1 L of 0.1 M $NaHCO_3$ aqueous solution saturated by CO_2 flow. However, the activity was decreased to about 125.1 μmol h^{-1} when 0.5 g Ga_2O_3 was used for the reaction, and it was further suppressed to 96.7 μmol h^{-1} if the amount of Ga_2O_3 was increased to 1.5 g. This implied that there were probably active sites on the surfaces of Ga_2O_3 working for the backward reaction of formed H_2 and O_2 into H_2O, which decreased the formation rate of H_2 when the amount of Ga_2O_3 was increased.

Table 3. Summarizing photocatalyst performance with and without $Zn(OH)_2$ during the photocatalytic conversion of CO_2 by H_2O.

Entry	Cat.	Cocat.	Formation rates (μmol h^{-1})			e^-/h^+	CO Selectivity (%)
			H_2	O_2	CO		
1	$NaTaO_3$	none	93.6	48.1	6.8	1.04	6.7
2		$Zn(OH)_2$	51.9	61.6	75.3	1.03	59.2
3	$MgTa_2O_6$	none	21.8	11.5	1.0	0.99	4.6
4		$Zn(OH)_2$	2.1	28.0	52.4	0.97	96.2
5	$SrTa_2O_6$	none	1483.2	683.8	3.1	1.09	0.2
6		$Zn(OH)_2$	191.5	187.4	217.5	1.09	53.2
7	$Sr_{0.2}Na_{0.8}TaO_3$	none	33.0	16.1	0.4	1.04	1.3
8		$Zn(OH)_2$	37.0	33.6	29.8	0.99	44.6
9	Ta_2O_5	none	55.4	26.9	0.2	1.03	0.4
10		$Zn(OH)_2$	6.6	11.3	16.5	1.00	71.4
11	$ZnGa_2O_4$	none	332.5	188.1	76.1	1.09	18.6
12		$Zn(OH)_2$	153.8	191.3	228.2	1.00	59.7
13	Ga_2O_3	none	125.1	57.4	0.8	1.09	0.6
14		$Zn(OH)_2$	265.1	246.5	249.9	1.04	48.5

Photocatalysts: 0.5 g, $Zn(OH)_2$: 10 mol%, reaction solution: 0.1 M aqueous $NaHCO_3$ (1 L), CO_2 flow rate: 30 mL min^{-1}, light source: 400-W high-pressure Hg lamp.

Table 4. formation rate of H_2 over bare Ga_2O_3 in dependence of the photocatalyst amounts. Reaction solution: 1 L of 0.1 M $NaHCO_3$ aqueous solution, flow rate of CO_2: 30 mL min^{-1}, light source: 400 W high-pressure Hg lamp.

Entry	Amount (g)	Formation rates (μmol h^{-1})			Selectivity of CO (%)
		H_2	O_2	CO	
1	0.1	281.0	115.9	2.8	1.0
2	0.5	125.1	57.4	0.8	0.6
3	1.5	96.7	36.4	1.3	1.3

Conclusion

In this work, the author demonstrated that $Zn(OH)_2$ is a promising cocatalyst for the photoreduction of CO_2 using H_2O as the electron donor. $Zn(OH)_2$ showed excellent activity and selectivity toward CO evolution over $ZnTa_2O_6$ synthesized by the solid-state reaction method (i.e., $ZnTa_2O_6$(S)). Dissolved Zn ions and ZnO-rich surfaces were found to be critical factors for CO evolution, which is probably due to the formation of $Zn(OH)_2$ on the $ZnTa_2O_6$(S) surface that requires a certain equilibrium concentration of Zn ions in solution, and the high-pH alkaline electrical double layer. $Zn(OH)_2$ also performs well on various photocatalysts; it is an inexpensive and universal cocatalyst for the evolution of CO during the photoreduction of CO_2 by H_2O. To the best knowledges of the author, $Zn(OH)_2$ is the only candidate cocatalyst identified to date that performs as well as Ag.

References

1. G. W. Crabtree and N. S. Lewis. Physics today 2007, 3, 37-42.
2. L. R. Penalonga and B. Y. M. Soria. Energies 2017, 10, 1235.
3. G. M. J. Herbert, S. Iniyan, E. Sreevalsan and S. Rajapandian. Renew. Sustain. Energy Rev. 2007, 11, 1117–1145.
4. E. F. Moran, M. C. Lopez, N. Moore, N. Müller and D. W. Hyndman. PNAS 2018, 115, 47, 11891-11898.
5. J. Goldemberg, World energy assessment: energy and the challenge of sustainability. (UN. 2001).
6. J. Hansen, R. Ruedy, M. Sato and K. Lo. Rev. Geophys. 2010, 48, 1–29.
7. J. Hansen, L. Nazarenko, R. Ruedy, M. Sato, J. Wills, A. D. Genio, D. Koch, A. Lacis, K. Lo, S. Menon, T. Novakov, J. Perlwitz, G. Russell, G. A. Schmidt and N. Tausnev. Science 2005, 308, 1431–1436.
8. T. M. Bruton. Sol. Energy Mater. Sol. Cells 2002, 72, 3–10.
9. R. Fu, T. L. James and M. Woodhouse. IEEE Journal of Photovoltaics 2015, 5, 2, 515–524.
10. Q. Wang and K. Domen. Chem. Rev. 2020, 120, 919–985.
11. L. I. Granone, F. Sieland, N. Zheng, R. Dillert and D. W. Bahnemann. Green Chem. 2018, 20, 1169-1192.
12. R. Pang, K. Teramura and T. Tanaka. Current Developments in Photocatalysis and Photocatalytic Materials 2020, 179–190.
13. A. K. Jena, A. Kulkarni and T. Miyasaka. Chem. Rev. 2019, 119, 3036–3103.
14. B. Han, X. Ou, Z. Deng, Y. Song, C. Tian, H. Deng, Y. Xu and Z. Lin. Angew. Chemie. Int. Ed. 2018, 57, 16811–16815.
15. W. Zhong, R. Sa, L. Li, Y. He, L. Li, J. Bi, Z. Zhuang, Y. Yu and Z. Zou. J. Am. Chem. Soc. 2019, 141, 7615–7621.
16. Y. Men, Y. You, Y. Pan, H. Cao, Y. Xia, D. Cheng, J. Song, D. Cui, N. Wu, Y. Li, S. Xin and J. B. Goodenough. J. Am. Chem. Soc. 2018, 140, 13071–13077.

17. M. F. Kuehnel, K. L. Orchard, K. E. Dalle and E. Reisner. J. Am. Chem. Soc. 2017, 139, 7217-7223.
18. K. Iizuka, T. Wato, Y. Miseki, K. Saito and A. Kudo. J. Am. Chem. Soc. 2011, 133, 20863–20868.
19. H. Nakanishi, K. Iizuka, T. Takayama, A. Iwase and A. Kudo. ChemSusChem 2017, 10, 112–118.
20. K. Teramura, H. Tatsumi, Z. Wang, S. Hosokawa and T. Tanaka. Bull. Chem. Soc. Jpn. 2015, 88, 431–437.
21. Z. Huang, K. Teramura, S. Hosokawa and T. Tanaka. Applied Catalysis B: Enviromental 2016, 199, 272–281.
22. A. Anzai, N. Fukuo, A. Yamamoto and H. Yoshida. Catalysis communications 2017, 100, 134–138.
23. Z. Wang, K. Teramura, S. Hosokawa and T. Tanaka. Applied Catalysis B: Environmental 2015, 163, 241–247.
24. S. Wang, K. Teramura, T. Hisatomi, K. Domen, H. Asakura, S. Hosokawa and T. Tanaka. ACS Appl. Energy Mater. 2020, 3, 1468–1475.
25. R. Pang, K. Teramura, H. Asakura, S. Hosokawa and T. Tanaka. ACS Sustainable. Chem. Eng. 2019, 7, 2083–2090.
26. T. Yoshida, N. Yamamoto, T. Mizutani, M. Yamamoto, S. Ogawa, S. Yagi, H. Nameki and H. Yoshida. Catalysis. Today, 2018, 303, 320–326.
27. Z. Wang, K. Teramura, S. Hosokawa and T. Tanaka. J. Mater. Chem. A. 2015, 3, 11313–11319.
28. R. Pang, K. Teramura, H. Asakura, S. Hosokawa and T. Tanaka. Applied Catalysis B: Environmental 2017, 218, 770–778.
29. S. Iguchi, K. Teramura, S. Hosokawa and T. Tanaka. Catal. Sci. Technol. 2016, 6, 4978–4985.
30. M. Ishida, S. Kikkawa, K. Hori, K. Teramura, H. Asakura, S. Hosokawa and T. Tanaka. ACS Appl. Energy Mater. 2020, 3, 6552-6560.

31. M. Ma, K. Liu, J. Shen, R. Kas and W. A. Smith. ACS Energy Lett. 2018, 3, 1301-1306.
32. Y. C. Hsieh, S. D. Senanayake, Y. Zhang, W. Xu and D. E. Polyansky. ACS Catal. 2015, 5, 5349-5356.
33. F. Liao, Y. Huang, J. Ge, W. Zheng, K. Tedsree, P. Collier, X. Hong and S. C. Tsang. Angew. Chem. 2011, 123, 2210–2213.
34. F. C. Meunier. Angew. Chem. Int. Ed. 2011, 50, 4053–4054.
35. D. H. Won, H. Shin, J. Koh, J. Chung, H. S. Lee, H. Kim and S. I. Woo. Angew. Chem Int. Ed. 2016, 55, 9297–9300.
36. J. Rosen, G. S. Hutchings, Q. Lu, R. V. Forest, A. Moore and F. Jiao. ACS Catal. 2015, 5, 4586-4591.
37. T. Zhang, X. Li, Y. Qiu, P. Su, W. Xu, H. Zhong and H. Zhang. Journal of Catalysis 2018, 357, 154–162.
38. Z. Wang, K. Teramura, Z. Huang, S. Hosokawa, Y. Sakata and T. Tanaka. Catal. Sci. Technol. 2016, 6, 1025–1032.
39. K. Teramura, Z. Wang, S. Hosokawa, Y. Sakata and T. Tanaka. Chem. Eur. J. 2014, 20, 9906–9909.
40. S. Wang, K. Teramura, H. Asakura, S. Hosokawa and T. Tanaka. Doi:10.1021/acs.jpcc.0c08464.
41. Y. Li, S. Sanna, K. Norrman, D. V. Christensen, C. S. Pedersen, J. M. G. Lastra, M. L. Traulsen, V. Esposito and N. Pryds. Appl. Surf. Sci. 2019, 470, 1071–1074.
42. C. S. Pedersen, J. H. Chang, Y. Li, N. Pryds and J. M. G. Lastra. APL Mater. 2020, 8, 071108.
43. R. Simpson, R. G. White, J. F. Watts and M. A. Baker. Appl. Surf. Sci. 2017, 405, 79–87.
44. R. Marsalek. Apcbee Procedia 2014, 9, 13–17.
45. S. Yan, L. Wan, Z. Li, Y. Zhou and Z. Zou. Chem. Commun. 2010, 46, 6388–6390.

46. X. Song, N. Jiang, Y. Li, D. Xu and G. Qiu. Mater. Chem. Phys. 2008, 110, 128–135.

Chapter 4

Exploring effective non-metal inorganic cocatalysts for the photocatalytic conversion of CO_2 using H_2O as an electron donor

Abstract

The author has surveyed a wide range of non-metal inorganic cocatalysts showing good selectivity toward CO evolution for the photocatalytic conversion of CO_2 using H_2O as an electron donor. A variety of non-metal inorganic cocatalysts containing Si, Ga, Mg, and Zn enhance the formation rate of CO. In particular, Zn-based compounds, such as $Zn(OH)_2$, $ZnSiO_3$, and $ZnGa_2O_4$, that are highly dispersed on the surface exhibit the best performance among these cocatalysts. The counter anions in the Zn-based compounds influence the cocatalyst properties, including activities and stabilities.

1. Introduction

Various sustainable energies, such as solar [1], nuclear [2], wind [3], and hydro [4] powers, have been developed in recent years to replace fossil fuels because of growing energy [5] and environmental problems [6], [7]. The conversion of solar energy has special advantages over these energy strategies because it integrates sustainability, safety, and harmlessness to ecology. Si is currently the most widely used material in the industrialization of solar-driven electricity [8]; however, its manufacture by the Siemens process [9] is expensive. In recent years, many chemists have been interested in the development of new pathways for the conversion of solar energy, including the production of hydrogen from water (H_2O) [10] and the conversion of biomass [11] and carbon fuels from carbon dioxide (CO_2) [12] and perovskite photovoltaic cells [13]. Among these strategies, the photocatalytic conversion of CO_2 by H_2O into carbon monoxide (CO) is a promising method for using solar energy. In this reaction, two indicators are important for the successful conversion of CO_2 using H_2O as the electron donor. One is the balance between the electrons provided by H_2O (O_2 evolution) and those consumed by CO_2 and protons (CH_xO_y and H_2 evolution), as calculated in equation (1). The other is the selectivity of the products derived from CO_2 photoreduction over H_2 from water splitting, as calculated in equation (2).

$$e^-/h^+ = (2R_{HCOOH} + 2R_{CO} + 4R_{HCHO} + 6R_{CH_3OH} + 8R_{CH_4} + 2R_{H_2})/4R_{O_2}, \quad (1)$$

$$\text{Selectivity} = (2R_{HCOOH} + 2R_{CO} + 4R_{HCHO} + 6R_{CH_3OH} + 8R_{CH_4})/(2R_{HCOOH} + 2R_{CO} + 4R_{HCHO} + 6R_{CH_3OH} + 8R_{CH_4} + 2R_{H_2}) \times 100\%, \quad (2)$$

where R represents the rate of formation of each product by the photocatalytic conversion of CO_2 by H_2O.

Although many photocatalysts, such as $NaTaO_3$ [14], $CaTiO_3$ [15], $SrTiO_3$ [16], Ga_2O_3 [17] and $ZnGa_2O_4$ [18], and $SrNb_2O_6$ [19], are capable of extracting electrons from H_2O, they produce H_2 as the main product because the redox potential of the former (−0.41 V vs SHE) is more positive than that of the latter (−0.52 V vs SHE). This results in a situation

in which a proper cocatalyst is mostly a critical component for the evolution of CO in the photocatalytic conversion of CO_2 by H_2O. To the best knowledges of the author, people have achieved the highly selective reduction of CO_2 in electrochemical conversion over various metal electrodes, such as Zn [20], Au [21], Cu [22], and Ag [23]. However, only Ag cocatalysts show universal selectivity for the photocatalytic conversion of CO_2 using H_2O over many photocatalysts. In previous works, Iguchi et al. has investigated various metals, including Au, Pt, Cu, Ni [24], Pd, and Ag [25], as cocatalysts loaded on $ZnTa_2O_6$ for the photocatalytic conversion of CO_2 by H_2O in an aqueous $NaHCO_3$ solution. The results indicate that only Ag nanoparticles can increase the formation rate of CO and the selectivity toward CO evolution. Further, the particularity of the Ag cocatalyst in the promotion of CO evolution has been confirmed by other research groups, such as Ag-modified $NaTaO_3$ [14], $CaTiO_3$ [15], and $K_2Ti_6O_{13}$ [26]. Currently, the effective conversion of CO_2 in electrochemistry and photocatalysis is dominated by metal cocatalysts.

The author believes that, owing to the limited amounts of cocatalyst materials for the electrochemical and photocatalytic conversion of CO_2, researchers do not have a clear and systematic map to determine how H_2 is suppressed and CO_2 is converted in high activity and selectivity. Taking the Ag cocatalyst as an example, it is still impossible to confidently conclude which properties are critical for providing a high formation rate of CO and effective selectivity toward CO evolution for the photocatalytic conversion of CO_2 by H_2O. However, the size, morphology, and growth orientation of Ag nanoparticles have been characterized using advanced technologies. A possible scientific strategy to achieve this goal may be to establish a library of situations where CO_2 can be reduced with excellent efficiencies by studying large amounts of cocatalysts and then extracting the common things from them. Based on this strategy, researchers will have a chance to find the universal critical factors for the effective photocatalytic conversion of CO_2 by H_2O and use these principles to guide the design of new materials. For this purpose, the first thing researchers should do is break through the family of metal cocatalysts, which many research groups have preferentially focused on. Beyond the Ag cocatalyst in the

photocatalytic conversion of CO_2 by H_2O, the author has found that the selectivity toward CO evolution over $ZnTa_2O_6$ synthesized by the solid-state reaction method can be tuned by adding trace amounts of Na_2CrO_4 [27]. The active sites for water splitting are almost completely passivated by just 5 μmol Na_2CrO_4, and the active sites are shifted toward CO evolution, which results in the selectivity of 80% for CO_2 photoreduction. Subsequently, the author has reported that $Zn(OH)_2$ [28] acts as a very effective and universal cocatalyst for the selective photocatalytic conversion of CO_2 into CO by H_2O over various Ta- and Ga-based photocatalysts, including Ta_2O_5, Ga_2O_3, MTa_2O_6 (M: Sr, Zn, Mg), $ZnGa_2O_4$, $NaTaO_3$, and $Sr_{0.2}Na_{0.8}TaO_3$. Motivated by the excellent performance of $Zn(OH)_2$, the author has investigated a relatively broad range of non-metal cocatalysts based on Ta-, Ga-, Ti-, Zr-, and Nb-based photocatalysts to further expand the capability of non-metal inorganic cocatalysts for the effective photocatalytic conversion of CO_2 using H_2O as the electron donor.

2. Experimental section

2.1. Preparation of photocatalysts

Information about all reagents used for the synthesis of the main photocatalysts and cocatalysts is listed in Table 1. Except for commercial photocatalysts, the main photocatalysts used in this study were fabricated by solid-state reaction (SSR) or flux methods. The detailed conditions of the specific photocatalysts are listed in Table 2. The cocatalysts, such as $Zn(OH)_2$, $ZnGa_2O_4$, and $ZnSiO_3$, were loaded onto the main photocatalysts by precipitation at room temperature. ZnO was modified by calcining $Zn(OH)_2$-loaded photocatalysts when necessary. The detailed conditions for the specific situations are listed in Table 3.

Table 1. Reagents used in this work.

Reagent	Company	Purity
$Na_2CrO_4•4H_2O$	Wako	99.0%
ZnO	Wako	99.0%
Ta_2O_5	High purity chemicals	99.9%
$SrCO_3$	Wako	99.99%
H_3BO_3	Wako	99.5%
$NaHCO_3$	Wako	99.5-100.3%
Ga_2O_3	High purity chemicals	99.99%
$Al(NO_3)_3•9H_2O$	Wako	97.0%
NaOH	Wako	97.0%
$Ga(NO_3)_3•xH_2O$	High purity chemicals	99.999%
$ZrO(NO_3)_2•2H_2O$	Wako	97.0%
$Cr(NO_3)_3•9H_2O$	Kanto Chemicals	95.0%
$Zn(NO_3)_2•6H_2O$	Wako	99.9%
$Mg(NO_3)_2•6H_2O$	Wako	99.5%
$Na_2SiO_3•9H_2O$	Wako	98.0%
HCl	Wako	0.1 M
$Fe(NO_3)_3•9H_2O$	Wako	99.9%
$Ni(NO_3)_2•6H_2O$	Wako	99.9%
$Na_3PO_4•12H_2O$	Wako	99.0%
Na_2CO_3	Wako	99.8%
$NaAl_2O_4$	Wako	100%
$NaNO_3$	Wako	99.0%
Nb_2O_5	Wako	99.9%
ZrO_2	Wako	98.0%
$CaCO_3$	Wako	99.5%
TiO_2	Wako	99.9%

Table 2. Synthesis of photocatalysts used in this work.

Photocatalyst	Precursors	Pre-treatment	Conditions	Post-treatment
$ZnTa_2O_6$ (SSR)	$ZnO + Ta_2O_5$	Physical mixture	1273 K, 12 h	
$SrTa_2O_6$ (SSR)	$SrCO_3 + Ta_2O_5$	Physical mixture	1423 K, 24 h	
Ga_2O_3	Commercial			
Ta_2O_5	Commercial			
$NaTaO_3$	$Na_2CO_3 + Ta_2O_5$	Physical mixture	1423 K, 20 h	
$SrNb_2O_6$	$SrCO_3 + Nb_2O_5$	Physical mixture	1423 K, 24 h	
$SrZrO_3$	$SrCO_3 + ZrO_2$	Physical mixture	1423 K, 24 h	
$CaZrO_3$	$CaCO_3 + ZrO_2$	Physical mixture	1423 K, 24 h	
$CaTiO_3$	$CaCO_3 + TiO_2 + 1.5$ NaCl	Physical mixture	1373 K, 10 h	Wash in water, 353 K, 2 h
$NaGaO_2$	$Na_2CO_3 + Ga_2O_3$	Physical mixture	1173 K, 6 h	
$ZnGa_2O_4$	$ZnO + Ga_2O_3$	Physical mixture	1273 K, 12 h	

Table 3. Modifications of cocatalysts by precipitation methods.

Cocat.	A	B	Pre-treatment before reaction
$Zn(OH)_2$	$Zn(NO_3)_2•6H_2O$	NaOH	
$Zr(OH)_4$	$ZrO(NO_3)_2•2H_2O$	NaOH	
$Cr(OH)_3$	$Cr(NO_3)_3•9H_2O$	NaOH	
$Ga(OH)_3$	$Ga(NO_3)_3•xH_2O$	NaOH	
$Mg(OH)_2$	$Mg(NO_3)_2•6H_2O$	NaOH	
H_2SiO_3	$Na_2SiO_3•9H_2O$	HCl	
$Al(OH)_3$	$Al(NO_3)_3•9H_2O$	NaOH	
$Fe(OH)_3$	$Fe(NO_3)_3•9H_2O$	NaOH	
$Ni(OH)_2$	$Ni(NO_3)_2•6H_2O$	NaOH	
ZnO	$Zn(NO_3)_2•6H_2O$	NaOH	473 K , 2 h
$ZnSiO_3$	$Zn(NO_3)_2•6H_2O$	$Na_2SiO_3•9H_2O$	
$ZnGa_2O_4$	$Zn(NO_3)_2•6H_2O$	$NaGaO_2$	
$ZnAl_2O_4$	$Zn(NO_3)_2•6H_2O$	$NaAl_2O_4$	
$Zn_3(PO_4)_2$	$Zn(NO_3)_2•6H_2O$	$Na_3PO_4•12H_2O$	
$AlPO_4$	$Al(NO_3)_3•9H_2O$	$Na_3PO_4•12H_2O$	

2.2. Characterization of the photocatalysts

The structures of the main photocatalysts synthesized in this work were determined by X-ray diffraction (XRD) using a Rigaku Ultima IV powder diffractometer with Cu Kα radiation. The measurements were performed at a voltage of 40 kV and a current of 40 mA (Figure 1).

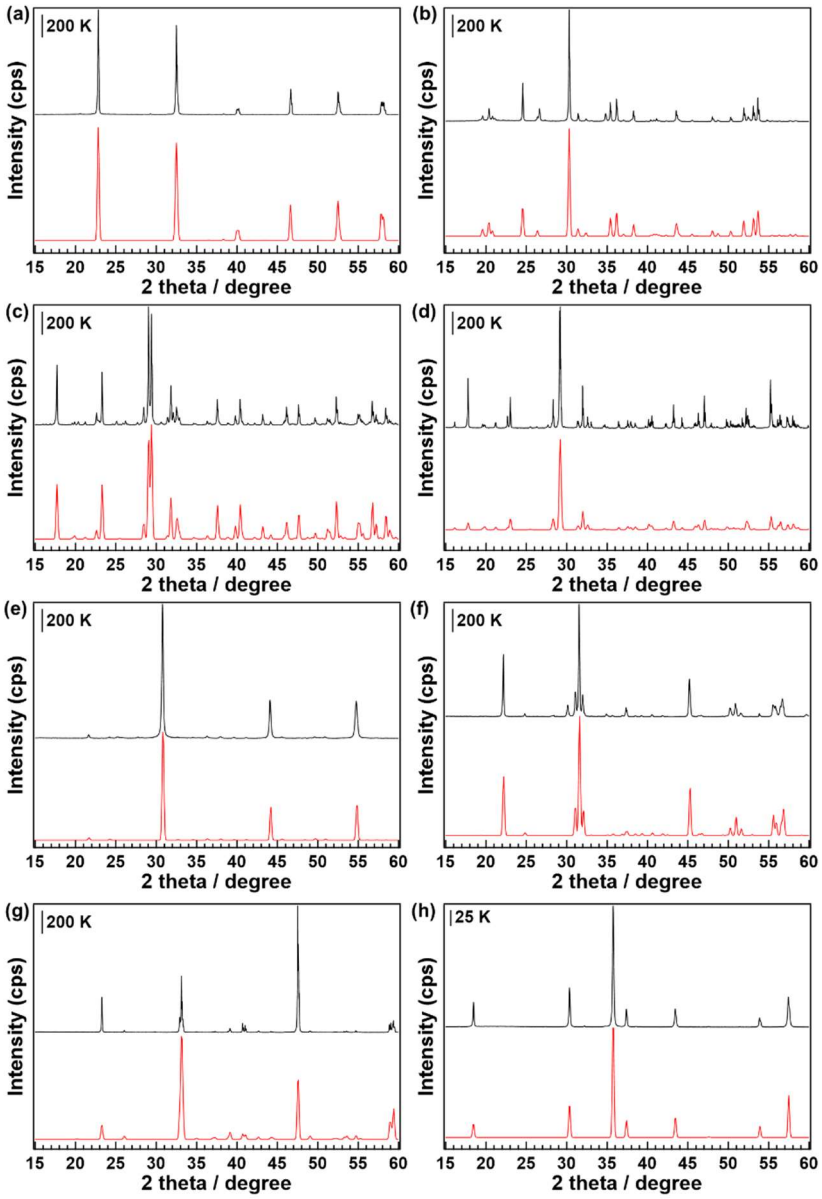

Figure 1. XRD patterns of (a) $NaTaO_3$, (b) $ZnTa_2O_6$ (SSR), (c) $SrTa_2O_6$ (SSR), (d) $SrNb_2O_6$ (SSR), (e) $SrZrO_3$ (SSR), (f) $CaZrO_3$ (SSR), (g) $CaTiO_3$ (flux) and (h) $ZnGa_2O_4$ (SSR). Black: synthesized samples; Red: references from ICSD database.

2.3. Reaction procedure

The photocatalytic conversion of CO_2 by H_2O over various photocatalysts was conducted in an inner irradiation reactor equipped with a quartz jacket connected to the cooling system. The reaction temperature was controlled from 298 to 303 K. The light source was a 400 W high-pressure mercury lamp (Sen Lights Corp.). During the reactions, specific amounts of photocatalyst were added to the reactor, and the reactor was purged with CO_2 (5N) at 60 mL min^{-1} to remove the residual air in the system. Subsequently, the flow rate of CO_2 was increased to 30 mL min^{-1} during photoirradiation. The products, including H_2, O_2, and CO, were detected using thermal conductivity detector (TCD)- and flame ionization detector (FID)-equipped GC−8A gas chromatographs from Shimadzu Corp.

3. Results and Discussion

3.1. Mapping the non-metal inorganic cocatalysts

Various metal hydroxides (Zr, Cr, Zn, Ga, Mg, Si, Al, Fe, and Ni) were surveyed to find effective cocatalysts for the selective photocatalytic conversion of CO_2 using H_2O as an electron donor, as shown in Table 4. Bare $ZnTa_2O_6$ produced CO with an activity of 11.2 μmol h^{-1} and a selectivity of 45.2% (Entry 1). After the modifications with $Zr(OH)_4$ (Entry 2) and $Cr(OH)_3$ (Entry 3) as the cocatalysts, the formation rates of CO, 11.2 and 11.7 μmol h^{-1}, respectively, were similar to that over bare $ZnTa_2O_6$; additionally, the formation rates of H_2 were unaffected. This indicates that the hydroxides of Zr and Cr showed no catalytic performance in the promotion of CO and the suppression of H_2 for the photocatalytic conversion of CO_2 by H_2O. In particular, the formation rate of O_2 for the $Cr(OH)_3$ cocatalyst was 4.9 μmol h^{-1}, which was considerably lower than the stoichiometric amount, based on equation (1). This was caused by the oxidation of Cr^{3+} to Cr^{6+} during the reaction. This could be easily confirmed by the color change of the solutions before (transparent) and after (slightly yellow) the reactions. With the leaching of $Cr(OH)_3$ into the solution as dissolved chromate ions, the formation rate of CO during the time course (Figure 2) rapidly increased to 29.7 μmol h^{-1} and gradually decreased to

20.3 μmol h^{-1}. Additionally, the evolution rate of H_2 was suppressed from 15.6 to 5.9 μmol h^{-1} as $Cr(OH)_3$ was leached. This result conformed to previous conclusion of the author [27] that a certain number of chromate ions in the solution would enhance the evolution of CO and inhibit that of H_2 for the photocatalytic conversion of CO_2 by H_2O. $Fe(OH)_3$ suppressed the evolution of H_2 over Ga_2O_3, as shown in Entry 10, and the selectivity toward CO evolution was slightly promoted. However, it showed almost no positive influence on the formation rate of CO (0.8 vs. 1.6 μmol h^{-1}). $Al(OH)_3/ZnTa_2O_6$ (Entry 5) and $Ni(OH)_2/Ga_2O_3$ (Entry 11) enhanced the formation rate of H_2; however, they decreased the formation rate of CO during the reactions. This means that $Al(OH)_3$ and $Ni(OH)_2$ acted as effective cocatalysts for overall water splitting rather than for the photocatalytic conversion of CO_2. Notably, the effect of the Al-based cocatalysts on the evolution of H_2 depended on the counter anions of Al^{3+}, such as OH^-, PO_4^{3-}, and NO_3^{2-} (Figure 3). The formation rate of H_2 was enhanced when OH^- and PO_4^{3-} were used as counter anions, whereas it was drastically reduced by $Al(NO_3)_3$.

Table 4. Summary of various metal hydroxides as the cocatalysts on $ZnTa_2O_6$ from SSR and Ga_2O_3 for the photocatalytic conversion of CO_2 by H_2O [a].

Entry	Main Cat.	Cocat.	Amount of Cocat. (mol %)	Formation rate of products (μmol h^{-1})			Selec. toward CO (%)
				H_2	O_2	CO	
1	$ZnTa_2O_6$	none	0	13.6	12.5	11.2	45.2
2		$Zr(OH)_4$	3	14.1	13.3	11.2	44.2
3		$Cr(OH)_3$	10	15.6	4.9	11.7	42.8
4		$Zn(OH)_2$	10	7.0	39.4	67.6	90.6
5		$Al(OH)_3$	10	30.5	15.1	0.3	1.0
6		$Ga(OH)_3$	10	104.3	34.6	27.7	21.0
7		$Mg(OH)_2$	10	76.3	16.5	39.5	34.1
8		H_2SiO_3	10	48.5	20.7	53.0	52.2
9	Ga_2O_3	none	0	125.1	57.4	0.8	0.6
10		$Fe(OH)_3$	3	34.7	16.9	1.6	4.4
11		$Ni(OH)_2$	30	297.9	136.9	0.2	0.1
12		$Ga(OH)_3$	10	681.2	337.0	32.8	4.6

[a] Photoirradiation time: 0.5 h; main photocatalyst: 0.5 g; reaction solution: 1 L of a 0.1 M

$NaHCO_3$ aqueous solution; CO_2 flow rate: 30 mL min^{-1}; light source: 400 W high-pressure Hg lamp.

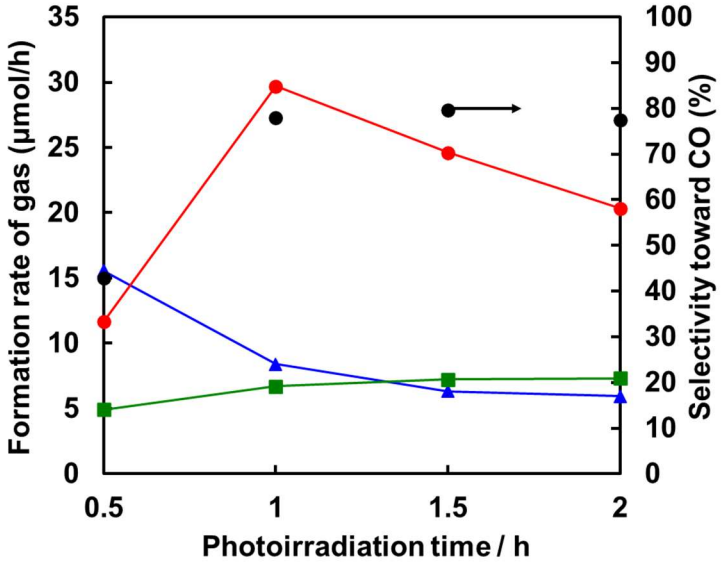

Figure 2. Formation rates of H_2 (blue), O_2 (green) and CO (red) and selectivity toward CO evolution (black dot) in the time courses of CO_2 photoreduction by H_2O over $Cr(OH)_3$-modified $ZnTa_2O_6$. Main photocatalyst: 0.5 g; reaction solution: 1 L of a 0.1 M $NaHCO_3$ aqueous solution; CO_2 flow rate: 30 mL min^{-1}; light source: 400 W high-pressure Hg lamp.

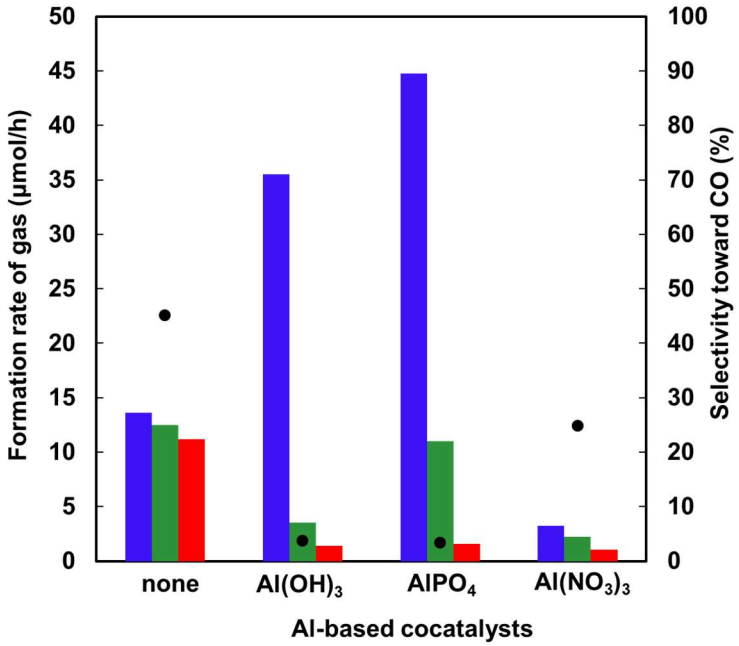

Figure 3. Formation rates of H_2 (blue), O_2 (green) and CO (red) and selectivity toward CO evolution (black dot) for the photocatalytic conversion of CO_2 by H_2O over Al-based cocatalysts-modified $ZnTa_2O_6$ fabricated by SSR method ($Al(OH)_3$ and $AlPO_4$: 10 mol%; $Al(NO_3)_3$: 5 μmol). Photoirradiation time: 0.5 h; main photocatalyst: 0.5 g; reaction solution: 1 L of a 0.1 M $NaHCO_3$ aqueous solution; CO_2 flow rate: 30 mL min^{-1}; light source: 400 W high-pressure Hg lamp.

Interestingly, the hydroxides of Zn, Ga, Mg, and Si increased the formation rate of CO for the photocatalytic conversion of CO_2 by H_2O compared to bare photocatalysts, as shown in Entries 4, 6, 7, 8, and 12. Additionally, 10 mol% of $Zn(OH)_2$ decoration on the surface of $ZnTa_2O_6$ promoted the formation rate of CO from 11.2 to 67.6 μmol h^{-1}, whereas the evolution of H_2 was inhibited from 13.6 to 7.0 μmol h^{-1} (Entry 4) for the photocatalytic conversion of CO_2 by H_2O. Further, the formation rate of CO increased from 11.2 to 27.7 μmol h^{-1} for $Ga(OH)_3$ as the cocatalyst on $ZnTa_2O_6$ (Entry 6). Unfortunately, as the formation rate of H_2 increased to 104.3 μmol h^{-1}, the selectivity toward CO evolution decreased to 21.0%, as compared to bare $ZnTa_2O_6$. For $Ga(OH)_3$-modified Ga_2O_3 (Entry 12), the formation rates of CO and H_2 increased to 32.8 and 681.2 μmol h^{-1}, respectively. This reveals that $Ga(OH)_3$ functioned as a good cocatalyst for both the overall water splitting and the photocatalytic conversion of CO_2. To investigate the performance of $Ga(OH)_3$ as a cocatalyst in detail, the modification amounts were optimized on Ga_2O_3, as displayed in Figure 4. Further, 1 mol% $Ga(OH)_3$ exhibited limited promotion in the formation rate of CO (3.3 μmol h^{-1}), and the highest formation rate of CO was achieved at the loading amount of 15 mol% (44.9 μmol h^{-1}). With a further increase in the loading amount to 20 mol%, the formation rate of CO was decreased to 25.1 μmol h^{-1}. Notably, the modification of $Ga(OH)_3$ promoted the production of CO and the evolution of H_2 (highest: 813 μmol h^{-1} at 15 mol%) for the photocatalytic conversion of CO_2; thus, the selectivity toward CO evolution was not increased (lower than 6.0%). Surprisingly, the formation rate of CO over $ZnTa_2O_6$ increased to 39.5 and 53.0 μmol h^{-1}

when 10 mol% of $Mg(OH)_2$ (Entry 7) and H_2SiO_3 (Entry 8) were used as the cocatalysts, respectively. Notably, the formation rate of O_2 over $Mg(OH)_2$ and H_2SiO_3 as cocatalysts was significantly below the stoichiometric amount. This could be caused by the strong adsorption of O_2 evolved on the surface of the photocatalysts. $Mg(OH)_2$ and H_2SiO_3 could not provide electrons for the reduction of H^+ and CO_2. Although $Mg(OH)_2$ and H_2SiO_3 promoted the formation rate of CO for the photocatalytic conversion of CO_2 by H_2O, their stabilities were considerably poor. The $Mg(OH)_2$ and H_2SiO_3 species were not stabilized on the surface of $ZnTa_2O_6$. As seen in Figure 5(a), the formation rate of CO gradually decreased from 39.5 to 12.2 μmol h^{-1} for 2 h for the $Mg(OH)_2$ cocatalyst. Meanwhile, the evolution of O_2 was close to the stoichiometric amount after 2 h. H_2SiO_3-decorated $ZnTa_2O_6$ underwent a similar trend for the photocatalytic conversion of CO_2 by H_2O, as shown in Figure 5(b), in which the formation rate of CO decreased from 53.0 to 20.6 μmol h^{-1}. The same trend was observed for the evolution of O_2 in H_2SiO_3. Note that the promotion of CO activity using H_2SiO_3 as a cocatalyst was not caused by the presence of chloride ions, even though H_2SiO_3 was derived from the precipitation of Na_2SiO_3 and HCl (chloride ions might be adsorbed on the surface when H_2SiO_3 was decorated on the surface of $ZnTa_2O_6$). To exclude this possibility, the author subsequently injected 200 μmol NaCl *in-situ* into the reaction, and after 2 h, the formation rates of both CO and H_2 were not significantly affected. This indicated that the concentration of chloride ions did not influence the photocatalyst.

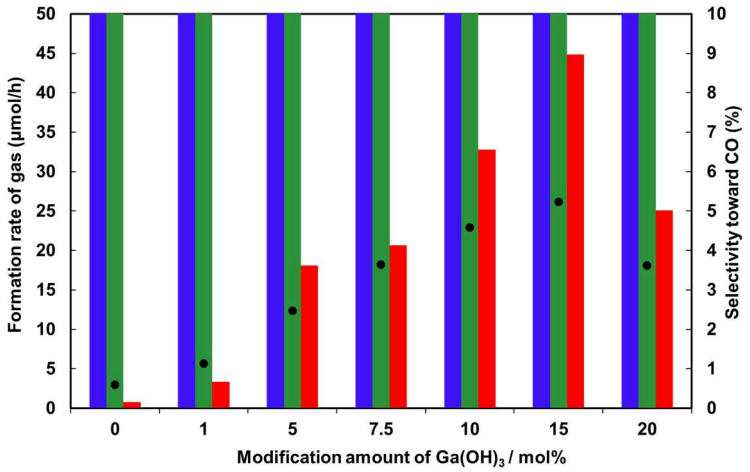

Figure 4. Formation rates of H_2 (blue), O_2 (green), and CO (red) and selectivity toward CO evolution (black dot) for the photocatalytic conversion of CO_2 by H_2O over $Ga(OH)_3$-modified Ga_2O_3. Photoirradiation time: 0.5 h; main photocatalyst: 0.5 g; reaction solution: 1 L of a 0.1 M $NaHCO_3$ aqueous solution; CO_2 flow rate: 30 mL min^{-1}; light source: 400 W high-pressure Hg lamp.

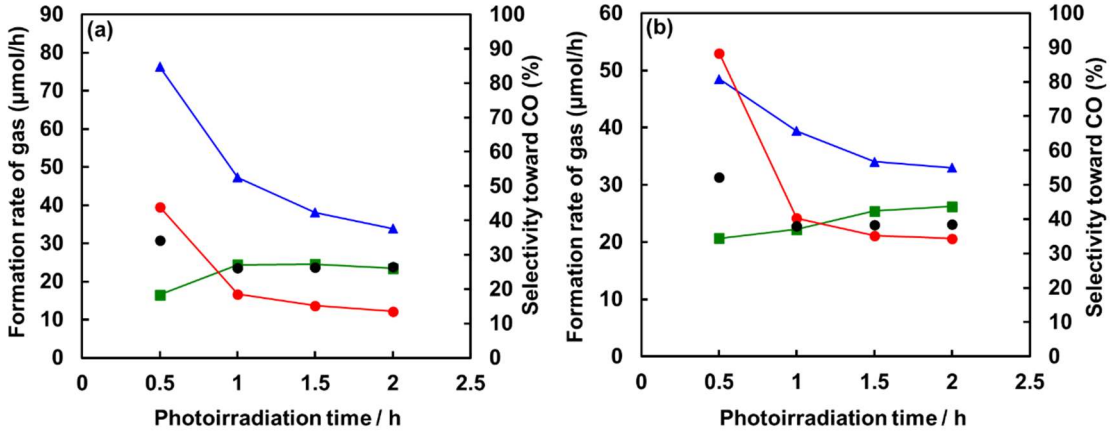

Figure 5. Formation rates of H_2 (blue), O_2 (green), and CO (red) and selectivity toward CO evolution (black dot) in the time courses of CO_2 photoreduction by H_2O over (a) $Mg(OH)_2$ and (b) H_2SiO_3-decorated $ZnTa_2O_6$. Main photocatalyst: 0.5 g; reaction solution: 1 L of a 0.1 M $NaHCO_3$ aqueous solution; CO_2 flow rate: 30 mL min^{-1}; light source: 400 W high-pressure Hg lamp.

3.2. Zn-based non-metal cocatalysts

Based on the discussion in Section 3.1, the author found that the $Zn(OH)_2$ cocatalyst showed considerably better performance for the selective photocatalytic conversion of CO_2 by H_2O than the Ga, Si, and Mg hydroxides. Conversely, the cocatalysts were subjected to counter anions. The author considered the possible synergistic catalytic performances of Zn–Ga, Zn–Si, and Zn–Al and the effect of counter anions on Zn^{2+}. Therefore, the author investigated a series of Zn compounds as cocatalysts on the surface of $ZnTa_2O_6$ using SSR, as summarized in Table 5. $ZnSiO_3$ and $ZnGa_2O_4$ (Entry 2 and 3) showed better performances (98.4 and 79.2 μmol h^{-1}, respectively) than the other 7 kinds

of Zn-based cocatalysts, including $Zn(OH)_2$. This was because the active sites of Ga and Si contributed to the improvement in the formation rate of CO with Zn^{2+} in the compounds $ZnSiO_3$ and $ZnGa_2O_4$. As shown in Table 4, hydroxides containing Ga and Si, such as $Ga(OH)_3$ and H_2SiO_3, also function as good cocatalysts for the photocatalytic conversion of CO_2 by H_2O. Interestingly, the addition of $Zn(NO_3)_3$ resulted in a lower formation rate of CO (entry 9: 22.2 μmol h^{-1}) than other Zn-based cocatalysts, even though H_2 evolution was effectively suppressed. This is probably because the active sites for CO evolution on the surface of $ZnTa_2O_6$ were poisoned by the adsorption of nitrate ions. Figure 6(a) shows the influence of nitrate ions on the CO evolution activity over bare $ZnTa_2O_6$ using the SSR method. The formation rate of CO was 22.2 μmol h^{-1} without the nitrate ions, while the rate was decreased to 12.4 μmol h^{-1} when 60 μmol of $NaNO_3$ was added. As the number of nitrate ions was increased to 90 μmol, the formation rate of CO was decreased to 8.8 μmol h^{-1}. At this concentration, the balance of $\boldsymbol{e^-/h^+}$ decreased to 0.6, indicating that the nitrate ions began to be reduced. To confirm the effect of nitrate ions, the author injected sodium nitrate *in-situ* into the reaction of $Zn(OH)_2$-decorated $ZnTa_2O_6$, as displayed in Figure 6(b), which shows that nitrate ions poisoned the CO production activity.

Table 5. Summarized performances of various Zn-based cocatalysts on $ZnTa_2O_6$ from SSR for the photocatalytic conversion of CO_2 by H_2O.[a]

Entry	Cocat.	Amount of Cocat. (mol %)	Formation rate of products (μmol h^{-1})			Selec. toward CO (%)
			H_2	O_2	CO	
1	none	0	13.6	12.5	11.2	45.2
2	$ZnSiO_3$	10	3.8	42.0	98.4	96.3
3	$ZnGa_2O_4$	10	15.3	38.0	79.2	83.8
4	ZnO	10	8.3	35.0	60.9	88.0
5	$ZnAl_2O_4$	10	14.9	11.6	11.4	43.4
6	$Zn_3(PO_4)_2$	10	2.3	28.3	57.6	96.1
7	$Zn(OH)_2$	10	7.0	39.4	67.6	90.6
8	$Zn(NO_3)_2$	3.7	4.4	17.5	28.0	86.5
9	$Zn(NO_3)_2$	6.8	2.3	21.8	22.2	90.6

[a] Photoirradiation time: 0.5 h; main photocatalyst: 0.5 g; reaction solution: 1 L of a 0.1 M $NaHCO_3$ aqueous solution; CO_2 flow rate: 30 mL min^{-1}; light source: 400 W high-pressure Hg lamp.

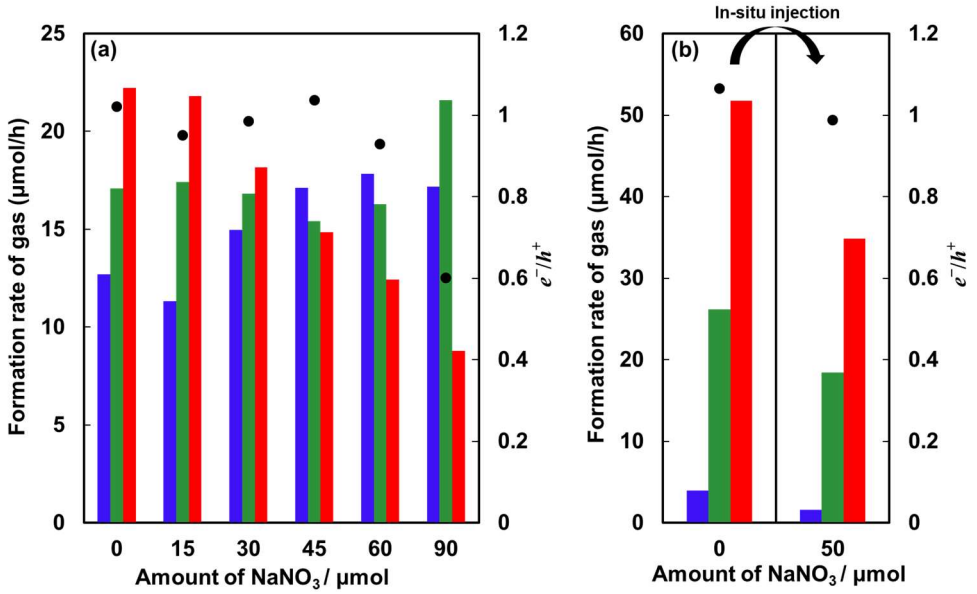

Figure 6. (a) Formation rates of H_2 (blue), O_2 (green), and CO (red) and e^-/h^+ balance (black dot) in the photocatalytic conversion of CO_2 by H_2O over $ZnTa_2O_6$ fabricated by

SSR method with nitrate ions; (b) the influence of *in-situ*-injected nitrate ions on the $Zn(OH)_2$-decorated $ZnTa_2O_6$. Photoirradiation time: 0.5 h; main photocatalyst: 0.5 g; reaction solution: 1 L of a 0.1 M $NaHCO_3$ aqueous solution; CO_2 flow rate: 30 mL min^{-1}; light source: 400 W high-pressure Hg lamp.

The Zn-based cocatalysts showed excellent universality for Ta- and Ga-based photocatalysts, such as $ZnGa_2O_4$ and $NaTaO_3$, in promoting the evolution rate of CO in the photocatalytic conversion of CO_2, as presented in Table 6. However, these cocatalysts had almost no positive influence on the CO production over the Nb-, Ti-, and Zr-based photocatalysts. Contrarily, the counter anions ($(Ga_2O_4)^{2-}$, SiO_3^{2-}, and OH^-) in these Zn compounds had obvious effects on their catalytic stability. For $Zn(OH)_2$-decorated $NaTaO_3$ (Entry 13), the initial $\boldsymbol{e}^-/\boldsymbol{h}^+$ balance in the first 0.5 h was approximately 0.3, indicating that the Zn^{2+} ions were reduced into Zn^0 during the reaction. As the reaction proceeded, the final $\boldsymbol{e}^-/\boldsymbol{h}^+$ balance was maintained at approximately 1.0; however, the selectivity toward CO evolution decreased to 58.9% from 87.7% (Figure 7(a)). The appearance of Zn^0 was visibly confirmed by the color change of the $Zn(OH)_2$-decorated $NaTaO_3$ from white to grey before and after the reaction. The reduction of Zn^{2+} over the surface of $NaTaO_3$ was suppressed when SiO_3^{2-} was used as the counter anion. Figure 7(b) shows that the $\boldsymbol{e}^-/\boldsymbol{h}^+$ balance was always close to 1.0 when $ZnSiO_3$ was used as the cocatalyst on $NaTaO_3$, and the selectivity toward CO evolution was maintained above 90%. When GaO^{2-} was the counter anion, the H_2 evolution in the initial stages of the reactions was slightly increased for $NaTaO_3$ and $ZnGa_2O_4$, and the selectivity toward CO evolution was 69.6% and 63.6%, respectively. The formation rates of H_2 gradually decreased to 9.5 and 15.3 μmol h^{-1} with increased photoirradiation time, as displayed in Figures 8(a) and 8(b), and correspondingly, the selectivity toward CO evolution reached 89.9% and 87.7%, respectively.

Table 6. Summarized performances of amorphous $Zn(OH)_2$, $ZnSiO_3$, and $ZnGa_2O_4$ cocatalysts on various main photocatalysts for the photocatalytic conversion of CO_2 by H_2O.[a]

Entry	Cocat.	Main Cat.	Amount of Cocat. (mol %)	Formation rate of products (μmol h^{-1})			Selec. toward CO (%)
				H_2	O_2	CO	
1	$ZnSiO_3$	$NaTaO_3$	10	5.1	30.3	58.8	92.1
2		$SrTa_2O_6$	10	120.6	108.9	155.2	56.3
3		$SrNb_2O_6$	10	29.1	4.1	2.6	8.1
4		Ga_2O_3	10	618.1	322.0	141.8	18.7
5	$ZnGa_2O_4$	$NaTaO_3$	10	35.0	43.5	80.3	69.6
6		$SrTa_2O_6$	10	1245.0	571.6	98.1	7.3
7		$SrNb_2O_6$	10	8.2	3.7	4.5	35.1
8		$ZnGa_2O_4$	10	70.1	90.4	122.5	63.6
9		Ga_2O_3	10	749.7	439.5	231.5	22.2
10	$Zn(OH)_2$	$SrZrO_3$	10	224.4	90.1	12.7	5.4
11		$CaZrO_3$	10	41.8	7.7	4.9	10.5
12		$CaTiO_3$	10	13.3	7.1	1.9	12.4
13		$NaTaO_3$	10	7.0	81.1	49.5	87.7
14	none	$NaTaO_3$	0	161.5	78.0	8.9	5.2
15		$SrTa_2O_6$	0	767.5	280.3	1.5	0.2
16		$SrNb_2O_6$	0	9.1	4.9	0.6	6.1
17		Ga_2O_3	0	125.1	57.4	0.8	0.6
18		$CaTiO_3$	0	11.4	5.0	1.1	8.8
19		$SrZrO_3$	0	331.8	127.2	17.4	5.0
20		$CaZrO_3$	0	39.0	13.1	4.2	9.7

[a] Photoirradiation time: 0.5 h; main photocatalyst: 0.5 g; reaction solution: 1 L of a 0.1 M $NaHCO_3$ aqueous solution; CO_2 flow rate: 30 mL min^{-1}; light source: 400 W high-pressure Hg lamp.

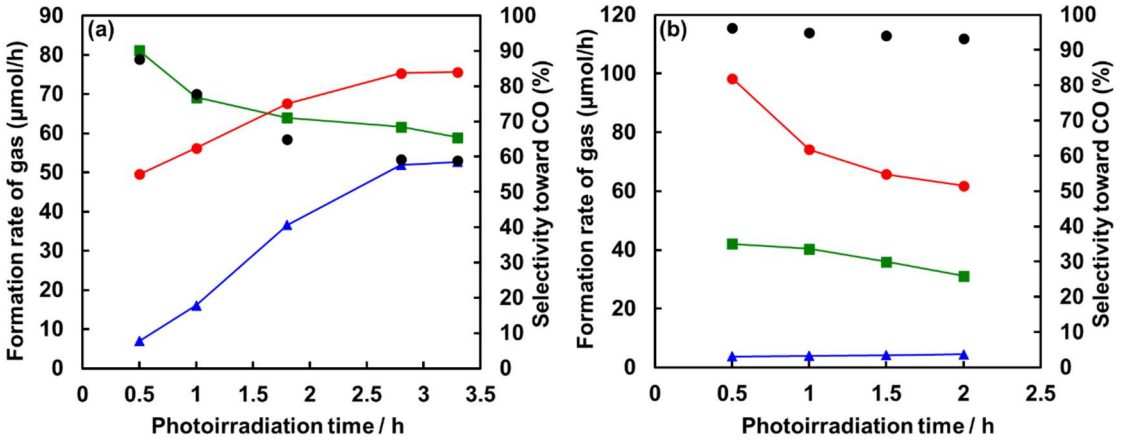

Figure 7. Formation rates of H_2 (blue), O_2 (green), and CO (red) and selectivity toward CO evolution (black dot) in the time course of (a) 10 mol% $Zn(OH)_2/NaTaO_3$ and (b) 10 mol% $ZnSiO_3/NaTaO_3$ for the photocatalytic conversion of CO_2 by H_2O. Main photocatalyst: 0.5 g; reaction solution: 1 L of a 0.1 M $NaHCO_3$ aqueous solution; CO_2 flow rate: 30 mL min^{-1}; light source: 400 W high-pressure Hg lamp.

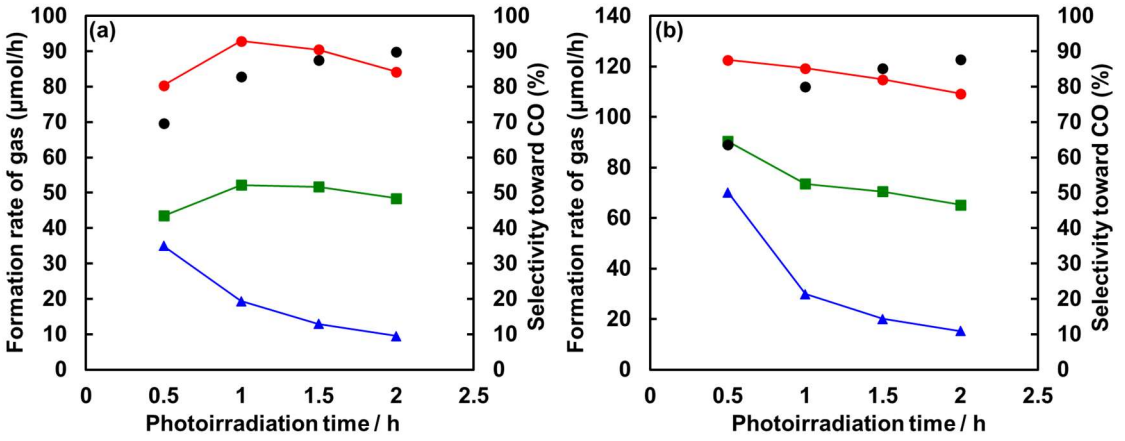

Figure 8. Formation rates of H_2 (blue), O_2 (green), and CO (red) and selectivity toward CO evolution (black dot) in the time course of (a) 10 mol% amorphous $ZnGa_2O_4/NaTaO_3$ and (b) 10 mol% amorphous $ZnGa_2O_4/ZnGa_2O_4$ for the photocatalytic conversion of CO_2 by H_2O. Main photocatalyst: 0.5 g; reaction solution: 1 L of a 0.1 M $NaHCO_3$ aqueous solution; CO_2 flow rate: 30 mL min^{-1}; light source: 400 W high-pressure Hg lamp.

4. Conclusion

The author mapped a series of non-metal cocatalysts and found that Si-, Mg-, Zn-, and Ga-based cocatalysts enhanced the evolution of CO over Ta- and Ga-based photocatalysts. Among them, Zn-based cocatalysts showed the best performance for the photocatalytic conversion of CO_2 using H_2O as an electron donor. The counter anions, such as $(Ga_2O_4)^{2-}$, SiO_3^{2-}, NO_3^-, and PO_4^{3-}, in the Zn-based compounds influenced their catalytic performance in the evolution of CO, both in terms of stability and activity. Conversely, Zn-based cocatalysts showed no effect on Nb- and Ti-based photocatalysts, and the author believes that the reason underlying this phenomenon should be investigated for an enhanced understanding of the mechanisms of the Zn-based cocatalysts.

References

1. Crabtree, G. W.; Lewis, N. S. Physics today 2007, 3, 37-42.
2. Penalonga, L. R.; Soria, B. Y. M. Energies 2017, 10, 1235.
3. Herbert, G. M. J.; Iniyan, S.; Sreevalsan, E; Rajapandian, S. Sustain. Energy Rev. 2007, 11, 1117–1145.
4. Moran, E. F.; Lopez, M. C.; Moore, N.; Müller, N.; Hyndman, D. W. PNAS 2018, 115, 47, 11891-11898.
5. Goldemberg, J. World energy assessment: energy and the challenge of sustainability. (UN. 2001).
6. Hansen, J.; Ruedy, R.; Sato, M.; Lo, K. Rev. Geophys. 2010, 48, 1–29.
7. Hansen, J.; Nazarenko, L.; Ruedy, R.; Sato, M.; Wills, J.; Genio, A. D.; Koch, D.; Lacis, A.; Lo, K.; Menon, S.; Novakov, T.; Perlwitz, J.; Russell, G.; Schmidt, G. A.; Tausnev, N. Science 2005, 308, 1431–1436.
8. Bruton, T. M. Sol. Energy Mater. Sol. Cells 2002, 72, 3–10.
9. Fu, R.; James, T. L.; Woodhouse, M. IEEE Journal of Photovoltaics 2015, 5, 2, 515–524.
10. Wang, Q.; Domen, K. Chem. Rev. 2020, 120, 919–985.
11. Granone, L. I.; Sieland, F.; Zheng, N.; Dillert, R.; Bahnemann, D. W. Green Chem. 2018, 20, 1169-1192.
12. Pang, R.; Teramura, K.; Tanaka, T. Current Developments in Photocatalysis and Photocatalytic Materials 2020, 179–190.
13. Jena, A. K.; Kulkarni, A.; Miyasaka, T. Chem. Rev. 2019, 119, 3036–3103.
14. Nakanishi, H.; Iizuka, K.; Takayama, T.; Iwase, A.; Kudo, A. ChemSusChem 2017, 10, 112–118.
15. Anzai, A.; Fukuo, N.; Yamamoto A.; Yoshida, H. Catalysis communications 2017, 100, 134–138.
16. Wang, S. Y.; Teramura, K.; Hisatomi, T.; Domen, K.; Asakura, H.; Hosokawa, S.; Tanaka, T. Chem. Sci. 2021, 12, 4940-4948.

17. Yamamoto, M.; Yoshida, T.; Yamamoto, N.; Yoshida, H.; Yagi, S. e-J. Surf. Sci. Nanotech. 2014, 12, 299-303.
18. Wang, Z.; Teramura, K.; Hosokawa, S.; Tanaka, T. J. Mater. Chem. A. 2015, 3, 11313–11319.
19. Pang, R.; Teramura, K.; Asakura, H.; Hosokawa, S.; Tanaka, T. Applied Catalysis B: Environmental 2017, 218, 770–778.
20. Rosen, J.; Hutchings, G. S.; Lu, Q.; Forest, R. V.; Moore, A.; Jiao, F. ACS Catal. 2015, 5, 4586-4591.
21. Verma, S.; Hamasaki, Y.; Kim, C.; Huang, W.; Lu, S.; Jhong, H. R. M.; Gewirth, A. A.; Fujigaya, T.; Nakashima, N.; Kenis, P. J. A. ACS Energy Lett. 2018, 3,193-198.
22. Cao, L.; Raciti, D.; Li, C.; Livi, K. J. T.; Rottmann, P. F.; Hemker, K. J.; Mueller T.; Wang, C. ACS Catal. 2017, 7, 8578-8587.
23. Hsieh, Y. C.; Senanayake, S. D.; Zhang, Y.; Xu W. Q.; Polyansky. D. E. ACS Catal. 2015, 5, 5349-5356.
24. Iguchi, S.; Teramura, K.; Hosokawa, S.; Tanaka, T. Catal. Sci. Technol. 2016, 6, 4978–4985.
25. Pang, R.; Teramura, K.; Asakura, H.; Hosokawa, S.; Tanaka, T. ACS Sustainable Chem. Eng. 2019, 7, 2083-2090.
26. Zhu, X.; Yamamoto, A.; Imai, S.; Tanaka, A.; Kominami, H.; Yoshida, H. Chem. Commun. 2019, 55, 13514-13517.
27. Xu, X. W.; Teramura, K.; Asakura, H.; Hosokawa, S.; Tanaka, T. Applied Catalysis B: Environmental 2021, 298, 120508.
28. Xu, X. W.; Teramura, K.; Asakura, H.; Hosokawa, S.; Tanaka, T. doi: 10.1002/cctc.202100633.

Chapter 5

Cadmium hydroxide universal cocatalyst for the selective evolution of CO during the photocatalytic conversion of CO_2 using H_2O as an electron donor

Abstract

In this study, cadmium hydroxide ($Cd(OH)_2$) was utilized as an excellent cocatalyst for the selective evolution of CO in the photocatalytic conversion of CO_2 using H_2O as an electron donor. After modifying the $ZnTa_2O_6$ photocatalyst fabricated by an optimized solid-state reaction method with the $Cd(OH)_2$ cocatalyst, the selectivity toward CO evolution relative to H_2 exceeded 95%. The catalytic performance of Cd^{2+} species strongly depended on the type of counter anions that were able to effectively accept photogenerated electrons, such as nitrate ions. Furthermore, $Cd(OH)_2$ was universally applicable for various photocatalysts, including Ga_2O_3, $ZnGa_2O_4$, $NaTaO_3$, and Ta_2O_5. Its main role was to selectively suppress the backward reduction of evolved O_2 gas at the catalytically active sites for CO formation.

1. Introduction

Owing to the advances in science and technology throughout the human history, people have moved from the agricultural age to the industrial and informational ages over the past 200 years. However, this process has been accompanied by the significant consumption of fossil fuels, which emits large amounts of carbon dioxide (CO_2) [1] causing serious problems for the mankind, such as the global warming [2] and shortage of energy [3]. Although new energy sources, including nuclear energy [4] and wind power [5], have been developed as viable alternatives to fossil fuels, they considerably damage the environment [5,6]. Solar energy [7] represents the best option because it is sustainable and environmentally friendly. The photocatalytic conversion of CO_2 [8] using water (H_2O) as an electron donor involves artificial photosynthesis, which utilizes solar energy to drive the chemical conversion of CO_2 to useful compounds such as CO, CH_4, and CH_3OH. The successful photocatalytic conversion of CO_2 by H_2O must satisfy two criteria described by equations (1) and (2). Here, ***R*** is the formation rate of each product generated by the photocatalytic conversion of CO_2 by H_2O.

$$e^-/h^+ = (2R_{HCOOH} + 2R_{CO} + 4R_{HCHO} + 6R_{CH_3OH} + 8R_{CH_4} + 2R_{H_2})/4R_{O_2} \quad (1)$$

$$\text{Selectivity} = (2R_{HCOOH} + 2R_{CO} + 4R_{HCHO} + 6R_{CH_3OH} + 8R_{CH_4})/(2R_{HCOOH} + 2R_{CO} + 4R_{HCHO} + 6R_{CH_3OH} + 8R_{CH_4} + 2R_{H_2}) \times 100\% \quad (2)$$

A balance close to 1.0 between the electrons consumed by the reduction of CO_2 and holes consumed by the oxidation of H_2O indicates that the electrons in this process originate from H_2O rather than sacrificial reagents such as carbon impurities. Meanwhile, achieving high selectivity toward the formation of specific carbon compounds (such as CO) is also very important because the separation of gases is an expensive process.

It is not easy to obtain high selectivity toward CO evolution for the photocatalytic conversion of CO_2 by H_2O because H_2O splitting is a strong competitive reaction to the reduction of CO_2, which requires a much lower redox potential. Kudo et al. found that Ag nanoparticles were able to produce more CO than H_2 over $BaLa_4TiO_{15}$ [8]. Recently, their

research group has achieved higher selectivity (90%) and activity for CO evolution over alkaline earth metal-doped $NaTaO_3$ [9]. Ag nanoparticles utilized as a cocatalyst for the selective photocatalytic conversion of CO_2 by H_2O were universally applicable for various photocatalysts, including $ZnGa_2O_4$ [10], $CaTiO_3$ [11], $SrNb_2O_6$ [11], Al-doped $SrTiO_3$ [12], and $ZnTa_2O_6$ (ZTO) [13]. Other metal materials such as Cu [14], Zn [15] , and Au [16] treated by certain methods favored the selective formation of CO during the electrochemical reduction of CO_2. However, they failed to achieve the same performance for the photocatalytic conversion of CO_2 by H_2O, as shown in the previous work [17]. For a long time, researchers have not been able to reach high selectivity toward CO evolution without Ag nanoparticles used as a cocatalyst in the photocatalytic conversion of CO_2 by H_2O.

The author believes that the mechanism of the selective CO_2 reduction competing with water splitting involves a variety of comparable processes. This prevents researchers from elucidating it because the Ag cocatalyst alone cannot provide many comparable cases. Recently, Wang et al. has found that ZnO/ZTO [18] fabricated at high temperature exhibits a selectivity of approximately 80% toward CO evolution without using Ag nanoparticles as a cocatalyst during the photocatalytic conversion of CO_2 by H_2O. This discovery motivated the author to consider the fact that some non-metal cocatalysts also possessed high selectivity toward CO evolution. By exploring various nonmetal cocatalysts, it can be possible to determine the main factors affecting their CO_2 conversion selectivity. In the subsequent studies, the author found that the in situ addition of chromate ions to ZTO promoted CO formation over H_2 evolution during the photocatalytic conversion of CO_2 by H_2O, which significantly increased the CO selectivity from 5 to 80% [19]. Recently, the author reported the successful use of $Zn(OH)_2$ [20] as a universal co-catalyst for the highly selective formation of CO over various Ta-based and Ga-based photocatalysts. To the best knowledges of the author, it was the first study, in which the $Zn(OH)_2$ cocatalyst was found to be universally applicable for the photocatalytic conversion of CO_2 by H_2O (similar to Ag nanoparticles). In this work, the

author utilized the $Cd(OH)_2$ cocatalyst for the selective photocatalytic conversion of CO_2 by H_2O on various photocatalysts, including $NaTaO_3$, $ZnGa_2O_6$, Ta_2O_5, and ZTO.

2. Experimental section

2.1. Preparation of photocatalysts

The reagents used in this study for the syntheses of photocatalysts are listed in Table 1. ZTO was prepared by the solid-state reaction of ZnO with Ta_2O_5 at 1423 K for 36 h. The detailed synthesis conditions for the other photocatalysts are specified in Table 2. $Cd(OH)_2$ was modified onto photocatalysts by precipitation method.

Table 1. Reagents used in this work.

Reagent	Company	Purity
$Cd(NO_3)_2 \cdot 4H_2O$	Sigma-Aldrich	99.0%
$CdCl_2 \cdot 2.5H_2O$	Wako	98.0%
$3CdSO_4 \cdot 8H_2O$	Wako	99.9%
HCl	Wako	0.1 M

Table 2. Synthesis conditions of photocatalysts used in this work.

Photocatalyst	Precursors	Pre-treatment	Conditions	Post-treatment
$ZnTa_2O_6$	$ZnO + Ta_2O_5$	Physical mixture	1273-1423 K, 3-99 h	
$SrTa_2O_6$	$SrCO_3 + Ta_2O_5$	Physical mixture	1423 K, 24 h	
Commercial Ga_2O_3	Commercial			
$NaGaO_2$	Commercial Ga_2O_3 + NaOH	Physical mixture	1173 K, 12 h	
$NaTaO_3$	$Na_2CO_3 + Ta_2O_5$	Physical mixture	1423 K, 20 h	
α-Ga_2O_3	$NaGaO_2$ + HCl	Suspension	Room Temperature	723 K for 3h
β-Ga_2O_3	Commercial Ga_2O_3		1423 K, 24 h	
Ta_2O_5	Commercial			
$Ta_2O_5/ZnTa_2O_6$	0.7 ZnO + Ta_2O_5	Physical mixture	1423 K, 36 h	
$ZnGa_2O_4$	$ZnO + Ga_2O_3$	Physical mixture	1173-1423 K, 9-36 h	

2.2. Characterization of photocatalysts

X-ray diffraction (XRD) patterns of the photocatalysts were recorded using a Rigaku

Ultima IV powder diffractometer (Cu Kα, 40 kV, and 40 mA). The XRD patterns of synthesized photocatalysts are presented in Figure 1.

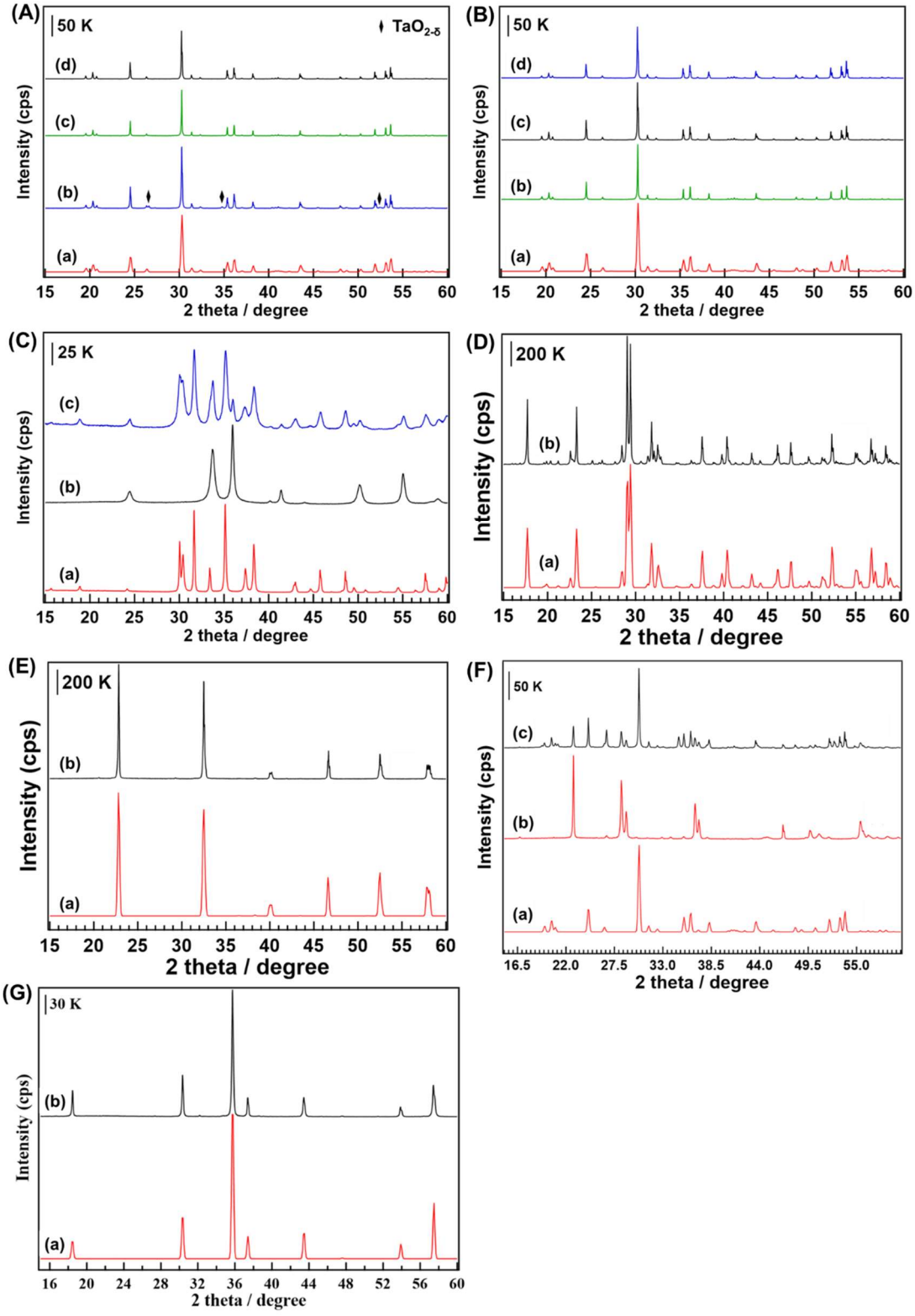

Figure 1. XRD patterns of (A) Synthesized $ZnTa_2O_6$ under controlled calcination temperature for 36 h. (a) reference from ICSD database, (b) 1273 K, (c) 1373 K and (d) 1423 K. (B) Synthesized $ZnTa_2O_6$ with controlled calcination time at 1423 K. (a) reference from ICSD database, (b) 3 h, (c) 36 h and (d) 99 h. (C) Synthesized (a) β-Ga_2O_3, (b) α-Ga_2O_3 and (c) commercial Ga_2O_3. (D) $SrTa_2O_6$ (a) reference from ICSD data and (b) synthesized $SrTa_2O_6$. (E) $NaTaO_3$ (a) reference from ICSD data and (b) synthesized $NaTaO_3$. (F) $ZnTa_2O_6$ reference from ICSD data, (b) commercial Ta_2O_5 and (c) synthesized $Ta_2O_5/ZnTa_2O_6$. (G) $ZnGa_2O_4$ reference from ICSD data and (b) synthesized $ZnGa_2O_4$ at 1273 K for 12h.

2.3. Reaction parameters

The photocatalytic conversion of CO_2 by H_2O was conducted in an inner irradiation reactor equipped with a quartz jacket connected to a cooling system. The reaction temperature was varied between 298 and 303 K. A 400-W high-pressure mercury lamp (Sen Lights Corp.) served a light source. Before photoirradiation, the system was purged with CO_2 to remove residual air. The products, including H_2, O_2, and CO, were detected using GC-8A (Shimadzu Corp) gas chromatographs equipped with TCD and FID detectors.

3. Results and Discussion

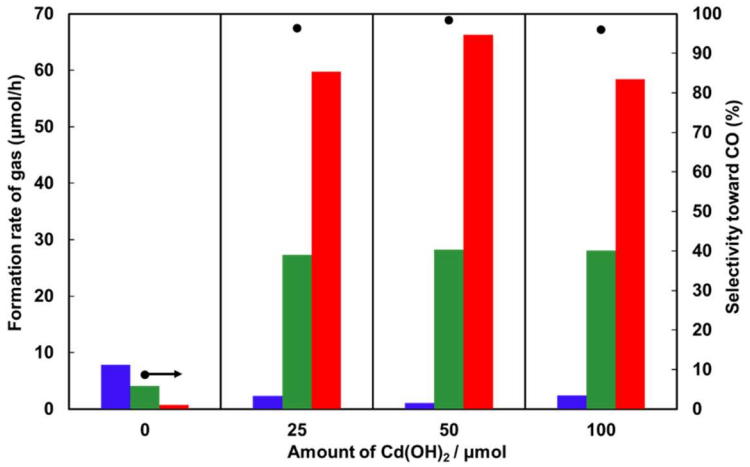

Figure 2. Formation rates of H_2 (blue), O_2 (green), and CO (red) gases and selectivities

toward CO evolution (black dots) determined for the photocatalytic conversion of CO_2 by H_2O over ZTO modified by various amounts of $Cd(OH)_2$. Photoirradiation time: 0.5 h, ZTO amount: 0.5 g, reaction solution: 1.0 L of a 0.1 M $NaHCO_3$ aqueous solution, CO_2 flow rate: 30 mL min^{-1}, light source: 400-W high-pressure Hg lamp.

Figure 1(A) shows the XRD pattern of the fabricated ZTO with a reference spectrum. The ZTO sample synthesized at 1423 K for 36 h consisted of the pure ZTO phase, indicating that the high calcination temperature completely removed $TaO_{2-\delta}$ impurities as compared with the samples synthesized at 1273 K in a previous study [19]. The bare ZTO sample produced H_2 at a rate of 7.8 μmol h^{-1}, while the formation rate of CO during the photocatalytic conversion of CO_2 by H_2O was only 0.75 μmol h^{-1} (Figure 2). By adding 25 μmol of the $Cd(OH)_2$ cocatalyst, the selectivity toward CO evolution was significantly increased from 8.7% to 96.3%; the formation rate of CO decreased to 59.8 μmol h^{-1}; and the formation rate of H_2 was reduced to 2.3 μmol h^{-1}. After increasing the $Cd(OH)_2$ amount to 50 μmol, the CO formation rate slightly increased to 66.3 μmol h^{-1} while that of H_2 decreased to 1.0 μmol h^{-1}. The higher $Cd(OH)_2$ amount of 100 μmol had a negative effect on the formation rate of CO (58.4 μmol h^{-1}). The chemical states of Cd^0, Cd^+, and Cd^{2+} species could not be determined from their binding energies due to undistinguishable differences. As a result, it was difficult to directly identify the actual form of the active cadmium species. However, the author inferred that Cd^{2+} ions were not reduced and likely acted as the active species because the electron–hole balance ($\boldsymbol{e^-}/\boldsymbol{h^+}$) during the reaction remained very close to 1.0. From these results, it was concluded that Cd^{2+} exhibited excellent catalytic performance for the selective evolution of CO during the photocatalytic conversion of CO_2 by H_2O over ZTO.

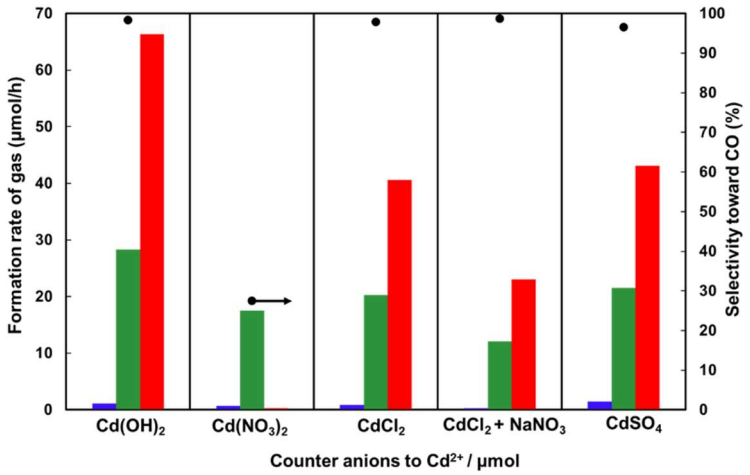

Figure 3. Formation rates of H_2 (blue), O_2 (green), and CO (red) gases and selectivities toward CO evolution (black dots) determined for the photocatalytic conversion of CO_2 by H_2O over ZTO with various Cd^{2+} species. Cd^{2+} amount: 50 μmol, $NaNO_3$ amount: 30 μmol, photoirradiation time: 0.5 h, ZTO amount: 0.5 g, reaction solution: 1.0 L of a 0.1 M $NaHCO_3$ aqueous solution, CO_2 flow rate: 30 mL min^{-1}, light source: 400-W high-pressure Hg lamp.

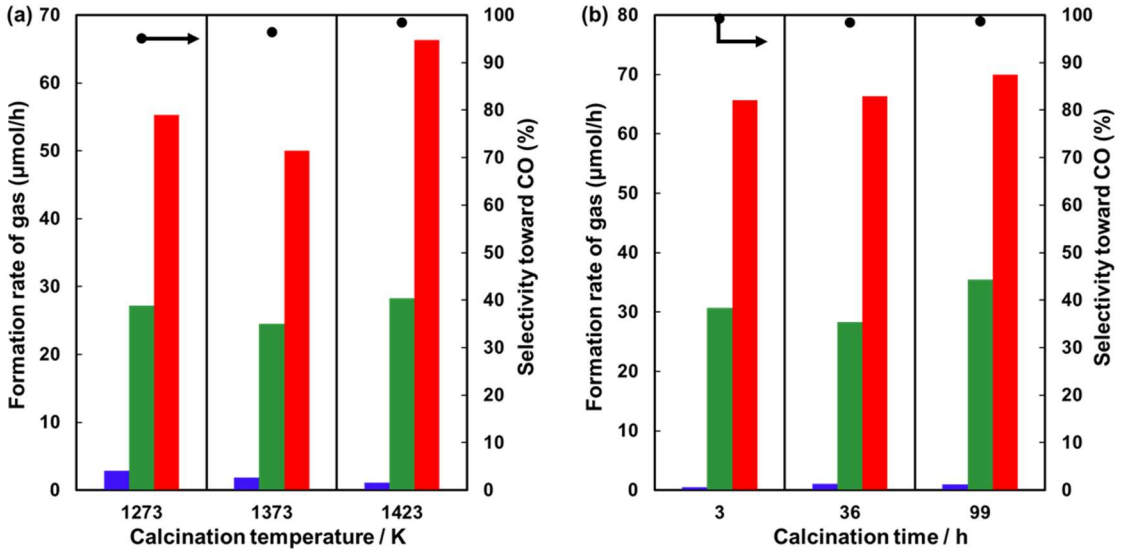

Figure 4. Formation rates of H_2 (blue), O_2 (green), and CO (red) gases and selectivities toward CO evolution (black dot) determined for the photocatalytic conversion of CO_2 by H_2O over ZTO. The optimal calcination (a) temperature and (b) time for ZTO fabrication are equal to 36 h and 1423 K, respectively. $Cd(OH)_2$ amount: 50 μmol, photoirradiation

time: 0.5 h, ZTO amount: 0.5 g, reaction solution: 1.0 L of a 0.1 M $NaHCO_3$ aqueous solution, CO_2 flow rate: 30 mL min^{-1}, light source: 400-W high-pressure Hg lamp.

Table 3. Formation rates of H_2, O_2 and CO and e^-/h^+ balance in the photocatalytic conversion of CO_2 by H_2O over $ZnTa_2O_6$ fabricated by SSR method in the presence of $NaNO_3$.

Entry	$NaNO_3$ (μmol)	Formation rate of products (μmol h^{-1})			e^-/h^+
		H_2	O_2	CO	
1	0	12.7	17.1	22.2	1.02
2	15	11.3	17.4	21.8	0.95
3	30	15.0	16.8	18.2	0.99
4	45	17.1	15.4	14.9	1.04
5	60	17.8	16.3	12.4	0.93
6	90	17.2	21.6	8.8	0.60

Figure 3 shows that the catalytic performance of Cd^{2+} ions strongly depend on the composition of the counter anions. Only 0.3 μmol h^{-1} of CO was produced during the reaction conducted using the $Cd(NO_3)_2$ cocatalyst. Although the selectivity toward CO evolution increased from 8.7% to 27.5% due to the almost complete suppression of the H_2 production (0.7 μmol h^{-1}), $Cd(NO_3)_2$ was not a preferred cocatalyst. Meanwhile, O_2 gas was produced at a nonstoichiometric rate (17.5 μmol h^{-1}) with respect to the amounts of CO and H_2 gases (e^-/h^+: 0.03) in the presence of nitrate ions. This indicates that nitrate ions strongly occupied and poisoned the reductive sites for the evolution of CO on the photocatalyst surface. In the case of $CdCl_2$, the photocatalyst could still produce CO as the main product (40.6 μmol h^{-1}) with a selectivity of 97.9%. Moreover, a stoichiometric

amount of O_2 evolved with respect to the amounts of CO and H_2 ($e^-/h^+ = 1.03$), indicating that chloride ions did not provide electrons as a sacrificial reagent. The formation rate of CO was lower than that of $Cd(OH)_2$ because chloride ions strongly adsorbed on Cd^{2+} species, which negatively affected the catalytic performance. To confirm the negative influence of nitrate ions, the author added a mixture of $CdCl_2$ and $NaNO_3$ to the reaction system. As expected, the formation rate of CO decreased to 23.1 μmol h^{-1}. Note that a stoichiometric amount of O_2 evolved in the presence of 30.0 μmol $NaNO_3$ was still observed against the amounts of CO and H_2 because the low concentration of nitrate ions was difficult to reduce due to the high overpotential of reduction (Table 3). This phenomenon confirmed that nitrate ions poisoned the reductive sites for CO evolution instead of reacting with photogenerated electrons during CO_2 conversion. The addition of $CdSO_4$ produced CO at a rate 43.1 μmol h^{-1} with a selectivity of 96.6%. The comparable results presented in Figure 3 imply that electron-inert counter anions (which cannot be reduced by photogenerated electrons) are critical to the high catalytic performance of Cd^{2+} ions for CO evolution. Figure 4 shows the formation rates of various products and selectivity values toward CO evolution obtained for the photocatalytic conversion of CO_2 by H_2O over the $Cd(OH)_2$-modified ZTO photocatalysts fabricated at various temperatures and calcination times. Figure 4(a) indicates that ZTO modified with $Cd(OH)_2$ exhibits a CO formation rate of 66.3 μmol h^{-1} at a calcination temperature of 1423 K, which was slightly higher than those obtained at 1273 K (55.3 μmol h^{-1}) and 1373 K (50.0 μmol h^{-1}). However, the formation rates of CO remained almost the same (65.6–69.9 μmol h^{-1}) for the ZTO samples fabricated at different calcination times and the same temperature of 1423 K (Figure 4(b)). By comparing the XRD patterns of the ZTO samples manufactured at different calcination times and temperatures, it was found that the $TaO_{2-\delta}$ impurity phases with the characteristic peaks located at 26.6°, 34.7°, 38.0°, and 52.5° were formed at a low calcination temperature of 1273 K (Figure 1(A)). These impurity phases were not detected in the ZTO samples fabricated at 1423 K (Figure 1(B)) despite the short calcination time of 3 h. The impurities on the ZTO surface produced a

negative influence on the CO evolution activity.

In this work, the author failed to obtain comparable results for the $Cd(OH)_2$-modified ZTO samples fabricated under controlled conditions for the photocatalytic conversion of CO_2 by H_2O. Therefore, it was very difficult to determine the effect of the $Cd(OH)_2$ cocatalyst on the selective evolution of CO. To solve this problem, the author investigated a series of photocatalysts including Ga_2O_3, $ZnGa_2O_4$, and $NaTaO_3$ combined with the $Cd(OH)_2$ cocatalyst (Table 4). The addition of $Cd(OH)_2$ to the commercial Ga_2O_3 catalyst (entries 1 and 2) did not suppress the evolution of H_2 (125.0 vs. 130.7 μmol h^{-1}), which was different from its effect on the homemade α-Ga_2O_3 and β-Ga_2O_3 catalysts (entries 3–7). In particular, the influence of $Cd(OH)_2$ on the CO evolution over commercial Ga_2O_3 was much stronger (by 54 times, from 0.8 to 43.5 μmol h^{-1}) than those over α- Ga_2O_3 and β-Ga_2O_3 (by 2.5 and 8.1 times, respectively). Note that α- Ga_2O_3 [21] and β-Ga_2O_3 [22] possess opposite zeta potentials. However, the formation rates of CO over the two samples modified with the same amount of $Cd(OH)_2$ were very close, which indicated that zeta potential was not a critical parameter affecting the $Cd(OH)_2$ catalytic activity. This conclusion was confirmed by varying the concentration of $NaHCO_3$ used for the photocatalytic conversion of CO_2 by H_2O over β-Ga_2O_3 from 0.1 (pH = 6.80) to 1.0 (pH = 7.60) M. The obtained results revealed that the CO formation rate over β-Ga_2O_3 modified with $Cd(OH)_2$ did not depend on the pH value. Similarly, the evolution of CO over $SrTa_2O_6$ was also enhanced by $Cd(OH)_2$ addition (from 5.5 to 15.3 μmol h^{-1}); however, the evolution of H_2 was effectively suppressed, which resulted in low selectivity. Meanwhile, $ZnGa_2O_4$ produced H_2 at a relatively low rate of 28.2 μmol h^{-1} (entries 10 and 11), and the formation rate of CO considerably increased from 19.1 to 56.2 μmol h^{-1} by the presence of $Cd(OH)_2$. As a result, the selectivity toward CO evolution over $Cd(OH)_2$-modified $ZnGa_2O_4$ increased from 40.4% to 83.2%. Similar results were obtained for $NaTaO_3$ (entries 13 and 14, from 0.6% to 91.3%), Ta_2O_5 (entries 15 and 16, from 2.6% to 67.0%), and $Ta_2O_5/ZnTa_2O_6$ (entries 17 and 18, from 46.0% to 91.5%).

Bare $ZnGa_2O_4$ produced considerable amounts of CO and H_2, and $Cd(OH)_2$

noticeably enhanced its catalytic performance. Therefore, this catalyst was selected to elucidate the mechanism, by which $Cd(OH)_2$ promoted the photocatalytic conversion of CO_2 by H_2O. Figure 5 shows that the formation rates of CO and H_2 drastically decreased to 2.4 and 0.0 μmol h^{-1}, respectively, after the introduction of O_2 into the feed gases (cycles 1 and 2). This indicates that an O_2 reduction reaction (ORR) occurred strongly at the catalytically active sites for CO and H_2 evolution. Interestingly, the formation rate of CO was selectively recovered to 17.7 μmol h^{-1} after the in situ addition of 50 μmol $CdSO_4$, whereas that of H_2 remained at a low level of 1.8 μmol h^{-1}. Furthermore, the amount of O_2 was not recorded in cycles 2 and 3, which suggested that the active sites for CO evolution were selectively protected by the Cd^{2+} species adsorbed on the $ZnGa_2O_4$ surface. Thus, $Cd(OH)_2$ mainly suppresses the ORR, which competes with the evolution of CO during the photocatalytic conversion of CO_2 by H_2O. In previous work [20], the author found that $Zn(OH)_2$ acted as an effective cocatalyst for the selective evolution of CO in the photocatalytic conversion of CO_2 by H_2O, and that the dissolved Zn^{2+} species strongly influenced its performance. Therefore, the author added 50 μmol $ZnSO_4$ to the reaction mixture in cycle 3. The obtained results revealed that the ORR could not be suppressed in the presence of $ZnSO_4$ (Figure 6). However, it was also found that the dissolved Cd^{2+} ions almost did not affect the catalytic performance of $Cd(OH)_2$ (Figure 7). Hence, the photocatalytic conversion mechanism of CO_2 by H_2O in the presence of Cd^{2+} was different from that of the reaction occurred in the presence of Zn^{2+}. Initially, the author anticipated that the adsorption of Cd^{2+} on the photocatalyst surface would produce positive charges (see Scheme 1). As a result, an alkaline electrical double layer consisting of hydroxide, bicarbonate, and carbonate anions was generated to suppress the evolution of H_2 during the photocatalytic conversion of CO_2 by H_2O (Table 4).

Table 4. Formation rates of H_2, O_2, and CO gases and selectivities toward CO evolution determined for the photocatalytic conversion of CO_2 by H_2O over various photocatalysts modified with the $Cd(OH)_2$ cocatalyst. [a]

Entry	Photocatalyst	$Cd(OH)_2$ (μmol)	Additives (mol L^{-1})	Formation rate of products (μmol h^{-1})			Selec. Toward CO (%)
				H_2	O_2	CO	
1	Commercial Ga_2O_3	0	0.1	125.0	57.5	0.8	0.6
2		100	0.1	130.7	82.6	43.5	25.0
3	α-Ga_2O_3	0	0.1	319.7	151.2	5.7	1.7
4		50	0.1	168.7	74.4	14.1	7.7
5	β-Ga_2O_3	0	0.1	263.4	124.7	3.1	1.1
6		50	0.1	153.9	88.2	25.0	14.0
7		50	1.0	151.2	90.0	24.8	14.1
8	$SrTa_2O_6$	0	0.1	927.6	365.7	5.5	0.6
9		100	0.1	437.6	215.0	15.3	3.4
10	$ZnGa_2O_4$	0	0.1	28.2	23.0	19.1	40.4
11		50	0.1	11.3	30.6	56.2	83.2
12	$NaTaO_3$	0	0.1	156.0	57.4	0.8	0.6
13		50	0.1	3.1	16.9	32.3	91.3
14	Ta_2O_5	0	0.1	40.6	20.4	1.1	2.6
15		100	0.1	8.5	13.9	17.3	67.0
16	$Ta_2O_5/ZnTa_2O_6$	0	0.1	6.3	5.5	5.4	46.0
17		100	0.1	5.6	33.2	60.5	91.5

[a] $Cd(OH)_2$ amount: 50 μmol, photoirradiation time: 0.5 h; photocatalyst amount: 0.5 g; reaction solution: 1.0 L of a 0.1 M $NaHCO_3$ aqueous solution, CO_2 flow rate: 30 mL min^{-1}, light source: 400-W high-pressure Hg lamp.

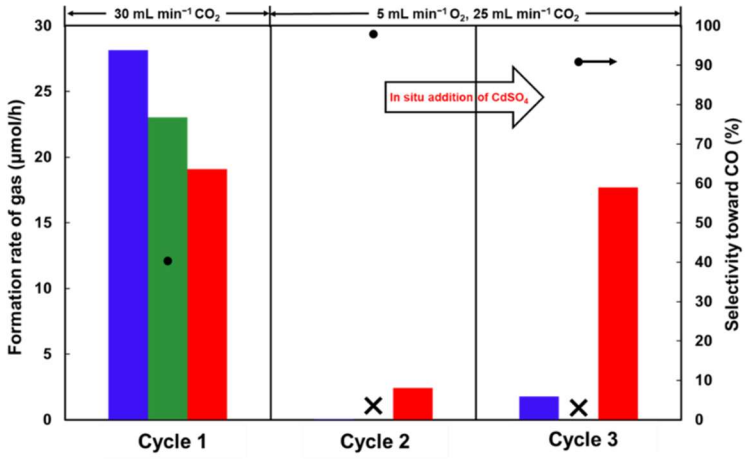

Figure 5. Formation rates of H_2 (blue), O_2 (green), and CO (red) gases and selectivities

toward CO evolution (black dots) determined for the photocatalytic conversion of CO_2 by H_2O over bare $ZnGa_2O_4$ under controlled reaction conditions. Cycle 1: 30 mL min^{-1} CO_2; cycle 2: 5 mL min^{-1} O_2 and 25 mL min^{-1} CO_2; cycle 3: 5 mL min^{-1} O_2, 25 mL min^{-1} CO_2, and 50 μmol $CdSO_4$. Photoirradiation time: 0.5 h for each cycle, $ZnGa_2O_4$ amount: 0.5 g, reaction solution: 1.0 L of a 0.1 M $NaHCO_3$ aqueous solution, light source: 400-W high-pressure Hg lamp.

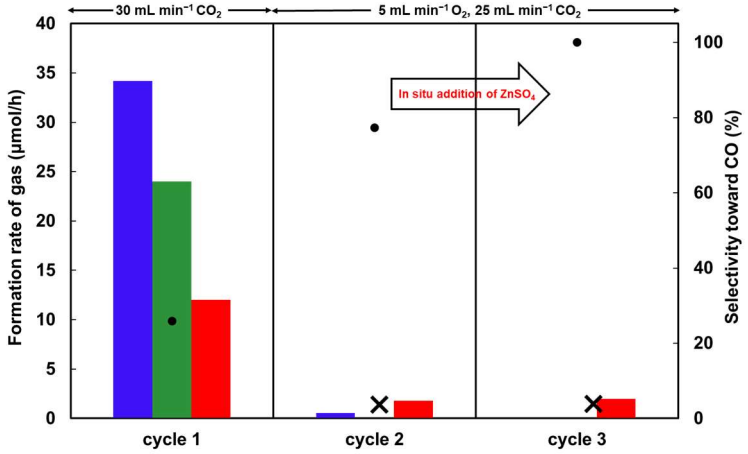

Figure 6. Formation rates of H_2 (blue), O_2 (green), and CO (red) and selectivity toward CO evolution (black dot) for the photocatalytic conversion of CO_2 by H_2O over bare $ZnGa_2O_4$ under controlled reaction conditions. Cycle 1: CO_2 30 mL min^{-1}; cycle 2: O_2 5 mL min^{-1}, CO_2 25 mL min^{-1}; cycle 3: O_2 5 mL min^{-1}, CO_2 25 mL min^{-1} and 50 μmol $ZnSO_4$. Photoirradiation time: 0.5 h for each cycle; amount of $ZnGa_2O_4$: 0.5 g; reaction solution: 1.0 L of a 0.1 M $NaHCO_3$ aqueous solution; light source: 400 W high-pressure Hg lamp.

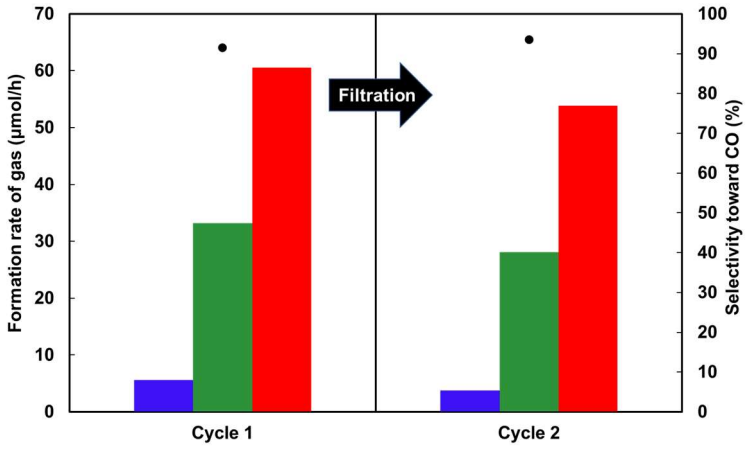

Figure 7. Formation rates of H_2 (blue), O_2 (green), and CO (red) and selectivity toward CO evolution (black dot) for the photocatalytic conversion of CO_2 by H_2O in Cycle 1: 0.5 g $Ta_2O_5/ZnTa_2O_6$ and 100 μmol $Cd(OH)_2$ and Cycle 2: the photocatalysts reacted in Cycle 1 were collected by filtration and then used in Cycle 2 directly. Photoirradiation time: 0.5 h for each cycle; CO_2 30 mL min^{-1}; reaction solution: 1.0 L of a 0.1 M $NaHCO_3$ aqueous solution; light source: 400 W high-pressure Hg lamp.

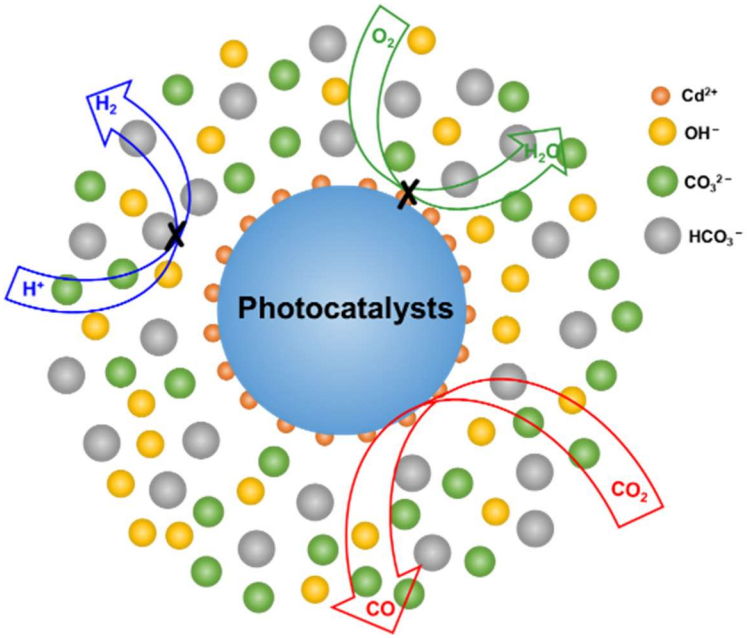

Scheme 1. Proposed mechanism of the suppression of H_2 evolution and enhancement of CO evolution by Cd^{2+} ions during the photocatalytic conversion of CO_2 by H_2O.

4. Conclusion

In this study, $Cd(OH)_2$ exhibited excellent catalytic performance during the selective photocatalytic conversion of CO_2 into CO using H_2O as an electron donor. By utilizing the $ZnTa_2O_6$ photocatalyst fabricated by a solid-state reaction, $Cd(OH)_2$ produced CO at a rate of 66.3 μmol h^{-1} and selectivity of 98.4%. The performance of the Cd^{2+} co-catalyst was significantly affected by the type of the counter anions. In particular, reducible counter anions, such as nitrate ions, significantly decreased the catalytic activity of Cd^{2+}, whereas hydroxide, chloride, and sulfate ions increased it. Furthermore, Cd^{2+} ions effectively protected the catalytically active sites, generating CO as a product of O_2 poisoning during the reaction. Finally, $Cd(OH)_2$ was universally applicable for various photocatalysts, such as Ga_2O_3, $NaTaO_3$, Ta_2O_5, and $ZnGa_2O_4$.

References

1. C. Oertel, J. Matschullat, K. Zurba, F. Zimmermann and S. Erasmi. Chemie der Erde 2016, 76, 327–352.
2. W. D. Nordhaus. American Economic Review 2006, 96, 2, 31-34.
3. T. R. Ayodele and J. L. Munda. Int. J. Hydrogen Energy 2019, 44, 17669–17687.
4. M. V. Ramana. Energy and Environment 2018, 7, 4, e289.
5. S. A. Calero. J. Polit. Ecol. 2017, 24, 992–1012.
6. B. A. Thayer. Security Studies 2008, 3, 428–493.
7. D. M. Gates. Science 1966, 151, 523–529.
8. K. Iizuka, T. Wato, Y. Miseki, K. Saito and A. Kudo. J. Am. Chem. Soc. 2011, 133, 20863–20868.
9. H. Nakanishi, K. Iizuka, T. Takayama, A. Iwase and A. Kudo. ChemSusChem 2017, 10, 112–118.
10. Z. Wang, K. Teramura, S. Hosokawa and T. Tanaka. J. Mater. Chem. A 2015, 3, 11313–11319.
11. A. Anzai, N. Fukuo, A. Yamamoto and H. Yoshida. Catal. Commun. 2017, 100, 134–138.
12. S. Wang, K. Teramura, T. Hisatomi, K. Domen, H. Asakura, S. Hosokawa and T. Tanaka. ACS Appl. Energy Mater. 2020, 3, 1468–1475.
13. S. Wang, K. Teramura, H. Asakura, S. Hosokawa and T. Tanaka. J. Phys. Chem. C 2021, 125, 1304–1312.
14. Z. Chen, T. Wang, B, Liu, D. Cheng, C. Hu, G. Zhang, W. Zhu, H. Wang, Z. J. Zhao and J. Gong. J. Am. Chem. Soc. 2020, 142, 6878-6883.
15. W. Luo, J. Zhang, M. Li and A. ZüTtel. ACS Catal. 2019, 9, 5, 3783-3791.
16. A. Goyal, G. Marcandalli, V. A. Mints and M. T. M. Koper. J. Am. Chem. Soc 2020, 142, 4154-4161.
17. S. Iguchi, K. Teramura, S. Hosokawa and T. Tanaka. Catal. Sci. Technol 2016, 6, 4978.

18. S. Wang, K.Teramura, H.Asakura, S. Hosokawa and T. Tanaka. J. Phys. Chem. C 2021, 125, 1304–1312.
19. X. Xu, K. Teramura, H. Asakura, S. Hosokawa and T. Tanaka. Appl. Catal. B Environ. 2021, 298, 120508.
20. X. Xu, K. Teramura, H. Asakura, S. Hosokawa and T. Tanaka. ChemCatChem 2021, 13, 4313–4317.
21. J. N. Díaz de León. Appl. Catal. B Environ. 2016, 181, 524–533.
22. S. Mandal, K. Arts, H. C. M. Knoops, J. A. Cuenca, G. M. Klemencic and O. A. Williams. Carbon 2021, 181, 79–86.

Part III

Investigations on Ag cocatalyst for the photocatalytic conversion of CO_2 using H_2O as an electron donor

Chapter 6

Tuning Ag-modified $NaTaO_3$ to achieve high CO selectivity for the photocatalytic conversion of CO_2 using H_2O as the electron donor

Abstract

Ag-loaded $NaTaO_3$ was used for the photocatalytic conversion of CO_2 using H_2O as the electron donor, and the effect of the nanoparticle size, Ag loading, and crystal structure on the photocatalytic activity and CO selectivity were investigated. The sizes of the Ag nanoparticles could be tuned by controlling the photodeposition time, and relatively larger Ag nanoparticles were found to show higher CO selectivity. During the photocatalytic reaction, the initially polycrystalline Ag nanoparticles became single crystalline owing to the dissolution and redeposition of Ag, and the change in morphology reduced the CO selectivity. To solve this problem, Ag-Cr dual cocatalysts having a core–shell structure was developed. Subsequently, the locations and sizes of the Ag nanoparticles on the surfaces of $NaTaO_3$ were maintained during the reaction because of the protection of the chromium shell, thus providing stable and selective CO production via the photocatalytic conversion of CO_2 by H_2O.

1. Introduction

Since the first industrial revolution, humans have been dependent on fossil fuels. Although renewable energy sources, such as wind [1] and hydro [2] power are now in use, fossil fuels are still the main energy source. However, CO_2, a potent greenhouse gas, is emitted during the combustion of fossil fuels [3], and this has resulted in global warming [4]. Therefore, the exploitation of solar energy as a replacement for fossil fuels using photovoltaic cells [5], for the photocatalytic conversion of biomass [6], for H_2O splitting [7], and for CO_2 conversion [8], has drawn attention. In particular, the photocatalytic conversion of CO_2 using H_2O as the electron donor is a promising pathway for the capture and reuse of CO_2, thus storing solar energy and contributing to the fight against global warming. The products from the photocatalytic conversion of CO_2 with H_2O as the electron donor are H_2 and organic molecules derived from CO_2. Independent of the selectivity for the conversion of CO_2 to different products (see Equation (1)), syngas [9], which consists of H_2 and CO, is always produced. In contrast, the production of other organic species, including CHOOH, CH_3OH, and CH_4, requires high overpotentials. The successful photocatalytic conversion of CO_2 by H_2O should satisfy the balance between the consumed photogenerated electrons and holes, as shown in Equation (2). The production of a stoichiometric amount of O_2 in the reaction is an important indicator that the electrons used in the reaction originate from H_2O rather than sacrificial reagents, such as carbon impurities, which are typically present.

$$\textbf{Selectivity} = (2R_{HCOOH} + 2R_{CO} + 4R_{HCHO} + 6R_{CH_3OH} + 8R_{CH_4})/(2R_{HCOOH} + 2R_{CO} + 4R_{HCHO} + 6R_{CH_3OH} + 8R_{CH_4} + 2R_{H_2}) \times 100\% \quad (1)$$

$$e^-/h^+ = (2R_{HCOOH} + 2R_{CO} + 4R_{HCHO} + 6R_{CH_3OH} + 8R_{CH_4} + 2R_{H_2})/4R_{O_2} \quad (2)$$

CO is an important precursor in the production of a range of industrial reagents such as aldehydes, polycarbonates, and polyurethanes. Therefore, the production of CO with high selectivity in the photocatalytic conversion of CO_2 using H_2O as an electron donor is attractive. Ag-modified $MLa_4Ti_4O_{15}$ (M = Ca, Sr, and Ba) [10], which was first reported

by Kudo et al., was the first photocatalyst to produce CO in quantities exceeding those of H_2 for this reaction. Recently, Ag nanoparticles have been used as cocatalysts and have been found to show high selectivity toward the evolution of CO over other photocatalysts for CO_2 reduction, such as $CaTiO_3$ [11], $K_2Ti_6O_{13}$ [12], $SrNb_2O_6$ [13], and $ZnGa_2O_4$ [14]. Although many types of photocatalysts modified with Ag nanoparticles can satisfy Equation (2), few produce CO with high selectivity; examples of these photocatalysts include Ta_2O_5 (18%) [15], $NaTaO_3$(4%) [16], $ZnTa_2O_6$ (43.4%) [17], Ga_2O_3 (40%) [18], and $Na_2Ti_6O_{13}$ (60%) [19]. Further, basic metal oxides have been used to modify Ag-loaded photocatalysts for the photocatalytic conversion of CO_2 using H_2O as the electron donor, for example, $NaTaO_3$:Sr(Ca) [16], SrO/Ta_2O_5 [15], $Al/SrTiO_3$ [20], $ZnO/ZnTa_2O_6$ [21], and ZnO/Ga_2O_3 [22]. In previous studies, Iguchi et al. compared the effects of various metal cocatalysts, including Ag, Pt, Au, Ni, Cu [17], and Pd [23] on the photocatalytic conversion of CO_2 using H_2O as the electron donor, and the results showed that only Ag nanoparticles resulted in high selectivity toward CO. In addition, Wang et al. observed that the conversion of CO_2 and CO selectivity also depended on the amount and size of Ag nanoparticles, which can be easily controlled by adjusting the loading method (impregnation, photodeposition, or chemical reduction) used[11,14]. Hori et al. [24] found that the morphology of the Ag electrode had a significant effect on CO evolution in the electrochemical reduction of CO_2. The partial current density for CO production over the Ag (110) facet was remarkably higher than those of the (111) and (100) facets, and Ishida et al. also observed this in previous work, in which it was found that Ag electrodes pretreated with O_3 had higher activity and CO selectivity at the same applied voltages than those that had not received pretreatment [25]. Further, the importance of the structure of the metal cocatalyst used for the selective reduction of CO_2 was also confirmed in a study of Au electrodes, which are rich in grain boundaries [26,27].

The use of dual cocatalysts, such as Ag@M (M: Cr [28], Co [29], Mn [30], and Fe [31]), has also been reported to promote the production of CO in the photocatalytic conversion of CO_2 using H_2O as an electron donor dramatically. However, although they are considered

to follow the same mechanism, the Ag@Co and Ag@Fe dual cocatalysts did not perform in the same way regarding the stability of CO production. In particular, the Ag@Co dual cocatalyst showed poor stability.

Therefore, the author has found that the activity, CO selectivity, and stability of catalysts for the photocatalytic conversion of CO_2 using H_2O as an electron donor depend on many factors, such as the surface modification and morphology of the photocatalyst, size and microstructure of the metal cocatalyst, and presence of dual cocatalysts. In this work, the author tuned the size and number of Ag nanoparticles loaded on $NaTaO_3$ by optimizing the photodeposition time and carried out surface modification with chromium(III) species and investigated the effects of these modifications of the selectivity and stability of CO evolution during the photocatalytic conversion of CO_2 using H_2O as the electron donor.

2. Experimental section

2.1. Synthesis of photocatalysts

$NaTaO_3$ (NTO) was synthesized using a solid-state reaction. Stoichiometric amounts of Ta_2O_5 and Na_2CO_3 were ground together well and calcined at 1423 K for 20 h in an aluminum crucible. Ag nanoparticles were loaded onto the photocatalysts via photodeposition. The photodeposition time and amount of Ag precursor were controlled to investigate their effects on photocatalyst performance. In addition, dual cocatalysts (Ag@M, M = Cr, Cu, Mo, Fe, or Mn) were obtained by the co-photodeposition of $AgNO_3$ and Na_2CrO_4, $Cu(NO_3)_2$, Na_2MoO_4, $Fe(NO_3)_3$, and $KMnO_4$, respectively.

2.2. Photocatalyst characterization

The morphologies of the photocatalysts were observed using field-emission scanning electron microscopy (FE-SEM, SU-8220, Hitachi High-Technologies) at an accelerating voltage of 3.0–5.0 kV and emission current of 10 μA. The microstructures of the Ag nanoparticles were characterized by transmission electron microscopy (TEM, JEM-2100F, JEOL). The X-ray diffraction (XRD) patterns of the synthesized $NaTaO_3$ samples were obtained using a Rigaku Ultima IV powder diffractometer (Cu-K_α radiation,

40 kV, 40 mA). The absorption spectra of the Ag nanoparticles were recorded using a JASCO V-670 spectrometer. To determine the chemical states of the loaded Ag nanoparticles, X-ray photoelectron spectroscopy (XPS) measurements were conducted using an ESCA 3400 instrument (Shimadzu Corp.). Leached ions in solution were examined using inductively coupled plasma–optical emission spectrometry (ICP-OES, iCAP7400, Thermo Fisher Scientific, Inc.).

2.3. Photocatalytic reaction procedure

The reactions were conducted in an inner irradiation reactor with a quartz jacket which was connected to cooling water, and the temperature during the reactions was controlled between 298 and 303 K. A 400-W high-pressure mercury lamp (Sen Lights Corp.) was used as the light source. The products derived from H_2O and CO_2 were detected using gas chromatography (GC, GC-8A, Shimadzu Corp.) using a thermal conductivity detector (TCD) and flame ionization detector (FID), respectively.

3. Results and discussion

3.1. Morphology of $NaTaO_3$

The XRD pattern presented in Figure 1 shows that the pure $NaTaO_3$ (NTO) phase was successfully obtained through the solid-state reaction method used in this work. The (100) and (110) facets were obtained after calcination, as confirmed by the SEM image of the synthesized NTO (Figure 2), which shows that the particles were nearly cubic in shape enclosed by the (100) and (110) facets. As a typical perovskite material, perfect $NaTaO_3$ should have a cubic habit. The formation of the (110) facet indicates that defects were formed in the NTO during calcination. Undoubtedly, some sodium species evaporated during calcination because the Na_2CO_3 precursor has a low melting point. This means that the sodium component in the final product was not stoichiometric with the tantalum component. For comparison, Na-poor and Na-rich NTO samples were synthesized by tuning the ratio of Na^+ to Ta^{5+} (0.9 and 1.1, respectively) in the precursors. Figure 3(a) shows that larger (110) facets were formed in the Na-poor NTO sample compared with the NTO fabricated from a stoichiometric amount of Na^+ and Ta^{5+}

precursors. However, the formation of the (110) facet was almost completely inhibited when 10 mol% of excess sodium precursor was used to prepare Na-rich NTO (Figure 3(b)). Based on the XRD patterns of the Na-poor and Na-rich NTO samples in Figure 4, it is clear that the intensity of the reflection arising from the (110) facet in the Na-rich NTO is much lower than that of the Na-poor NTO. Therefore, it is reasonable to conclude that the formation of the (110) facet in NTO is caused by the loss of sodium species during calcination.

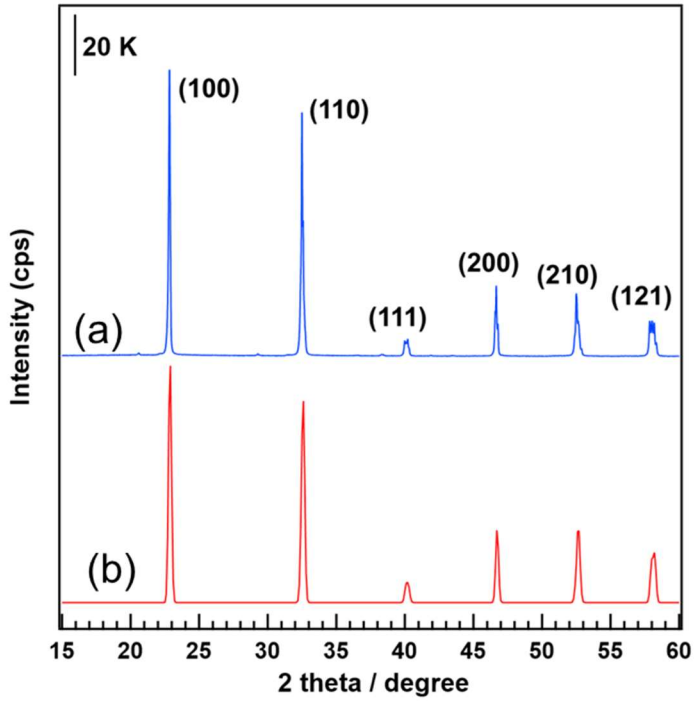

Figure 1. XRD pattern of (a) synthesized $NaTaO_3$ and (b) the Inorganic Crystal Structure Database (ICSD) reference pattern (No. 88375).

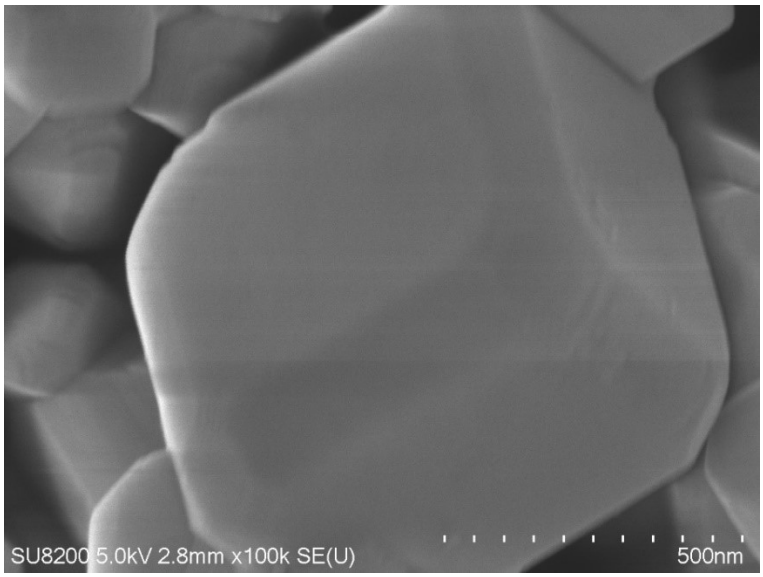

Figure 2. SEM image of synthesized $NaTaO_3$.

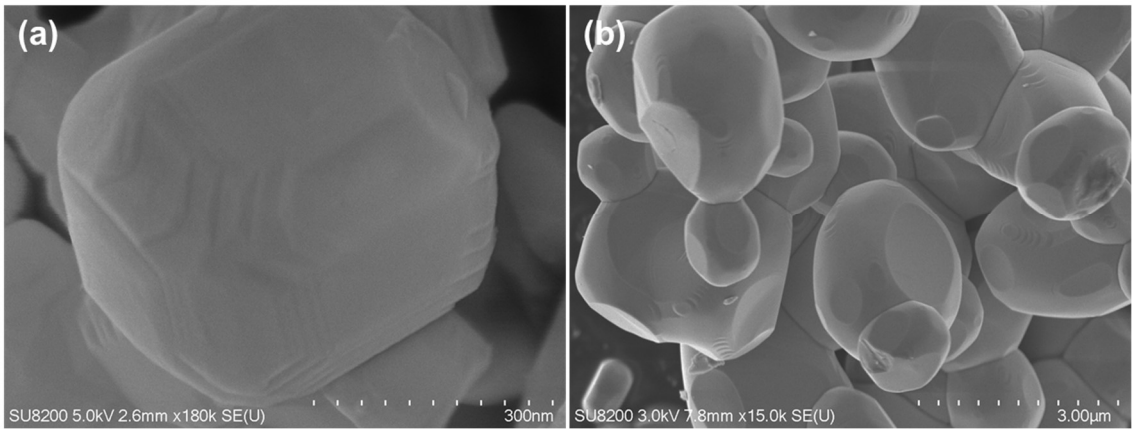

Figure 3. SEM images of (a) Na-poor NTO and (b) Na-rich NTO.

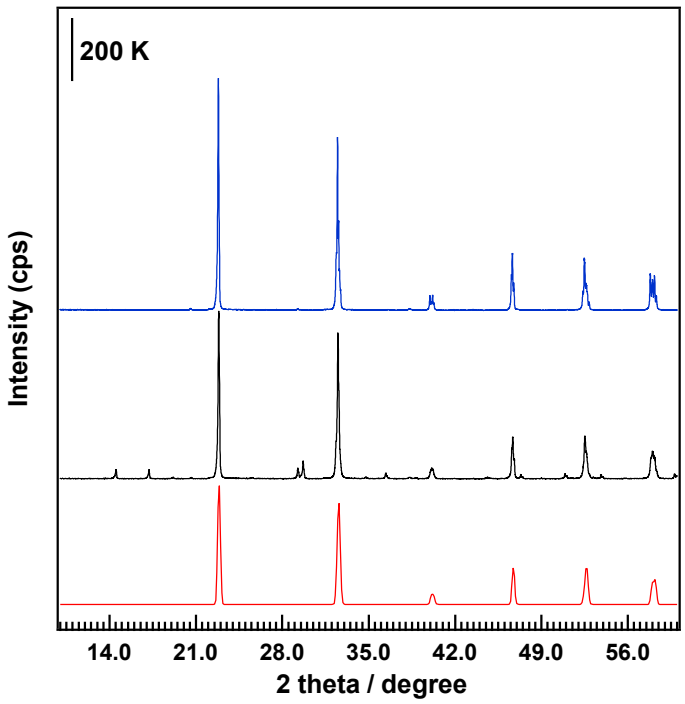

Figure 4. XRD patterns of Na-poor NTO (black), Na-rich NTO (blue) and the reference (red).

3.2. Photodeposition time for Ag nanoparticle loading

Figure 5 shows SEM images of Ag nanoparticles on the surface of the NTO particles prepared by photodeposition for different periods. Large numbers of Ag nanoparticles were observed on the (100) facet when the photodeposition time was 0.5 h, as shown in Figure 5(a). However, the number of Ag particles decreased significantly when the photodeposition time was increased to 1 h, as shown in Figure 5(b), and the number of particles decreased further when the photodeposition time was increased to 3 and 5 h. In particular, there are very few Ag nanoparticles on the surface of NTO after 3 h of photodeposition (Figure 5(c)), and they are absent after photodeposition for 5 h (Figure 5(d)), possibly as a result of the presence of very small-sized Ag nanoparticles. Strangely, a small number of Ag nanoparticles were observed again when the photodeposition time was increased to 7 and 12 h, as shown in Figures 5(e) and 5(f), indicating the growth of the nanoparticles after these times. Next, the author performed ICP-OES measurements

of the sample solutions after photodeposition to determine the Ag loading. Based on the analysis of the remaining reaction solution, almost 100% of the precursor Ag had been loaded onto the surface of NTO after 0.5 h photodeposition (Figure 6). Similarly, no Ag^+ ions were found in solution after photodeposition for up to 12 h, indicating that the Ag nanoparticles initially photodeposited on the surface of NTO were not leached into the solution during longer photoirradiation periods.

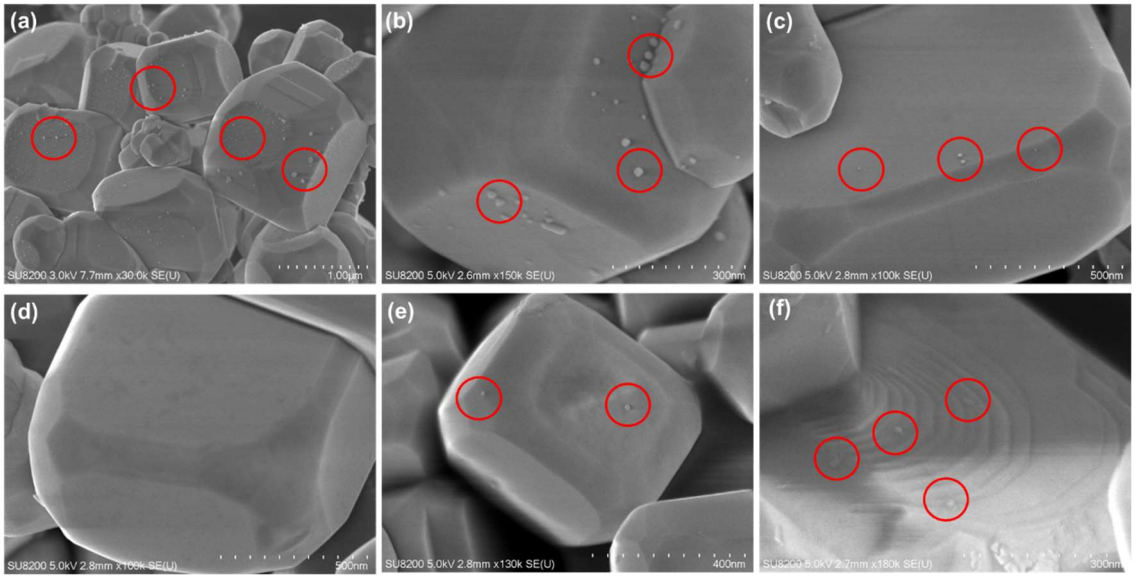

Figure 5. SEM images of Ag/NTO prepared at photodeposition times of (a) 0.5, (b) 1, (c) 3, (d) 5, (e) 7, and (f) 12 h. Ag nanoparticles are highlighted with red circles. Ag loading: 0.29 wt%.

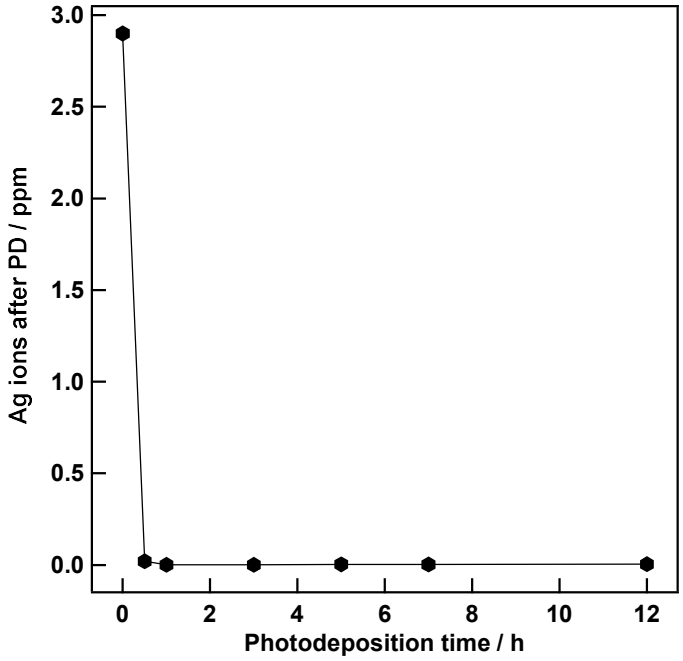

Figure 6. ICP characterizations on the concentration of residual Ag^{+} in the loading solution after photodeposition.

Figure 7 shows the UV-Vis diffuse reflectance spectra of the Ag/NTO photocatalysts prepared using different photodeposition times. Peaks originating from the surface plasmon resonance (SPR) were observed in the spectra of the Ag/NTO samples at 382 and 465 nm. These two peaks were probably caused by the coupling of the resonance of adjacent Ag particles having heterogenous sizes [32]. However, the peak intensities of the Ag nanoparticles decreased with increase in the photodeposition time from 1 to 7 h but increased slightly when the photodeposition time was prolonged to 12 h, again indicating that the size of the Ag nanoparticles increased. Next, the chemical states of the Ag nanoparticles were characterized using XPS. The peaks at 368 and 352 eV in the 3d Ag XPS (368 eV) and Auger electron spectra (352 eV) did not change, as shown in Figures 8(a) and 8(b), which indicates that the chemical state of the nanoparticles was not affected by the photodeposition time. The Auger parameters revealed that all nanoparticles comprised Ag^{0} (720.0 eV), which is easily distinguished from Ag^{+} (718.5 eV) and Ag^{2+}

(718.9 eV).

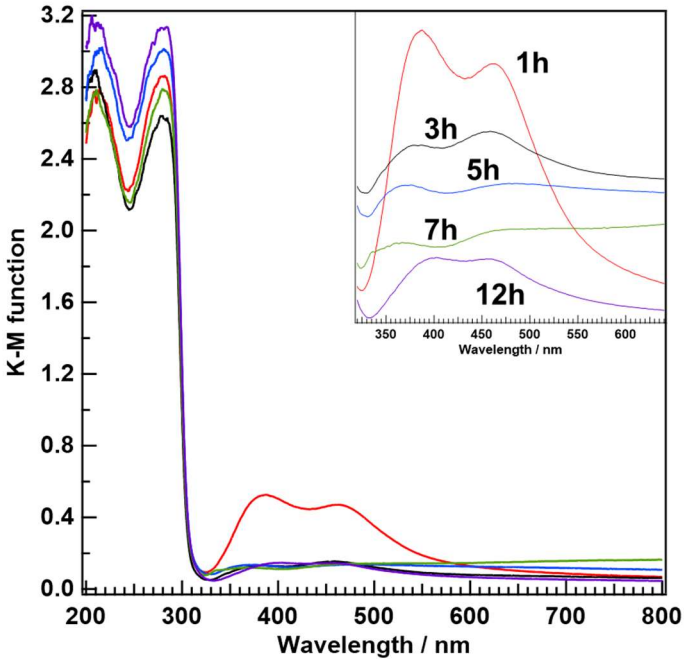

Figure 7. UV-Vis diffuse reflectance spectra of Ag/NTO prepared using different photodeposition times. Ag loading: 0.29 wt%. Inset shows an enlarged image of the SPR peaks arising from the Ag nanoparticles. K-M = Kubelka–Munk function.

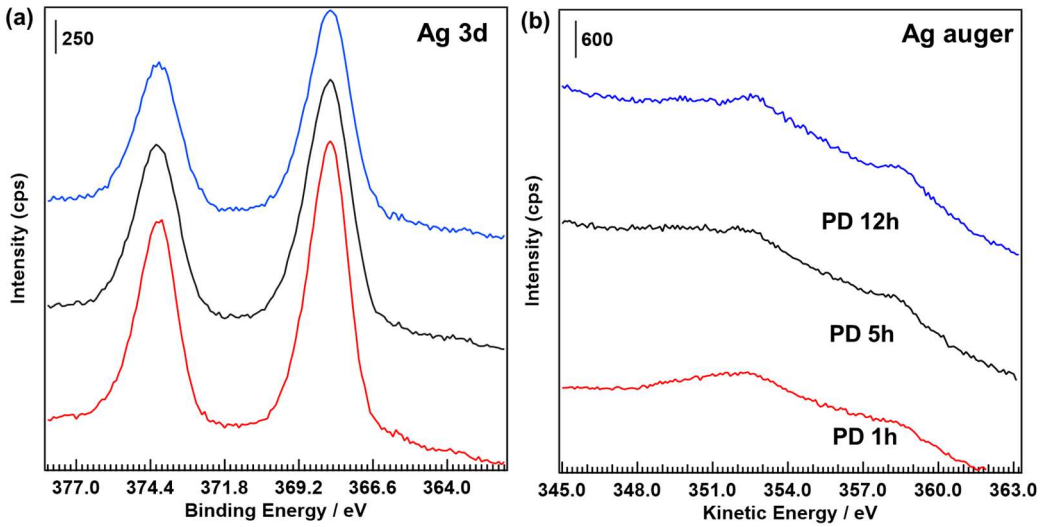

Figure 8. X-ray photoelectron spectra of Ag nanoparticles loaded on NTO by controlling the photodeposition time. (a) binding energy of Ag and (b) kinetic energy of auger electrons. 1 h (red), 5 h (black) and 12 h (blue).

Figure 9 shows the activity and selectivity of the prepared photocatalysts toward CO evolution during the photocatalytic conversion of CO_2 using H_2O as the electron donor. The rate of formation of O_2, which indicates the total photocatalyst activity (see Equation (2)), increased gradually for the samples photodeposited for 1 to 5 h (36 to 57 μmol h^{-1}) and then decreased in the samples photodeposited for periods up to 12 h (30 μmol h^{-1}). The same trend was observed in overall water splitting over bare NTO (Figure 10); this trend arises because there is a trade-off relationship between Na^+ leaching from the surface of NTO and the growth of the (110) facet over time. The author also observed an increase in the pH from 6.6 to 8.0 during the reaction, and there are two explanations for this: (1) protons could be strongly adsorbed on the surfaces of NTO or (2) protons could be exchanged for Na^+ on the surfaces. Both scenarios would cause an increase in the pH because OH^- would be left in the bulk solution. By comparing the XRD patterns (Figure 11) before and after the photocatalytic reaction, it was found that the intensity of the reflection corresponding to the (110) facet increased relative to that of the (100) facet after reaction, indicating that the (110) facets grew selectively. This can be confirmed by comparing the SEM images before and after the photocatalytic reaction (see Figures 12(a) and 12(b)). As shown in these images, the smooth (100) facet became rough owing to the formation of the (110) facet. Based on Figure 3, it is reasonable to conclude that the formation of the (110) facet during the water splitting reaction is caused by the leaching of Na^+ ions from the (100) facet to the solution. Therefore, the author believes that the change in pH was caused by ion exchange between the Na^+ ions in the NTO framework and the protons in the solution, which resulted in a high concentration of OH^- near the NTO surfaces under photoirradiation. Therefore, the author carried out Ag nanoparticle loading onto NTO under high pH (11.4) conditions (Figure 13) and found that larger Ag nanoparticles were formed. Therefore, the observed decrease in the size of the Ag particles with increasing photodeposition time should not be caused by the rapid increase in pH arising from ion exchange. As discussed, with increase in photodeposition time, the number of active sites on NTO increased and subsequently decreased as a result of the

trade-off between the formation of the (110) facet and leaching of Na^+. The former enhances the separation of charge carriers between the (100) and (110) facets, whereas the latter inevitably creates more defects on the surfaces of NTO, which results in the increased recombination of photogenerated electrons and holes. Metal nanoparticles, such as Pt, have been reported to act as recombination centers for photogenerated electrons and holes when they exceed specific sizes [33,34]. This means that photogenerated holes, as well as electrons, could be capable of migrating to the Ag nanoparticles under photoirradiation. The author believes that the reduction of Ag^+ and oxidation of Ag^0 reaches dynamic equilibrium during photoirradiation, and Ag^0 would be redeposited on the surfaces of NTO, thus resulting in changes to the number of active sites under photoirradiation, as well as changes to the size of the Ag nanoparticles.

Interestingly, the CO selectivity of Ag/NTO was significantly influenced by the photodeposition time. Specifically, the large Ag nanoparticles (1 h) produced CO as the main product with an activity of 92 μmol h^{-1}, and the CO selectivity reached 88%. For the sample photodeposited for 5 h, the CO formation rate decreased to 46 μmol h^{-1}, and the H_2 formation rate increased from 13 to 105 μmol h^{-1}. Thus, the selectivity toward CO evolution shows a "V"-like trend, reaching 75% with a CO formation rate of 67 μmol h^{-1} for the sample photodeposited for 12 h. Therefore, the CO selectivity is dependent on the size of the Ag nanoparticles, as shown in Figures 5 and 9. In addition, the chemical state of Ag^0 was maintained both before and after the reaction (Figures 8 and 14).

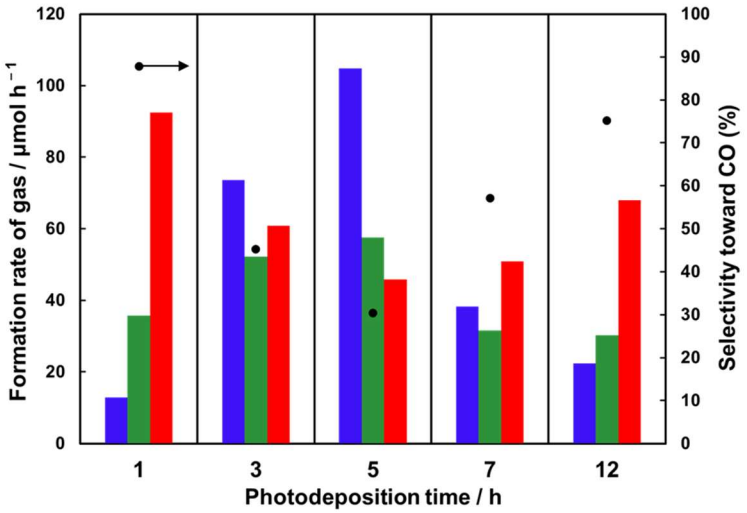

Figure 9. Formation rates of H_2 (blue), O_2 (green), and CO (red) and CO selectivity (black dots) for the photocatalytic reaction over Ag/NTO prepared using different photodeposition times. Photocatalyst: 0.5 g; Ag loading: 0.29 wt%; photoirradiation time: 1 h; reaction solution: 1 L of aqueous 0.1 M $NaHCO_3$; CO_2 flow rate: 30 mL min^{-1}; light source: 400-W high-pressure Hg lamp.

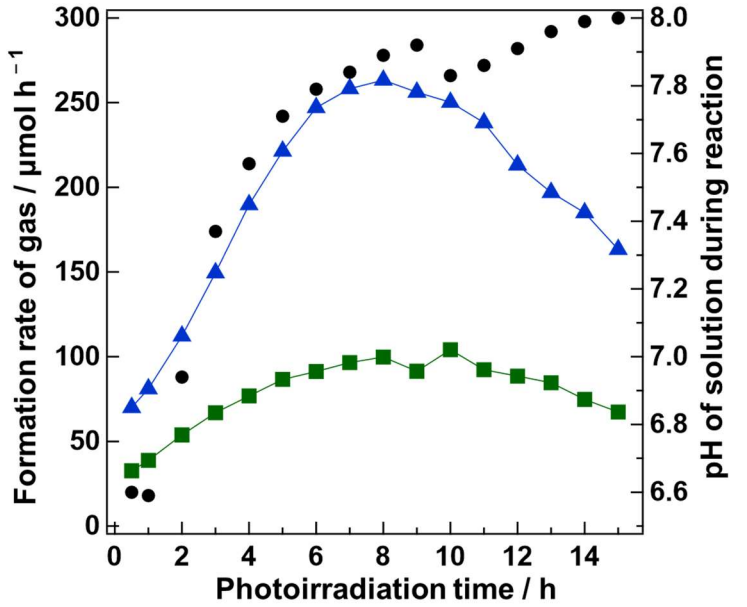

Figure 10. Formation rates of H_2 (blue), O_2 (green) and pH value of solution (black dot)

for overall water splitting over bare NTO. Photocatalyst: 0.5 g; reaction solution: 1 L pure H_2O; Ar flow rate: 30 mL min^{-1}; light source: 400 W high-pressure Hg lamp.

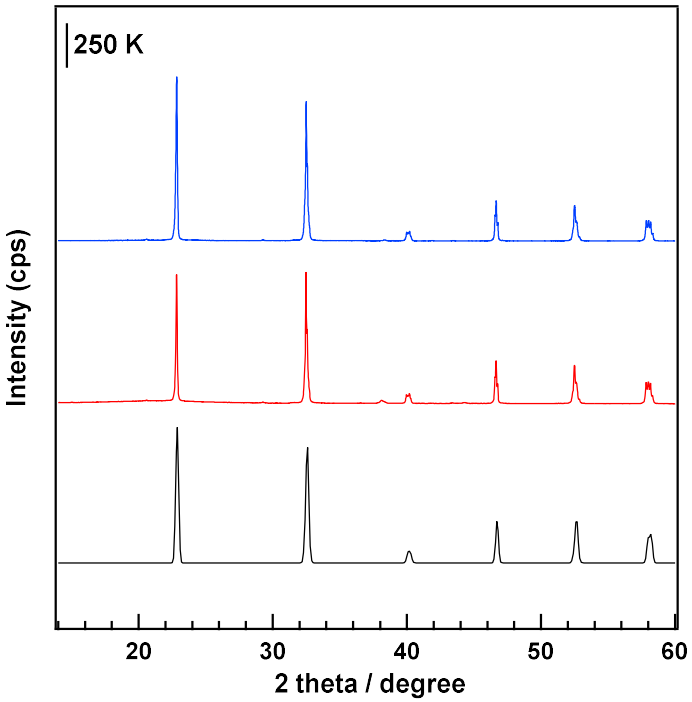

Figure 11. XRD patterns of NTO before (blue) and after (red) overall water splitting. Black: reference from ICSD database (No. 88375).

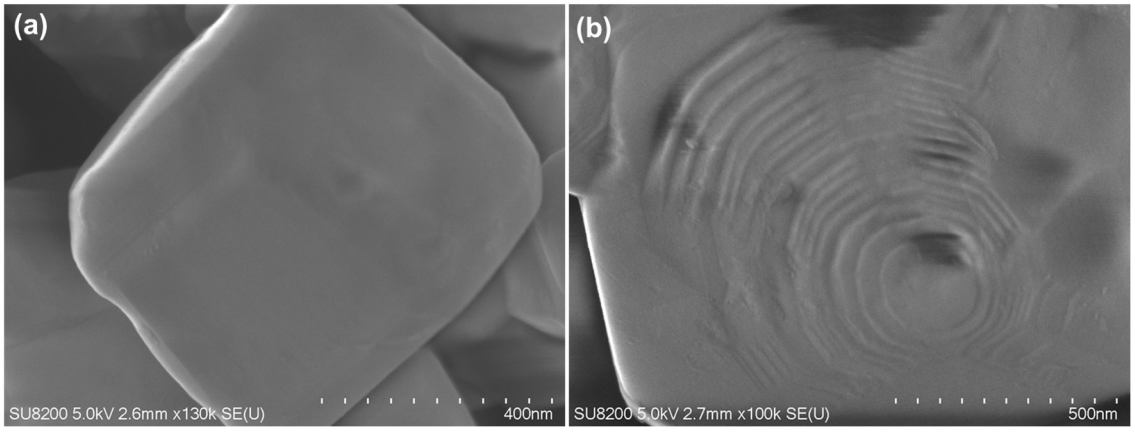

Figure 12. SEM images of NTO (a) before and (b) after overall water splitting.

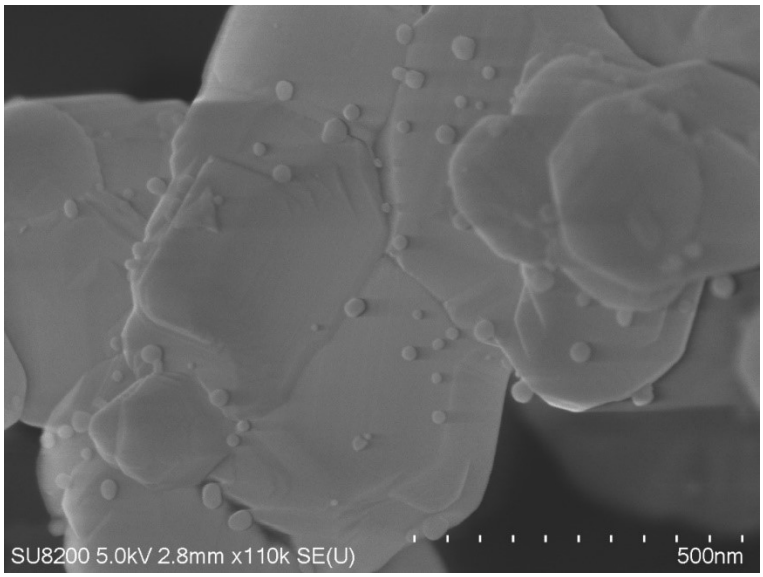

Figure 13. SEM image of Ag-loaded NTO by photodeposition method at pH 11.4.

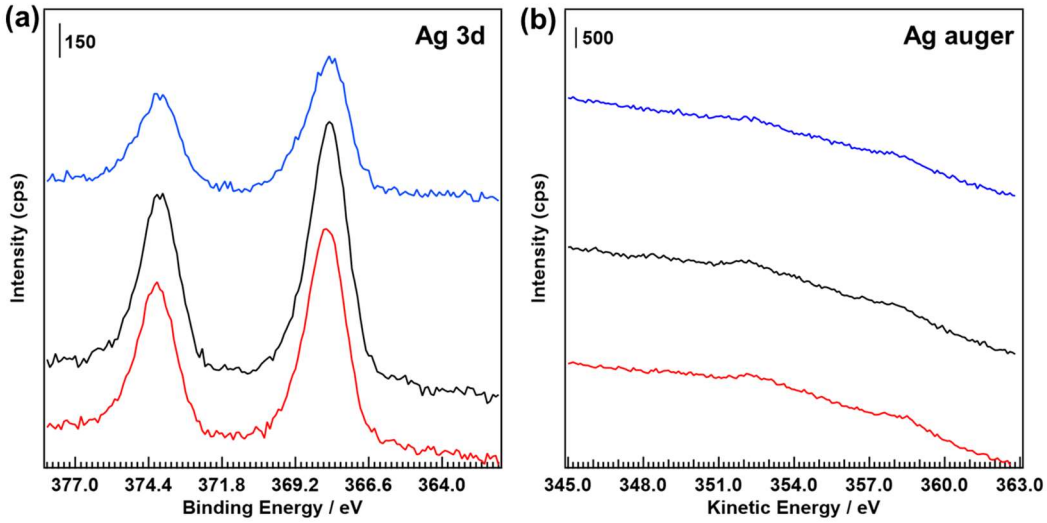

Figure 14. X-ray photoelectron spectra of Ag nanoparticles loaded on NTO with various photodeposition time after the photocatalytic conversion of CO_2 by H_2O. (a) binding energy of Ag and (b) kinetic energy of auger electrons. 1 h (red), 5h (black) and 12 h (blue).

3.3. Amount of Ag loaded on NTO

The photodeposition time and Ag loading also affect the size of the Ag nanoparticles. Figure 15 shows SEM images of Ag/NTO particles prepared with different Ag loadings.

The Ag nanoparticles produced using 0.02, 0.05, and 0.10 wt% of the Ag precursor were too small to be observed, as shown in Figures 15(a–c), and the size of the Ag nanoparticles increased gradually with increase in Ag loading, as shown in Figures 15(d–f). However, the density of the Ag nanoparticle dispersion did not change significantly. This indicates that the successful reduction of Ag^{+} ions in the precursor solutions proceeded on the surfaces of the previously deposited small Ag nanoparticles, and these particles grew slowly. Crucially, if further growth had not occurred on the initially deposited seed particles, the density of Ag particles would have increased. Based on the Section 3.2 discussion, the Ag nanoparticles of 0.29 wt% Ag/NTO should be capable of scavenging the photogenerated electrons completely from the surface of NTO because the density of Ag nanoparticles did not increase with an increase in the loading amount. Next, the author monitored the H_2, O_2, and CO formation rates for the photocatalytic reaction over Ag/NTO, as shown in Figure 16. The CO selectivity varied significantly with respect to Ag loading from 0.02 to 3.0 wt%. In addition, the formation rate of H_2 was increased significantly with an increase of loading amount of Ag nanoparticles from 0.02 to 1.0 wt% during the reaction. Interestingly, the formation rate of H_2 formation rate was not almost changed over 5 h of reaction in the case of the 3.0 wt% Ag/NTO. This unstable performance is not a result of changes in the surface properties of NTO during the photocatalytic reaction because bare NTO showed stable performance under the same conditions (Figure 17). Further, the CO formation rate decreased gradually for all samples, regardless of the Ag loading.

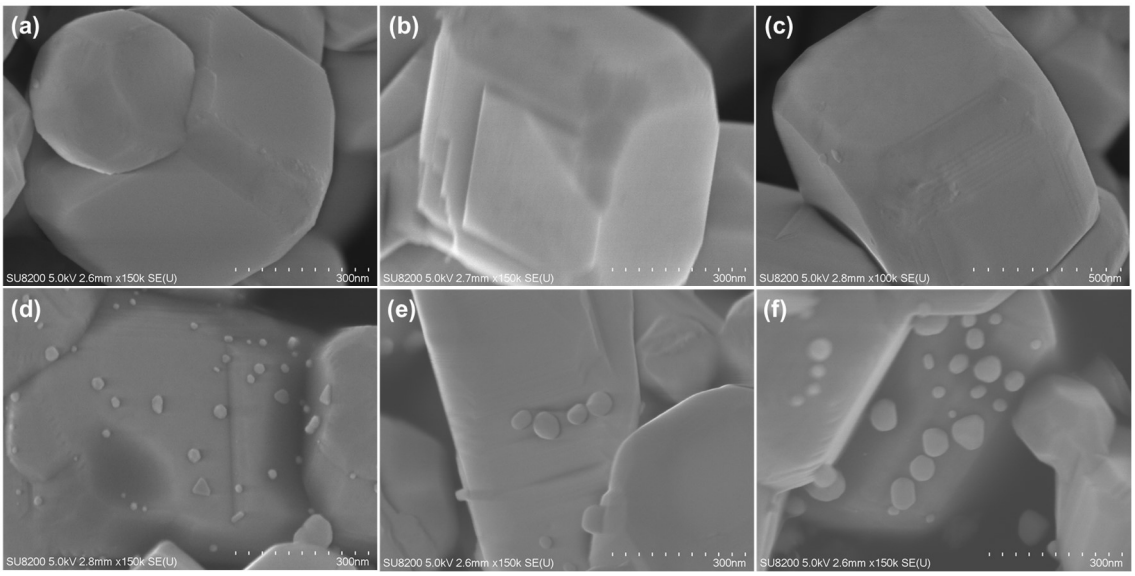

Figure 15. SEM images of Ag/NTO catalysts prepared with different Ag loadings: (a) 0.02, (b) 0.05, (c) 0.1, (d) 0.6, (e) 1.0, and (f) 3.0 wt%. Photodeposition time: 1 h.

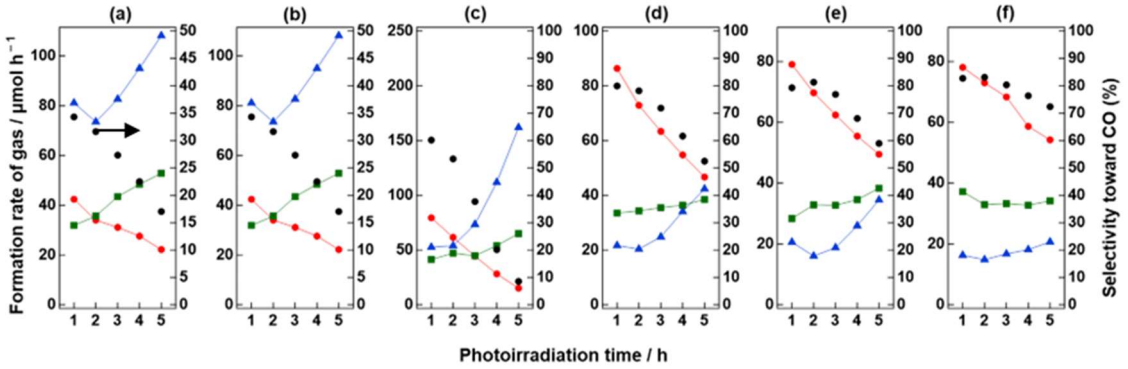

Figure 16. Formation rates of H_2 (blue), O_2 (green), and CO (red) and CO selectivity (black dots) with respect to time during the photocatalytic reaction over Ag/NTO prepared with different Ag loadings: (a) 0.02, (b) 0.05, (c) 0.1, (d) 0.6, (e) 1.0, and (f) 3.0 wt%. Photocatalyst: 0.5 g; reaction solution: 1 L of aqueous 0.1 M $NaHCO_3$; CO_2 flow rate: 30 mL min^{-1}; light source: 400-W high-pressure Hg lamp. Photodeposition time for Ag loading: 1 h.

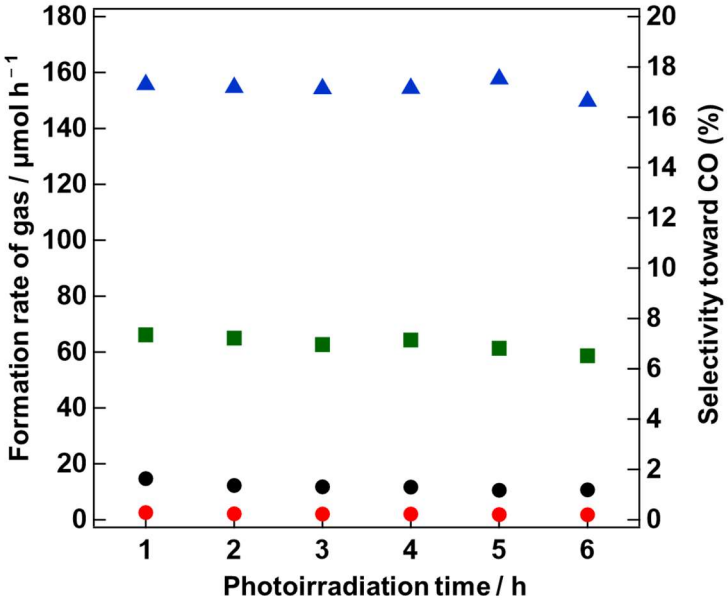

Figure 17. Formation rates of H_2 (blue), O_2 (green) and CO (red) and selectivity toward CO evolution (black dot) for the photocatalytic conversion of CO_2 by H_2O over bare NTO. Photocatalyst: 0.5 g; reaction solution: 1 L of a 0.1 M $NaHCO_3$ aqueous solution; CO_2 flow rate: 30 mL min−1; light source: 400 W high-pressure Hg lamp.

Figure 18 displays SEM images of Ag/NTO particles prepared with different Ag loadings after the photocatalytic reaction. For the sample prepared with a Ag loading of 0.6 wt%, the size of the Ag nanoparticles decreased from 30 nm before reaction to 20 nm after reaction. The size-reduction phenomenon was even more significant for the catalyst prepared with a Ag loading of 0.29 wt%, for which the Ag nanoparticles disappeared after the reaction. In contrast, for the sample prepared with a Ag loading of 0.60 wt%, the particles after the reaction (Figure 18(b)) remained larger than those prepared with 0.29 wt% Ag before the reaction (15 nm) (Figures 5(b)). This result reveals that the change in the CO formation rate was not caused by a decrease in the size of the Ag nanoparticles. Figure 19 shows the TEM images of the Ag/NTO catalyst prepared with a Ag loading of 0.29 wt% before and after the reaction. The lattice fringes of the Ag nanoparticles before the reaction indicate a polycrystalline structure, showing growth in multiple directions,

as well as the presence of a large number of grain boundaries (Figure 19(a)). Interestingly, the Ag lattice planes became aligned after the reaction, indicating a transformation from a polycrystalline to single-crystalline structure, as shown in Figure 19(b). Thus, during the photocatalytic reaction, the number of grain boundaries in the Ag nanoparticles is reduced. It has been widely reported that the presence of grain boundaries enhances the selectivity toward CO evolution in the electrochemical reduction of CO_2 [27,35,36], suggesting that the observed reduction in the number of grain boundaries in the catalyst would result in a reduction in the CO selectivity with time. Therefore, the poor stability in CO selectivity during the photocatalytic reaction is considered to be caused by the loss of grain boundaries in the Ag nanoparticles.

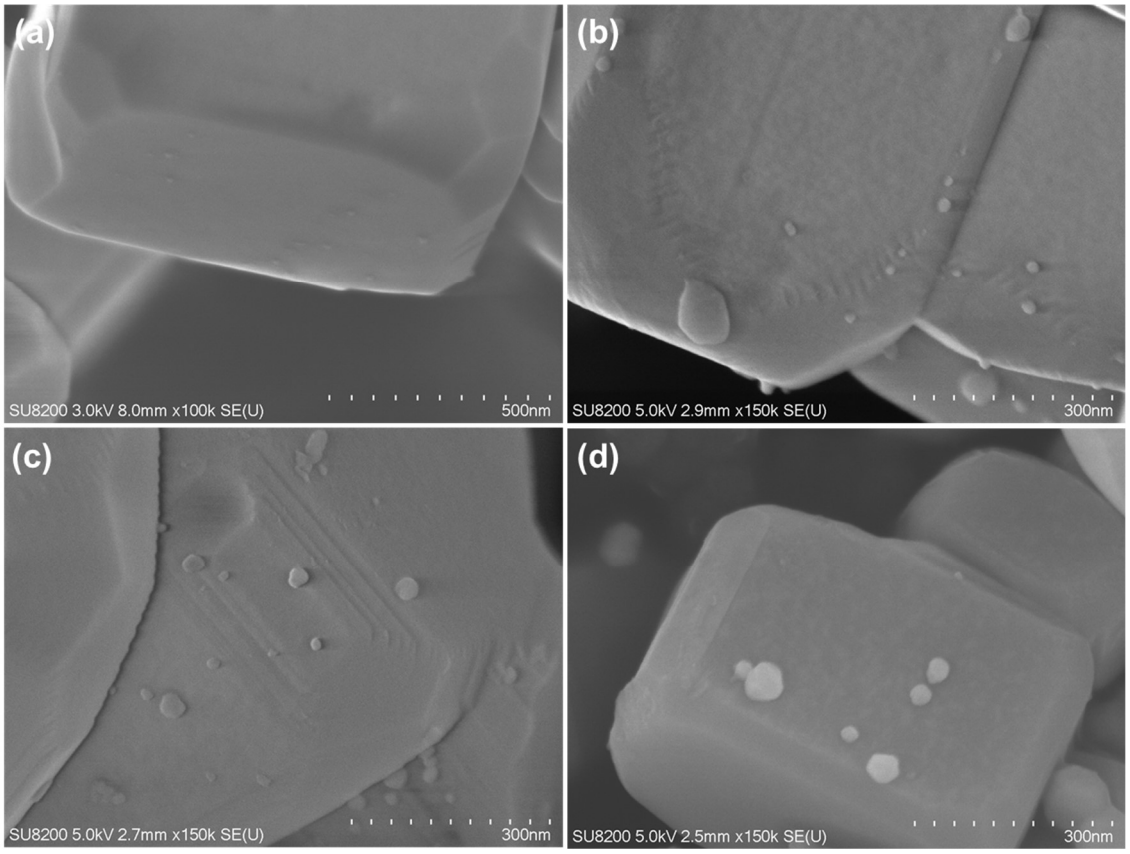

Figure 18. SEM images of catalyst particles after the photocatalytic reaction. Ag/NTO was prepared with different Ag loadings: (a) 0.29, (b) 0.60, (c) 1.00, and (d) 3.00 wt%.

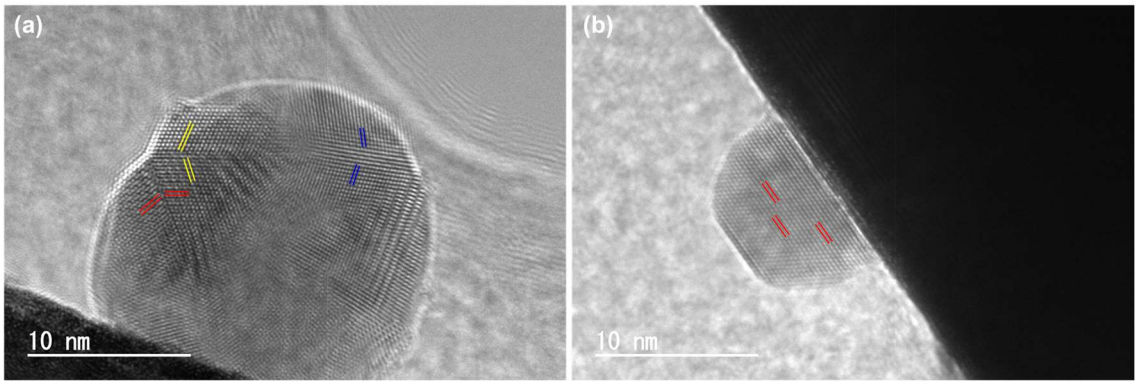

Figure 19. TEM images of Ag/NTO (a) before and (b) after reaction. Amount of Ag: 0.29 wt%.

3.4. Effect of modification of the Ag nanoparticles

Pang et al. previously reported that the addition of a shell of chromium hydroxide on Ag nanoparticles enhanced the CO selectivity of Ag-loaded Ga_2O_3 [23]. Therefore, the author prepared a series of Ag@M (M = Cu, Mo, Fe, Mn, or Cr) dual cocatalysts on NTO for the photocatalytic conversion of CO_2 using H_2O as the electron donor. The performance of the dual cocatalysts for this reaction are summarized in Table 1. Only the Ag@Cr cocatalyst prepared by the co-photodeposition of $AgNO_3$ and Na_2CrO_4 yielded a high CO selectivity (87.7% compared to 81.1% for the Ag/NTO catalyst). Next, XPS Ag 3d and Cr 2p spectra (see Figures 20(a) and 20(b), respectively) were obtained, and these reveal that Ag and Cr were present as Ag^0 and Cr^{3+}, respectively, and the intensity ratio of Ag to Cr species was approximately 0.29. After Ar^+-ion sputtering, peaks corresponding to Cr^0 species were observed in the XPS profile, possibly as a result of the strong reducing power of the Ar^+-ion sputtering process. However, the Ag-to-Cr ratio (for Cr, both Cr^{3+} and Cr^0) increased to 0.61. Because the escape depth of the electrons excited by X-rays in XPS measurements is generally several nanometers, the author believes that the Ag^0 species were covered by a shell of Cr^{3+} species and were exposed after sputtering. After the second cycle of Ar^+ sputtering, the ratio of Ag-to-Cr peak intensities remained at 0.57, indicating that the shell of Cr species on Ag had been completely removed, and

the remaining Cr species were located on the surface of the NTO. Furthermore, the modification with Cr^{3+} species improved the photocatalytic stability of the Ag/NTO catalyst, as shown in Figure 21. Comparing Figures 16(c–e), it can be seen that the formation of H_2 was suppressed, resulting in stable and high CO selectivity (80.0%). Unlike the Ag/NTO catalyst, for which the Ag nanoparticles were selectively deposited on the (100) facet of NTO on photoirradiation, the Ag@Cr dual cocatalysts showed no preference for any facet (Figure 22(a)), and the dual Ag@Cr cocatalyst particles were dispersed on both the (100) and (110) surfaces. As discussed Section 3.2, the Ag^0 species loaded on the surfaces of NTO would be redeposited during photoirradiation because of the simultaneous Na^+ leaching and growth of the (110) facets. This probably resulted in the polycrystalline-to-single crystalline transformation of the Ag nanoparticles, as discussed in Section 3.3, which reduced the CO selectivity during the photocatalytic reaction. In contrast, the position, number, and size of the dual Ag-Cr nanoparticles did not change significantly, as shown in Figure 22(b), suggesting that the Ag nanoparticle morphology was preserved as a result of the Cr^{3+} shell. Therefore, the NTO catalyst modified with Ag and Cr produced CO stably with high selectivity.

Table 1. Formation rates of H_2, O_2, and CO and CO selectivity in the photocatalytic conversion of CO_2 using H_2O as an electron donor over Ag@M-loaded NTO. [a]

Cocatalyst	Formation rate / μmol h^{-1}			Selec. Toward CO (%)
	H_2	O_2	CO	
Ag	12.9	35.7	92.4	87.7
Ag-Cu	107.4	46.8	1.7	1.6
Ag-Mo	623.8	283.8	0.3	0.0
Ag-Fe	26.5	26.6	24.2	47.8
Ag-Mn	16.7	18.5	19.7	54.0
Ag-Cr	8.1	22.7	34.8	81.1

[a] Photocatalyst:0.5 g; reaction solution:1 L of aqueous 0.1 M $NaHCO_3$; CO_2 flow rate: 30 mL min^{-1}; photoirradiation time: 1 h; light source: 400-W high-pressure Hg lamp. Ag-to-M molar ratio: 1.00; Ag@M photodeposition time: 1 h.

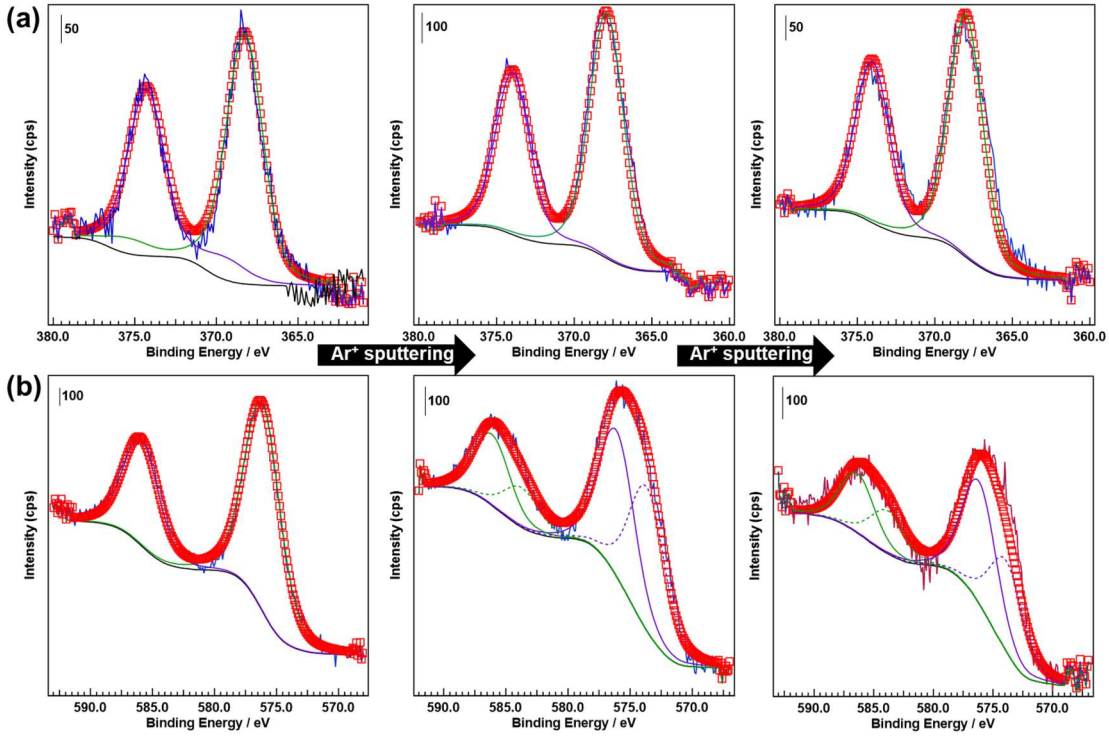

Figure 20. XPS (a) Ag 3d and (b) Cr 2p spectra of Ag@Cr-loaded NTO.

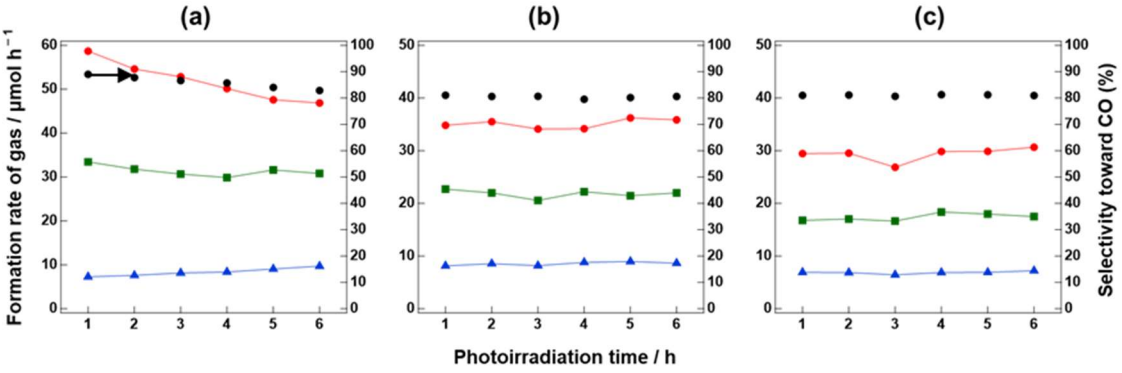

Figure 21. Formation rates of H_2 (blue), O_2 (green), and CO (red) and CO selectivity (black dots) during the photocatalytic conversion of CO_2 by H_2O over Ag@Cr loaded NTO prepared using different amounts of Ag: (a) 0.1, (b) 0.6, and (c) 1.0 wt%. The molar ratio of $AgNO_3$ to Na_2CrO_4 was 1.00 in all cases. Reaction conditions: photodeposition time: 1 h; photocatalyst: 0.5 g; reaction solution: 1 L of aqueous 0.1 M $NaHCO_3$; CO_2 flow rate: 30 mL min^{-1}; light source: 400-W high-pressure Hg lamp.

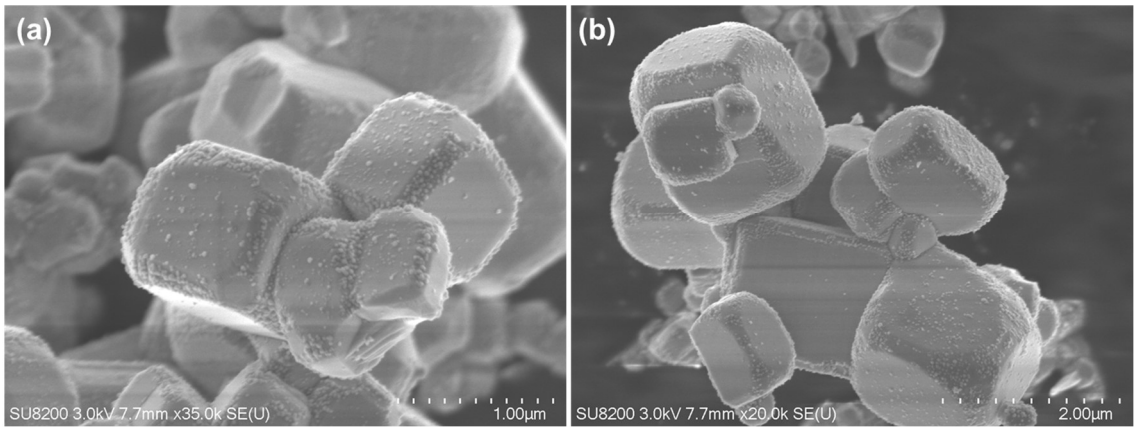

Figure 22. SEM images of Ag@Cr loaded NTO (a) before and (b) after reaction.

4. Conclusion

Ag nanoparticles were loaded on a $NaTaO_3$ photocatalyst, and their number and size were effectively tuned by varying the photodeposition time and amount of loaded Ag. In addition, surface modification using chromium species was also carried out. The author found that the size of the Ag nanoparticles was strongly affected by the photodeposition time, and the largest Ag nanoparticles resulted in the highest CO selectivity in the photocatalytic conversion of CO_2 using H_2O as an electron donor. However, the Ag-loaded $NaTaO_3$ catalyst showed poor stability in terms of CO selectivity at all Ag loading amounts. The author found that the Ag nanoparticles underwent a polycrystalline to single crystalline transition, and the consequent loss of grain boundaries, as well as the changes in the size of the Ag nanoparticles, were responsible for this loss of CO selectivity. The changes to the morphology of the Ag nanoparticles during the photocatalytic reaction could be prevented by covering them with a chromium (III) shell. Using this strategy, the CO selectivity was maintained.

References

1. A. M. Foley, P. G. Leahy, A. Marvuglia and E. J. McKeogh. Current methods and advances in forecasting of wind power generation. Renew. Energy 2012, **37**, 1–8.
2. T. S. Kishore, E. R. Patro, V. S. K. V. Harish and A. T. Haghighi. A comprehensive study on the recent progress and trends in development of small hydropower projects. Energies 2021, 14, 2882.
3. N. Abas, A. Kalair and N. Khan. Reviews of fossil fuels and future energy technologies. Futures, 2015, 69, 31-49.
4. T. L. Frölicher, M. Winton and J. L. Sarmiento. Continued global warming after CO_2 emissions stoppage. Nature Climate Change 2014, 4, 40-44.
5. R. W. Miles, G. Zoppi and I. Forbes. Inorganic photovoltaic cells. Mater. Today 2007, 10, 20–27.
6. L. I. Granone, F. Sieland, N. Zheng, R. Dillert and D. W. Bahnemann. Photocatalytic conversion of biomass into valuable products: a meaningful approach? Green Chem. 2018, 20, 1169-1192.
7. T. Hisatomi, J. Kubota and K. Domen. Recent advances in semiconductors for photocatalytic and photoelectrochemical water splitting. Chem. Soc. Rev 2014, 43, 7520.
8. W. Tu, Y. Zhou and Z. Zou. Photocatalytic conversion of CO_2 into renewable hydrocarbon fuels: state of the art accomplishment, challenges and prospects. Adv. Mater. 2014, 26, 4607–4626.
9. A. Li, T. Wang, X. X. Chang, Z. J. Zhao, C. C. Li, Z. Q. Huang, P. P. Yang, G. Y. Zhou and J. L. Gong. Tunable syngas production from photocatalytic CO_2 reduction with mitigated charge recombination driven by spatially separated cocatalysts. Chem. Sci. 2018, 9, 5334.
10. K. Iizuka, T. Wato, Y. Miseki, K. Saito and A. Kudo. Photocatalytic reduction of carbon dioxide over Ag cocatalyst loaded $ALa_4Ti_4O_{15}$ (A= Ca, Sr and Ba) using water as a reducing reagent. J. Am. Chem. Soc. 2011, 133, 20863–20868.

11. A. Anzai, N. Fukuo, A. Yamamoto and H. Yoshida. Highly selective photocatalytic reduction of carbon dioxide with water over silver loaded calcium titanate. Catal. Commun. 2017, 100, 134–138.
12. X. Zhu, A. Yamamoto and H. Yoshida. Alkaline hexatitanate photocatalysts with various morphologies for selective reduction of carbon dioxide with water. Dalt. Trans. 2021, 50, 7976–7983.
13. X. Zhu, A. Yamamoto, S. Imai, A. Tanaka, H. Kominami and H. Yoshida. Facet selective deposition of a silver manganese dual cocatalyst on potassium hexatitanate photocatalyst for highly selective reduction of carbon dioxide by water. Appl. Catal. B Environ. 2020, 274, 119085.
14. Z. Wang, K. Teramura, S. Hosokawa and T. Tanaka. Highly efficient photocatalytic conversion of CO_2 into solid CO using H_2O as a reductant over Ag modified $ZnGa_2O_4$. J. Mater. Chem. A 2015, 3, 11313–11319.
15. K. Teramura, H. Tatsumi, Z. Wang, S. Hosokawa and T. Tanaka. Photocatalytic conversion of CO_2 by H_2O over Ag loaded SrO modified Ta_2O_5. Bull. Chem. Soc. Jpn. 2015, 88, 431–437.
16. H. Nakanishi, K. Iizuka, T. Takayama, A. Iwase and A. Kudo. Highly active $NaTaO_3$ based photocatalysts for CO_2 reduction to from CO using water as the electron donor. ChemSusChem 2017, 10, 112–118.
17. S. Iguchi, K. Teramura, S. Hosokawa and T. Tanaka. A $ZnTa_2O_6$ photocatalyst synthesized via solid state reaction for conversion of CO_2 into CO in water. Catal. Sci. Technol. 2016, 6, 4978–4985.
18. M. Yamamoto, S. Yagi and T. Yoshida. Effect of Ag cocatalyst on CO_2 adsorption states over Ga_2O_3 photocatalyst. Catal. Today 2018, 303, 334–340.
19. X. Zhu, A. Anzai, A. Yamamoto and H. Yoshida. Silver loaded sodium titanate photocatalysts for selective reduction of carbon dioxide to carbon monoxide with water. Appl. Catal. B Environ. 2019, 243, 47–56.
20. S. Wang, K. Teramura, T. Hisatomi, K. Domen, H. Asakura, S. Hosokawa and T.

Tanaka. Effective driving of Ag loaded and Al doped $SrTiO_3$ under irradiation at $\lambda > 300$ nm for the photocatalytic conversion of CO_2 by H_2O. ACS Appl. Energy Mater. 2020, 3, 1468–1475.

21. S. Wang, K. Teramura, H. Asakura, S. Hosokawa and T. Tanaka. Effect of Zn in Ag loaded Zn modified $ZnTa_2O_6$ for photocatalytic conversion of CO_2 by H_2O. J. Phys. Chem. C 2021, 125, 1304–1312.
22. Z. Wang, K. Teramura, Z. A. Huang, S. Hosokawa, Y. Sakata and T. Tanaka. Tuning the selectivity toward CO evolution in the photocatalytic conversion of CO_2 with H_2O through the modification of Ag loaded Ga_2O_3 with $ZnGa_2O_4$. Catal. Sci. Technol. 2016, 6, 1025–1032.
23. R. Pang, K. Teramura, H. Asakura, S. Hosokawa and T. Tanaka. Effect of thickness of chromium hydroxide layer on Ag cocatalyst surface for highly selective photocatalytic conversion of CO_2 by H_2O. ACS Sustain. Chem. Eng. 2019, 7, 2083–2090.
24. N. Hoshi, M. Kato and Y. Hori. Electrochemical reduction of CO_2 on single crystal electrodes of silver Ag (111), Ag (100) and Ag (110). J. Electroanal. Chem. 1997, 440, 283–286.
25. M. Ishida, S. Kikkawa, K. Hori, K. Teramura, H. Asakura, S. Hosokawa and T. Tanaka. Effect of surface reforming via O_3 treatment on the electrochemical CO_2 reduction activity of a Ag cathode. ACS Appl. Energy Mater. 2020, 3, 6552–6560.
26. X. Feng, K. Jiang, S. Fan and M. W. Kanan. Grain boundary dependent CO_2 electrochemical activity. J. Am. Chem. Soc. 2015, 137, 4606–4609.
27. R. G. Mariano, K. McKelvey, H. S. White and M. W. Kanan. Selective increase in CO_2 electroreduction activity at grain boundary surface terminations. Science 2017, 358, 1187–1192.
28. R. Pang, K. Teramura, M. Morishita, H. Asakura, S. Hosokawa and T. Tanaka. Enhanced CO evolution for photocatalytic conversion of CO_2 by H_2O over Ca modified Ga_2O_3. Commun. Chem. 2020, 3, 1–8.

29. S. Wang, K. Teramura, T. Hisatomi, K. Domen, H. Asakura, S. Hosokawa and T. Tanaka. Dual Ag/Co cocatalyst synergism for the highly effective photocatalytic conversion of CO_2 by H_2O over Al-$SrTiO_3$. Chem. Sci. 2021, 12, 4940–4948.

30. X. Zhu, A. Yamamoto, S. Imai, A. Tanaka, H. Kominami and H. Yoshida. A silver-manganese dual catalyst for selective reduction of carbon dioxide over a potassium hexatitanate photocatalyst with water. Chem. Commun. 2019, 55, 13514–13517.

31. S. Wang, K. Teramura, T. Hisatomi, K. Domen, H. Asakura, S. Hosokawa and T. Tanaka. Highly selective photocatalytic conversion of carbon dioxide by water over Al-$SrTiO_3$ photocatalyst modified with silver-metal dual cocatalysts. ACS Sustain. Chem. Eng. 2021, 9, 9327–9335.

32. J. H. Yoon, Y. Zhou, M. G. Blaber, G. C. Schatz and S. Yoon. Surface plasmon coupling compositionally heterogeneous core-satellite nanoassemblies. J. Phys. Chem. Lett 2013, 4, 1371-1378.

33. M. Sadeghi, W. Liu, T. G. Zhang, P. Stavropoulos and B. Levy. Role of photoinduced charge carrier separation distance in heterogeneous photocatalysis: oxidative degradation of CH_3OH vapor in contact with Pt/TiO_2 and cofumed TiO_2-Fe_2O_3. J. Phys. Chem. 1996, 100, 19466-19474.

34. W. N. Wang, W. J. An, B. Ramalingam, S. Mukherjee, D. M. Niedzwiedzki, S. Gangopadhyay and P. Biswas. Size and structure matter: enhanced CO_2 photoreduction efficiently by size resolved ultrafine Pt nanoparticles on TiO_2 single crystals. J. Am. Chem. Soc 2012, 134, 11276-11281.

35. W. Yang, W. Ma, Z. Zhang and C. Zhao. Ligament size dependent electrocatalytic activity of nanoporous Ag network for CO_2 reduction. Faraday Discuss. 2018, 210, 289–299.

36. C. W. Li, J. Ciston and M. W. Kanan. Electroreduction of carbon monoxide to liquid fuel on oxide-derived nanocrystalline copper. Nature 2014, 508, 504–507.

Chapter 7

High selectivity toward CO evolution for the photocatalytic conversion of CO_2 by H_2O as an electron donor over Ag-loaded β-Ga_2O_3

Abstract

A wide range of investigations on Ag-loaded Ga_2O_3 have exhibited poor selectivity toward the evolution of CO during the photocatalytic conversion of CO_2 using H_2O as an electron donor. Herein, the performances of Ag-loaded commercial Ga_2O_3 (composite of α- and β-Ga_2O_3), pure α-, and β-Ga_2O_3 were examined for this reaction. Ag-loaded β-Ga_2O_3 exhibited high selectivity for CO evolution if the proper loading methods and Ag nanoparticle contents were controlled. Using the chemical reduction method with NaH_2PO_2, 2 wt% Ag nanoparticles on β-Ga_2O_3 produced CO with an activity of 201.3 μmol h^{-1} and selectivity of 83.5%. However, 8 wt% Ag nanoparticles were required to achieve the same selectivity when prepared using the photodeposition method. Ag-loaded α-Ga_2O_3 exhibited low selectivity toward CO evolution regardless of the loading extent and preparation method. By varying the amount of Ag-loaded β-Ga_2O_3 for photocatalytic conversion using H_2O, it was found that the selectivity toward CO evolution was largely dependent on the amounts of Ag-loaded β-Ga_2O_3 used for the photocatalytic conversion of CO_2 using H_2O. The reduction of O_2 occupies the active sites for H_2 evolution at high amounts of Ag-loaded β-Ga_2O_3, resulting in a high selectivity for CO evolution.

1. Introduction

The emission of greenhouse gases [1], mainly carbon dioxide (CO_2), has enhanced the effect of global warming [2] over the past 100 years. To address this challenge, various technologies for renewable energy [3] have been developed to replace fossil fuels. Among these alternative strategies, the utilization of solar energy [4] has attracted considerable attention owing to its sustainable and environmentally-friendly characteristics. This field can be divided into two branches from the perspective of energy conversion pathways: from solar to electricity directly, exemplified by silicon cells [5] and photovoltaic cells [6], and chemical pathways involving the conversion of biomass [7], water (H_2O) splitting [8], and CO_2 photoreduction [9]. Recently, the photocatalytic conversion of CO_2 using H_2O as the electron donor has been achieved over many photocatalysts including Ag-loaded $NaTaO_3$ [10], $CaTiO_3$ [11], Ga_2O_3 [12], and $ZnGa_2O_4$ [13] among others. The successful photocatalytic conversion of CO_2 by H_2O should simultaneously satisfy a balance between photogenerated electrons and holes (Eq. (1)) and high selectivity (Eq. (2)).

$$e^-/h^+ = (2R_{HCOOH} + 2R_{CO} + 4R_{HCHO} + 6R_{CH_3OH} + 8R_{CH_4} + 2R_{H_2})/4R_{O_2} \quad (1)$$

$$\text{Selectivity} = (2R_{HCOOH} + 2R_{CO} + 4R_{HCHO} + 6R_{CH_3OH} + 8R_{CH_4})/(2R_{HCOOH} + 2R_{CO} + 4R_{HCHO} + 6R_{CH_3OH} + 8R_{CH_4} + 2R_{H_2}) \times 100\% \quad (2)$$

Many studies have revealed that bare Ga_2O_3 exhibits low selectivity toward the evolution of CO during the photocatalytic conversion of CO_2 by H_2O when only Ag nanoparticles are used as a cocatalyst. Kawaguchi et al. [14] compared the performances of commercial and homemade Ga_2O_3 modified with Ag nanoparticles for the photocatalytic conversion of CO_2 using H_2O. Their results showed that CO evolution selectivity failed to exceed 40%, regardless of loading method. Li et al. [15] achieved a selectivity of 65.3% for the formation of CO on Ni-doped β-Ga_2O_3 modified by Ag nanoparticles. However, the CO production activity was quite low. Previously [12,16–18], a similar level of selectivity toward the evolution of CO over Ag-loaded Ga_2O_3 (29.9–51.0%) for the photocatalytic conversion of CO_2 by H_2O was achieved by Teramura et al.. In contrast, modifications of

Zn species [19,20] as well as rare earth elements such as Pr and Ce [16,17] on Ga_2O_3 were shown to enhance the selectivity toward CO evolution (>80%) with Ag nanoparticles as the cocatalyst. In addition, a shell of $Cr(OH)_3$ covering the surface of Ag-loaded Ga_2O_3 promoted the selectivity for CO evolution (83%) during the photocatalytic conversion of CO_2 by H_2O [12]. Given these phenomena, it is possible that the selectivity for CO evolution over Ag-loaded Ga_2O_3 during the photocatalytic conversion of CO_2 by H_2O is largely dependent on the surface properties of Ga_2O_3. Herein, the performances of Ag-loaded commercial Ga_2O_3 (containing α and β phases) and homemade pure α- and β-Ga_2O_3 were examined for the photocatalytic conversion of CO_2 using H_2O. High selectivity toward CO evolution was achieved over Ga_2O_3 even though only Ag nanoparticles were used as the cocatalyst by controlling the loading extent and methods of the Ag nanoparticles. In addition, the selectivity was significantly affected by the phases of Ga_2O_3.

2. Experimental

2.1. Photocatalyst preparation

Commercial Ga_2O_3 (c-Ga_2O_3) was purchased from KOJUNDO CHEMICAL LABORARTORY Co., Ltd.. For the synthesis of α-Ga_2O_3, GaOOH was first fabricated by protonation of $NaGaO_2$ by HCl. The obtained GaOOH was dried at 358 K and washed at 358 K for 1 h. After drying, the powder was calcined at 723 K for 3 h. The β-Ga_2O_3 was obtained by calcinating commercial powder at 1423 K for 24 h in an aluminum crucible. The Ag nanoparticles were loaded into the above photocatalysts by various methods, including photodeposition, impregnation, and chemical reduction. The loading conditions are described in detail in Table 1.

Table 1. Synthesis conditions for photocatalysts used in this work.

Entry	Sample	Precursors	Conditions	Post-treatment
1	Ag/c-Ga_2O_3 (CR_P)	0.5 g commercial Ga_2O_3, 100 mL H_2O, *x* wt% Ag^+ ($AgNO_3$), NaH_2PO_2 (5 times of molar Ag^+)	358 K, 1.5 h	Washed by H_2O at R.T.
2	Ag/c-Ga_2O_3 (CR_B)	2 g commercial Ga_2O_3, 400 mL H_2O, 2 wt% Ag^+ ($AgNO_3$), $NaHBO_4$ (5 times of molar Ag^+)	358 K, 1.5 h	Washed by H_2O at R.T.
3	Ag/c-Ga_2O_3 (CR_CP)	0.5 g commercial Ga_2O_3, 100 mL H_2O, 2 wt% Ag^+ ($AgNO_3$), NaH_2PO_2 (5 times of molar Ag^+), 0.4 g citrate acid	358 K, 1.5 h	Washed by H_2O at R.T.
4	Ag/β-Ga_2O_3 (CR_P)	0.5 g β-Ga_2O_3, 100 mL H_2O, 2 wt% Ag^+ ($AgNO_3$), NaH_2PO_2 (5 times of molar Ag^+)	358 K, 1.5 h	Washed by H_2O at R.T.
5	Ag/α-Ga_2O_3 (CR_P)	0.5 g α-Ga_2O_3, 100 mL H_2O, *x* wt% Ag^+ ($AgNO_3$), NaH_2PO_2 (5 times of molar Ag^+)	358 K, 1.5 h	Washed by H_2O at R.T.
6	Ag/β-Ga_2O_3 (IM)	0.25 g β-Ga_2O_3, 2 wt% Ag^+ ($AgNO_3$), 2 mL H_2O, impregnation	723 K, 3 h	
7	Ag/β-Ga_2O_3 (PD)	0.25 g β-Ga_2O_3, *x* wt% Ag^+ ($AgNO_3$), 1000 mL H_2O.	Photodeposition 0.5 h in Ar 30 mL/min	

2.2. Photocatalyst characterization

The structures of the obtained Ga_2O_3 used herein were determined using a Rigaku Ultima IV powder diffractometer (Cu Kα, 40 kV, and 40 mA). The morphologies of the photocatalysts were observed using a field-emission scanning electron microscope (FE-SEM, SU-8220, Hitachi High-Technologies). UV-vis diffuse reflectance spectroscopy (UV-vis DRS) of the photocatalysts was performed using a JASCO V-670 spectrometer.

2.3. Reaction procedure

An inner irradiation reactor equipped with a quartz jacket was used for the photocatalytic conversion of CO_2 using H_2O. The reactor was connected to cooling water to maintain the temperature between 298 and 303 K during the reactions. The light source was a 400 W high pressure mercury lamp (Sen Lights Corp.). Before the reactions, the system was purged with CO_2 to remove any residual air. The production of H_2, O_2, and CO was detected using GC-8A (Shimadzu Corp) gas chromatographs with TCD and FID detectors.

3. Results and Discussion

Figure 1(a) shows the XRD patterns of the Ga-containing samples fabricated herein. The structure of GaOOH was successfully obtained by the protonation of $NaGaO_2$ by HCl. After calcination at 723 K, the GaOOH phase was converted to pure α-Ga_2O_3, as shown

in Figure 1(b). According to Figure 1(b), c-Ga_2O_3 consisted of α- and β-Ga_2O_3 simultaneously, and pure β-Ga_2O_3 was obtained via calcination of c-Ga_2O_3 at 1423 K for 24 h. However, the half-width of the crystalline phase in α-Ga_2O_3 was visibly larger than that in β-Ga_2O_3, implying that the crystalline size of α-Ga_2O_3 was much smaller than that of β-Ga_2O_3.

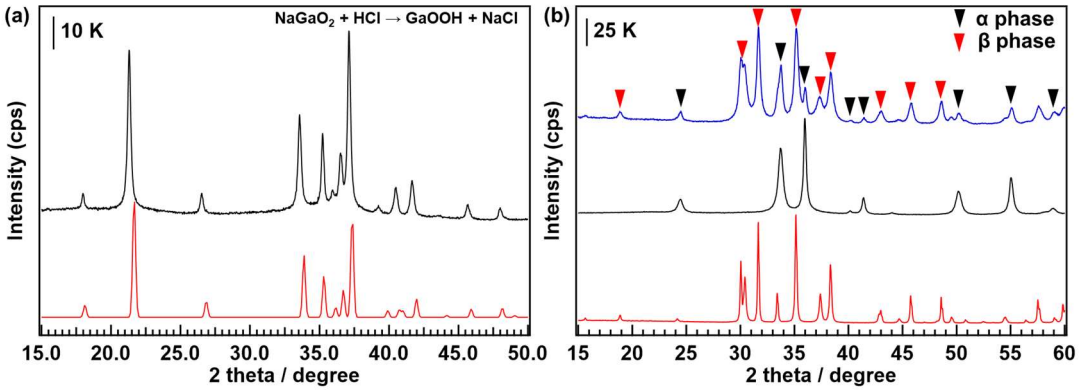

Figure 1. XRD patterns of (a) synthesized GaOOH (black) and reference from ISCD database (red); (b) c-Ga_2O_3 (blue), α-Ga_2O_3 (black), and β-Ga_2O_3 (red).

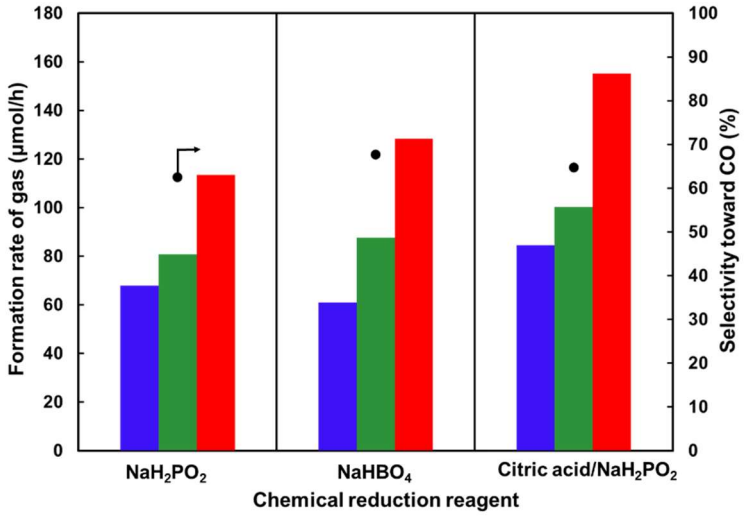

Figure 2. Formation rates of H_2 (blue), O_2 (green), and CO (red) as well as selectivity toward CO evolution (black dots) for the photocatalytic conversion of CO_2 by H_2O over Ag/c-Ga_2O_3 (CR_P), Ag/c-Ga_2O_3 (CR_B), and Ag/c-Ga_2O_3 (CR_CP). Photoirradiation time: 0.5 h; Ag content: 2 wt%; photocatalyst loading: 0.25 g; reaction solution: 1.0 L of a 0.1 M $NaHCO_3$ aqueous solution; CO_2 flow rate: 30 mL min^{-1}; light source: 400 W

high-pressure Hg lamp.

Figure 2 shows the photocatalytic performance of Ag-loaded c-Ga_2O_3 fabricated via chemical reduction of NaH_2PO_2 (Ag/c-Ga_2O_3 (CR_P)), $NaHBO_4$ (Ag/c-Ga_2O_3 (CR_B)), and a mixture of citric acid and NaH_2PO_2 (Ag/ c-Ga_2O_3 (CR_CP)) for the photocatalytic conversion of CO_2 by H_2O. A loading of 2 wt% Ag/c-Ga_2O_3 (CR_P) exhibited 62.5% selectivity toward CO evolution during the photocatalytic conversion of CO_2 by H_2O, wherein CO and H_2 were formed at rates of 113.4 and 68.0 μmol h^{-1}, respectively. Although the formation rate of CO was slightly higher for Ag/c-Ga_2O_3 (CR_B) (128.4 μmol h^{-1}) and Ag/c-Ga_2O_3 (CR_CP) (155.3 μmol h^{-1}), the selectivity was similar (62.5% to 67.8%).

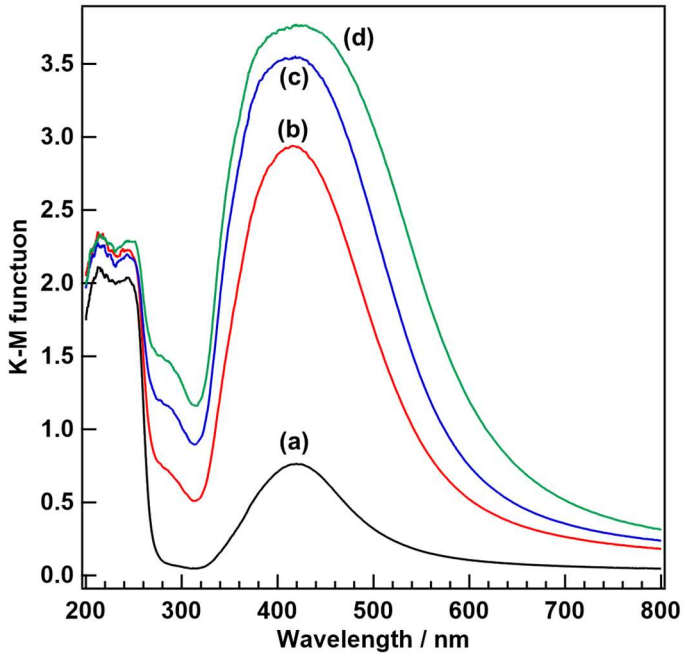

Figure 3. UV-vis diffuse reflectance spectra of c-Ga_2O_3 with various Ag loadings by chemical reduction of NaH_2PO_2: (a) 1 wt%, (b) 2 wt%, (c) 3 wt%, and (4) 4 wt% Ag.

Figure 3 shows the UV-vis diffuse reflectance spectra of c-Ga_2O_3 loaded with optimized amounts of Ag nanoparticles via chemical reduction with NaH_2PO_2. A clear surface plasmon resonance (SPR) absorption peak was observed at 420 nm for 1 wt% Ag

nanoparticle loading (Figure 3(a)). With increased loading to 2 wt% Ag, the absorption intensity was significantly enhanced, whereas the absorptive position remained unchanged, indicating that the Ag nanoparticle size was constant. A shoulder absorption peak appeared at 290 nm, which was attributed to the transverse plasmon absorption band of nonspherical Ag nanoparticles. Higher loading of Ag nanoparticles did not change the absorption positions but further enhanced the intensities of both the transverse and longitudinal absorption peaks. Figure 4 shows the SEM images of Ag-loaded c-Ga_2O_3 samples corresponding to those in Figure 3. The Ag nanoparticle size was approximately 10 nm at 1 wt% loading and the coverage ratio of Ag nanoparticles on the surface of c-Ga_2O_3 was very low (Figure 4(a)). As the loading was increased to 2 wt% (Figure 4(b)), the near-elliptical Ag nanoparticles remained largely unchanged (approximately 10 nm), as supported by Figure 3. It was previously reported that the absorption bands of metal nanoparticles largely depend on their sizes [21,22]. However, the coverage ratio of Ag nanoparticles on the surfaces of c-Ga_2O_3 at this loading visibly increased, resulting in a drastically enhanced absorption intensity. As shown in Figure 4(c) and 4(d), 3 and 4 wt% Ag/c-Ga_2O_3 contained similarly sized Ag nanoparticles as in the 2 wt% Ag/c-Ga_2O_3 sample. This indicates that the chemical reduction by NaH_2PO_2 changed the coverage ratio on the surface of c-Ga_2O_3 while maintaining the Ag nanoparticle size.

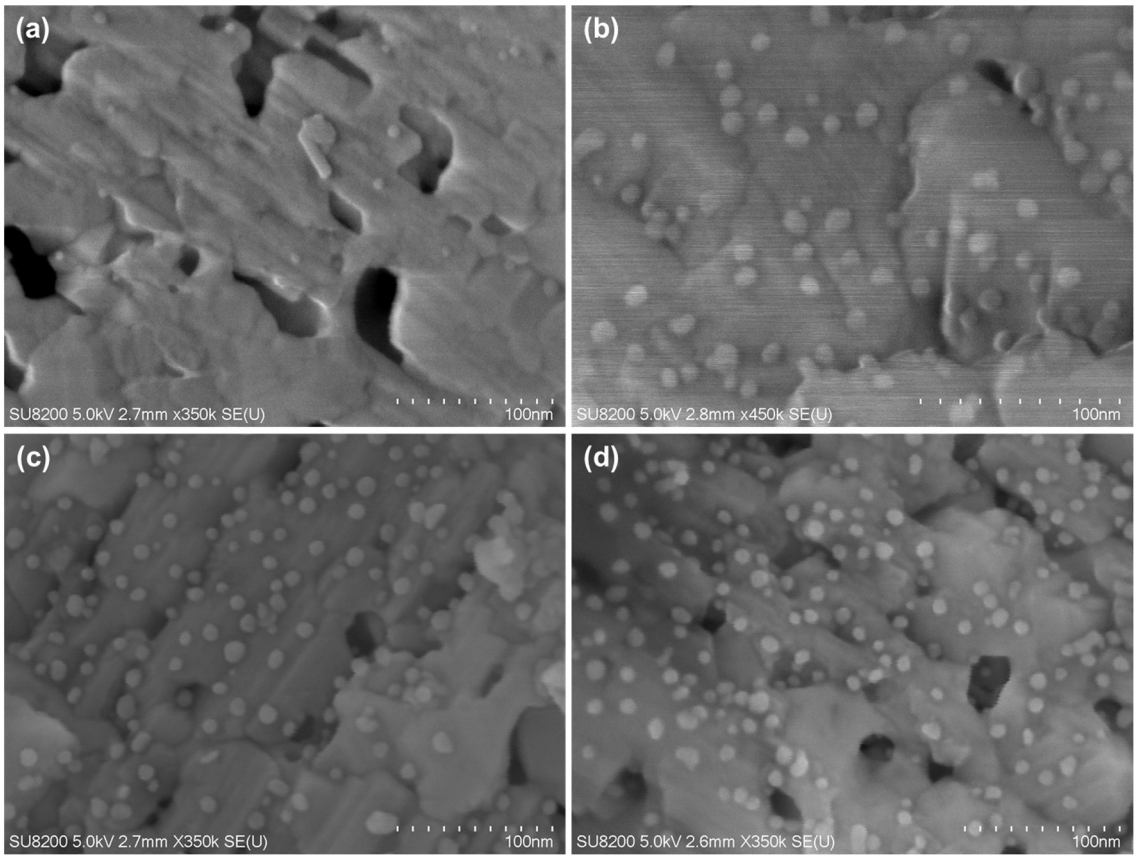

Figure 4. SEM images of Ag/c-Ga_2O_3 (CR_P) at various loadings: (a) 1 wt%, (b) 2 wt%, (c) 3 wt%, and (d) 4 wt% Ag.

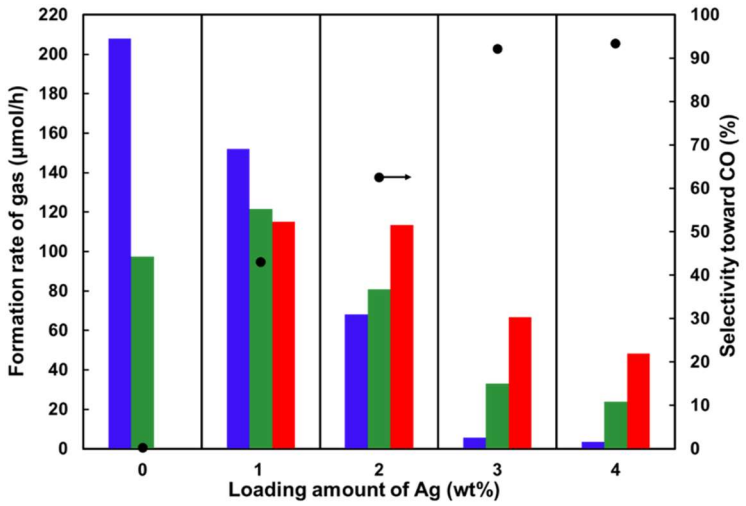

Figure 5. Formation rates of H_2 (blue), O_2 (green), and CO (red) as well as selectivity toward CO evolution (black dots) for the photocatalytic conversion of CO_2 by H_2O over Ag/c-Ga_2O_3 (CR_P) with various Ag cocatalyst loadings. Photoirradiation time: 0.5 h;

photocatalyst content: 0.25 g; reaction solution: 1.0 L of a 0.1 M $NaHCO_3$ aqueous solution; CO_2 flow rate: 30 mL min^{-1}; light source: 400 W high-pressure Hg lamp.

Figure 5 shows the catalytic performance of Ag/c-Ga_2O_3 (CR_P) with controlled Ag loading for the photocatalytic conversion of CO_2 using H_2O. Bare c-Ga_2O_3 produced H_2 with an activity of 207.9 μmol h^{-1}, whereas CO was produced with an activity of just 0.3 μmol h^{-1} for the photocatalytic conversion of CO_2 by H_2O. When c-Ga_2O_3 was modified with 1 wt% Ag nanoparticles, the formation rate of CO increased to 115.1 μmol h^{-1} and that of H_2 was suppressed to 152.0 μmol h^{-1}. The selectivity toward CO evolution was 43%, similar to the results reported previously [12,14,17]. Interestingly, the selectivity toward CO evolution drastically increased to 93.4% at 4 wt% Ag nanoparticles. To the best knowledges of the author, such a high selectivity toward CO evolution over bare Ga_2O_3 has not been reported when only Ag nanoparticles are used as the cocatalyst (generally selectivities of <50% have been achieved [12,14,16–18]). Following this trend, the formation rate of H_2 was suppressed to 3.4 μmol h^{-1}, whereas that of CO remained stable at 2 wt% then decreased to 48.4 μmol h^{-1} at 3 wt%. Based on Figures 3 and 4, the properties of the Ag nanoparticles loaded on c-Ga_2O_3, including their size and shape, remained unchanged with varying loadings. Thus, it could be concluded that the increased selectivity toward CO evolution was caused by the coverage ratio of Ag nanoparticles on the surfaces of c-Ga_2O_3. It has been reported that the α- and β-Ga_2O_3 phases in c-Ga_2O_3 exhibit positive [23] and negative [24] zeta potentials at pH values of the reactions in this work (about 6.8), respectively, whereas Ag nanoparticles exhibit negative zeta potential [25–27]. Therefore, the Ag nanoparticles formed during chemical reduction are selectively captured by the α phase of Ga_2O_3 owing to the Coulomb force. With saturated coverage of Ag nanoparticles on the α phase, Ag nanoparticles were then deposited on the surface of β phase of Ga_2O_3, as depicted in Scheme 1. In other words, Ag-loaded β-Ga_2O_3 showed high selectivity toward CO evolution for the photocatalytic conversion of CO_2 by H_2O.

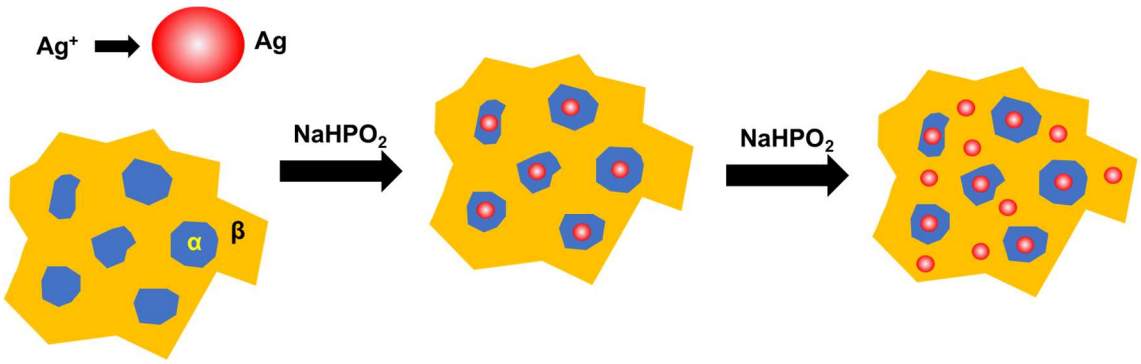

Scheme 1. The loading process of Ag nanoparticles on c-Ga_2O_3.

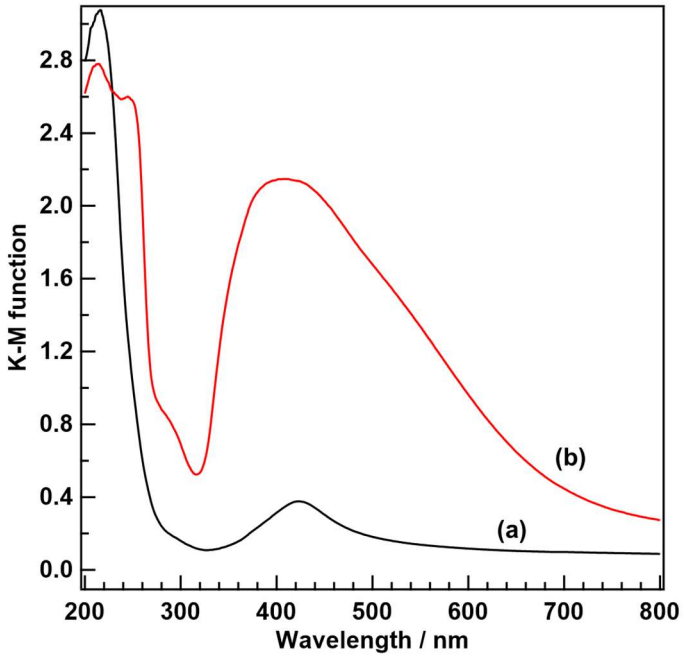

Figure 6. Absorption spectra of (a) Ag/α-Ga_2O_3 (CR_P) and (b) Ag/β-Ga_2O_3 (CR_P) with 2 wt% Ag.

Figure 6 shows the UV-vis diffuse reflectance spectra of 2 wt% Ag-loaded α-Ga_2O_3 and β-Ga_2O_3 obtained via chemical reduction with NaH_2PO_2. The α-Ga_2O_3 and β-Ga_2O_3 showed absorption edges of 240 and 260 nm, respectively, corresponding to band gaps of 5.17 [28] and 4.77 eV [29], respectively. The Ag nanoparticles loaded in α-Ga_2O_3 exhibited an absorption band at 422 nm, whereas the peak was shifted to 410 nm for the Ag nanoparticles on β-Ga_2O_3. Figure 7 compares the photocatalytic performances of Ag/α-

Ga_2O_3 (CR_P) and Ag/β-Ga_2O_3 (CR_P) with 2 wt% Ag nanoparticle loading, including the product formation rate and selectivity toward CO evolution. Ag/α-Ga_2O_3 (CR_P) produced CO (25.3 μmol h^{-1}) with a selectivity of 33.4%. For Ag/β-Ga_2O_3 (CR_P), the CO formation rate reached 201.3 μmol h^{-1}, whereas that of H_2 was lowered to as much as 39.8 μmol h^{-1}. The selectivity of 83.5% over Ag/β-Ga_2O_3 (CR_P) conformed to the phenomenon observed in Figure 5 and Scheme 1, and the β phase of Ga_2O_3 modified with Ag nanoparticles accounted for the high selectivity toward CO evolution. Figure 8 shows the photocatalytic performance of the optimized Ag-loaded α-Ga_2O_3 prepared via chemical reduction with NaH_2PO_2 for the photocatalytic conversion of CO_2 by H_2O. The H_2 formation rate was suppressed from 50.2 to 31.0 μmol h^{-1} as the loading of Ag nanoparticles increased from 2 to 5 wt%, whereas the CO evolution was largely unaffected (25.3 vs. 23.5 μmol h^{-1}). The H_2 evolution was further inhibited to 14.4 μmol h^{-1} when the loading of Ag nanoparticles reached 8 wt%, resulting in enhanced selectivity toward CO evolution (61.9%). Although a stronger suppression of H_2 evolution (12.4 μmol h^{-1}) was observed at higher Ag nanoparticle loading (10 wt%), the activity and selectivity for CO evolution also started to decline (16.4 μmol h^{-1}, 57.0%, respectively). This implies that the low selectivity for CO evolution over Ag-loaded α-Ga_2O_3 is likely caused by the properties of α-Ga_2O_3 rather than the Ag nanoparticle loading.

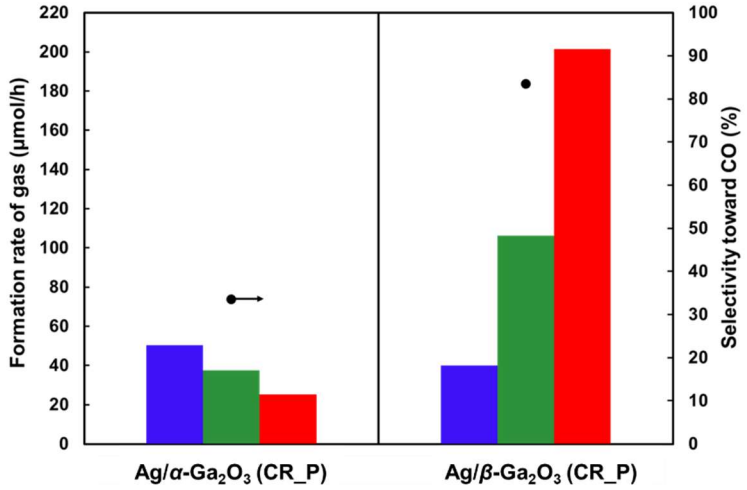

Figure 7. Formation rates of H_2 (blue), O_2 (green), and CO (red) as well as selectivity toward CO evolution (black dots) for the photocatalytic conversion of CO_2 by H_2O over

Ag/α-Ga_2O_3 (CR_P) and Ag/β-Ga_2O_3 (CR_P). Photoirradiation time: 0.5 h; photocatalyst content: 0.25 g; Ag loading: 2 wt%; reaction solution: 1.0 L of a 0.1 M $NaHCO_3$ aqueous solution; CO_2 flow rate: 30 mL min^{-1}; light source: 400 W high-pressure Hg lamp.

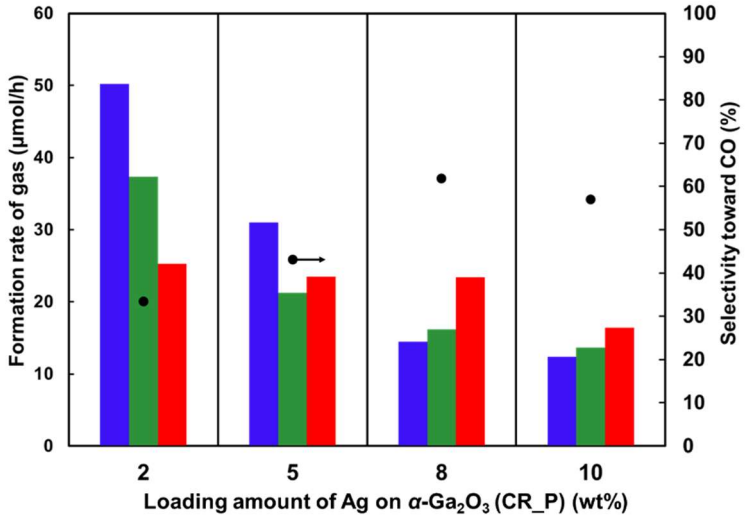

Figure 8. Formation rates of H_2 (blue), O_2 (green), and CO (red) as well as selectivity toward CO evolution (black dots) for the photocatalytic conversion of CO_2 by H_2O over Ag/α-Ga_2O_3 (CR_P) with controlled loading of Ag nanoparticles. Photoirradiation time: 0.5 h; photocatalyst content: 0.25 g; reaction solution: 1.0 L of a 0.1 M $NaHCO_3$ aqueous solution; CO_2 flow rate: 30 mL min^{-1}; light source: 400 W high-pressure Hg lamp.

Figure 9 shows the photocatalytic performance of 2 wt% Ag-loaded β-Ga_2O_3 loaded by various methods, including chemical reduction, impregnation (IMP), and photodeposition (PD). Ag/β-Ga_2O_3 (IMP) showed 70.9% selectivity toward CO evolution with an activity of 120.4 μmol h^{-1}. In contrast, Ag/β-Ga_2O_3 (PD) produced CO with a selectivity of 47.4% over H_2, even though the activity reached 163.1 μmol h^{-1}. Figure 10 shows the influence of the Ag loading on β-Ga_2O_3 through the photodeposition method on the photocatalytic conversion of CO_2 using H_2O. Similar to Ag/α-Ga_2O_3 (CR_P), the H_2 formation rates were significantly suppressed (181.4 to 74.1 and 52.3 μmol h^{-1}) over Ag/β-Ga_2O_3 (PD) when the Ag nanoparticle loadings were increased from 2 to 4 and 8 wt%, respectively. Interestingly, the CO evolution activity was not significantly affected

with increased Ag nanoparticle loading (163.2, 191.1, and 187.6 μmol h^{-1} respectively). As a result, selectivity toward CO evolution was effectively increased from 47.4% to 78.2%.

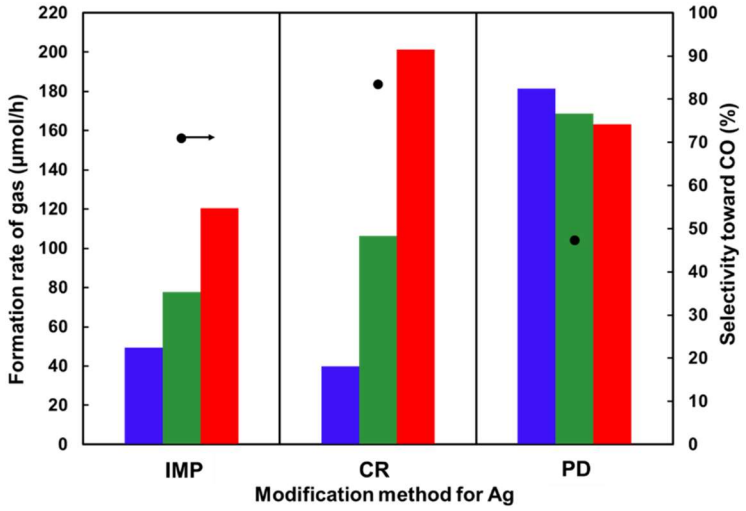

Figure 9. Formation rates of H_2 (blue), O_2 (green), and CO (red) as well as selectivity toward CO evolution (black dots) for the photocatalytic conversion of CO_2 by H_2O over Ag/β-Ga_2O_3 loaded through impregnation (IM), chemical reduction (NaH_2PO_2), and photodeposition (PD) methods. Photoirradiation time: 0.5 h; photocatalyst content: 0.25 g; Ag loading: 2 wt%; reaction solution: 1.0 L of a 0.1 M $NaHCO_3$ aqueous solution; CO_2 flow rate: 30 mL min^{-1}; light source: 400 W high-pressure Hg lamp.

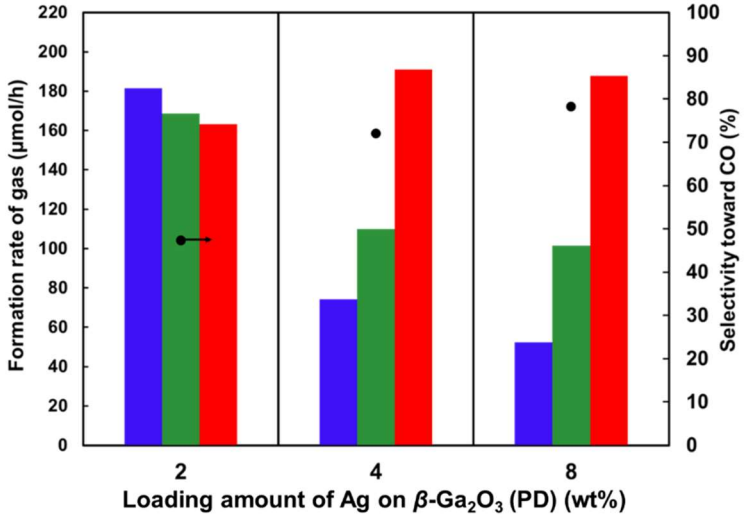

Figure 10. Formation rates of H_2 (blue), O_2 (green), and CO (red) as well as selectivity

toward CO evolution (black dots) for the photocatalytic conversion of CO_2 by H_2O over Ag/β-Ga_2O_3 (PD) with controlled loading of Ag nanoparticles. Photoirradiation time: 0.5 h; photocatalyst content: 0.25 g; reaction solution: 1.0 L of a 0.1 M $NaHCO_3$ aqueous solution; CO_2 flow rate: 30 mL min^{-1}; light source: 400 W high-pressure Hg lamp.

The origin of the high selectivity toward CO evolution over Ag-loaded β-Ga_2O_3 for the photocatalytic conversion of CO_2 using H_2O was also investigated. Figure 11 shows the dependence of Ag/β-Ga_2O_3 (CR_P) loading on selectivity toward CO evolution for the photocatalytic conversion of CO_2 using H_2O. 5 mg Ag/β-Ga_2O_3 (CR_P) produced H_2 and CO with activities of 11.4 and 7.3 μmol h^{-1} which could be normalized as 2280 and 1460 μmol g^{-1} h^{-1}, respectively. When the amount of catalyst was increased to 53 mg, CO evolution selectivity increased from 39.2% to 72.1% and the normalized activities for H_2 and CO were 433.9 and 1124.5 μmol g^{-1} h^{-1}, respectively. At a catalyst loading of 106 mg, the H_2 formation rate decreased to 266.0 μmol g^{-1} h^{-1}, whereas 867.9 μmol g^{-1} h^{-1} for CO, respectively. At 250 mg, the H_2 formation rate dropped to 159.2 μmol g^{-1} h^{-1} but that of CO (805.2 μmol g^{-1} h^{-1}) remained largely unchanged. The normalized activities imply that H_2 evolution was drastically suppressed with increasing Ag/β-Ga_2O_3 (CR_P) loading, whereas CO was negligibly affected. Moreover, Figure 12 shows the dependence of the 8 wt% Ag/β-Ga_2O_3 (PD) photocatalyst loading on the CO evolution selectivity for the photocatalytic conversion of CO_2 by H_2O. The loading of 5 mg Ag/β-Ga_2O_3 (PD) produced H_2 with an activity of 14.8 μmol h^{-1}, greatly exceeding that of CO (3.3 μmol h^{-1}). When the amount of photocatalyst was increased to 51 mg, the H_2 and CO formation rates increased 38.5 and 51.9 μmol h^{-1}, respectively. Correspondingly, the selectivity for CO evolution increased from 18.2% to 57.4%. Higher amounts of Ag/β-Ga_2O_3 (PD) (106 and 250 mg) exhibited limited effects on the evolution of H_2 (45.5 and 52.3 μmol h^{-1} respectively), whereas the CO formation rates increased by 2.1 and 3.6 times (107.9 and 187.6 μmol h^{-1}), respectively. Consequently, the selectivity toward CO evolution increased to 78.2% at 250 mg.

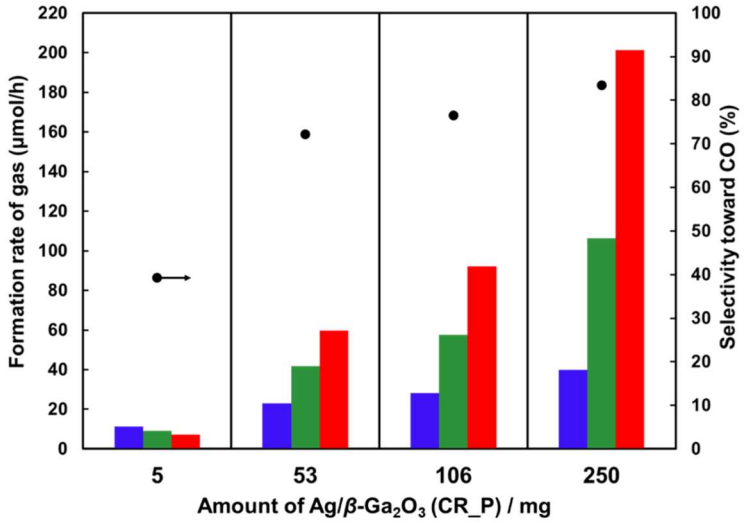

Figure 11. Formation rates of H_2 (blue), O_2 (green), and CO (red) as well as selectivity toward CO evolution (black dots) for the photocatalytic conversion of CO_2 by H_2O over different amounts of Ag/β-Ga_2O_3 (CR_P). Photoirradiation time: 0.5 h for each amount; Ag loading: 2 wt%; reaction solution: 1.0 L of a 0.1 M $NaHCO_3$ aqueous solution; CO_2 flow rate: 30 mL min^{-1}; light source: 400 W high-pressure Hg lamp.

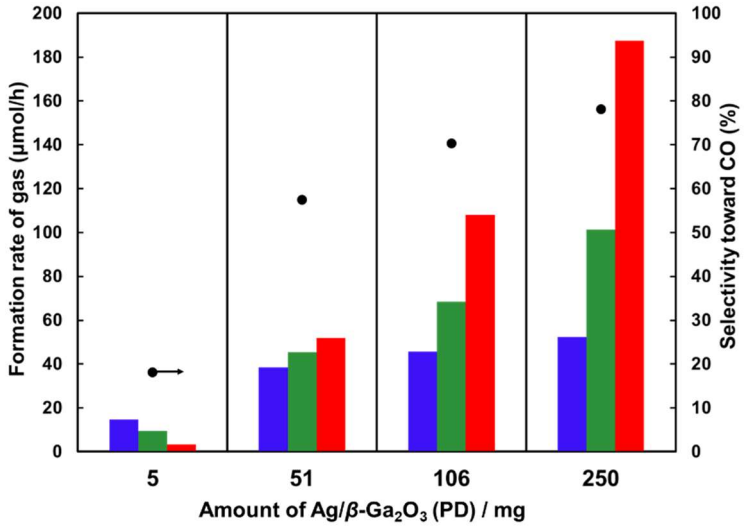

Figure 12. Formation rates of H_2 (blue), O_2 (green), and CO (red) as well as selectivity toward CO evolution (black dots) for the photocatalytic conversion of CO_2 by H_2O over different amounts of Ag/β-Ga_2O_3 (PD). Photoirradiation time: 0.5 h for each amount; Ag loading: 8 wt%; reaction solution: 1.0 L of a 0.1 M $NaHCO_3$ aqueous solution; CO_2 flow

rate: 30 mL min^{-1}; light source: 400 W high-pressure Hg lamp.

As shown in Figure 5, 0.25 g bare Ga_2O_3 failed to produce CO with high selectivity during the photocatalytic conversion of CO_2 by H_2O, indicating that Ag nanoparticles are essential for achieving high selectivity. However, the dependence of CO selectivity on the amount of Ag-loaded β-Ga_2O_3 implied that the Ag nanoparticles were not the sole contributor. Scheme 2 depicts the proposed mechanism by which Ag-loaded β-Ga_2O_3 photocatalysts obtained from proper synthesis methods exhibit high selectivity toward CO evolution in the photocatalytic conversion of CO_2 by H_2O. Undoubtedly, higher amounts of photocatalysts increase the number of photocatalyst particles, which would correspond to increased O_2 evolution from H_2O. A high concentration of aqueous O_2 and a large number of suspended photocatalyst particles would inevitably allow for sufficient contact between O_2 and the particles. Because the redox potential of O_2 is much lower than that of protons and the reduction of O_2 consumes large amounts of protons, O_2 would selectively poison the active sites for H_2 evolution. Finally, O_2 reduction at the sites of H_2 evolution and H_2O oxidation at the sites of O_2 evolution forms a dynamic loop, resulting selective suppression of H_2 evolution relative to CO. However, the O_2 and photocatalyst particles failed to sufficiently contact each other because of the low O_2 and particle concentrations when the amount of photocatalyst was kept low levels such as 5.0 mg. As a result, the active sites for H_2 evolution were not poisoned by O_2 reduction. In this case, CO is produced with poor selectivity from the photocatalytic conversion of CO_2 by H_2O. In other words, the high selectivity for CO evolution was not caused by the Ag nanoparticles alone, but by the synergistic effects between the Ag nanoparticles and O_2 poisoning of the active sites for H_2 evolution.

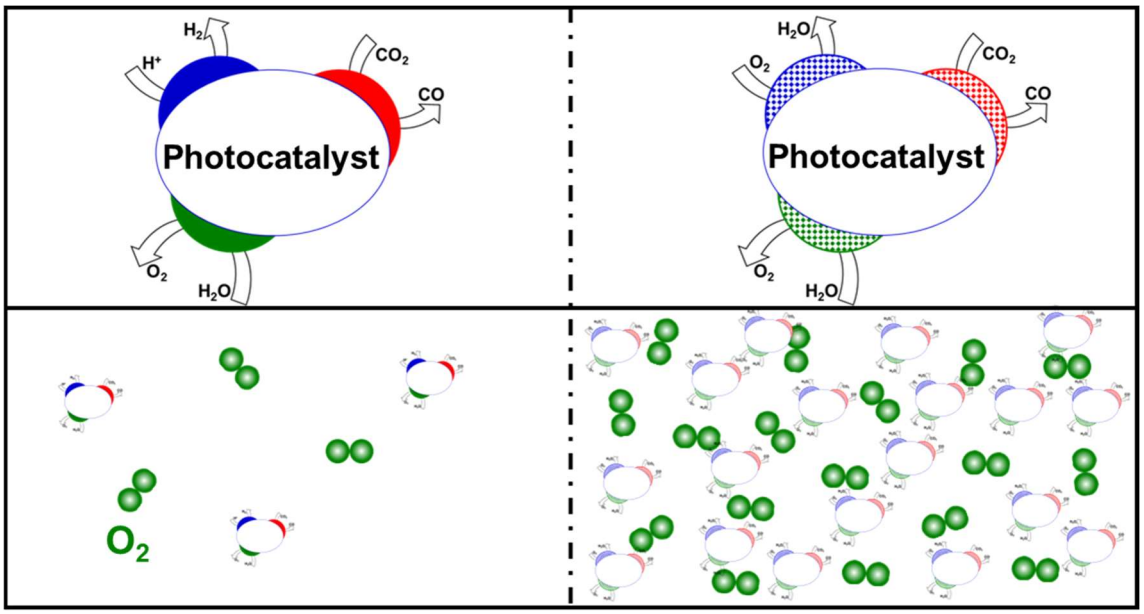

Scheme 2. Dependence of CO evolution selectivity on the amount of photocatalyst used in the photocatalytic conversion of CO_2 by H_2O.

To confirm the proposed mechanism, the dependence of CO evolution selectivity on the amount of photocatalyst Ag/α-Ga_2O_3 (CR_P) (2 wt%) and Ag/β-Ga_2O_3 (PD) (2 wt%) was examined, as presented in Figure 13. From Figure 13(a), 11 mg of Ag/α-Ga_2O_3 (CR_P) prepared via chemical reduction method produced CO with an activity of 13.9 μmol h^{-1} and selectivity of 39.8%. The selectivity toward CO during the photocatalytic conversion of CO_2 by H_2O was not promoted (33.5%), producing CO and H_2 at 25.3 and 50.2 μmol h^{-1}, respectively, even when 250 mg of Ag/α-Ga_2O_3 (CR_P) was used. This indicates that the evolution of H_2 over Ag/α-Ga_2O_3 (CR_P) was not selectively suppressed with increasing amounts of photocatalysts. A similar trend was also observed for Ag/β-Ga_2O_3 (PD), as shown in Figure 13(b), where 5.6 mg Ag/β-Ga_2O_3 (PD) showed a selectivity of 23.9% toward CO evolution and CO and H_2 formation rates were 6.6 and 21.1 μmol h^{-1}, respectively. The selectivity increased to 50.4% with formation rates of 68.0 and 67.0 μmol h^{-1} for CO and H_2, respectively, when 101 mg of photocatalyst was used. However, the selectivity (47.4%) for CO evolution did not further increase with higher photocatalyst loadings (250 mg), even though the formation rates of CO (163.1 μmol h^{-1}) and H_2 (181.4

μmol h^{-1}) significantly increased.

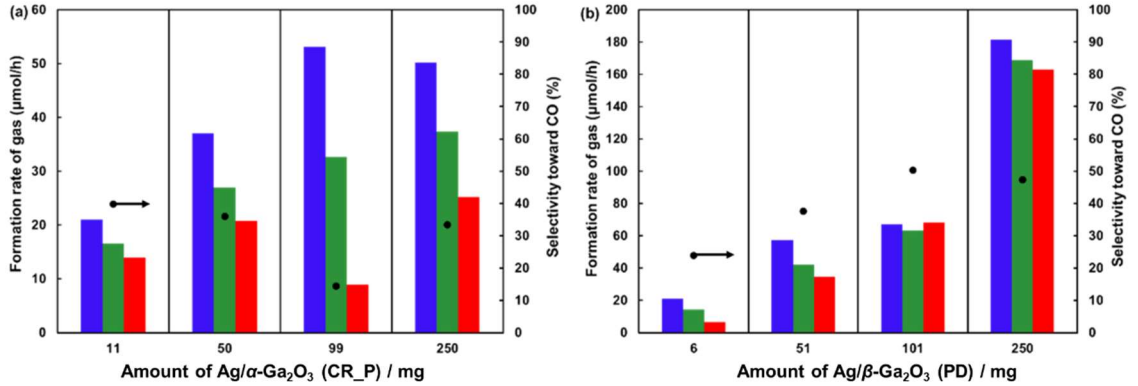

Figure 13. Formation rates of H_2 (blue), O_2 (green), and CO (red) as well as selectivity toward CO evolution (black dots) for the photocatalytic conversion of CO_2 by H_2O over different amounts of (a) Ag/α-Ga_2O_3 (CR_P) and (b) Ag/β-Ga_2O_3 (PD). Photoirradiation time: 0.5 h for each amount; Ag loading: 2 wt%; reaction solution: 1.0 L of a 0.1 M $NaHCO_3$ aqueous solution; CO_2 flow rate: 30 mL min^{-1}; light source: 400 W high-pressure Hg lamp.

4. Conclusion

Herein, the amounts and loading methods of Ag nanoparticles, including chemical reduction, photodeposition, and impregnation, were optimized on commercial Ga_2O_3 (composite of α-Ga_2O_3 and β-Ga_2O_3) as well as pure α-Ga_2O_3 and β-Ga_2O_3 photocatalysts for the photocatalytic conversion of CO_2 using H_2O as the electron donor. High selectivity towards CO evolution was achieved for this reaction when the proper catalyst amounts and loading methods were controlled using β-Ga_2O_3 as a starting material. After optimizing the amount of Ag-loaded β-Ga_2O_3 catalyst, the high CO evolution selectivity was determined to largely depend on the amount of the photocatalyst present. A large amount of Ag-loaded β-Ga_2O_3 enhanced active site poisoning for the evolution of H_2 via O_2 reduction, indirectly promoting selectivity toward CO evolution.

References

1. C. Oertel, J. Matschullat, K. Zurba, F. Zimmermann and S. Erasmi. Chemie der Erde 2016, 76, 327–352.
2. W. D. Nordhaus. American Economic Review 2006, 96, 2, 31-34.
3. N. L. Panwar, S. C. Kaushik and S. Kothari. Renew. Sustain. Energy Rev. 2011, 15, 1513–1524.
4. N. Kannan and D. Vakeesan. Renew. Sustain. Energy Rev. 2016, 62, 1092–1105.
5. A. Wang, J. Zhao and M. Green. Appl. Phys. Lett. 1990, 57, 602–604.
6. B. Parida, S. Iniyan and R. Goic. Sustain. Energy Rev. 2011, 15, 1625–1636.
7. I. L. Granone, F. Sieland, N. Zheng, R. Dillert and D. W. Bahnemann. Green Chem. 2018, 20, 1169-1192.
8. Q. Wang and K. Domen. Chem. Rev. 2020, 120, 2, 919-985.
9. W. Tu, Y. Zhou and Z. Zou. Adv. Mater. 22014, 6, 4607–4626.
10. H. Nakanishi, K. Iizuka, T. Takayama, A. Iwase and A. Kudo. ChemSusChem 2017, 10, 112–118.
11. A. Anzai, N. Fukuo, A. Yamamoto and H. Yoshida. Catal. Commun. 2017, 100, 134–138.
12. R. Pang, K. Teramura, H. Tatsumi, H. Asakura, S. Hosokawa and T. Tanaka. Chem. Commun 2018, 54, 1053-1056.
13. Z. Wang, K. Teramura, S. Hosokawa and T. Tanaka. J. Mater. Chem. A 2015, 3, 11313-11319.
14. Y. Kawaguchi, M. Akatsuka, M. Yamamoto, K. Yoshida A. Ozawa, Y. Kato and T. Yoshida. J. Photochem. Photobiol. A Chem. 2018, 358, 459–464.
15. Q. Li, Y. Zhang, L. Zhang, J. Xia, X. Liu, L. Hu, F. Wang, X. Chu, P Zhao, J. Yin and D. Yang. Catal. Commun. 2019, 120, 23–27.
16. Z. Huang, K. Teramura, H. Asakura, S. Hosokawa and T. Tanaka. J. Mater. Chem. A 2017, 5, 19351–19357.
17. Tatsumi, H. K. Teramura, Z. Huang, Z. Wang, H. Asakura, S. Hosokawa and T.

Tanaka. Langmuir 2017, 33, 13929–13935.

18. S. Iguchi, Y. Hasegawa, K. Teramura, S. Kidera, S. Kikkawa, S. Hosokawa, H. Asakura and T. Tanaka. Sustainable Energy Fuels 2017, 1, 1740-1747.
19. K. Teramura, Z. Wang, S. Hosokawa, , Y. Sakata and T. Tanaka. Chem. A Eur. J. 2014, 20, 9906–9909.
20. Z. Wang, K. Teramura, Z. Huang, S. Hosokawa, Y. Sakata and T. Tanaka. Catal. Sci. Technol 2014, 6, 1025.
21. B. Chen, X. Jiao and D. Chen. Crystal Growth & Design 2010, 10, 3378–3386.
22. J. Zhang, H. Liu, Z. Wang and N. Ming. Adv. Funct. Mater. 2007, 17, 3295–3303.
23. J. N. Díaz de León. Appl. Catal. B Environ. 2016, 181, 524–533.
24. S. Mandal, K. Arts, H. C. M. Knoops, J. A. Cuenca, G. M. Klemencic and O. A. Williams. Carbon 2021, 181, 79–86.
25. S. Kokura, O. Handa, T. Takagi, T. Ishikawa, Y. Naito and T. Yoshikawa. Nanomedicine: NBM 2010, 6, 570–574.
26. S. Magdassi, A. Bassa, Y. Vinetsky and A. Kamyshny. Chem. Mater. 2003, 15, 2208-2217.
27. L. Xu, G. Han, J. Hu, Y. He, J. Pan, Y. Li and J. Xiang. Phys. Chem. Chem. Phys. 2009, 11, 6490-6497.
28. A. Barthel, J. Roberts, M. Napari, M. Frentrup, T. Huq, A. Kovacs, R. Oliver, P. Chalker, T. Sajavaara and F. Massabuau. Micromachines 2020, 11, 1–11.
29. M. Mohamed, I. Unger, C. Janowitz, R. Manzke, Z. Galazka, R. Uecker and R. Fornari. J. Phys. Conf. Ser. 2011, 286, 012027.

Summary

In this thesis, the author has discussed the development of effective cocatalysts for the photocatalytic conversion of CO_2 using H_2O as the electron donor. Focusing on the CO evolution selectivity and activity over Ta- and Ga-based photocatalysts, cocatalysts including the chromates ions, Zn(Cd)-based non-metal compounds and Ag nanoparticles have been studied. A general conclusion of this thesis is described as follows.

Chapter 1. The formation rate and selectivity of CO evolution for the photocatalytic conversion of CO_2 by H_2O as an electron donor over $ZnTa_2O_6$ was improved by the in situ addition of trace amounts of chromate ions. The selectivity toward CO evolution was achieved at 80% and the formation rate of CO (6.0 μmol h^{-1}; 0.1 g) was maintained well in comparison with Ag cocatalyst which was widely used. The $ZnTa_2O_6$ photocatalysts fabricated in this study contained two types of active surfaces with stoichiometric and Zn-excessive Zn:Ta ratios, respectively. The active sites of the synthesized $ZnTa_2O_6$ shifted from stoichiometric to Zn-excessive surfaces during the in-situ photodeposition of chromates.

Chapter 2. The effect of the in situ addition of chromate ions on the evolution of H_2 during the photocatalytic conversion of CO_2 in the presence of H_2O over a series of Ta- and Ga-based photocatalysts were investigated. The in situ addition of chromate ions suppressed the evolution of H_2 when the photocatalyst surfaces were highly protonated. It was because chromate ions adsorbed on the surface of the photocatalysts acted as recombination centers for photogenerated electrons and holes. In contrast, the in situ addition of chromate ions was found to enhance the evolution of H_2 during reactions when the concentration of H^+ was low near the photocatalyst surface. It was because the chromate-adsorbed $Cr(OH)_3$ shell on the surface acted as a corrosion inhibitor, suppressing the backward reduction of the produced O_2 into H_2O.

Chapter 3. $Zn(OH)_2$ was found to be a promising cocatalyst for the photoreduction of CO_2 using H_2O as the electron donor. $Zn(OH)_2$ showed excellent activity and

selectivity toward CO evolution over a series of Ta- and Ga-based photocatalysts. Dissolved Zn ions and ZnO-rich surfaces were found to be critical factors for CO evolution. To the best knowledges of the author, $Zn(OH)_2$ is the only candidate cocatalyst identified to date that performs as well as Ag.

Chapter 4. A series of non-metal cocatalysts were mapped. It was found that Si-, Mg-, Zn-, and Ga-based cocatalysts enhanced the evolution of CO over Ta- and Ga-based photocatalysts. Among them, Zn-based cocatalysts showed the best performance for the photocatalytic conversion of CO_2 using H_2O as an electron donor. The counter anions, such as $(Ga_2O_4)^{2-}$, SiO_3^{2-}, NO_3^-, and PO_4^{3-}, in the Zn-based compounds influenced their catalytic performance in the evolution of CO, both in terms of stability and activity. Conversely, Zn-based cocatalysts showed no effect on Nb- and Ti-based photocatalysts.

Chapter 5. $Cd(OH)_2$ exhibited excellent catalytic performance during the selective photocatalytic conversion of CO_2 into CO using H_2O as an electron donor on various photocatalysts, such as Ga_2O_3, $NaTaO_3$, Ta_2O_5, and $ZnGa_2O_4$. The performance of the Cd^{2+} co-catalyst was significantly affected by the type of the counter anions. It is considered that Cd^{2+} ions effectively protected the catalytically active sites, generating CO as a product of O_2 poisoning during the reaction.

Chapter 6. The Ag-loaded $NaTaO_3$ photocatalyst was used for the photocatalytic conversion of CO_2 using H_2O as an electron donor. The size of the Ag nanoparticles was tuned by the photodeposition time, and large Ag nanoparticles resulted in high CO selectivity. The Ag-loaded $NaTaO_3$ catalyst showed poor stability in terms of CO selectivity at all Ag loading amounts. It was because the Ag nanoparticles underwent a polycrystalline to single crystalline transition. The changes to the morphology of the Ag nanoparticles during the photocatalytic reaction could be prevented by covering them with a chromium (III) shell. Using this strategy, the CO selectivity was maintained.

Chapter 7. The amounts and loading methods of Ag nanoparticles, including chemical reduction, photodeposition, and impregnation, were optimized on commercial Ga_2O_3 (composite of α-Ga_2O_3 and β-Ga_2O_3) as well as pure α-Ga_2O_3 and β-Ga_2O_3

photocatalysts for the photocatalytic conversion of CO_2 using H_2O as the electron donor. High selectivity towards CO evolution was achieved for this reaction when the proper catalyst amounts and loading methods were controlled on β-Ga_2O_3. The high CO evolution selectivity was determined to largely depend on the amount of the photocatalyst present. A large amount of Ag-loaded β-Ga_2O_3 enhanced active site poisoning for the evolution of H_2 via O_2 reduction, indirectly promoting selectivity toward CO evolution.

Publications

Chapter 1

This is the peer-reviewed version which has been published in final form at DOI: 10.1016/j.apcatb.2021.120508.

1. Shift of active sites via in-situ photodeposition of chromate achieving highly selective photocatalytic conversion of CO_2 by H_2O over $ZnTa_2O_6$

   Xuanwen Xu, Kentaro Teramura, Hiroyuki Asakura, Saburo Hosokawa, and Tsunehiro Tanaka.

   Applied Catalysis B: Environmental, 2021, 298, 120508.

Chapter 2

This is the peer-reviewed version which has been published at DOI: 10.1016/j.cattod.2022.05.045.

2. Effect of the in situ addition of chromate ions on H_2 evolution during the photocatalytic conversion of CO_2 using H_2O as the electron donor

   Xuanwen Xu, Hiroyuki Asakura, Saburo Hosokawa, and Tsunehiro Tanaka, Kentaro Teramura.

   Catalysis Today, accepted.

Chapter 3

This is the peer-reviewed version which has been published in final form at DOI: 10.1002/cctc.202100633.

3. Development of zinc hydroxide as an abundant and universal cocatalyst for the selective photocatalytic conversion of CO_2 by H_2O

   Xuanwen Xu, Kentaro Teramura, Hiroyuki Asakura, Saburo Hosokawa, and Tsunehiro Tanaka.

   ChemCatChem 2021, 13, 4313-4317.

Chapter 4

4. Exploring effective non-metal inorganic cocatalysts for the photocatalytic conversion of CO_2 using H_2O as an electron donor

   Xuanwen Xu, Hiroyuki Asakura, Saburo Hosokawa, and Tsunehiro Tanaka, Kentaro Teramura.

   Langmuir, submitted.

Chapter 5

5. Cadmium hydroxide universal cocatalyst for the selective evolution of CO during the photocatalytic conversion of CO_2 using H_2O as an electron donor

   Xuanwen Xu, Tsunehiro Tanaka, and Kentaro Teramura

   ACS Catalysis, submitted.

Chapter 6

6. Tuning Ag-modified $NaTaO_3$ to achieve high CO selectivity for the photocatalytic conversion of CO_2 using H_2O as the electron donor

   Xuanwen Xu, Hiroyuki Asakura, Saburo Hosokawa, and Tsunehiro Tanaka, Kentaro Teramura.

   Applied Catalysis B: Environmental, submitted.

Chapter 7

7. High selectivity toward CO evolution for the photocatalytic conversion of CO_2 by H_2O as an electron donor over Ag-loaded β-Ga_2O_3

   Xuanwen Xu, Tsunehiro Tanaka, and Kentaro Teramura

   ACS Sustainable Chemistry & Engineering, submitted.